Towards a global modelling of transit spectroscopy for a better characterisation of exoplanet atmospheres in young and main-sequence stars

William Dethier

To cite this version:

William Dethier. Towards a global modelling of transit spectroscopy for a better characterisation of exoplanet atmospheres in young and main-sequence stars. Astrophysics [astro-ph]. Université Grenoble Alpes [2020-..], 2023. English. NNT : 2023GRALY054 . tel-04457261

HAL Id: tel-04457261
https://theses.hal.science/tel-04457261v1

Submitted on 14 Feb 2024

THÈSE

Pour obtenir le grade de

DOCTEUR DE L'UNIVERSITÉ GRENOBLE ALPES

École doctorale : PHYS - Physique
Spécialité : Astrophysique et Milieux Dilués
Unité de recherche : Institut de Planetologie et d'Astrophysique de Grenoble

Vers une modélisation globale de la spectroscopie de transit pour une meilleure caractérisation des atmosphères d'exoplanètes autour d'étoiles jeunes et de la séquence principale

Towards a global modelling of transit spectroscopy for a better characterisation of exoplanet atmospheres in young and main-sequence stars

Présentée par :

William DETHIER

Direction de thèse :

Jérôme BOUVIER DIRECTEUR DE RECHERCHE, CNRS DELEGATION ALPES	Directeur de thèse
Vincent BOURRIER Université de Genève	Co-encadrant de thèse

Rapporteurs :

MARIA ROSA ZAPATERO OSORIO
PROFESSEURE, CENTRO DE ASTROBIOLOGIA, CSI-CINTA
NUNO C. SANTOS
ASSISTANT PROFESSOR, UNIVERSIDADE DO PORTO

Thèse soutenue publiquement le **17 novembre 2023**, devant le jury composé de :

ISABELLE BOISSE ASTRONOME ADJOINTE, AIX-MARSEILLE UNIVERSITE	Examinatrice
XAVIER DELFOSSE ASTRONOME, UNIVERSITE GRENOBLE ALPES	Président
CHRISTOPHE LOVIS ASSOCIATE PROFESSOR, UNIVERSITE DE GENEVE	Examinateur
MARIA ROSA ZAPATERO OSORIO PROFESSEURE, CENTRO DE ASTROBIOLOGIA, CSI-CINTA	Rapporteure
NUNO C. SANTOS ASSISTANT PROFESSOR, UNIVERSIDADE DO PORTO	Rapporteur

Invités :

VINCENT BOURRIER
ASSISTANT PROFESSOR, UNIVERSITE DE GENEVE

Abstract

Transit spectroscopy has led to outstanding progress in understanding and characterising the atmosphere of exoplanets. Analysing their absorption spectrum is one of the main diagnostics to study their properties and has provided valuable insights for our comprehension of planetary evolution. However, it has been recently highlighted that faithfully identifying absorption signatures of an atmosphere in absorption spectra is not straightforward. Indeed, the variation of the stellar spectrum over the apparent stellar surface (e.g. stellar rotation and centre-to-limb variations) introduces residual spectral features in the absorption spectrum akin to the signature of an atmosphere. These stellar contaminations can potentially mislead the interpretations of transit observations and jeopardise the quality of the derived atmospheric properties.

In this thesis, I examine in detail these stellar contaminations, their origin, their behaviour, and, in particular, their impact on atmospheric absorption signatures. To this end, I used and developed a global approach with the EVaporating Exoplanets (EVE) code, which consists in modelling self-consistently the delicate interplay between the transiting planet, its atmosphere and the stellar spectrum they absorb. As examples, I focus on two species that are commonly studied by the community, namely, sodium and helium. They are both tracers of complementary layers of planetary atmospheres; helium, in particular, being a tracer of atmospheric escape, relevant for planetary evolution.

Throughout the whole thesis, I demonstrate the relevance, flexibility and necessity of such a global approach, one in which the star, the planet and its atmosphere, their environment and the observer have equal importance. I do so by deriving novel results and interpretations about the atmosphere of two well-known exoplanets of particular interest, HD 209458 b and MASCARA-1 b, but also via applications to hypothetical transiting planets in young stars embedded in protoplanetary discs.

This thesis work establishes solid bases for improving and facilitating future exoplanetary atmospheric characterisations and, ultimately, our knowledge and understanding of the plethora of worlds that surround us.

Résumé

La spectroscopie de transit a permis des progrès remarquables dans la compréhension et la caractérisation des atmosphères exoplanétaires. L'analyse de leur spectre d'absorption est l'un des principaux diagnostics permettant d'étudier leurs propriétés et qui nous permet d'obtenir des informations précieuses pour notre compréhension de l'évolution de ces planètes. Cependant, il a été récemment mis en évidence qu'il n'est pas simple d'identifier de manière fidèle les signatures d'absorption d'une atmosphère dans les spectres d'absorption. En effet, la variation du spectre stellaire sur la surface stellaire apparente (par exemple, la rotation stellaire et les variations centre-bord) introduit des signatures spectrales résiduelles dans le spectre d'absorption qui s'apparentent à celles d'une atmosphère. Ces contaminations stellaires peuvent potentiellement induire des erreurs d'interprétation des observations de transit et compromettre la qualité des propriétés atmosphériques qui en sont déduites.

Dans cette thèse, j'examine en détail ces contaminations stellaires, leur origine, leur comportement et, en particulier, leur impact sur les signatures d'absorption atmosphérique. Pour cela, j'ai utilisé et développé une approche globale avec le code EVaporating Exoplanets (EVE), qui consiste à modéliser de manière autocohérente la délicate interaction entre la planète en transit, son atmosphère et le spectre stellaire qu'elles absorbent. À titre d'exemple, je me concentre sur deux espèces couramment étudiées par la communauté, à savoir le sodium et l'hélium. Ils sont tous deux des traceurs de couches complémentaires des atmosphères planétaires; l'hélium, en particulier, est un traceur de l'échappement atmosphérique, phénomène important dans l'étude de l'évolution planétaire.
Tout au long de la thèse, je démontre la pertinence, la flexibilité et la nécessité d'une telle approche globale, dans laquelle l'étoile, la planète, son atmosphère, leur environnement et l'observateur ont une importance égale. Je le fais en obtenant de nouveaux résultats et interprétations sur l'atmosphère de deux exoplanètes bien connues et d'un intérêt particulier, HD 209458 b et MASCARA-1 b, mais aussi via des applications à d'hypothétiques planètes en transit autour d'étoiles jeunes enfouies dans leur disque protoplanétaire.

Ce travail de thèse établit des bases solides pour améliorer et faciliter les futures caractérisations atmosphériques des exoplanètes et, finalement, notre connaissance et notre compréhension de l'abondance de mondes qui nous entourent.

Acknowledgement

I would like to thank my two supervisors, Dr. Jérôme Bouvier and Dr. Vincent Bourrier. They are at the origin of this project and I want to thank them for trusting my capability to achieve the objectives they had established. I also thank them for giving me their support when I needed some and especially for making themselves available even during the twelve months of mandatory teleworking. I am grateful that they gave me the opportunity to work on this subject in such facilitated environments and I am grateful of the confidence they had in me during these three years and a half.

I would like to thank Dr. María Rosa Zapatero Osorio and Dr. Nuno C. Santos for having dedicated their time to review and examine this thesis manuscript. I also thank the other members of the jury, Dr. Isabelle Boisse, Dr. Christophe Lovis and the president of the jury Dr. Xavier Delfosse for accepting to be part of the jury of this thesis. The questions and the comments that each member of the jury asked and made were constructive and made me go deeper into the thinking about the results I presented.

I want to say an immense thank you to Dr. Benjamin Tessore. He has helped me in my work on a daily basis. I have learned a lot through long discussions with him on various topics. If it was not for him there would have been several things in my work that I would not have been able to concretise. He was always there to motivate me when in doubt and he never doubted me. I could never thank him enough. He has become a true friend along the way.

I thank all the SPIDI members, Alana, Anthony, George, Kim, Noemi and Rajeev they have been the nicest to me and made the workplace a serene environment. I also thank them for the numerous discussions, questions and comments about the work I conducted.Each of them has become more than a coworker.

I especially thank my partner, Ariana, who has always been there to support me in many ways and never doubted my choices. She has accompanied me on this journey and managed to make it easier.

I would like to thank the people from the GAD at IPAG who offer psychological support and who are open for discussions about personal issues.

I thank the University of Geneva who has given me permission for the purpose of my work, to use and develop the numerical code EVaporating Exoplanets. I thank all the people from the Geneva observatory for the good times I had every time I visited. Danny who provided me with nice plots to use in the manuscript of my thesis. Casper who gave me advice on spectrographs. Michal who provided me with great observed spectra of MASCARA-1, that I used in this work. Omar for psychological support. Yassin for all the discussions on the EVE code, for all the rides to the observatory and for introducing me to the rest of the team and also for all the Swiss francs he exchanged me. Mathilde for the long discussions about a lot of stuffs.

I thank the staff of the IPAG. Especially, David Gillier who has helped me with technical issues on several occasions. Valérie Chopin who has helped me with administrative tasks and curiosities. Martina Angelini and Claire Dupoux who have made the SPIDI team run smooth.

I thank the University of Grenoble Alpes and Prof. Thibaut Devillers for giving me the opportunity the teach instrumental optics classes to first year biology students.

I dearly thank Dr. Nuria Casasayas-Barris for sharing with me transit observational data of two systems that I used in my publication and in this thesis.

I want to thank all the persons who gave me support of any kind to complete this work.

Finally, I thank any person who will read this work and hope they enjoy it.

This work has made use of the MARCS and VALD database, operated at Uppsala University, the Institute of Astronomy RAS in Moscow, and the University of Vienna. This work has intensively made use of the Turbospectrum code for spectral synthesis. I therefore thank Dr. Bertrand Plez and the collaborators for making this tool publicly available as it has greatly helped me in my work.

This thesis has received funding from the European Research Council (ERC) under the European Union’s Horizon 2020 research and innovation programme (grant agreement No 742095; SPIDI: Star-Planets-Inner Disk Interactions, `http://www.spidi-eu.org`)

Remerciements

Je tiens à remercier mes deux superviseurs, le Dr Jérôme Bouvier et le Dr Vincent Bourrier. Ils sont à l'origine de ce projet et je tiens à les remercier d'avoir eu confiance en ma capacité à atteindre les objectifs qu'ils avaient fixés. Je les remercie également de m'avoir apporté leur soutien quand j'en avais besoin et surtout de s'être rendus disponibles même pendant les douze mois de télétravail obligatoire. Je leur suis reconnaissant de m'avoir donné l'opportunité de travailler sur ce sujet dans un environnement aussi privilégié et je leur suis reconnaissant de la confiance qu'ils ont eue en moi pendant ces trois ans et demi.

Je tiens à remercier le Dr María Rosa Zapatero Osorio et le Dr Nuno C. Santos pour le temps qu'ils ont consacré à la relecture et à l'examen de ce manuscrit de thèse. Je remercie également les autres membres du jury, Dr. Isabelle Boisse, Dr. Christophe Lovis et le président du jury Dr. Xavier Delfosse d'avoir accepté de faire partie du jury de cette thèse. Les questions et les commentaires que chaque membre du jury a posés et faits ont été constructifs et m'ont permis d'approfondir la réflexion sur les résultats que j'ai présentés.

Je tiens à dire un immense merci au Dr. Benjamin Tessore. Il m'a aidé dans mon travail au quotidien. J'ai beaucoup appris grâce aux longues discussions que j'ai eues avec lui sur différents sujets. Sans lui, il y aurait eu plusieurs choses dans mon travail que je n'aurais pas pu concrétiser. Il a toujours été là pour me motiver en cas de doute et il n'a jamais douté de moi. Je ne pourrai jamais le remercier assez. Il est devenu un véritable ami au fil du temps.

Je remercie tous les membres de SPIDI, Alana, Anthony, George, Kim, Noemi et Rajeev, qui ont été si accueillants avec moi et ont fait du lieu de travail un environnement serein. Je les remercie également pour les nombreuses discussions, questions et commentaires sur le travail que j'ai effectué. Chacun d'entre eux est devenu plus qu'un collègue de travail.

Je remercie tout particulièrement ma compagne, Ariana, qui a toujours été là pour me soutenir à bien des égards et qui n'a jamais douté de mes choix. Elle m'a accompagné dans cette aventure et a réussi à le rendre plus facile.

Je remercie les personnes du GAD de l'IPAG qui offrent un soutien psychologique et qui sont ouvertes à la discussion sur des sujets personnels.

Je remercie l'Université de Genève qui m'a donné la permission, dans le cadre de mon travail, d'utiliser et de développer le code numérique EVaporating Exoplanets. Je remercie toutes les personnes de l'observatoire de Genève pour les bons moments que j'ai passés à chaque fois que j'y suis allé. Danny qui m'a fourni de jolies figures à utiliser dans le manuscrit de ma thèse. Casper qui m'a donné des conseils sur les spectrographes. Michal qui m'a fourni d'excellents spectres observés de MASCARA-1, que j'ai utilisés dans ce travail. Omar pour son soutien psychologique. Yassin pour toutes les discussions sur le code EVE, pour tous les trajets vers l'observatoire et pour m'avoir présenté au reste de l'équipe, ainsi que pour tous les francs suisses qu'il m'a échangés. Mathilde pour les longues discussions sur un tas de choses.

Je remercie le personnel de l'IPAG. En particulier, David Gillier qui m'a aidé à plusieurs reprises sur des questions techniques. Valérie Chopin qui m'a aidé pour dans de curieuses tâches administratives. Martina Angelini et Claire Dupoux qui ont assuré le bon fonctionnement de l'équipe SPIDI.

Je remercie l'Université de Grenoble Alpes et le Prof. Thibaut Devillers pour m'avoir donné l'opportunité de donner des cours d'optique instrumentale aux étudiants de première année de biologie.

Je remercie vivement le Dr. Nuria Casasayas-Barris d'avoir partagé avec moi les données d'observation de transit de deux systèmes que j'ai utilisées dans ma publication et dans cette thèse.

Je tiens à remercier toutes les personnes qui m'ont apporté leur soutien, quel qu'il soit, pour mener à bien ce travail.

Enfin, je remercie toutes les personnes qui liront ce travail et j'espère qu'elles l'apprécieront.

Ce travail a utilisé les bases de données MARCS et VALD, exploitées à l'Université d'Uppsala, à l'Institut d'astronomie RAS de Moscou et à l'Université de Vienne. Ce travail a fait un usage intensif du code Turbospectrum pour la synthèse spectrale. Je remercie donc le Dr Bertrand Plez et ses collaborateurs d'avoir mis cet outil à la disposition du public, car il m'a grandement aidé dans mon travail.

Cette thèse a été financée par le Conseil européen de la recherche (ERC) dans le cadre du programme de recherche et d'innovation Horizon 2020 de l'Union européenne

(accord de subvention n° 742095 ; SPIDI : Star-Planets-Inner Disk Interactions, http://www.spidi-eu.org).

Contents

List of notations

CLV : centre-to-limb variations

BLD : broadband limb darkening

LOS: line of sight

$\boldsymbol{i_{\mathrm{pl}}}$: planetary orbital inclination

$\boldsymbol{\lambda_{\mathrm{pl}}}$: sky-projected spin orbit angle of the planet

$\boldsymbol{i_{*}}$: stellar inclination. Angle between stellar rotation axis and LOS of an observer

$\mathbf{v_{eq}}$: stellar equatorial rotational velocity

$\mathbf{v_{eq}\sin(\boldsymbol{i_{*}})}$: sky-projected stellar rotational velocity

$\mathbf{F_{out}}$: out-of-transit spectrum

$\mathbf{F_{in}}$: in-transit spectrum

$\mathbf{F_{abs}}$: absorbed spectrum

$\boldsymbol{\mathcal{A}}$: absorption spectrum

$\mathbf{F_{loc}}$: local stellar spectrum from the planet-occulted region

$\mathbf{A_{\odot}}$: solar abundance

AU: astronomical unit

cTTs: classical T Tauri star

GIANO : infrared high resolution spectrograph mounted at Telescopio Nazionale Galileo located at Roque de Los Muchachos Observatory, La Palma, Spain

ESPRESSO : optical Echelle SPectrograph for Rocky Exoplanets and Stable Spectroscopic Observations installed at the Very Large Telescope, Atacama Desert, Chile

SPIRou : near-infrared spectropolarimeter installed at the Canada-France-Hawaii Telescope (CFHT), Maunakea, Hawaii

HARPS : High Accuracy Radial Velocity Planet Searcher, high-precision echelle planet-finding spectrograph installed at La Silla Observatory, Chile

Kepler: space-based telescope

CHEOPS: CHaracterising ExOPlanets Satellite, space-based telescope

TESS: Transiting Exoplanet Survey Satellite, space-based telescope

CoRoT: Convection, Rotation et Transits planétaires, space-based telescope

HST: Hubble space telescope, space-based spectrograph operating from UV to infrared wavelengths

Spitzer: space-based telescope and spectrograph operating in infrared wavelengths

JWST: James Webb space telescope, space-based telescope operating in the infrared wavelengths

EVE: EVaporating Exoplanets. A numerical code to simulate transiting planets and atmospheres

Introduction

1

The discovery of planets outside our own solar system has established a whole new field of research and has transformed our comprehension of the universe and the place humans occupy in it. Once again, our anthropocentrism has been undermined; hinting at the possibility that humanity might not be unique and alone. With the continuously growing number of confirmed exoplanets, more than 5 000[1] at the time of the redaction of this manuscript, researchers, driven by the human nature of constantly seeking to comprehend what surrounds us, have unveiled a vast richness of diverse exoplanetary systems. Some of these systems are the host to multiple planets, to gas giant planets similar in size to Jupiter and Neptune, to rocky planets with the size of Earth and Mars and to planets orbiting multiple stars. Some of these exoplanets were even found orbiting in the temperate zone of their host star, where they could, in theory, harbour liquid water, which is essential for the emergence of life as we know it on Earth. All the new areas of study that emerged from these discoveries allow today's astronomers to build a broader understanding of our own world not as a unique piece but as being part of a whole.

Legitimately, to the eyes of the general public, the study of exoplanets, at first glance, might seem unnecessary and not useful to society. However, there are many reasons that motivate astronomers to do so. As mentioned above, the exoplanetary systems discovered are various and, most of the time, quite different from our solar system. This finding raises questions about the evolution and formation process of planets in general, and studying exoplanets could help understand how Earth and its companions have formed and why they are placed in such a configuration. In turn, studying exoplanets around stars that are similar to the past, current and future Sun might help us understand how planets react under different stellar conditions, which ultimately could give us some insights about the past and future of Earth.
Furthermore, observing exoplanets can lead astronomers to identify the characteristics of their atmospheres, such as their structure, the ranges of temperatures and pressures they can have, the different molecular and atomic compositions they are able to maintain and even their internal dynamics. Comparing these results from many exoplanets could provide clues about what makes Earth's atmospheric conditions so singular as to host life. Finally, the idea of life elsewhere in the universe has inspired science fiction for many decades and has deeply fuelled people's creativity.

---

[1] From the exoplanet.eu website, visited in August 2023.

In fact, a significant portion of the community aims at studying the habitability of extrasolar planets and even at detecting possible indicators of a form of life in their atmospheres. These particular studies have definitively made these thoughts seem more tangible, which eventually might revive the general public's interest and trust in such branches of science.

As mentioned above, atmospheres are undeniably open gateways to plenty of critical planetary properties, and astronomers have not waited long before they dived into their hunt. The first signs of the presence of an atmosphere around an exoplanet were detected on HD 209458 b half a decade after the first exoplanet, 51 Pegasi b, orbiting a main sequence star was found and confirmed (Mayor & Queloz 1995; Charbonneau et al. 2002). Among the many ways astronomers have found to tackle down the problem of studying objects so small, so dim, and so far (see, e.g. Perryman 2018), the transit technique has clearly demonstrated to be the most profitable one. Figures 1.1 and 1.2 show the distribution of planets detected so far in a diagram of radius and mass as a function of their orbital periods, respectively. Furthermore, transit spectroscopy, which studies the change in the spectrum of a star as a function of wavelength during the transit of a planet – either being in low or high spectral resolution – is a powerful technique that allows researchers to study in depth the atmospheric characteristics of exoplanets. Comparing the results of such observations with theoretical predictions and models has led to the detection of numerous atomic and molecular species (see Table 1 of Guillot et al. 2022). Moreover, the analyses of the absorption signatures that these species induce in the observational data when the exoplanetary atmosphere transits even allow for inferring the dynamical properties as well as the composition and thermal structure of these atmospheres (Wyttenbach et al. 2017; Seidel et al. 2020; Yan et al. 2020).

1.1 Motivation

Observing facilities and the instruments that they are equipped with are some of the most essential tools for astronomy. They are evolving and improving fast, allowing astronomers to have more opportunities to study exoplanets in better conditions through observational data of greater quality. In turn, the techniques and models used to post-process transit observations must be up to the quality of these data to permit the most faithful interpretations and characterisations of exoplanets and their atmospheres. However, in recent years, some crucial physics had been left out in most of these models. These omissions even led, in some cases, to potential false detections of atmospheric species. A concern that was properly brought to light by the work of Casasayas-Barris et al. (2020, 2021). At the origin of these misinterpretations is the oversight of critical stellar phenomena. These

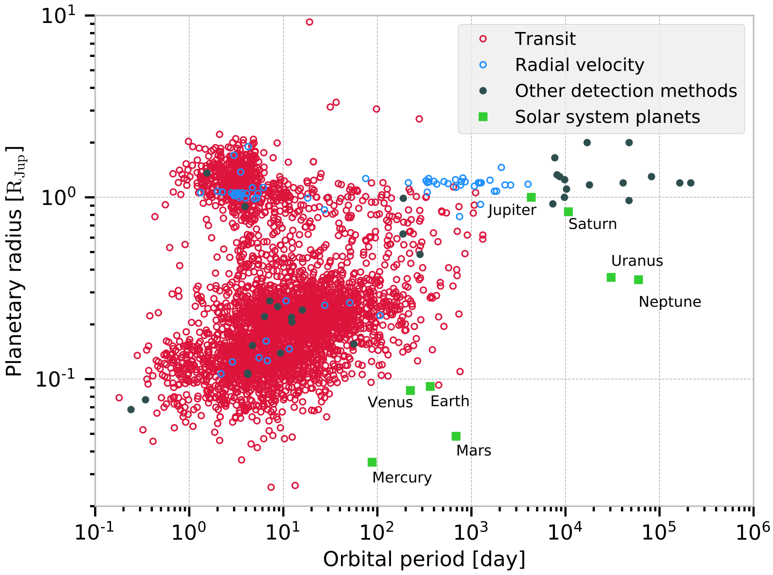

Fig. 1.1.: Planetary radius distribution as a function of the orbital period for confirmed exoplanets. The colours indicate different techniques of detection. Data are from exoplanet.eu using the API tutorial.

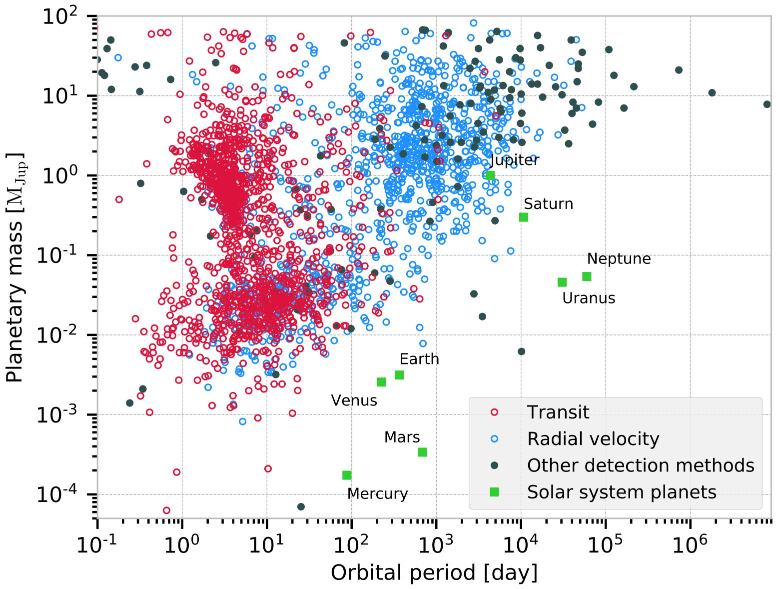

Fig. 1.2.: Planetary mass distribution as a function of the orbital period for confirmed exoplanets. The colours indicate different techniques of detection. Data are from exoplanet.eu using the API tutorial.

phenomena can actually induce some distortions in the absorption signature of a transiting planet. If these contaminations are not accounted for in the planetary transit models, then the interpretation of the atmospheric signal is subject to being compromised. Therefore, having a robust model for exoplanetary atmospheres is not sufficient. Without a proper model for the spectrum of the star, the values of temperature and density of specific planetary atmospheric elements that are extracted from spectroscopic observations could be inaccurate. Thus, there is a need to keep improving the models and tend towards simulations that account for the global picture of planetary transits so as to not focus only on specific parts of the phenomenon and ultimately lead to better characterisation of exoplanet atmospheres.

My thesis work is devoted to this endeavour. I used and upgraded a numerical code called EVaporating Exoplanet (EVE) (Bourrier & Lecavelier des Etangs 2013; Bourrier et al. 2015, 2016) to simulate realistic exoplanetary transits and study the absorption signatures that their atmosphere can create in high resolution spectroscopic observations.

One of my main objectives was to improve this code to account for a refined definition of the stellar spectrum it uses. This improvement allows the code to describe the local variations of the stellar spectrum over the apparent surface of the star with increased accuracy. In turn, it enables the code to generate more realistic synthetic transit observations. With this added feature, I was able to study in depth and better characterise the residual stellar contaminations that are present in transit absorption spectra.

Another one of my goals was to adapt the code to the environment of young stellar objects. As we study planetary atmospheres, we are interested in planets around main-sequence stars as they give us an insight into the current conditions on planets that are close in age to Earth. However, it is also interesting to look at very young planets in order to have a view of the initial conditions of planets at the time of their birth. Studying planets at all ages allows, once again, for a broader picture and understanding of the evolution of the conditions in planetary atmospheres, which is complementary to studying planetary habitability and the emergence of life.

The study of planets around young stars is still an emerging field. So far, few planets have been detected in transit around stars younger than $\sim$ 25 Myr old. Notable examples are the systems V1298 Tau (David et al. 2019), K2-33 (Mann et al. 2016), AUMic (Plavchan et al. 2020), HD 114082 b (Zakhozhay et al. 2022), HIP 67522 b (Rizzuto et al. 2020) and TOI-1097 (Wood et al. 2023). Only a handful of planets have been discovered around infant stars younger than $\sim$ 6-7 Myr old, known as classical T Tauri stars, but none were detected in a transit configuration. One of the most plausible reasons is because these stars are still surrounded by a circumstellar disc of gas and dust, which can interfere with transiting planets (Hartmann et al. 2016). In an attempt to facilitate future detection of transiting planets around young stellar objects, I upgraded the EVE code to account for the presence of a circumstellar disc. This way I can better understand and characterise its implications on the observations of transiting planets around such stars.

1.2 Thesis Structure

This manuscript is divided into four main chapters besides the introduction and conclusion. In Chapter 2, I introduce the scientific context of this thesis by concisely describing some key theoretical concepts relevant for the following chapters. In Chapter 3, I explore in depth the contamination effects that specific stellar phenomena induce in the extracted absorption signature of transiting exoplanetary atmospheres. Furthermore, I used a yet uncommon approach, based on the improvements I brought to the EVE code, to reinterpret existing transit data of two iconic and well-known exoplanets. In Chapter 4, I present a code I have developed to model the local stellar lines of the infrared He I triplet from observations of the stellar spectrum. In Chapter 5, I focus on young stellar objects and describe how I included the presence of a circumstellar disc in the EVE code. I also study the impact of this disc on the stellar contamination in the absorption signatures of transiting planets. Finally, I conclude this work with some perspectives and possible ways to keep improving analyses of planetary transit observations.

2

Scientific Background

In this chapter, the scientific context of my thesis is presented in a concise way, focusing on the key aspects relevant to my work, while more in-depth discussions and supplementary material can be found in the different references. I also introduce some fundamental theoretical concepts used in subsequent chapters to allow the reader to have the necessary background.

2.1 Planetary transits

The manifestation of a planetary transit is, in concept, a rather simple and straightforward physical phenomenon: a source of radiation, a star, is occulted by an opaque body that does not emit radiation, a planet. As a consequence, the initial amount of radiation received by an observer decreases (see Figure 2.1). Due to its orbital motion around its host star, a planet periodically passes by the same position, and if the geometrical configuration is adequate, an observer is able to witness a transit phenomenon on a recurring basis (see Figure 2.2). The chances for a planet to cross the line of sight of an observer looking at a star are rather slim, as it approximates to about the ratio of the stellar radius to the semi-major axis for planets on a circular orbit (Seager & Dotson 2010; Perryman 2018) ($\sim$0.5% for an Earth-sized planet orbiting a Sun-sized star at 1 AU). However, seven out of ten confirmed planets, so far, are in a transit configuration[1]. The high percentage of planets detected transiting their host star, despite the low observational probability, is in part due to the observational technique of transit photometry. Photometry aims at observing the faint decrease in the received amount of light when a planet transits the star. The yield of this technique was enhanced by space-based observatories such as CoRoT[2], Kepler[3], TESS[4] or CHEOPS[5]. Being in space gives these telescopes a few advantages to detect the faint signatures of a planetary transit. Their sensitivity is enhanced and they have the possibility to monitor large samples of stars repetitively and over long periods. Such observations allow for precise measurements of the flux of the observed stars and an accurate knowledge of their variations over time. This

---

[1] exoplanet.eu

[2] `https://www.esa.int/Science_Exploration/Space_Science/COROT_overview`

[3] `https://www.nasa.gov/mission_pages/kepler/overview/index.html`

[4] `https://www.nasa.gov/content/about-tess`

[5] `https://www.esa.int/Science_Exploration/Space_Science/Cheops/Cheops_overview2`

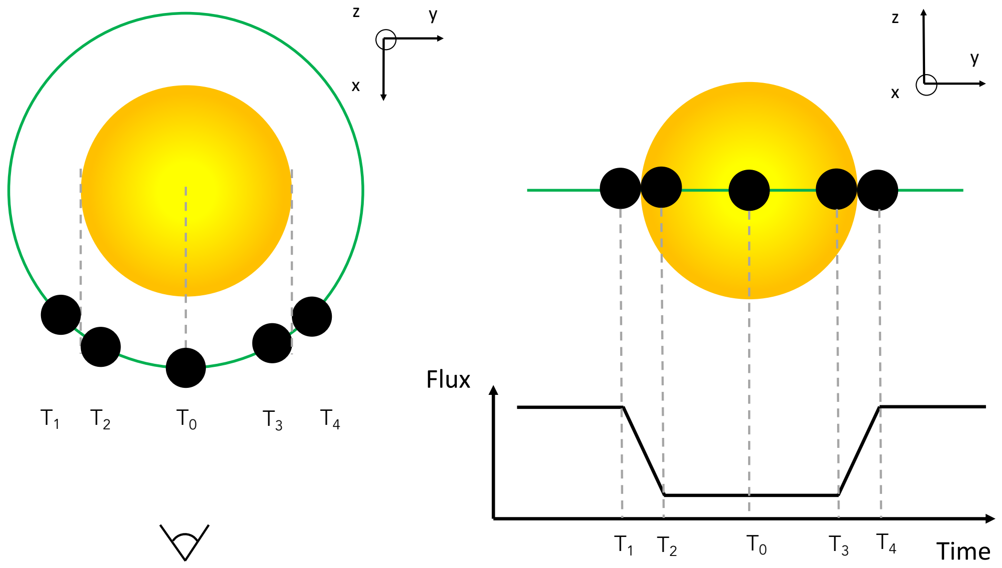

Fig. 2.1.: Sketch illustrating the five key times of a planetary transit for a circular aligned planetary orbit and an impact parameter of zero. It also shows that the flux received by a distant observer varies during the transit. The observer is placed along the x axis. Pole-on view of the orbit (left), edge-on view of the orbit (right). Adapted from Seager & Dotson (2010).

enhances the detectability of every slight change in their flux, which in some cases can be attributed to transit phenomena. So far, these four instruments have led to the detection of about 3700 transiting exoplanets[6] (only TESS and CHEOPS are still active out of these four instruments).

2.1.1 Transits as a means to characterise exoplanetary atmospheres

The photometric analysis of transiting planets offers more than just their detection. It gives us access to fundamental parameters, such as the planetary radius (Seager & Mallén-Ornelas 2003), which are crucial to understanding the formation and evolution of the planet. In addition, spectroscopic studies during a transit offer the possibility to probe the atmosphere of the planet, encoding key information on its internal composition, structure and dynamics. As the planet moves on its orbit in front of its host star, its atmosphere follows it as it is gravitationally bound to it. The atmosphere thus also absorbs part of the stellar radiation over an annulus region, which corresponds to the projection of the planetary atmosphere onto the plane of the sky. If it has optically thick layers, for example, the deep and dense layers, it can produce an increase of the apparent planetary absorbing radius over broad regions of the stellar spectrum (see Figure 2.3). On the contrary, if the atmosphere has

---

[6] `https://exoplanets.nasa.gov/discovery/exoplanet-catalog/`

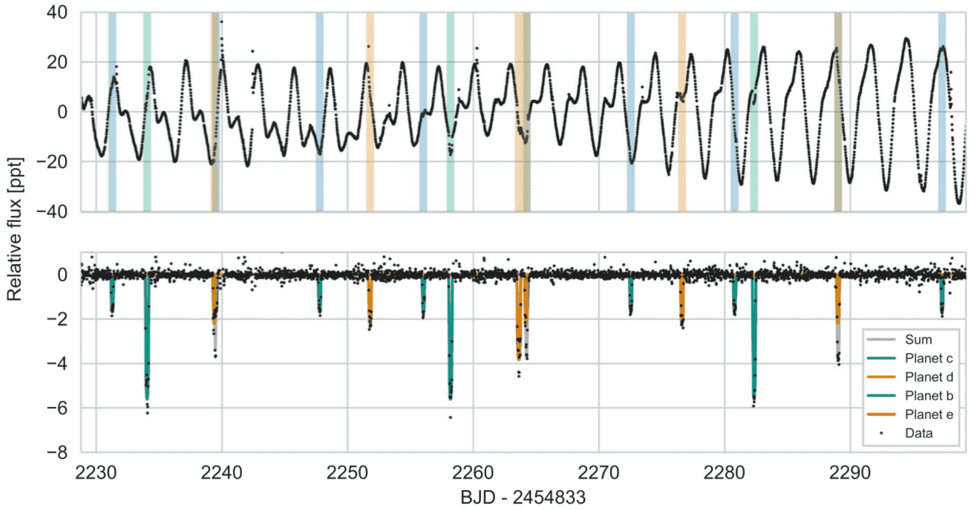

Fig. 2.2.: Real example of a lightcurve taken with Kepler, of a transiting planetary system with four planets. The different colours show the different planets. The black points represent the actual observed data points. Taken from Figure 1 of David et al. (2019).

optically thin layers, for example, the high altitude tenuous regions, it can produce additional absorption lines in the stellar spectrum, that is, on very narrow regions of the spectrum (see Figure 2.4).

A spectroscopic monitoring of the planet during a transit is necessary to detect these changes in the stellar spectrum at specific wavelengths. In this context, transit spectroscopy is preferred over photometric transit observations. Depending on the spectral resolution of the observations, spectroscopy allows for the detection of atomic and molecular species in the atmospheres of exoplanets. For example, high resolution transit spectroscopy allows for resolving individual spectral lines in the stellar spectrum. When the planet transits, if it contains a species in an optically thin region of its atmosphere, by absorbing the stellar radiation, the species creates additional spectral lines that add up to the observed stellar spectrum. The depth and width of the stellar lines for which the species has radiative transitions can thus increase. Because of the planetary motion and strong dynamics in the planetary and/or stellar atmospheres, the planetary species can create additional absorption lines outside of the observed stellar lines. By characterising these changes in the observed stellar spectrum and in the depth and width of individual spectral lines, astronomers are able to derive the properties of the species present in an exoplanet's atmosphere. Studying the properties of exoplanetary atmospheres is one of the best ways to get insights about the actual and current conditions on exoplanets. For example, by studying the spectra collected during transits over large wavelength bands, spectroscopy combined with atmospheric models can give access to the chemical composition of the planetary atmospheres and also to individual species density profiles (e.g. Guillot et al. 2022; Pluriel 2023). It also allows for deriving the

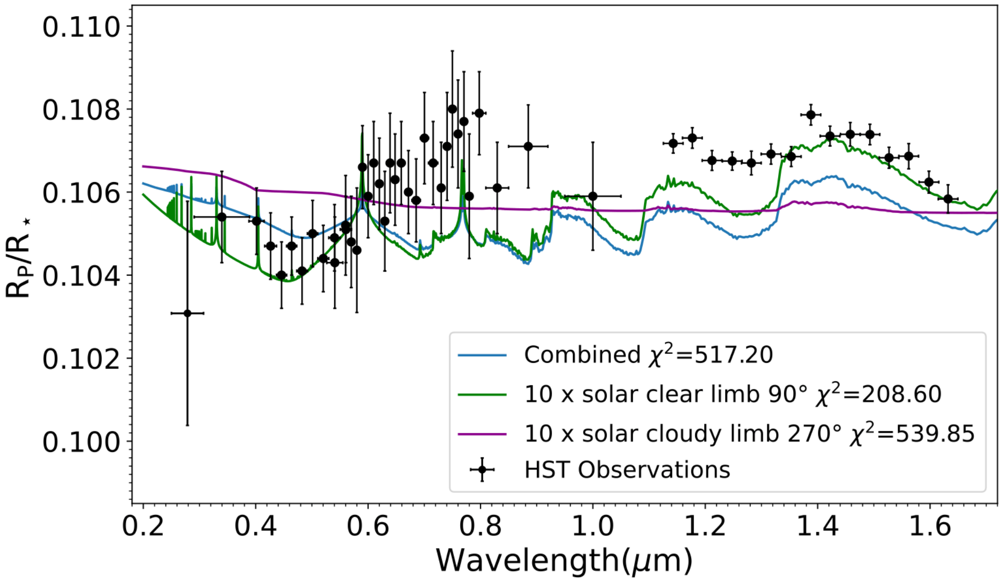

Fig. 2.3.: Low resolution transmission spectrum of the transit of the planet WASP-79 b computed from HST observations. It shows how a planetary atmosphere can absorb stellar light over a wide range of wavelengths and increase the measured planetary radius. Figure taken from Gressier et al. (2023).

temperature profiles and the dynamics of the atmosphere (e.g. Seidel et al. 2020; Ehrenreich et al. 2020). Finally, by targeting the absorption signatures of specific elements, it gives access to the current conditions of atmospheric escape on the planet, which is important knowledge to evaluate the temporal evolution of an exoplanet's atmosphere (e.g. Bourrier et al. 2016; Dos Santos et al. 2022; Czesla et al. 2022).

This is why high resolution spectroscopy has gained such a huge interest from the exoplanet community. Space-based observatories such as HST[7], Spitzer[8] or JWST[9] have the advantage of offering an access to the whole electromagnetic spectrum and are not prone to being impacted by atmospheric contamination. Nevertheless, they usually do not offer a spectral resolution that competes with ground-based observatories that are equipped with large aperture telescopes and high resolution spectrographs such as ESPRESSO[10], HARPS[11] or SPIRou[12]. The general purpose of a spectrograph is to separate a polychromatic light ray into monochromatic light rays, or in other words, to disperse light as a function of its wavelengths and then redirect individual light rays onto a detector. By doing so, the spectrograph can image photons that are close in terms of energy onto different pixels of the detector.

---

[7] `https://www.nasa.gov/mission_pages/hubble/about`

[8] `https://www.nasa.gov/mission_pages/spitzer/infrared/index.html`

[9] `https://webb.nasa.gov/content/about/faqs/facts.html`

[10] `https://www.eso.org/sci/facilities/paranal/instruments/espresso.html`

[11] `https://www.eso.org/public/teles-instr/lasilla/36/harps/`

[12] `https://www.cfht.hawaii.edu/Instruments/SPIRou/`

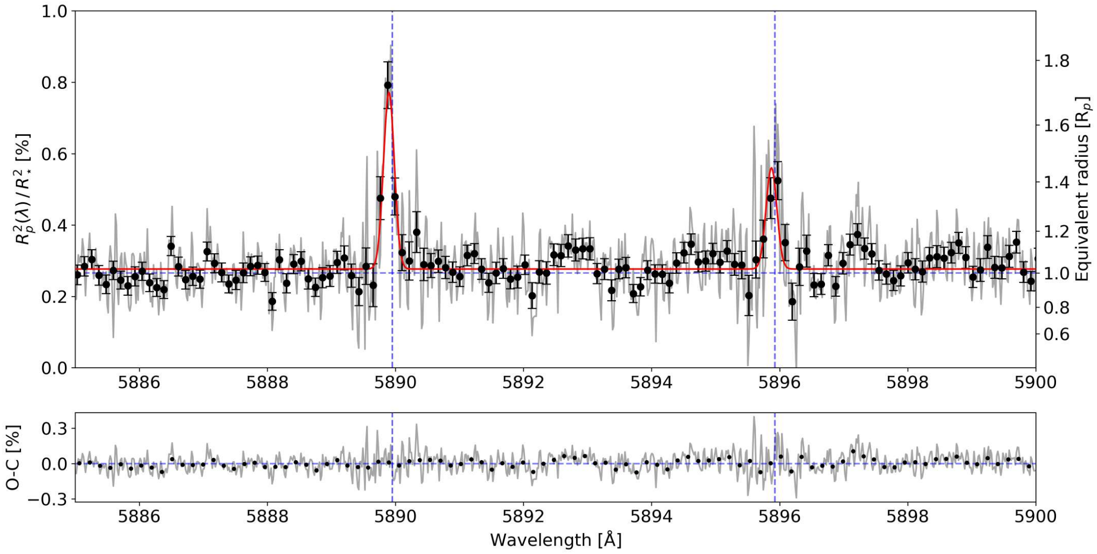

Fig. 2.4.: High resolution transmission spectrum of the transit of the planet KELT-11 b around the sodium doublet computed from HARPS observations. It shows how optically thin regions of the planetary atmosphere can absorb the stellar spectrum only in specific narrow spectral lines, here the Na I D2 and D1 lines. Figure taken from Mounzer et al. (2022).

By knowing which pixel of the detector corresponds to which expected wavelength, astronomers are able to reconstruct the spectrum of a star as a function of wavelength with a certain degree of precision (see Figure 2.5). Depending on the capabilities of the instrument, that is, for example, its aperture size, the number of pixels on the detector and the capabilities of the dispersion element, the spectral resolution of the reconstructed spectrum will differ. The aim of high resolution spectrographs is to deliver spectra for which individual spectral lines that are extremely close in terms of rest wavelength can be resolved, that is, can be distinguished from one another (see Figure 2.6). That way, when the depth of a stellar line increases during the transit of a planet and its atmosphere, astronomers are able to attribute this change to the absorption of the stellar spectrum by individual planetary species. This technique has a drawback which is that by separating the received light into different pixels, the number of photons per pixel per unit of time is reduced. It makes these observations more prone to being affected by the noise as the signal is inevitably fainter. Faint stars are thus not suitable targets for such instruments unless larger aperture telescopes are used and/or the time of the exposures is increased. The former, for now, is only technically feasible from the ground, while the latter can lead to other underlying contamination effects (see Sect. 2.2).

For more in-depth discussions about planetary transits and spectrographs see, for example, Gray (2005); Seager & Dotson (2010); Perryman (2018); Krasnopolsky (2019).

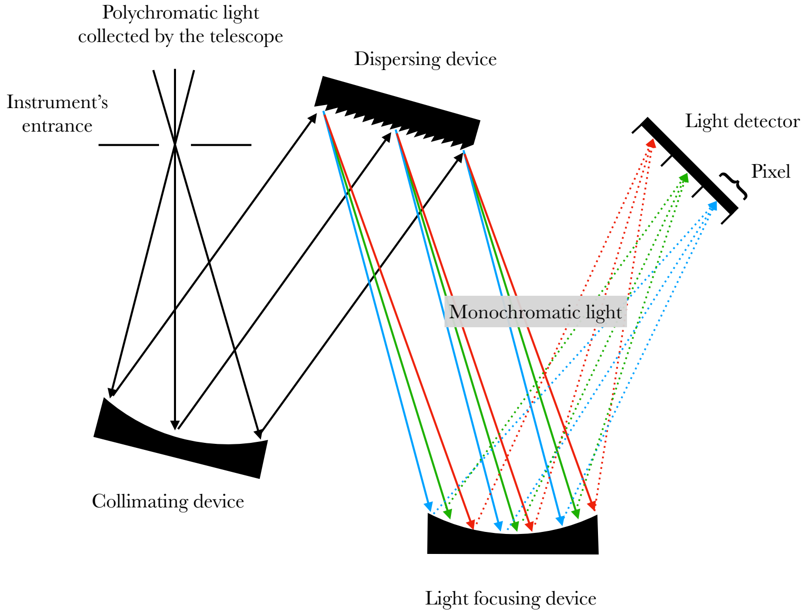

Fig. 2.5.: Simplified sketch of a spectrograph. It illustrates how the spectrograph separates light as a function of wavelength, here represented by the colours, and then images the different colours onto separate spatial regions of a detector.

2.2 Transit spectroscopy observations

In practice, planetary transits spectroscopy observations are made in two steps. The first step is to observe the host star outside of the planetary transit, before and/or after, for a relatively long time, typically on the order of the transit's duration, depending on the instrument's sensitivity and the star's brightness. This step allows the observers to collect the *disc-integrated spectrum* of the star, also called the *out-of-transit spectrum*, designated in this manuscript by F_{out}. This flux is thus measured contemporarily to the planetary transit but without planetary contamination and has a high signal-to-noise ratio. The out-of-transit spectrum is a crucial quantity because it serves as a reference in order to identify which parts of the stellar spectrum have been absorbed during the planetary transit. Having an out-of-transit spectrum close in time to the planetary transit is essential. Indeed, it limits the differences between the reference stellar spectrum and the stellar spectrum during the transit that could change due to stellar activity.

The second step is to observe the star during the planetary transit with a high temporal cadence to collect a series of *in-transit spectra*, designated in this manuscript by F_{in}. These spectra will contain the additional absorption signature of the planet

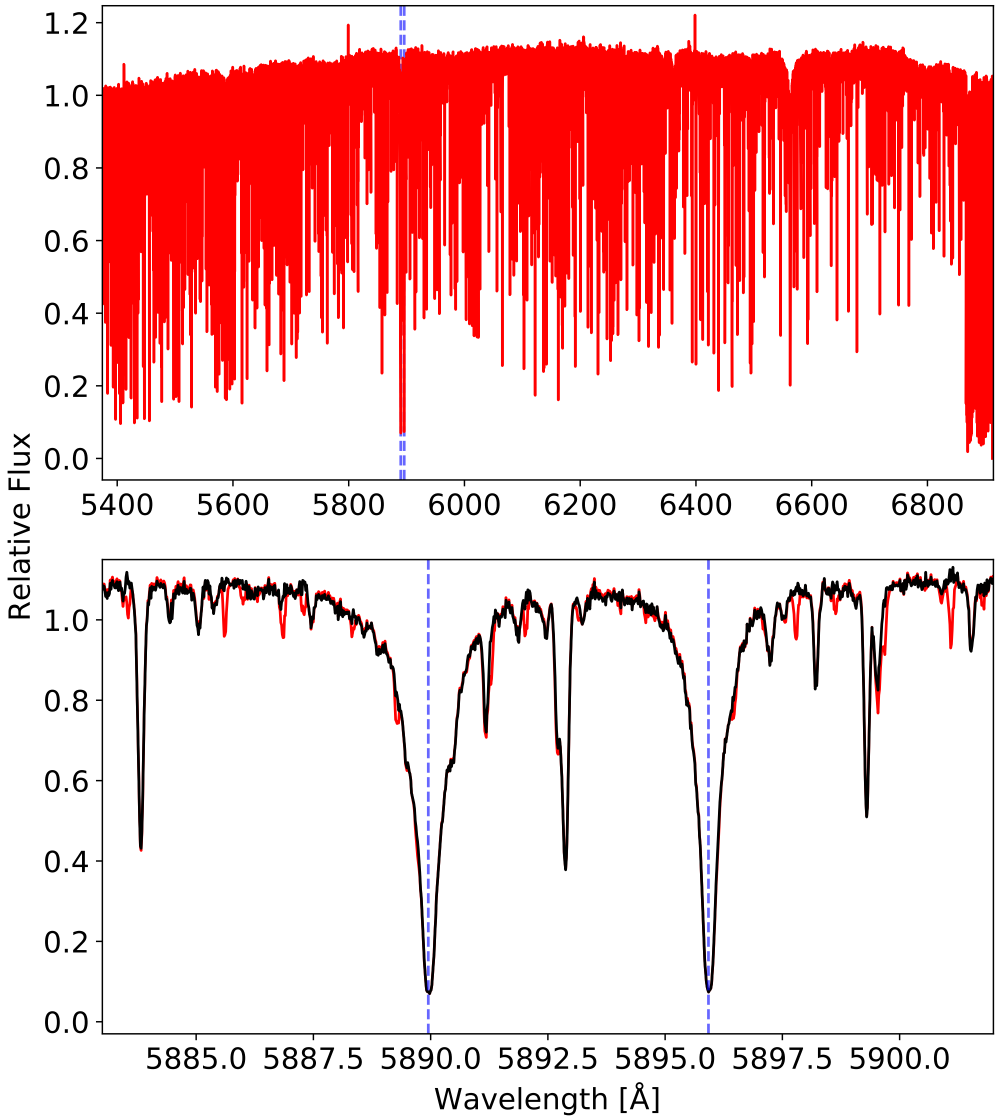

Fig. 2.6.: High resolution spectrum of the star KELT-11 observed with HARPS. This spectrum illustrates how atomic and molecular lines that are close in wavelength are clearly distinguishable thanks to the spectroscopic observations performed at high spectral resolution. The upper panel shows the spectrum over a wide range of wavelengths, and the bottom panel shows a zoom on the spectral region of the Na I doublet. The red curve is the original spectrum, and the black one is the spectrum corrected for telluric lines. Telluric lines are spectral lines added to the spectrum when radiation travels Earth's atmosphere, and so do not originate from the observed star or the transiting planet. These contaminations only affect ground-based observations. Image courtesy of Dany Mounzer.

and its atmosphere. In high resolution spectra, the flux level will be diminished uniformly by the opaque planetary body, which absorbs equally at all wavelengths. Moreover, the optically thin regions of the transiting planetary atmosphere will decrease the flux level in narrow wavelength ranges around the rest wavelengths of the radiative transitions of the elements it contains. The high temporal cadence of in-transit observations is needed to limit the displacement of the planet in front of the stellar disc during the exposure and avoid an effect called Doppler smearing. This effect induces an additional broadening in the absorbed line profile by the planet (Cauley et al. 2021; Seidel et al. 2023). However, the temporal cadence is usually balanced by the need for a high enough signal-to-noise ratio.

2.2.1 Extracting planetary atmospheric absorption signatures

To quantify the decrease in the observed flux level of the stellar spectrum due to the absorption by the transiting planet and atmosphere, the commonly used approach in the literature is first to subtract the in-transit spectrum from the out-of-transit spectrum and then divide the result by a reference spectrum, F_{ref}, which is usually the out-of-transit spectrum. Subtracting the in-transit spectrum from the out-of-transit spectrum allows one to derive the *absorbed spectrum*, designated in this manuscript by F_{abs}, which is the spectrum that has been absorbed by the planet and the atmosphere at a specific exposure time (see Figure 2.7). When dividing the absorbed spectrum by the reference spectrum, we compute what is called the *absorption spectrum*, designated in this manuscript by $\mathcal{A}$. The *transmission spectrum*, $\mathcal{T}$, which is also widely used in the literature, is simply derived as $\mathcal{T} = 1 - \mathcal{A}$. In this manuscript, I will prefer the use of the absorption spectrum. In absorption spectra, additional absorption signatures, such as those from an atmosphere, naturally have positive values, unlike in transmission spectra.

Let us consider that the spectrum of the star is uniform over its surface. The flux level of the absorption spectrum is equal to the ratio between the occulted stellar surface by the planetary opaque body and the apparent surface of the star. We can isolate the atmospheric excess absorption by subtracting this ratio from the absorption spectrum.

Let us write in a simplified fashion the out-of-transit spectrum as,

$$\mathrm{F}_{\mathrm{out}}(\lambda) = \sum_i I_i(\lambda) \frac{S_i}{\mathrm{R}_*^2} \tag{2.1}$$

where $I_i(\lambda)$ are the local spectral intensities at position i on the stellar disc and are constant over the apparent stellar disc, S_i are the unit surfaces on the apparent

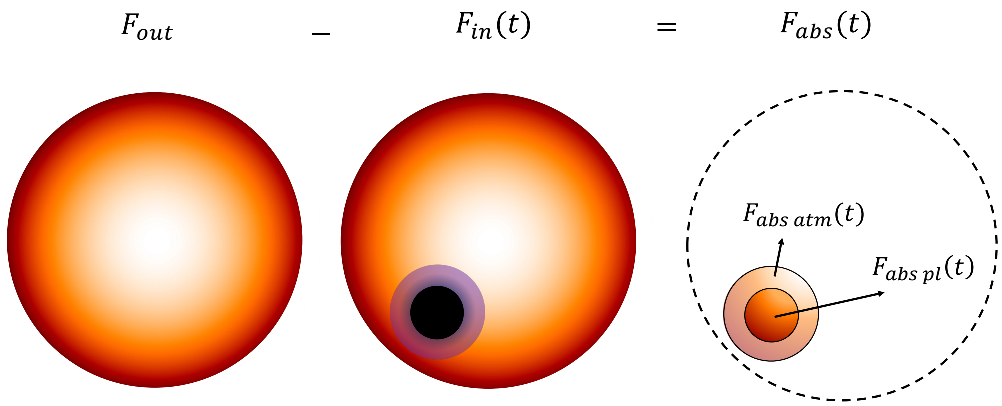

Fig. 2.7.: Sketch illustrating the different quantities used in the computation of an absorbed spectrum, F_{abs}, of a planetary transit at a specific exposure time t. The individual contributions of the planetary opaque disc and the planetary atmosphere to F_{abs} are $\mathrm{F}_{abs\ pl}$ and $\mathrm{F}_{abs\ atm}$, respectively.

stellar disc, and R_* is the stellar radius. Let us write in the same fashion the in-transit spectrum for a specific time step t as,

$$\mathrm{F}_{\mathrm{in}}(\lambda, t) = \sum_i I_i(\lambda)\delta_i(t)\frac{S_i}{\mathrm{R}_*^2} \tag{2.2}$$

where $\delta_i(t)$ is a transmission factor. It is equal to zero for the local spectra absorbed by the opaque planetary disc or by the opaque layers of the atmosphere. It is equal to one for local spectra that are not occulted by the planet nor by the atmosphere, and it takes values between zeros and one for local spectra absorbed by optically thin layers of the atmosphere. The absorption spectrum thus writes,

$$\mathcal{A}(\lambda, t) = \frac{\mathrm{F}_{\mathrm{out}}(\lambda) - \mathrm{F}_{\mathrm{in}}(\lambda, t)}{\mathrm{F}_{\mathrm{ref}}(\lambda, t)} = \frac{\mathrm{F}_{\mathrm{abs}}(\lambda, t)}{\mathrm{F}_{\mathrm{ref}}(\lambda, t)} \tag{2.3}$$

where $\mathrm{F}_{\mathrm{ref}}$ is often chosen to be equal to $\mathrm{F}_{\mathrm{out}}(\lambda)$ in the literature. In that case, Eq. 2.3 becomes,

$$\begin{aligned}\mathcal{A}(\lambda, t) &= \frac{\displaystyle\sum_i I_i(\lambda)\frac{S_i}{\mathrm{R}_*^2} - \sum_i I_i(\lambda)\delta_i(t)\frac{S_i}{\mathrm{R}_*^2}}{\displaystyle\sum_i I_i(\lambda)\frac{S_i}{\mathrm{R}_*^2}} \\ &= \frac{\displaystyle\sum_k I_k(\lambda)\frac{S_k}{\mathrm{R}_*^2} + \sum_l I_l(\lambda)[1-\delta_l(t)]\frac{S_l}{\mathrm{R}_*^2}}{\displaystyle\sum_i I_i(\lambda)\frac{S_i}{\mathrm{R}_*^2}}\end{aligned} \tag{2.4}$$

where k and l indicate that the local spectrum is absorbed by the planetary opaque body and the atmosphere, respectively. Considering that all the local spectra are equal over the apparent stellar disc (uniform stellar emission) and that all the unit surfaces are equal, Eq. 2.4 simplifies to,

$$\mathcal{A}(\lambda, t) = \frac{S_{pl} + \delta_{atm} S_{atm}}{S_*} \tag{2.5}$$

As mentioned above, Eq. 2.5 demonstrates that by subtracting the ratio between the planetary-occulted surface and the stellar surface, we can extract the absorption signature of the atmosphere. The result of these calculations is well illustrated in Fig. 2.4, where the flux level of the absorption spectrum is expressed in units of the planetary to stellar disc surface ratio. In this figure, the absorption spectrum is relatively flat at all wavelengths, which is the signature of the opaque planetary body absorption. The spectrum shows two distinctive absorption signatures in excess of the planetary absorption, which peak around the sodium doublet rest wavelengths. These two features are the signature of the atmospheric absorption. This result has led to the detection of sodium in the atmosphere of the exoplanet KELT-11 b by Mounzer et al. (2022).

Two ways are mainly used in the literature to display the absorption spectra. The first one is to look at the temporal evolution of the absorption spectrum during the transit and create a two-dimensional map as a function of time and wavelength (see Figure 2.8). These maps give access to the variation of the atmospheric absorption signature during the transit, which allows for inferring information about the dynamics of the target element in the atmosphere, such as winds and other climate phenomena. A notable example of the detection of planetary atmospheric dynamics is presented in Ehrenreich et al. (2020). By studying the temporal evolution of the absorption spectrum of WASP-76 b during its transit, the authors noticed a net blue shift in the absorption signature around iron lines during specific phases of the transit (see lower panel of Fig. 2.8). This blueshift is explained by a wind in the atmosphere of the planet driven by a strong temperature gradient between the hot day side and the cold night side of the planet.

As I mentioned before, in-transit spectra are collected over a short time, and the signal-to-noise ratio of the individual absorption spectra is thus not usually high. For this reason, astronomers often resort to an alternative way of visualising the absorption spectrum, which is by computing the mean of the individual absorption spectra along the time axis. The mean is usually taken between the contact times of the transit, either between T_1 and T_4 or T_2 and T3, see Fig. 2.1. Most of the time, the mean is calculated between T_2 and T_3 to avoid partial occultation effects during ingress and egress (see, e.g., the lower left panel of Figure 4 of Casasayas-Barris et al. (2020)). For instance, at these time-steps: the planet-occulted surface is not equal to πR_p^2; the surface over which the atmosphere absorbs is not the complete

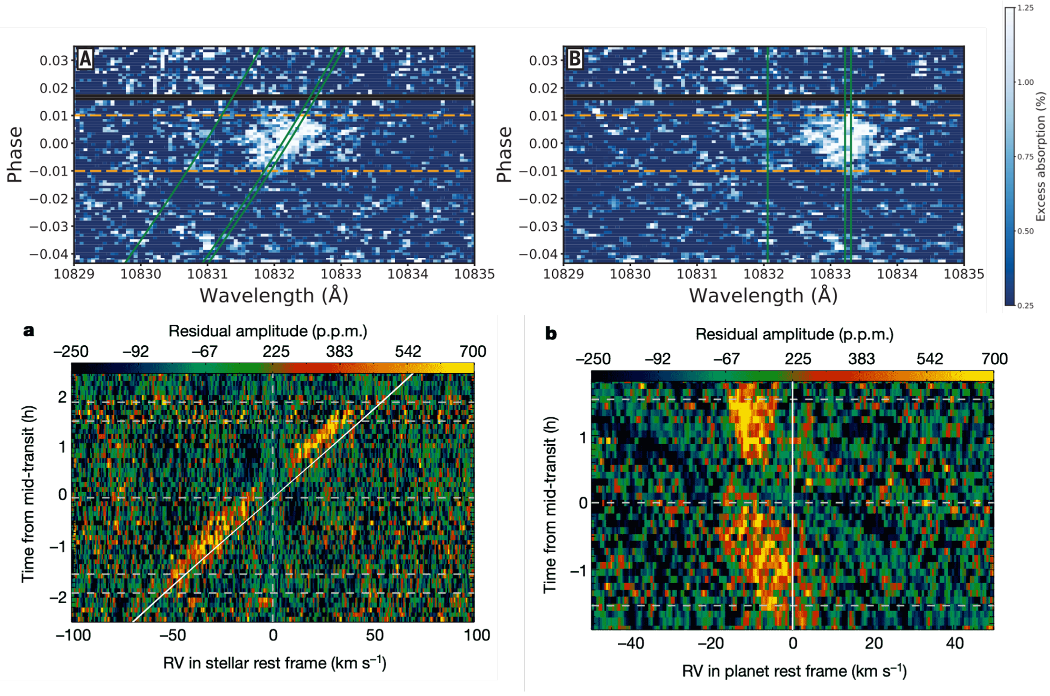

Fig. 2.8.: Temporal evolution of the absorption spectrum of a planetary transit reconstructed from high resolution transit spectroscopy data. **Upper panel**: from Allart et al. (2018), it shows the absorption spectrum of the planet HAT-P-11 b around the He I triplet at 10830 Å. The spectrum shows the clear excess absorption caused by helium atoms in the atmosphere of the planet. **Lower panel**: from Ehrenreich et al. (2020), it shows the absorption spectrum of WASP-76 b around the spectral lines formed by iron. The spectrum shows the clear excess absorption caused by iron atoms in the atmosphere of the planet. The authors have combined the absorption signatures of a series of iron lines to increase the signal-to-noise ratio. They also display the absorption spectrum as a function of the Doppler shift velocity from the rest wavelengths of the iron lines instead of wavelengths. Left panels show absorption spectra in the stellar rest frame, while right panels show them in the planet's rest frame.

atmospheric annulus, the absorption signature is thus not equivalent to the rest of the transit; strong stellar effects take place in the regions occulted by the planet (see Chapter 3). The computation of the mean increases substantially the signal-to-noise ratio and allows for detecting faint atmospheric absorption signatures (see Fig. 2.4). However, by making use of the mean absorption spectrum, we lose any trace of a possible temporal variation of the planetary atmospheric absorption during the transit. It is important to note that before computing the average absorption spectrum, astronomers usually have to shift individual absorption spectra in the rest frame of the planet (Wyttenbach et al. 2015). This is done by computing the Doppler shift induced by the planet's radial velocity at the time of each exposure. This is illustrated in Fig. 2.8 where the absorption spectrum is shown in the stellar and planetary rest frames. The upper right panel of this figure also demonstrates that in the planetary rest frame, the atmospheric absorption signatures are mostly aligned throughout the transit (considering there are no bulk dynamics in the atmosphere).

Therefore, in the planetary rest frame, the atmospheric absorption signatures stack up when the mean is computed, and the mean signal increases significantly. However, as shown in the lower right panel of this figure, when there are strong dynamics in the atmosphere, the absorption signatures do not necessarily align in the planetary rest frame. As mentioned above, if we were to compute the mean of the absorption spectra in this case, we would lose all the information about the temporal variations of the atmospheric absorption signatures.

The two methods used to study absorption spectra have their own drawbacks and advantages. Therefore, making use of them both can help lift ambiguities in the resulting observed absorption signatures.

2.3 Local variations in the stellar spectrum

The formula given in Eq. 2.3 seems to be a straightforward way to extract a clean absorption signature from the transiting planetary atmosphere. However, to get from Eq. 2.3 to Eq. 2.5, we needed to consider that the spectral intensities emerging from every position on the stellar disc were equal. This is, of course, a strong assumption, and it will not hold in most cases. In reality, stellar spectra are not homogeneous locally over the apparent surface of the star for an observer. Two of the main phenomena that make the local stellar spectrum vary from one position to another over the stellar surface are the stellar rotation and the centre-to-limb variations (CLV). These effects can have significant consequences on the extracted absorption spectrum and can induce distortions that alter the absorption signatures of atmospheres. The effects of stellar rotation and CLV on the absorption spectrum of a transiting planet are demonstrated in detail in Chapter 3.

2.3.1 Stellar rotation

For an observer, static with respect to a rotating star, one hemisphere of the star rotates towards its position while the other rotates away from its position. To the observer, the local spectra coming from the hemisphere rotating towards (respectively, away from) its position appear blueshifted (respectively, redshifted), which is caused by the Doppler effect[13]. Figure 2.9 illustrates this phenomenon in the case of the Sun. The amount by which the local spectra are shifted due to stellar rotation is determined by the rotational velocity of the local stellar surface projected on the line of sight (LOS) of the observer. In the case of a rotating star, the lines of the disc-integrated spectrum, F_{out}, do not exhibit a net shift in wavelength, but they ex-

---

[13] Only in a configuration where the line of sight of the observer is perfectly aligned with the rotation axis of the star, would a rotating star appear static to the observer

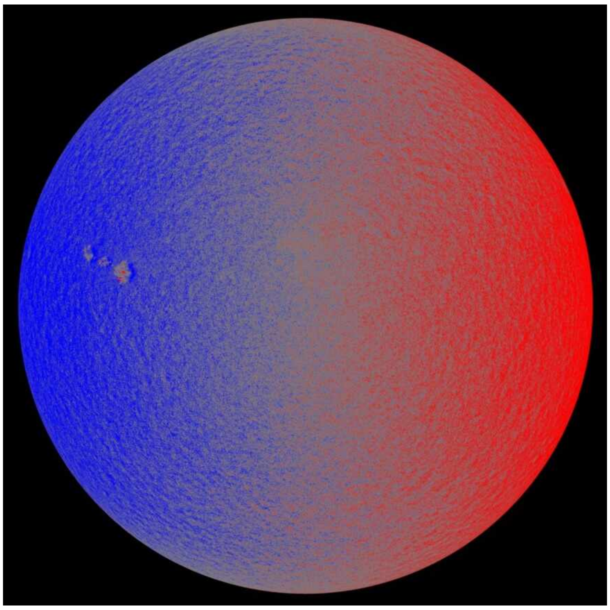

Fig. 2.9.: Observation of the Sun by the Helioseismic Magnetic Imager (Solar Dynamics Observatory) revealing the rotation of the Sun with a blueshifted and redshifted hemisphere. Image credit: solarsystem.nasa.gov

hibit a broadened profile. This is because F_{out} is made of the sum of all the apparent local spectra (that are shifted in wavelength). The effect of stellar rotation on the disc-integrated and local line profiles is illustrated in Figure 2.10. This figure shows the disc-integrated and local Na I D2 line profiles of a generic star rotating with a velocity of $\mathrm{v_{eq}}\sin(\mathrm{i}_*) = 20$ km s^{-1} for a series of μ[14] positions on the stellar disc. The figure clearly shows that the disc-integrated line profile does not correspond to the local line profiles anywhere on the stellar disc. At a time t, the spectrum absorbed by the planet is made of the local spectra of the stellar region it occults. The line profiles of $F_{abs}(t)$ are thus shifted in wavelength according to the radial velocity of the occulted stellar surface, but their shape is mostly not altered by rotation[15]. Therefore, if we divide $F_{abs}(t)$ by F_{out}, we divide line profiles that can be strongly distinct depending on the stellar rotational velocity. This simple mismatch between the position and shape of the disc-integrated and local line profiles is at the origin of the distortions that appear in absorption spectra, as is shown in Chapter 3. Studies highlighting the effect of stellar rotation in absorption spectra include, among others, Louden & Wheatley (2015); Borsa & Zannoni (2018); Casasayas-Barris et al. (2020, 2021); Borsa et al. (2021).

It is worth mentioning that other velocity-induced phenomena can affect the stellar spectrum. For example, the angular velocity of the star might change with latitude if

---

[14] For a star of radius equal to 1, $\mu = \sqrt{1-(x^2+y^2)}$ with (x, y) the coordinates of a point on the stellar disc in the Cartesian referential centred on the stellar disc. $\mu = 1$ at the centre of the stellar disc and 0 at the edge of the stellar disc.

[15] For large planets and/or very fast stellar rotation, the line profiles of F_{abs} can be broadened by stellar rotation, but significantly less than those of F_{out}.

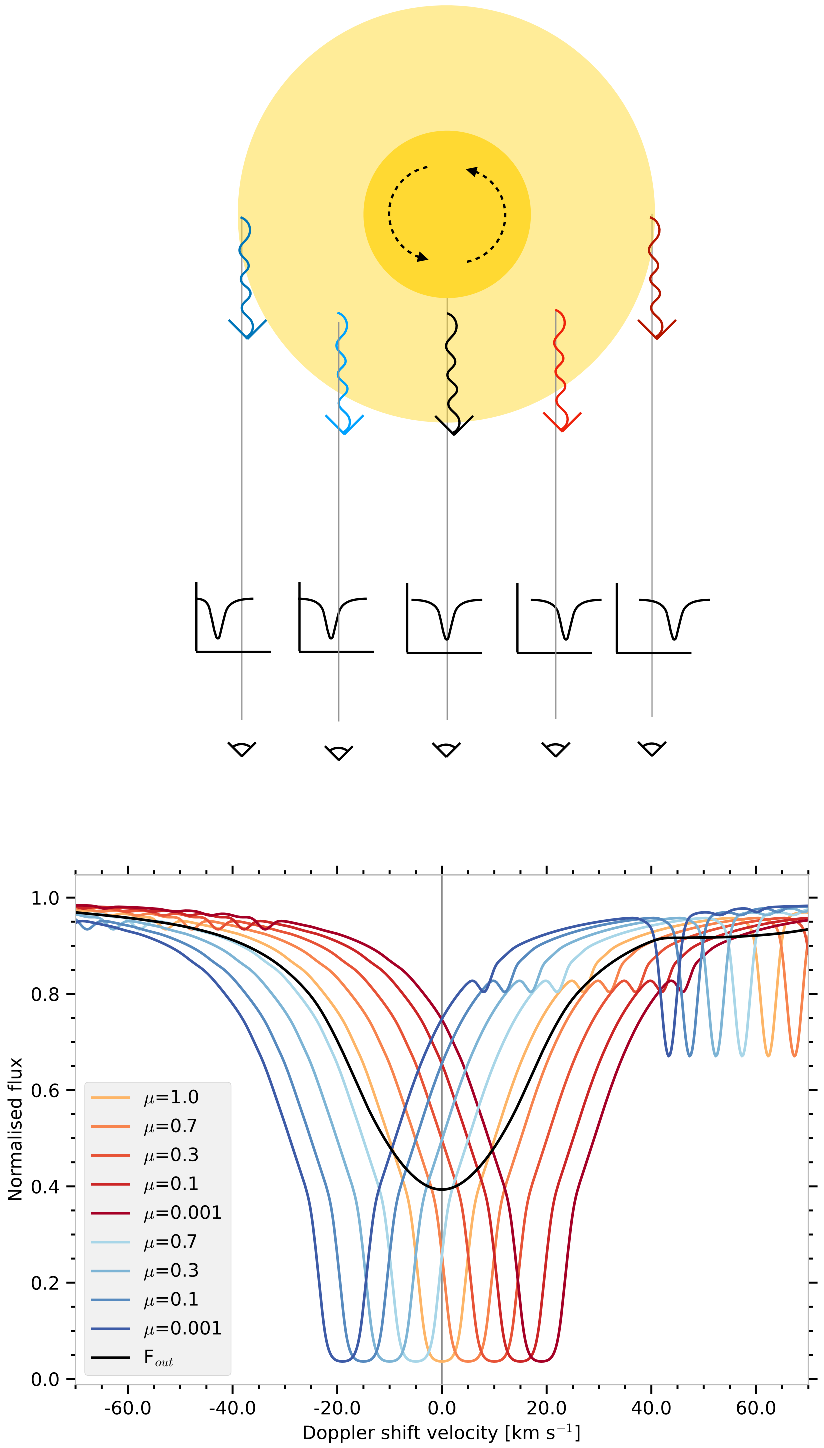

Fig. 2.10.: **Upper panel**: Sketch illustrating the effect of stellar rotation on local stellar spectra. **Lower panel**: Synthetic local and disc-integrated spectra of a generic rotating star of $v_{eq}\sin(i_*) = 20$ km s^{-1}, around the Na I D2 line profile at 5 889.95 Å, simulated with a spectral synthesis code (Sect. 2.4.2). The local intensity spectra were taken for different positions along the stellar equator to sample larger radial velocities. The blue (respectively red) curves show local spectra taken from the blueshifted (respectively redshifted) hemisphere. Here, the shape of the line profiles is the same everywhere on the disc as the stellar spectrum is not affected by centre-to-limb variations.

the star is not in a solid body rotation state. This would modify the exact local radial velocities on the stellar surface compared to a star in a solid body rotation. Another effect that can induce asymmetry and a net blueshift in the stellar line profiles is the convective blueshift, which comes from granulation in stellar photospheres. At the centre of a granulation cell, there is an up-flow of the hot matter of the photosphere, which thus induces a blueshift in stellar line profiles. The cooled matter that falls back down in the photosphere in inter-granular regions induces, on the contrary, a redshift in the line profiles. Due to a higher temperature, the intensities from the centre of the granulations are larger, which overall induces a net blueshift in the stellar lines. These effects will not be considered in the following. For more in-depth discussions on their implications, see, for example, Cegla et al. (2016) and Dravins (1982); Bergemann et al. (2019); Gallagher et al. (2020).

2.3.2 Centre-to-limb variations

Line profiles variation

The centre-to-limb variation (CLV) of the local stellar line profile is an observer effect that makes the observed stellar lines' shape change over the apparent stellar surface. This variation can be explained by the combination of two effects. The first one is related to the line formation process: different regions in a stellar atmosphere contribute to different parts of the emerging line profile. This process is illustrated in Figure 2.11, which shows the formation regions of different lines in the solar atmosphere (Vernazza et al. 1981). For instance, the core and the wings of the Hα line form at very different places, in terms of densities and temperatures, as is highlighted with colours in the figure. For more explanation on the formation of spectral lines in stellar atmospheres, see, for example, Rutten (1993, 2003).

The second is that, depending on where the observer is looking at on the stellar surface, photons from the deeper layers of the atmosphere might not reach the observer. Indeed, at the centre of the stellar disc, photons from both the deep and shallow layers can escape the atmosphere, and thus, the observer sees the complete line profile made of the core and the wings of the H_α line. Meanwhile, closer to the stellar limb, the photons from the deeper layers forming the wings cannot escape the atmosphere in the direction of the observer. This is because at the limb, the length of the path that photons have to travel in the direction of the observer before exiting the atmosphere increases. Their optical depth therefore becomes optically thick before they can reach the surface of the atmosphere. The observer thus only receives photons that originate from the shallow layers, the photons that contribute to the core in this example. The observed line profile at the limb is thus only made of the contribution of the core.

This phenomenon is illustrated in Figure 2.12. In the bottom panel of this figure,

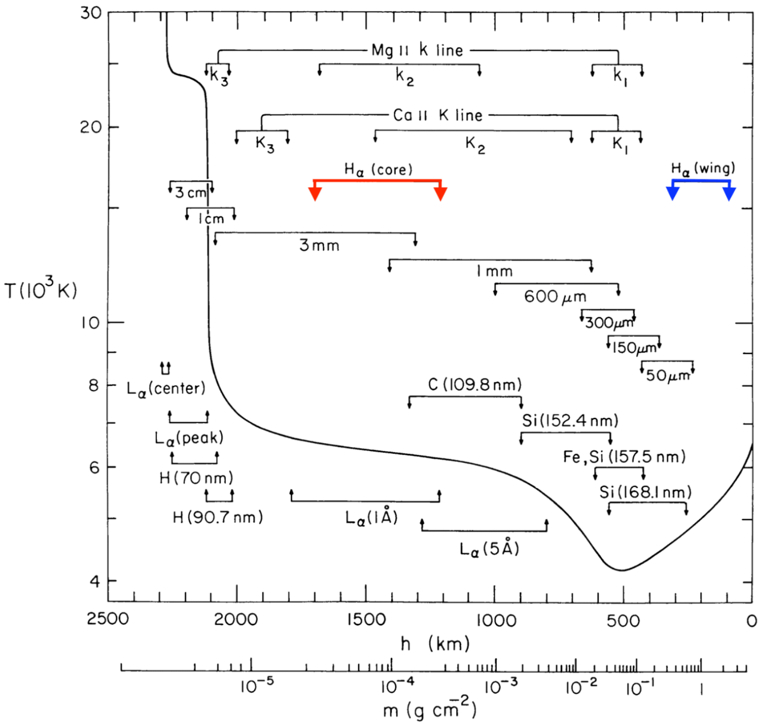

Fig. 2.11.: Temperature profile in the Sun's atmosphere as a function of height and column mass density. This figure shows the regions of formation of different parts of specific spectral lines in the Sun's atmosphere. The H_α line components are highlighted in colours for the purpose of the example given in the text. Figure 1 from Vernazza et al. (1981).

I simulated a series of local spectra around the Na I D2 line for different positions on the stellar disc using the spectral synthesis code *Turbospectrum* (Sect. 2.4.2). It shows clearly that for local spectra near the limb of the star, the emerging line profiles are composed almost exclusively of the core of the line. Meanwhile, closer to the centre of the star, the line profiles of the local spectra exhibit both core and wings components as explained previously. Fig. 2.12 also shows that the disc-integrated line profile, as in the case for stellar rotation, does not correspond to the local line profiles on the stellar disc. This is because the disc-integrated spectrum is made of the sum of all the local spectra from the apparent stellar disc, and thus, its line profile is affected by the global effect of CLV. Therefore, similarly to when stellar rotation is considered, if we divide $F_{abs}(t)$ by F_{out}, we divide line profiles that can be strongly different depending on the position of the planet in front of the star. This discrepancy in the shape of the disc-integrated and local line profiles is at the origin of the distortions that appear in absorption spectra. For studies that compare observations of the local solar spectrum to stellar models, see, for example, Allende Prieto et al. (2004); Pietrow et al. (2022). Studies highlighting the effect of CLV in absorption spectra include, among others, Czesla et al. (2015); Yan et al. (2017); Borsa & Zannoni (2018); Casasayas-Barris et al. (2020); Borsa et al. (2021).

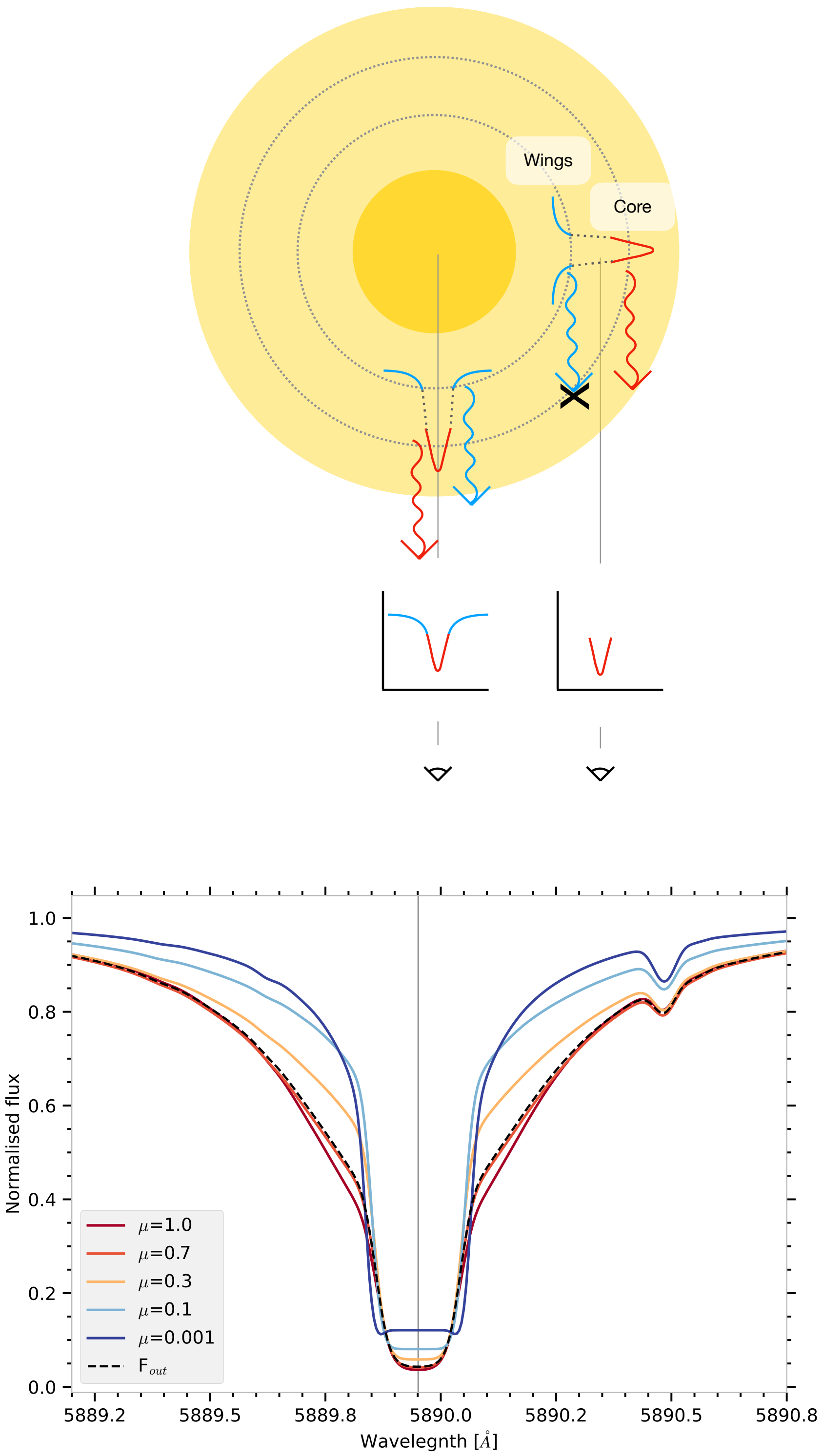

Fig. 2.12.: **Upper panel**: Visual representation of the centre-to-limb variation effect. **Lower panel**: synthetic local and disc-integrated spectra of a generic star with CLV and no stellar rotation around the Na I D2 line profile at 5 889.95 Å, simulated with the *Turbospectrum* code. The local line profiles that form near the limb ($\mu < 0.3$ here) display an almost constant core. The column density of the stellar atmosphere increases as the LOS gets closer to the limb. The contribution of the source function to the intensity of the lines thus increases, resulting in a flat bottom profile in the synthetic spectra.

Continuum variation or broadband limb darkening

Broadband limb-darkening (BLD) is another observer effect that makes the observed continuum of the spectrum decrease from the centre of the stellar disc to its limb. Figure 2.13 shows a real observation of the Sun, which reveals the brighter centre and the darker limb. In the Sun photosphere (see the region between 0 and ~ 500 km in Fig. 2.11), the deep layers have a higher temperature than the shallow layers. The source function of the photons coming from the hot and deep layers tends to be large, which thus translates to a high level of the continuum of their intensity (see Figure 2.14). Whereas, the source function of the photons coming from the cooler and shallow layers tends to be small, which makes the level of the continuum of their intensity be low (see Figure 2.14).

Similarly to spectral lines, depending on where the observer is looking at the apparent stellar surface, photons from the deeper layers of the atmosphere might not reach the observer. Indeed, at the centre of the stellar disc, photons from the deep, hot layers can escape the atmosphere, and thus, the observer perceives a spectrum with a strong continuum. Whereas, closer to the stellar limb, the photons from the hot and deep layers cannot escape the atmosphere in the direction of the observer, as explained in Sect. 2.3.2. The observer thus only receives photons from the shallow and cool layers and perceives a spectrum with a low continuum.
The opposite phenomenon, called limb brightening, happens when the temperature gradient is inverted in the stellar atmosphere, meaning that high temperatures are found at high altitudes while low temperatures are found in low altitudes regions.
For a study that compares observations of the local solar spectrum continuum variation to stellar models, see, for example, Pietrow et al. (2022). Also, Mounzer et al. (2022) highlights the effect of broadband limb darkening on the absorption spectra and atmospheric absorption signature.
As for stellar rotation, it is worth mentioning that any other phenomena affecting the local intensity distribution on the stellar disc will also affect the local and disc-integrated spectra, for example, dark and hot spots (Queloz et al. 2001; Boisse et al. 2009).

A thorough investigation of the impact of the centre-to-limb variation in line profiles and continua on the absorption spectra of transiting planets is discussed in Chapter 3.

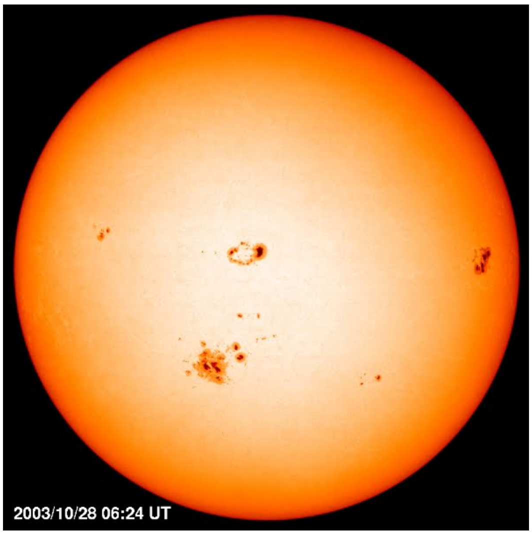

Fig. 2.13.: Observation of the Sun revealing the broadband limb darkening and some spots. Credits: Solar & Heliospheric Observatory (SOHO) https://soho.nascom.nasa.gov/gallery/

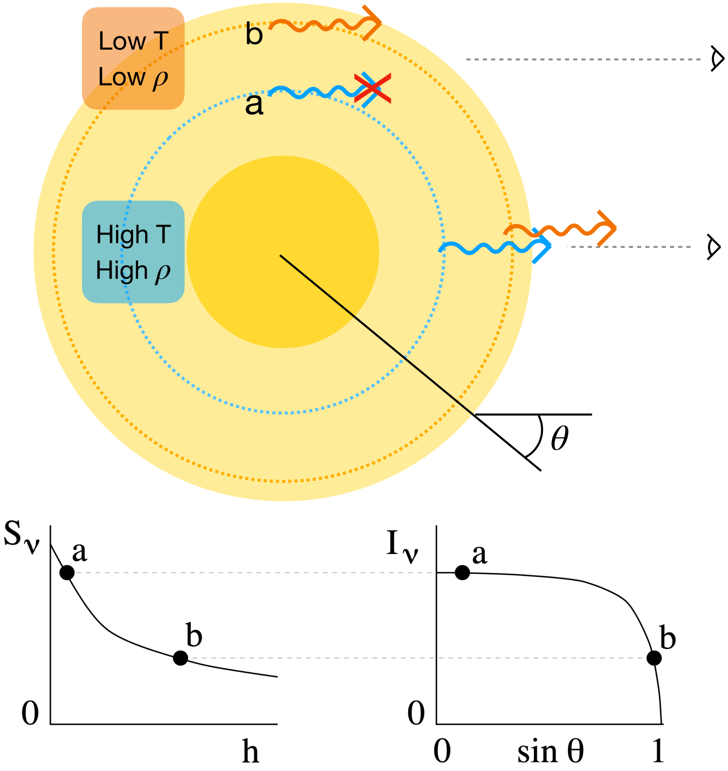

Fig. 2.14.: Visual representation of the solar limb darkening effect. Adapted from Rutten (2003)

2.3.3 Non local thermodynamic equilibrium

When modelling stellar atmospheres, an approximation that is usually made to facilitate calculations of the solution of the radiative transfer equation is to consider that locally, the gas is in thermodynamic equilibrium. Local thermodynamic equilibrium (LTE) is met for a dense local element of matter, where collisions dominate, and the local temperature (through collisions) governs the population of atomic energy levels. Additionally, there must be no gain nor loss of particles from the considered element of matter, and for any photon that is absorbed by the element of matter, a photon must be emitted. It also implies that in this element of matter, particles are subject to as many excitation processes as de-excitation processes. In the case of a LTE, the possible transitions that will emit photons can be determined from the temperature of the considered element of matter.
However, this configuration is only met in the deep and very dense layers of a stellar atmosphere. Indeed, this equilibrium breaks in higher layers as density gradually decreases and collisions between particles become rarer. The mean free path between two collisions thus becomes of the same order of magnitude as the mean free path of photons. This allows for radiation coming from outside the element of matter to interact more with its particles. Radiation-induced transitions are, therefore, more frequent, which leads to photons emitted with energies that would not be possible only through collision-induced transitions. Moreover, if it is possible to see a star, it is because photons from the uppermost layers are not absorbed and destroyed and eventually escape from the stellar atmosphere. This means that, locally, with less photons, there will be less excitation processes than de-excitation processes and the conditions for LTE are not met.

This departure from an equilibrium configuration is often referred to as non-local thermodynamic equilibrium (NLTE). In that case, computing stellar line profiles becomes more complex, as the local element of matter is coupled to the rest of the medium through the external radiation field; requiring simultaneous solution of the radiative transfer equation and the kinetic equilibrium equations. In turn, considering NLTE allows for computing more realistic spectral line profiles as is shown, for example, in Figure 2.15. This figure is taken from Alexeeva et al. (2018) and shows an example of the impact of including NLTE effects in a stellar model when computing stellar line profiles, here the Mg I line at 7.3 μm. Finally, as will be illustrated later in Sect. 3 (see also Casasayas-Barris et al. (2021)), accounting for NLTE effects in stellar models can be crucial as they may induce detectable changes in the absorption spectrum of a transiting exoplanet. For more detailed explanations about the physics of non-local thermodynamic equilibrium and its implications on spectral line formation, see the discussions of Rutten (2003); Gray (2005); Hubeny & Mihalas (2014).

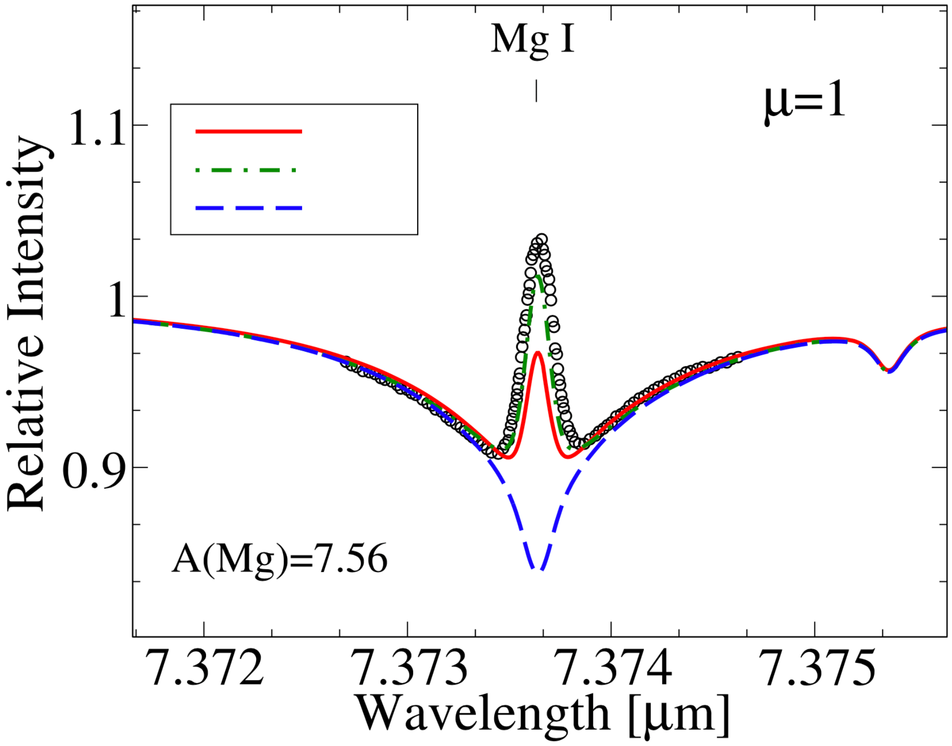

Fig. 2.15.: Mg I (7.3 μm) intensity line profile. Dots: intensity line profile from the centre of the solar disc. Blue dashed curve: synthetic line profile computed with LTE approximation. Red and green dashed-dotted curve: synthetic line profile computed under NLTE condition with two different atomic models. Figure taken from Alexeeva et al. (2018)

2.3.4 Orbital architecture

Now that I have introduced the fact that the stellar spectrum is not uniform over the apparent stellar disc, it is relevant to introduce a few parameters of the planetary orbital architecture that influence the position of the planet throughout its transit, i.e. the transit chord. If the transit chord is modified, the planet occults different regions of the stellar surface. It means that the planet absorbs different line profiles throughout its whole transit (due to stellar rotation and CLV). A variation of the transit chord can thus result in a change in the contaminations induced in the absorption spectrum. Here I present a few of the most relevant orbital parameters that can influence the resulting absorption spectrum.

Sky-projected spin-orbit angle

The sky-projected spin-orbit angle of the planet also called the obliquity, is the angle between the projection of the stellar spin axis onto the plane of the sky and the projection of the normal to the orbital plane onto the plane of the sky. Varying this angle changes the orientation of the planetary transit chord over the apparent stellar disc but does not change the transit duration (for spherical stars only).

Planetary orbital inclination and impact parameter

The planetary orbital inclination is the angle between the normal to the orbital plane and the observer's line of sight. The effect of inclination on the transit chord is better understood through the concept of the impact parameter. The impact parameter, b, is intimately linked to the orbital inclination through its definition given for a circular orbit by:

$$b = \frac{a}{R_*} \cos(i_{pl}) \tag{2.6}$$

where a is the semi-major axis of the planetary orbit, R_*, the radius of the host star and i_{pl} the planetary orbital inclination. See Figure 2.16, which shows a sketch of the impact parameter. The impact parameter is the distance between the stellar disc centre and the centre of the transit track, i.e. at T_0. It is given in units of stellar radius and is equal to zero when the transit chord passes by the stellar disc centre. If the impact parameter is greater than one, it means that the planet does not transit the star. For a fixed value of the semi-major axis, the impact parameter is controlled by the planetary orbital inclination. Varying the inclination moves the transit chord in latitude and, thus, changes the duration of the transit. If the inclination is of $90°$, no matter the value of obliquity, the planet will cover symmetrical stellar regions throughout the transit in terms of stellar radial velocities and μ values. Similarly, for a null obliquity, no matter the value of inclination, the planet will transit symmetrical

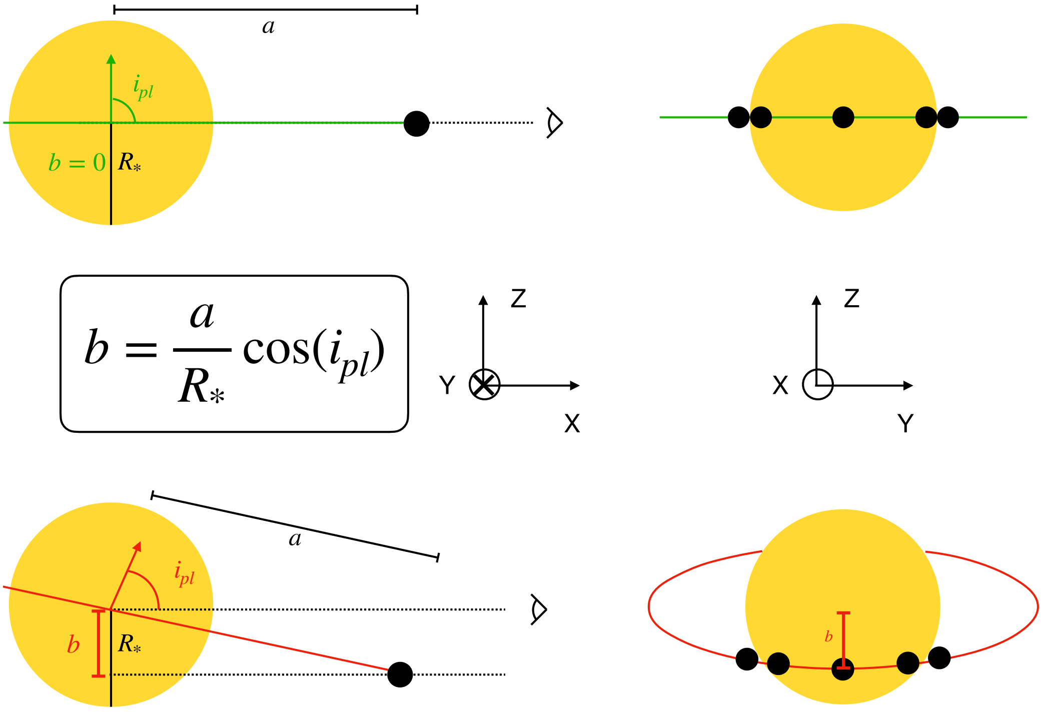

Fig. 2.16.: Sketch of the impact parameter of a planetary transit for a circular orbit and two different planetary orbital inclinations.

stellar regions. However, for specific combinations of planetary inclination and obliquity, the planet can end up transiting mostly the blue or redshifted part of the stellar surface (e.g. Bourrier et al. (2023)). See Figure 2.17, which shows the effect of obliquity and inclination on the transit chord.

2.4 Towards a global modelling approach with the EVE code

One of the most advanced approaches to analysing the absorption signature of a transiting planetary atmosphere relies on simulating the transit of a planet in front of a synthetic stellar spectral grid that represents the target star. By doing so, synthetic observables, that is the synthetic out-of-transit and in-transit spectra, can be generated, and a synthetic absorption spectrum can be computed. Generally, the synthetic observables are computed for the transit of an opaque planetary body in front of a star affected by CLV and stellar rotation. This allows for the distortions caused by stellar rotation and CLV to be included in the synthetic absorption spectrum. Once the absorption spectrum of the opaque planetary body is reconstructed, it is then directly subtracted from the one reconstructed from the observations. The

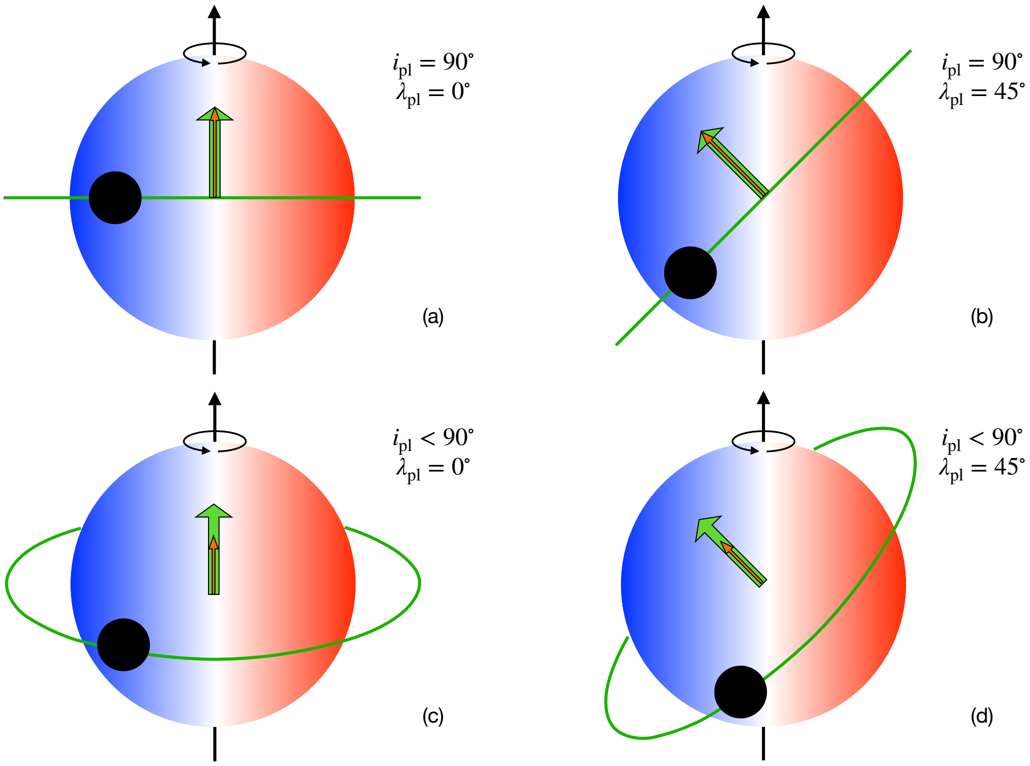

Fig. 2.17.: Effect of the planetary orbital inclination and sky-projected spin-orbit angle on the planetary transit chord. The orange arrow shows the normal axis to the plane of the planetary orbit. The green arrow shows the projection of the orange arrow on the plane of the sky.

residuals are supposed to trace the pure atmospheric absorption signature and can then be analysed to infer atmospheric properties (e.g. Borsa et al. 2021; Casasayas-Barris et al. 2020, 2021; Seidel et al. 2023). Alternatively, a Gaussian-like absorption profile, representing the absorption signature of the planetary atmosphere, can be multiplied by the synthetic absorption spectrum of the opaque planet. The resulting overall absorption spectrum can then be fitted to the observed one, and similarly, some atmospheric properties can be inferred (e.g. Yan & Henning 2018; Yan et al. 2019; Zhang et al. 2022).

Another technique worth mentioning was presented in Mounzer et al. (2022). In their study, the authors evaluate the expected distortion due to stellar rotation in their absorption spectrum by using the observed out-of-transit spectrum. They created a series of absorbed spectra exempt from atmospheric absorption and used them to recompute an absorption spectrum, which then only contained the distortions due to stellar rotation. To generate the absorbed spectra, the observed out-of-transit spectrum was scaled down and shifted by the radial velocity of the planet-occulted stellar surface at each exposure, see their Figure C 1.

2.4.1 The EVaporating Exoplanet code

A crucial physical phenomenon that is not realistically reproduced with the techniques mentioned in the paragraph above is the absorption of the local stellar spectrum by the atmosphere during the transit. Indeed, fitting an atmospheric absorption profile to the observed absorption spectrum only gives information about the average condition and properties of the atmosphere at a specific exposure. A more self-consistent way to simulate the absorption signature by the atmosphere is to directly include an atmosphere around the planet in the transit simulations. That way, it is possible to identify which regions of the atmosphere (that can have different properties) occult which regions of the stellar surface (that can also have different local spectra).

To account for the above-mentioned effects and simulate more self-consistently transits of a planet and its atmosphere, I use the EVaporating Exoplanets (EVE) code (Bourrier & Lecavelier des Etangs 2013; Bourrier et al. 2014, 2015, 2016) which is developed by the team in which I conducted my Ph.D. thesis. Figure 2.18 shows the simplified architecture of the EVE code, emphasising its capability to simultaneously compute absorption of the local stellar spectrum by the planet and the atmosphere.

There are realistic and complex models for simulating planetary atmospheres (e.g. Oklopčić & Hirata 2018; Lampón et al. 2020; Wardenier et al. 2021; Pluriel et al. 2022), and advanced studies on stellar contaminations in transit absorption spectra (e.g. Yan et al. 2017; Yan & Henning 2018; Casasayas-Barris et al. 2020, 2021; Borsa

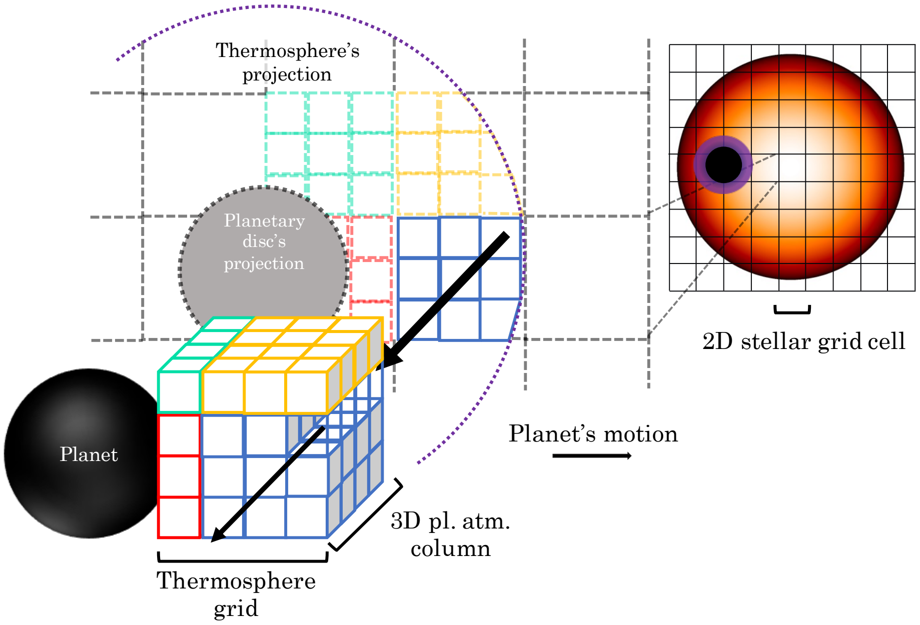

Fig. 2.18.: Simplified sketch of the architecture of the EVE code for the computation of the absorption of the stellar spectrum during the transit of a planet and its atmosphere. Different colours for the atmosphere grid cells mean that their projections fall on different stellar cells. The black arrows represent the stellar light coming out of the stellar surface. I only show a small fraction of the simulated atmosphere for clarity.

et al. 2021; Zhang et al. 2022), however, they are rarely seen being used together. Combining accurate stellar spectral variations and realistic atmospheric models in planetary transit simulations is one of the endeavours of the EVE code.

With the EVE code, I can use a global approach, which allows me to simulate the transit of a planetary body on a three-dimensional orbit in front of a synthetic spectral grid representing a star, accounting for stellar rotation, centre-to-limb variation, and broadband limb darkening. The code also allows me to include a three-dimensional atmosphere around the planet, with specific temperature, density and velocity structures. The absorption of the local stellar spectra by the planet and the atmosphere is done simultaneously at each position of the planet during its transit (see Fig. 2.18), contrasting with the technique presented at the beginning of the section. The code produces a time series of in-transit spectra at high spectral and temporal resolution. Eventually, the in-transit spectra are convolved with an instrumental response and can be re-sampled both in wavelength and time to match the spectral resolution and time cadence of actual transit observations. Finally, the code computes absorption spectra and compares them to those reconstructed from observations. With the EVE code, I am thus able to produce synthetic transit observations that are equivalent to real datasets, which I can then use for direct comparison with actual observations.

2.4.2 Synthetic stellar spectrum in EVE

A crucial ingredient in transit simulations is to have an accurate description of the stellar spectrum that is absorbed at each time step by the planet and its atmosphere. Following its orbital motion during the transit, the planet occults various regions of the stellar surface which emit local spectra with different line profiles mainly due to stellar rotation and CLV. To account for the variations in the stellar spectrum over the apparent surface of the star, the EVE code models the star as a disc discretised by a uniform 2D square grid of length equal to the stellar diameter. Each cell of the grid covering the stellar disc may then be filled with a local flux accounting for stellar spectral variations in various fashions that I describe below.

Using the out-of-transit spectrum

When I first handled the EVE code, it relied on the observed out-of-transit spectrum to estimate the local spectrum of a simulated star. To be considered as equivalent to the local spectrum at the centre of the stellar disc, the out-of-transit spectrum is first scaled down by the limb-darkening weighted stellar surface. Afterwards, the spectrum is distributed by the EVE code on the uniform 2D square grid (mentioned above) using the μ positions of the grid cells and an analytical limb darkening law. The spectrum of each cell is then multiplied by the exact surface of the grid cell. Next, the code computes the radial velocity of the grid cells, based on the $v_{\mathrm{eq}} \sin(i_*)$ value of the star, and applies the corresponding wavelength shift to their spectra.

However, using the out-of-transit spectrum to define the local spectra in each cell can introduce some biases, especially in the line profiles. Firstly, the limb darkening coefficients that are used to scale down the out-of-transit spectrum may not be adequate regarding the real limb darkening variation from the observed star. Secondly, the laws used to define the local effects of limb darkening are not universal. Thirdly, as shown below, the analytical laws do not reproduce CLV in the line profiles and only account for BLD. Finally, as discussed in Sects. 2.3.1 and 3.1.3, the resulting line profiles in the out-of-transit spectrum do not correspond to the local line profiles, as they are broadened by stellar rotation and affected by the global CLV of the star. Distributing the observed disc-integrated line profiles locally on the stellar surface and applying a velocity shift to them would result in accounting for stellar rotation twice. Using the out-of-transit spectrum to fill the stellar grid in EVE thus only holds for slow-rotating stars and spectral lines weakly affected by CLV.

To illustrate this last argument, I first computed a spectral stellar grid as explained above, but instead of the disc-integrated spectrum, I used the spectral intensity at disc's centre for a generic star, generated with the *Turbospectrum* code (see below for

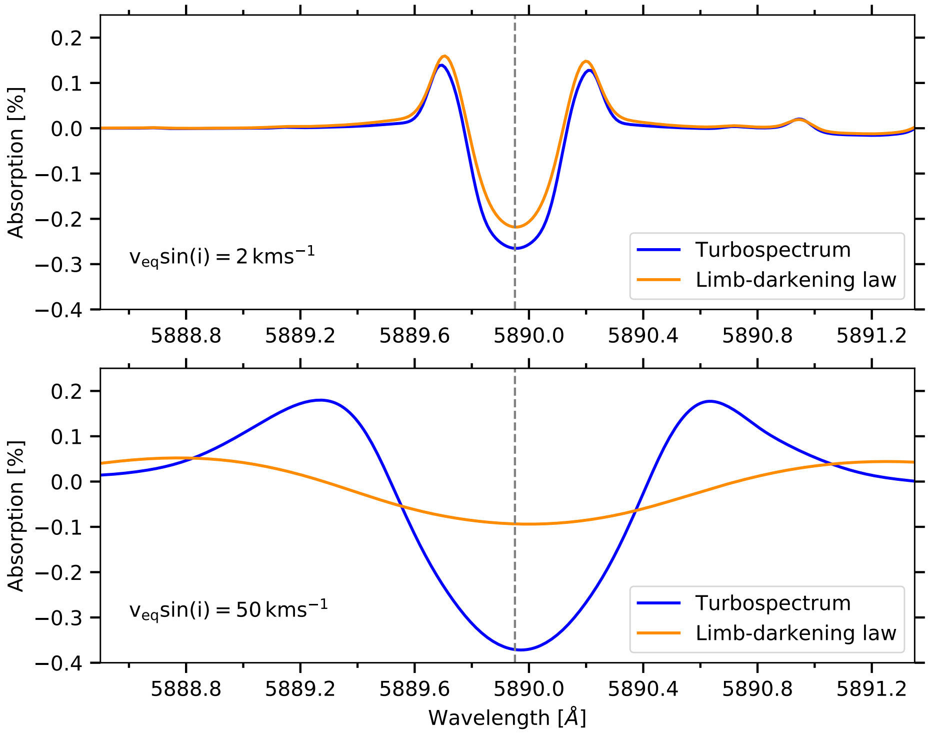

Fig. 2.19.: Mean theoretical absorption spectrum between contact times T_2 and T_3 in the planetary rest frame. The blue curves were computed using a stellar grid derived using the intensity at disc's centre from *Turbopsectrum*. The orange curves were computed using a stellar grid derived with a quadratic limb darkening law and the disc-integrated spectrum of the grids used to obtain the blue curves.

the methodology). Then, I computed a new stellar spectral grid using a quadratic limb darkening law and the disc-integrated spectrum of the first grid to distribute the spectra locally on the stellar grid, as explained above.

Finally, I used EVE to simulate the transit of a typical Hot Jupiter without atmosphere (using the system's parameters of HD 209458 b) in front of these stellar grids, and compute the corresponding absorption spectra. Figure 2.19 shows the absorption spectra derived for the two different grids described above for a $\mathrm{v_{eq}}\sin(\mathrm{i}_*) = 2$ km s^{-1} (slow-rotator) and 50 km s^{-1} (fast-rotator).

For the slow-rotator case, the distortions in the absorption spectra derived using either of the two grids are comparable, suggesting that using the out-of-transit spectrum as a proxy of the local stellar line profile remains a decent approximation. On the contrary, for the fast-rotator case, the distortions in the absorption spectrum, derived using a stellar spectral grid defined with a quadratic limb darkening law and the disc-integrated spectrum, depart significantly from the expected absorption spectrum. The disc-integrated spectrum is, therefore, an inappropriate estimator of the local stellar line profile in this case.

Using the spectral intensity at disc's centre

To circumvent this issue presented above, I made a first adaptation to the EVE code so that it could use a synthetic spectral intensity at disc's centre instead of the observed disc-integrated spectrum to fill the stellar grid. To generate this synthetic intensity for a set of parameters matching my target stars, I used the *Turbospectrum code for spectral synthesis* (Alvarez & Plez 1998; Plez 2012) (see next section). Then, I use this intensity (free of CLV effect by definition) in a limb darkening law to distribute the spectral intensity in each cell of the stellar grid without the need to scale it down first. As described before, these local intensities were also shifted in wavelength with respect to the radial velocity of the local stellar surface. Finally, the local intensities were scaled by the surface of a grid cell to have units of flux. This approach is slightly better than the initial one since the line profiles in the spectrum derived with *Turbospectrum* are not broadened by stellar rotation. Still, this approach remains biased because the limb darkening laws and coefficients might not be representative of the real limb darkening effect of the star and, more importantly, they do not render the spectral variations in the line profiles, as is demonstrated in the following figures.

In Figure 2.20, I show an example of the intensity as a function of wavelength derived with *Turbospectrum* for different μ positions on the stellar disc around the Na I D2 line for a star with a temperature of 6065 K, a log g of 4.361 cm s^{-2} and a metallicity [Fe/H] of 0. To highlight the drawbacks of using analytical limb darkening laws to distribute the local intensities, three spectral regions around the line are of interest: the continuum adjacent to the line, the line's core, and the line's wing. In Figures 2.21, 2.22 and 2.23, I show the variation of the intensity as a function of the μ position in these three spectral regions. I compared the values derived with *Turbospectrum* to those derived using the quadratic, logarithmic and square root limb darkening laws.

$$\text{Quadratic (Kopal 1950)}: \quad \frac{I_\mu}{I_{\mu=1}} = 1 - c_1(1-\mu) - c_2(1-\mu)^2 \tag{2.7}$$

$$\text{Logarithmic (Klinglesmith \& Sobieski 1970)}: \frac{I_\mu}{I_{\mu=1}} = 1 - c_1(1-\mu) - c_2\mu\ln(\mu) \tag{2.8}$$

$$\text{Square root (Diaz-Cordoves \& Gimenez 1992)}: \frac{I_\mu}{I_{\mu=1}} = 1 - c_1(1-\mu) - c_2(1-\sqrt{\mu}) \tag{2.9}$$

where $I_{\mu=1}$ is the spectral intensity at disc's centre and c_1 and c_2 are the limb-darkening coefficients used in the laws. These coefficients were derived for the

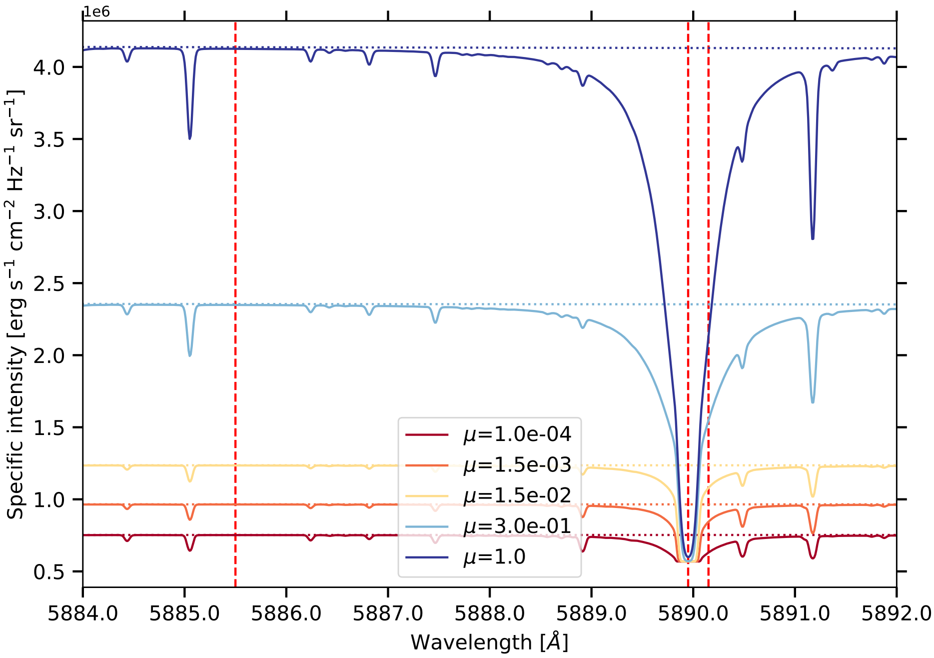

Fig. 2.20.: Specific intensity as a function of wavelength for a series of positions on the stellar disc derived using *Turbospectrum*. The vertical red dashed lines mark from left to right: the continuum, the line's core and the line's wing.

specific stellar properties using the EXOFAST[16] and the EXOCTK[17] websites. The coefficients are usually obtained by fitting synthetic spectra from stellar atmosphere models.

Overall, none of these laws are able to reproduce the centre-to-limb variation of the core and wing of the line. Still, their trend in the continuum agrees with *Turbospectrum*. The square root law gives the better match, particularly at low μ values, that is, close to the limb. These results are expected because the analytical laws are designed for the broadband (i.e. continuum) limb darkening. The rapid comparison given above illustrates the importance of defining the local spectrum of stars using tools such as *Turbospectrum* to account more self-consistently for both the broadband limb darkening and the centre-to-limb variation in the line profiles, which are both crucial phenomena in transit absorption spectra analyses as already mentioned before.

However, it is worth noting that the intensity spectra derived with *Turbospectrum* are also subject to biases that are inherent to the approximation used in the code and the atmospheric models it uses.

---

[16] `https://astroutils.astronomy.osu.edu/exofast/limbdark.shtml`

[17] `https://exoctk.stsci.edu/limb_darkening`

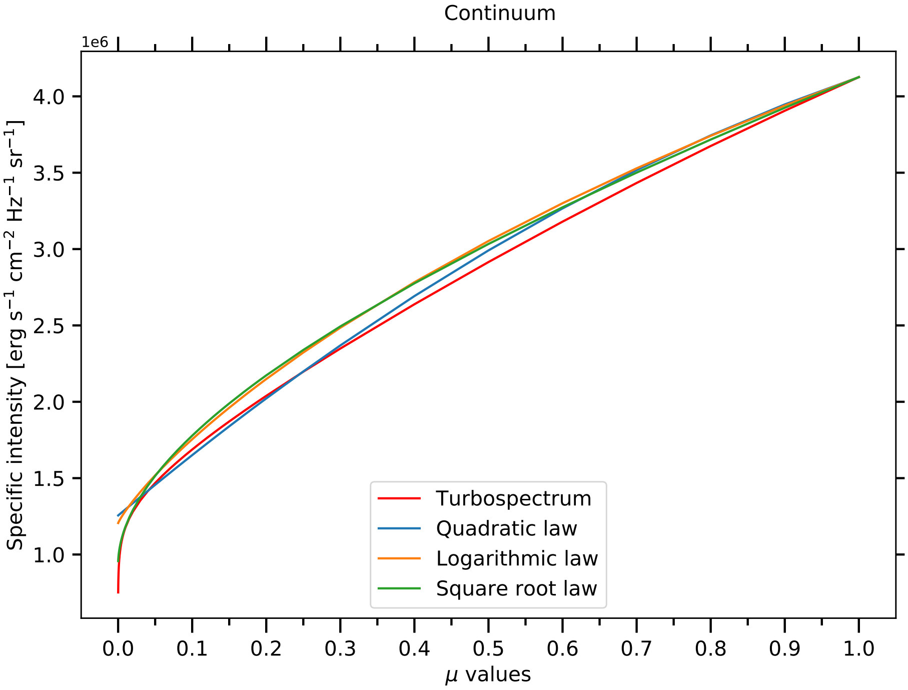

Fig. 2.21.: Specific intensity in the continuum at 5885.5 Å as a function of the position on the stellar disc derived with *Turbospectrum* and analytical limb darkening laws.

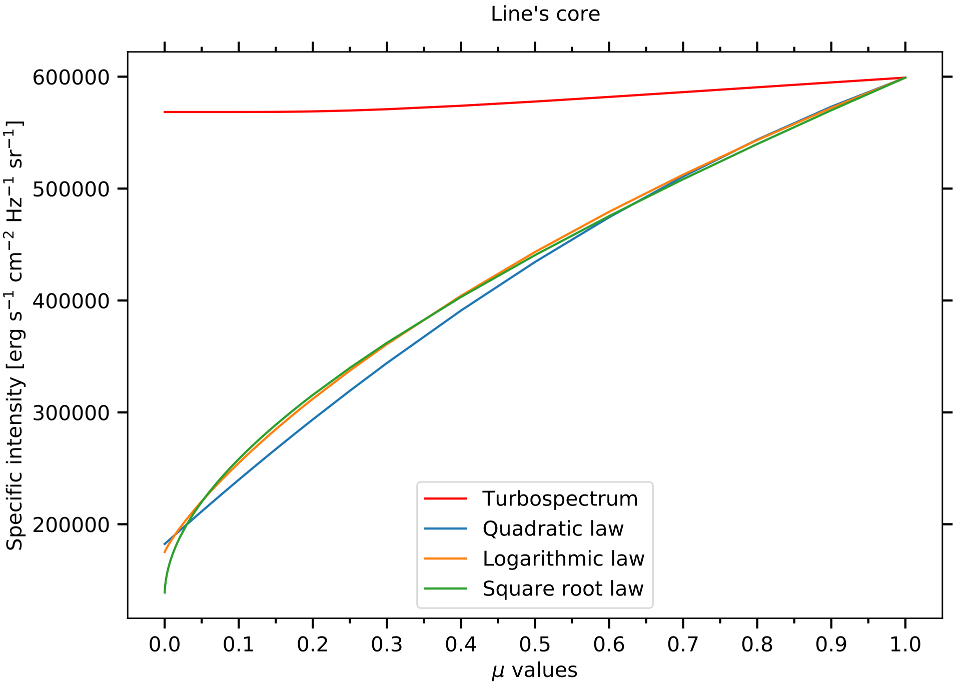

Fig. 2.22.: Specific intensity in the core of the Na I D2 line at 5889.95 Å as a function of the position on the stellar disc derived with *Turbospectrum* and analytical limb darkening laws.

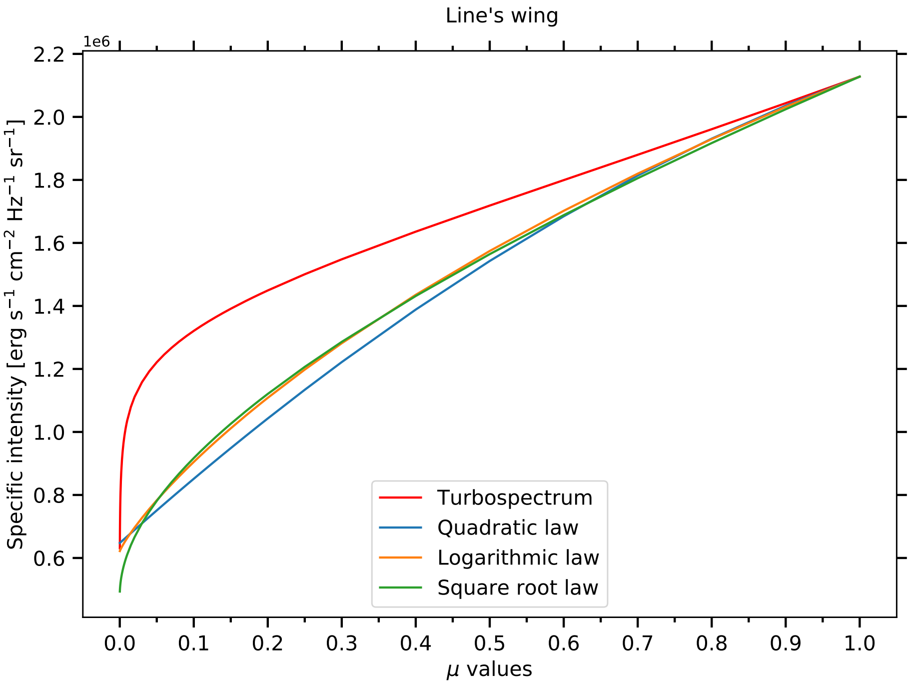

Fig. 2.23.: Specific intensity in the red wing of the Na I D2 line at 5890.15 Å as a function of the position on the stellar disc derived with *Turbospectrum* and analytical limb darkening laws.

Using synthetic local spectra

Here, I describe the systematic process I follow to derive the synthetic spectrum for a specific star in order to compute the stellar spectral grid used as input in the EVE code. With this approach, the EVE code can use detailed synthetic local stellar spectra that account for stellar rotation and centre-to-limb variations both in the line profiles and in the continuum. The first step is to search for the star's $\log(g)$ (surface gravity), effective temperature and metallicity values. For this, I usually visit the NASA exoplanet archive[18] and choose the values of the parameters from one of the most accurate references listed on the page. These values are needed to determine which stellar atmosphere model I will consider. Then, I select the adequate model from the MARCS database[19] of stellar photospheric models (Gustafsson et al. 2008). The models in this database are available with a step in effective temperature of 100 K between 2500 K and 4000 K and a step of 250 K between 4000 K and 8000 K; a step in $\log(g)$ of 0.5 between 3 and 5.5; a step in metallicity of 1 between -5 and -3, a step of 0.5 between -3 and -1, and a step of 0.25 between -1 and 1. These models provide a description of the photosphere of the star, that is, the temperature and the density profiles, along with other quantities relevant for the spectral synthesis. When the stellar parameters of a specific target do not fall on the grid of MARCS models,

---

[18] `https://exoplanetarchive.ipac.caltech.edu/overview/`

[19] Available at `https://marcs.astro.uu.se`

I use the available interpolating tools of the *Turbospectrum* package. These tools allow one to interpolate the MARCS models in effective temperature, log(g) and metallicity for the LTE version of the package, and they also manage the departure coefficients for the NLTE version[20]. They were developed by Thomas Masseron and Ekaterina Magg and are available for download[21]. Typically, eight MARCS models are needed for the interpolation, whose grid point values of effective temperature, log(g) and metallicity encompass the desired values of the target.

In addition to the photospheric model, a list of spectral lines to include in the spectrum, such as the VALD[22] linelists (Ryabchikova et al. 2015), is required. These lists contain the necessary information to model properly the spectral lines in a given wavelength range. Once I have the MARCS model interpolated for the suited stellar parameters and a list of the lines to account for, I can use them as an input of the *Turbospectrum* code. *Turbospectrum* computes local intensity spectra by solving the radiative transfer equation for specific stellar atmosphere models. I use this code to derive a series of intensity spectra along the stellar radius for a series of μ values following a logarithmic distribution. This allows me to have a finer spatial sampling of the intensity spectra close to the stellar limb, where CLV alters the observed stellar line profiles the most.

After that, I use a routine that I developed to transform the list of intensity spectra into a stellar grid format readable by the EVE code. The routine creates a uniform 2D square grid accounting for the exact surface of grid cells at the limb (using the same definition as in EVE to ensure compatibility). Then, it computes the μ values of the centre of each grid cell. Knowing the μ position of the cells, the routine interpolates the intensity spectra and fills the whole stellar grid with flux spectra by multiplying the interpolated intensities by the cell's surface. Finally, the routine computes the radial velocity of the grid cells, based on the $v_{\rm eq}\sin(i_*)$ value of the target star, and shifts in wavelength each spectrum accordingly (similarly to how it is done in the EVE code). I also optimised the routine by using the symmetries of the stellar grid when filling the cells with interpolated and shifted spectra. Namely, I compute the interpolated spectra in only one half quadrant of the disc and use the circular symmetry of CLV to fill the Northern hemisphere. Then, the spectra of the Northern hemisphere are shifted to account for stellar rotation. Finally, I use the symmetry of a rotating disc to copy the spectra of the Northern hemisphere into the Southern hemisphere of the grid.

---

[20] Departure coefficients are defined as the ratio of the non-LTE-to-LTE populations of a given atomic level (see Eq. 14.227 of Hubeny & Mihalas 2014). They are used to scale LTE populations to their non-LTE values without solving the non-LTE problem.

[21] LTE: `https://marcs.astro.uu.se/software.php`. NLTE: `https://github.com/bertrandplez/Turbospectrum_NLTE`

[22] available at `http://vald.astro.uu.se`

2.4.3 Planetary atmospheric profiles in EVE

The EVE code is designed to simulate the transit of a planet surrounded by an evaporating atmosphere. The regions of a planetary atmosphere relevant for the evaporation mechanism are the thermosphere and the exosphere. The exosphere is the uppermost region of a planetary atmosphere, where the collisions between particles become negligible. Typically, the exosphere is considered to begin where the mean free path of a particle is equal to its scale height. It means that a particle in the exosphere will escape from the planet if it reaches a positive radial velocity which is greater than the escape velocity of the planet as it will not undergo collisions and lose energy or be redirected towards the planet (Schunk & Nagy 2000; Krasnopolsky 2019). The exosphere is being fed with material by the layer underneath it, called the thermosphere. The thermosphere is a region of planetary atmospheres that can get heated up to high temperature values due to the thermalisation of the XUV flux it absorbs from the star. In hot Jupiters, which are planets that orbit extremely close to their host stars, the amount of XUV flux received is large. For such planets, the thermosphere can thus reach temperatures that are so high that the whole layer enters in a hydrodynamic expansion state with a supersonic bulk velocity. (Parker 1958, 1964; Lamers & Cassinelli 1999; Catling & Kasting 2017). Under that condition, the exosphere can be largely fed with material, and the planet can lose a substantial amount of mass through the evaporation of its atmosphere. The hydrodynamic expansion can be such that the thermosphere remains collisional up to distances greater than the Roche lobe radius of the planet, entering a state of *geometrical blow-off* (Lecavelier des Etangs et al. 2004). For planets further out, due to the larger orbital distance, the received XUV flux is usually insufficient to make the thermosphere enter in a state of hydrodynamic expansion. However, such planets can still lose material through a particle-by-particle process, called the Jeans' escape, which over a long period of time could also lead to substantial mass loss (Chamberlain 1963; Volkov et al. 2011; Catling & Kasting 2017). Figure 2.24 shows a sketch of the two thermal mechanisms of atmospheric escape. The mechanism of atmospheric evaporation is important as it is related to the temporal evolution of a planet's atmosphere and is being studied intensively, (Mansfield et al. 2018; Nortmann et al. 2018; Czesla et al. 2022; Kirk et al. 2022; Gully-Santiago et al. 2023; Owen & Schlichting 2023; Orell-Miquel et al. 2023; Bello-Arufe et al. 2023; Huang et al. 2023; Zhang et al. 2023) to give just a few of the recent publications that focused on detecting and characterising escaping atmospheres.

The two mechanisms introduced above are classified as *thermal escape* mechanisms. In addition, there are two other types of atmospheric escape which are not linked to temperature. Namely, *impact erosion* and *non-thermal escape* (Catling & Kasting 2017). Impact erosion states that a large amount of matter can be removed from a planet due to a collision with an external body. Non-thermal escape encompasses

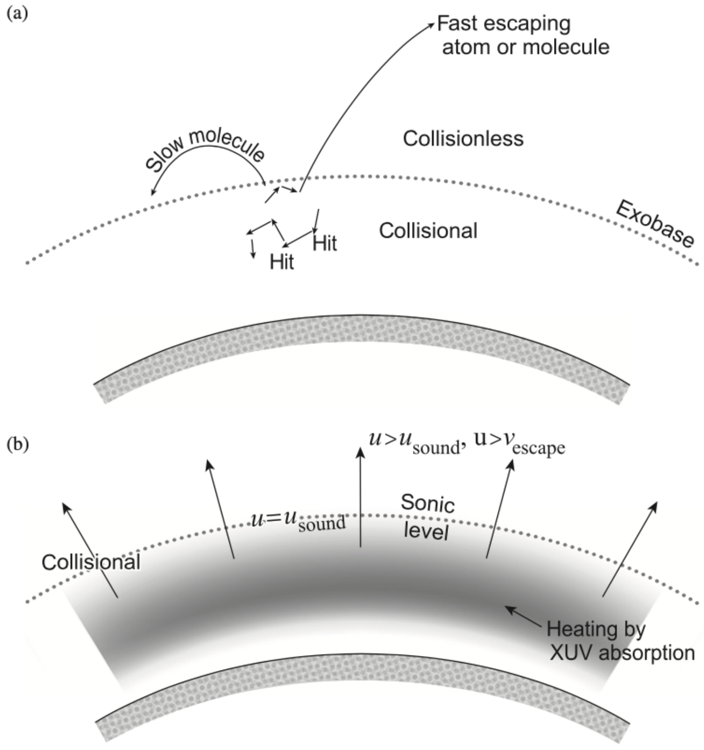

Fig. 2.24.: Sketch showing the two thermal atmospheric escape mechanisms. On the top, the particle-by-particle escape or Jeans' escape. On the bottom, the hydrodynamic expansion escape, with u standing for the bulk velocity of the atmosphere. Taken from Figure 5.2 in Catling & Kasting (2017).

different mechanisms through which an atmosphere can lose matter. To cite a few, photo-chemical reactions that can give enough energy to a particle in order to escape. Charge exchange between the neutral hydrogen atoms in the external layers of the atmosphere and the stellar wind protons. The EVE code can simulate the latter as presented in Bourrier et al. (2016). Ion escape through the planetary magnetic poles (Gunell et al. 2018). These mechanisms will not be further discussed nor used in this work. For more details about these escape mechanisms, see, for instance, Chapter 5 of Catling & Kasting (2017) and references therein.

Parker wind profile

Currently, most planets detected transiting their host star do so at very close orbital distances (exoplanet.eu). Thus, they are expected to receive large amounts of XUV flux, making their atmospheric temperature rise. Consequently, with high temperatures, their atmospheres are likely to be in a hydrodynamic escape state and to undergo strong mass loss (Lammer et al. 2003; Lecavelier des Etangs et al. 2004; Lecavelier Des Etangs 2007; Murray-Clay et al. 2009). The latter is directly linked to the long-term evolution of an atmosphere's composition and conditions. To compute

the one-dimensional temperature, density and velocity profiles of an atmosphere in hydrodynamic expansion, the code relies on the equations described in, for instance, Lamers & Cassinelli (1999) and Oklopčić & Hirata (2018), which were adapted from Parker (1958) who originally developed them for the solar wind.
The temperature profile is isothermal and given as

$$T(r) = cte. \tag{2.10}$$

The speed of sound can be computed as

$$v_s = \sqrt{\frac{k_b T}{<m>}}, \tag{2.11}$$

with k_b the Boltzmann constant and $<m>$ the mean atomic mass of all the species considered in the simulated atmosphere.

The radius of the sonic point, where the planetary wind becomes supersonic, is given by,

$$r_s = \frac{GM_p}{2v_s^2}, \tag{2.12}$$

with G the gravitational constant and M_p the mass of the planet.

The velocity profile can be derived using,

$$\frac{v(r)}{v_s} \exp\left[-\frac{v^2(r)}{2v_s^2}\right] = \frac{r_s^2}{r^2} \exp\left(-\frac{2r_s}{r} + \frac{3}{2}\right), \tag{2.13}$$

The density profile is computed using,

$$\frac{\rho(r)}{\rho_s} = \exp\left[\frac{2r_s}{r} - \frac{3}{2} - \frac{v^2(r)}{2v_s^2}\right], \tag{2.14}$$

where ρ_s is the density of the isothermal wind at the sonic point.
In the EVE code, the atmospheric profile is assumed to remain constant during the whole transit for circular orbits. For eccentric orbits, the density profiles are scaled with the inverse of the squared distance between the planet and the star during the transit to account for the change in stellar irradiation.
With these equations, the code can compute a density profile common to all the species considered in the atmosphere. From this common density profile, the code can define the density profiles of individual species. This is achieved by scaling down the common density profile via a chosen density value at a given altitude, either set directly or derived from a known mass loss rate.

The density profile of a specific species is derived as follows,

$$\frac{\frac{\rho_{\mathrm{sp}}(r)}{\rho_s}}{\frac{\rho_{\mathrm{sp}}(r_{\mathrm{top}})}{\rho_s}} = \frac{\exp\left[\frac{2r_s}{r} - \frac{3}{2} - \frac{v^2(r)}{2v_s^2}\right]}{\exp\left[\frac{2r_s}{r_{\mathrm{top}}} - \frac{3}{2} - \frac{v^2(r_{\mathrm{top}})}{2v_s^2}\right]}, \tag{2.15}$$

after simplification,

$$\rho_{\mathrm{sp}}(r) = \rho_{\mathrm{sp}}(r_{\mathrm{top}}) \exp\left[2r_s\left(\frac{1}{r} - \frac{1}{r_{\mathrm{top}}}\right) - \frac{v^2(r) - v^2(r_{\mathrm{top}})}{2v_s^2}\right], \tag{2.16}$$

where in this case, $\rho_{\mathrm{sp}}(r_{\mathrm{top}})$ is the value of the density of a specific species at the top of the atmosphere.

Once the one-dimensional atmospheric profiles have been defined, the code builds a three-dimensional homogeneous spherical grid around the planetary body with cubic cells. It then uses spherical symmetry and the 1D profiles to fill the entire atmospheric grid. The total optical depths of the atmosphere are computed along the line of sight of an external observer that goes through each atmospheric column that are perpendicular to the stellar surface (see Fig. 2.18). As mentioned earlier, the code can then compute, at each time step, the absorption of the local stellar spectra by the local regions of the atmosphere, which do not necessarily have the same properties.

In order to tend towards a more realistic description of thermospheric profiles under hydrodynamic atmospheric escape, the EVE code can now directly call the *p-winds* code (Dos Santos et al. 2022) based on the adaptation by Oklopčić & Hirata (2018); Lampón et al. (2020) of the formalism presented above. The *p-winds* code can compute the atmospheric profiles of hydrogen and helium atoms in an atmosphere, accounting for photo-chemistry of hydrogen and helium atoms and on the received XUV flux, which is one of the drivers of hydrodynamic escape.

Finally, the code can define an exospheric region above the thermosphere defined by the three-dimensional grid. The number of particles that end up in the exosphere is determined from the mass flux at a predefined transition radius. This mass flux can be computed from the profiles derived from the equations given above. In my work, I have not made use of this part of the code as the different concepts I investigated only required simulating an expanding thermosphere. The use of the exospheric part in transit simulations was demonstrated, for example, in Bourrier & Lecavelier des Etangs (2013); Bourrier et al. (2014, 2015, 2016).
All the transit simulations presented here and that contain a planetary atmosphere used the equations introduced above to compute the atmospheric profiles.

3

Combined analysis of stellar and planetary absorption lines via global forward-transit simulations

In this chapter, I present and expand on the results of my publication entitled *Combined analysis of stellar and planetary absorption lines via global forward-transit simulations* (Dethier & Bourrier 2023), which was published in the *Astronomy & Astrophysics* journal. This paper contains two main chapters, the first one aims at studying in detail the effect of stellar contamination caused by stellar rotation and CLV on the absorption spectrum of a generic exoplanet. The second one focuses on re-interpreting real transit datasets of two specific exoplanetary systems, using a global approach that combines the modelling of the stellar spectrum and the simulation of the planetary and atmospheric transits.

3.1 Stellar and orbital contamination in absorption spectra

To make a representative qualitative study of the effects of stellar contamination on the measured absorption spectrum of a transiting planet, I chose to simulate the idealised version of the transit of the planetary system HD 209458 b. By idealised, I mean that I considered the stellar and planetary parameters of the system (see Table 5.1), but I used an eccentricity of 0 and a planetary orbital inclination of 90° in order to have a circular planetary orbit that passes by the stellar disc's centre (impact parameter of 0). HD 209458 b is a natural choice as it is one of the first exoplanets to be detected by the transit method and one of the first for which an atmosphere was detected (Henry et al. 2000; Charbonneau et al. 2000, 2002). HD 209458 b is also featured in a series of numerous publications (see, e.g. exoplanetarchive.ipac.caltech.edu/HD20209458 and exoplanet.eu/hd209458b) and is thus a well-known exoplanet. Interestingly, though, the atmospheric sodium feature that was originally detected for this system (Charbonneau et al. 2002) has been challenged by Casasayas-Barris et al. (2020, 2021) who showed that the feature that is observed around the Na I D2 and D1 lines in the absorption spectrum most probably comes from stellar contamination caused by stellar rotation and CLV. This contradiction suggests that transit observations of such exoplanetary systems could be subject to contamination that can be the source of misinterpretation. Studying and characterising those types of contamination in such standard exoplanetary systems is therefore relevant to build a better understanding of their behaviour and to tend towards more reliable derived planetary properties.

To simulate the synthetic spectra of the planetary transits of HD 209458 b I use the EVE code. To simulate the synthetic stellar spectrum of HD 209458 in the spectral region of the Na I D2 and D1 lines, I use the *Turbospectrum* code (Alvarez & Plez 1998; Plez 2012) along with the interpolated MARCS photospheric model that matches the stellar parameters of the system HD 209458, as explained in Sect. 2.4.2. The idea in this section is, on the one hand, to study the impact of stellar rotation and CLV on the absorption spectrum of a transiting planet and, on the other hand, to study how the choice of the spectral profile used as proxy for the planet-occulted spectrum can influence the extracted absorption signature when computing absorption spectra. For this, I compute four different stellar spectra: for a non-rotating star without CLV; for a moderate-rotating star without CLV; for a fast-rotating star without CLV; and for a non-rotating star but affected by CLV. These particular choices allow me to study the impact of stellar rotation and CLV independently. I then use each of these stellar spectra as input in the EVE code to simulate synthetic spectra of a planetary transit with and without an atmosphere. Finally, with the resulting spectra, I compute the absorption spectrum using different proxies for the planet-occulted spectrum. The simulated planetary thermosphere follows a Parker wind description (Sect. 2.4.3) and is made of $\sim 90\%$ of hydrogen and $\sim 10\%$ of helium. Neutral sodium is included as a trace species, with an abundance of $\sim 0.0001\%$ (based on a value of ~ 7 ppm given in Nikolov et al. (2018)), with respect to the total thermospheric density. This composition yields a mean atomic mass of ~ 1.30746 units of atomic mass. The bulk density of the thermosphere is tuned so that the excess atmospheric absorption signature has a maximum value of approximately $1\ \%$ around the Na I D2 and D1 doublet, which is a typical value of Na I absorption signature measured for Hot Jupiters (e.g. Wyttenbach et al. 2017; Casasayas-Barris et al. 2018; Seidel et al. 2019). The resulting 1D atmospheric profiles are shown in Figure 3.1.

3.1.1 Uniform stellar emission

To serve as a benchmark, I start with a basic case in which the stellar line profiles are constant over the whole surface of the star, without influence from CLV and stellar rotation. Ideally, to extract the unaffected atmospheric absorption spectrum at a given exposure, $\mathrm{F_{ref}}$ (see Sect. 2.2.1) should be equal to the exact local spectrum emerging from the planet-occulted stellar surface for that exposure (i.e. $\mathrm{F_{loc}(t)}$).

Tab. 3.1.: HD 209458's stellar and planetary properties.

Parameter	Value
Stellar :	
Radius ($R_\odot$)	$1.155^{+0.015}_{-0.016}$
Mass ($M_\odot$)	1.119 ± 0.033
T_{eff} (K)	$6\,065 \pm 50$
Metallicity [Fe/H]	0.00 ± 0.05
$\log g$ (cm s^{-2})	$4.361^{+0.007}_{-0.008}$
Age (Gyr)	4.0 ± 2.0
$v_{\mathrm{eq}} \sin i_*$ (km s^{-1})	$4.228 \pm 0.007^{\dagger}$
Planetary :	
Radius (R_{Jup})	$1.359^{+0.016}_{-0.019}$
Mass (M_{Jup})	$0.682^{+0.015}_{-0.014}$
Semi-major axis (au)	$0.04707^{+0.00046}_{-0.00047}$
Period (days)	$3.52474859 \pm 0.00000038$
Inclination (deg)	$86.71 \pm 0.05^{\dagger\dagger}$
Sky-projected spin-orbit angle (deg)	$1.58 \pm 0.08^{\dagger\dagger\dagger}$

Note. Values are the same as those used or derived in Casasayas-Barris et al. (2020), except for the rotational velocity of the star and sky-projected spin-orbit angle of the planet, taken from Casasayas-Barris et al. (2021). Parameters that we vary in the study:(†) Sect. 3.1 set to 3 and 20. (††) Sect. 3.1 set to 90. († † †) Sect. 3.1 set to 0 and 45.

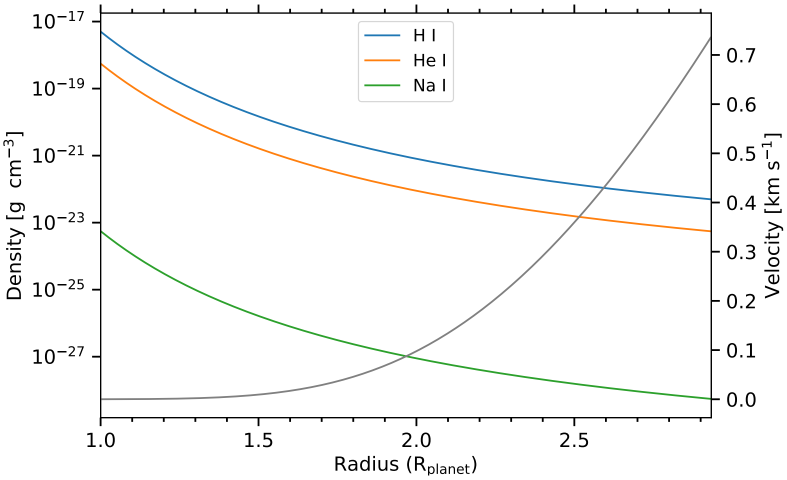

Fig. 3.1.: Planetary atmospheric profile of the simulated thermosphere as a function of altitude above the opaque planetary body radius. The density profiles of the three simulated species are shown in colour. The velocity profile of thermospheric gas is shown in grey. The simulated thermosphere was limited to the Roche lobe radius.

Indeed, using $\mathrm{F_{loc}(t)}$ in Eq. 2.3 and the notation for the flux introduced in Eq. B.3 gives,

$$\begin{aligned}\frac{\mathrm{F_{abs}}(\lambda,\mathrm{t})}{\mathrm{F_{loc}}(\lambda,\mathrm{t})} &= \frac{\sum\limits_k \mathrm{I}_k(\lambda)\ \Delta\Omega_k + \sum\limits_l \left[1-e^{-\tau_l}\right] \mathrm{I}_l(\lambda)\ \Delta\Omega_l}{\sum\limits_k \mathrm{I}_k(\lambda)\ \Delta\Omega_k} \\ &= \frac{\sum\limits_k \mathrm{I}_{\mu=1}(\lambda)\ \Delta\Omega_k + \sum\limits_l \left[1-e^{-\tau_l}\right] \mathrm{I}_{\mu=1}(\lambda)\ \Delta\Omega_l}{\sum\limits_k \mathrm{I}_{\mu=1}(\lambda)\ \Delta\Omega_k} \\ &= 1 + \frac{\mathrm{S_{atm}}^{\tau}}{\mathrm{S_{pl}}}.\end{aligned} \tag{3.1}$$

where $\mathrm{I}_{\mu=1}(\lambda)$ is the spectral intensity from the stellar disc's centre, $\mathrm{S_{pl}}$ is the stellar surface occulted by the planetary disc and $\mathrm{S}^{\tau}_{\mathrm{atm}}$ is the surface occulted by the thermosphere weighted by its attenuation function. In this case, the spectral intensity profiles (I_k and I_l) from all the stellar cells are equal to the spectral intensity profile at the centre of the stellar disc ($\mathrm{I}_{\mu=1}$), and therefore simplify in the above equation.

However, in practice, $\mathrm{F_{loc}(t)}$ is difficult to extract observationally and as a substitute, the disc-integrated spectrum, $\mathrm{F_{out}}$, is used as a reference. Using $\mathrm{F_{out}}$ in Eq. 2.3 gives,

$$\begin{aligned}\frac{\mathrm{F_{abs}}(\lambda,t)}{\mathrm{F_{out}}(\lambda)} &= \frac{\sum\limits_k \mathrm{I}_{\mu=1}(\lambda)\ \Delta\Omega_k + \sum\limits_l \left[1-e^{-\tau_l}\right] \mathrm{I}_{\mu=1}(\lambda)\ \Delta\Omega_l}{\sum\limits_i \mathrm{I}_{\mu=1}(\lambda)\ \Delta\Omega_i} \\ &= \frac{\mathrm{S_{pl}}}{\mathrm{S}_*} + \frac{\mathrm{S_{atm}}^{\tau}}{\mathrm{S}_*},\end{aligned} \tag{3.2}$$

with S_* the surface of the stellar disc. The same simplification as in Eq. 3.1 was applied, leading to an equation analogous to Eq. 2.5

In this specific case, the absorption spectra are equivalent, and the atmospheric absorption signature is unaffected, using either $\mathrm{F_{out}}$ or $\mathrm{F_{loc}(t)}$ as a reference for the planet-occulted line profile, apart form multiplicative and additional constant values. To illustrate this result, I simulated the transit of a planet in front of this uniform stellar spectral grid without an atmosphere and the transit of a planet with the atmosphere described at the beginning of Sect. 3.1. Figure 3.2 shows the absorption spectrum at the centre of transit for these simulations computed both with $\mathrm{F_{loc}(t)}$ and $\mathrm{F_{out}}$. In this figure, in order to compare the two absorption spectra and have them on the same flux level, I multiply the absorption spectrum derived with $\mathrm{F_{loc}(t)}$ by the ratio between the occulted surface by the planet ($\mathrm{S_{pl}}$) and the stellar surface (S_*). I also subtract the planetary disc contribution to the absorption to place the

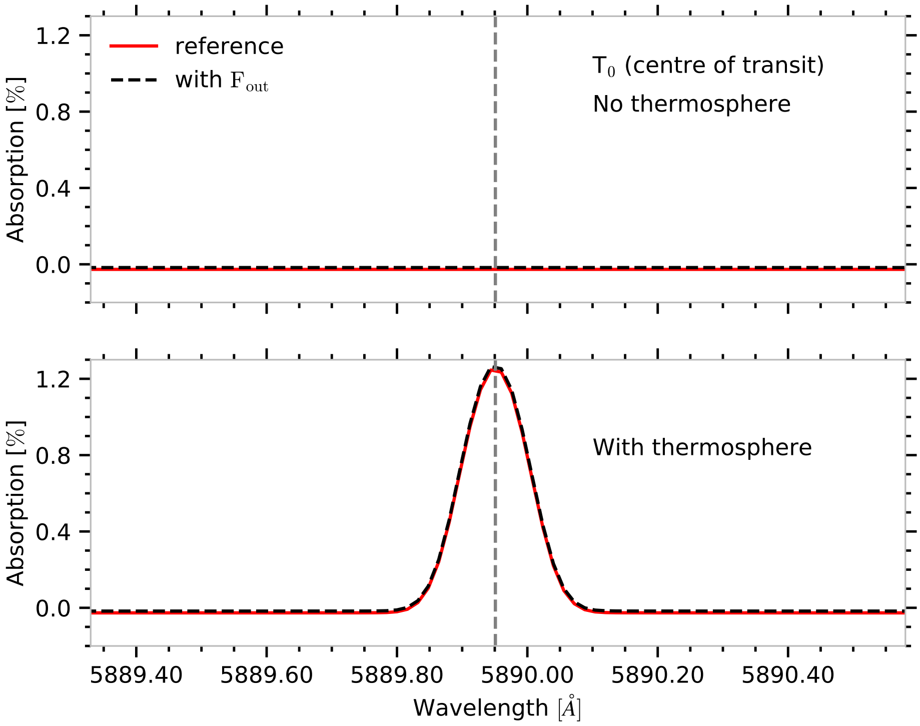

Fig. 3.2.: Theoretical absorption spectrum of the generic planet as a function of wavelength in the planet rest frame transiting a uniform stellar spectral grid without (*upper panel*) and with (*lower panel*) the atmosphere containing neutral sodium atoms. The spectra are shown for the centre of the transit and are computed using F_{out} (dashed black curve) or F_{loc} (red curve) as reference for the planet-occulted line profile.

continuum of the absorption spectra at zero[1]. In the case without atmosphere, the absorption spectrum is flat and constant as expected because the opaque planetary body absorbs the spectrum of the star equally at all wavelengths. In the other case, that is, with an atmosphere containing sodium atoms, the unaffected absorption signature of the atmosphere is clearly visible in excess of the continuum value around the rest wavelength of the Na I D2 line transition.

3.1.2 Impact of stellar rotation

In Sect. 3.1.1, I set a benchmark for the expected unaffected absorption spectrum for the transit of the test planet with and without an atmosphere. The case I showed in that section is similar to having a $v_{eq} \sin(i_*)$ value tending to zero, which causes the line profile of F_{out} to tend to be equal to the local planet-occulted line profile. This is because the planet-occulted regions have a negligible radial velocity, and the

---

[1] In Fig. 3.2 the continua are not exactly at zero because of numerical uncertainties in the computed surfaces due to the stellar grid resolution.

Tab. 3.2.: Simulations of Sect. 3.1.2

Case	$\mathrm{v_{eq}}\sin(\mathrm{i}_*)$ $[\mathrm{km\,s^{-1}}]$	λ_{pl} [°]	Atmosphere
1	3	0	No
2	3	0	Yes
3	3	45	No
4	3	45	Yes
5	20	0	No
6	20	0	Yes
7	20	45	No
8	20	45	Yes

broadening of the disc-integrated lines is almost null. Omitting any other effect, POLDs are negligible for slow-rotating stars (i.e. $\mathrm{v_{eq}}\sin(\mathrm{i}_*)$ close to 0 $\mathrm{km\,s^{-1}}$) and it is reasonable to use $\mathrm{F_{out}}$ as reference for the planet-occulted line profile to compute absorption spectra.

In the present section, I investigate the individual effect of stellar rotation on the absorption spectrum. This means that the stellar lines profiles do not vary over the stellar surface but are shifted in wavelength according to the radial velocity of the stellar region they emerge from, see Figure 2.10. To dissect the problem and have a representative study, I specifically look at two contrasted cases, one of a moderate-rotating star ($\mathrm{v_{eq}}\sin(i_*) = 3\,\mathrm{km\,s^{-1}}$) and another of a fast-rotating star ($\mathrm{v_{eq}}\sin(i_*) = 20\,\mathrm{km\,s^{-1}}$). I can, therefore, study the behaviour of the absorption spectrum with respect to the magnitude of the stellar rotational velocity. In addition, I investigate the effect of the sky-projected spin-orbit angle of the planet. With the same philosophy as for the stellar rotational velocity, I choose to use two contrasted values of the sky-projected spin-orbit angle to have representative cases: $\lambda_{\mathrm{pl}} = 0$ and $\lambda_{\mathrm{pl}} = 45°$. I decided to keep the impact parameter to zero for this study in order to separate the clear effect of obliquity and stellar rotation (See also Sect. 2.3.4). There are, thus, eight simulations in total, summarised in Table 3.2.

As I mentioned earlier, I also want to compare the derived absorption spectra as a function of the reference spectrum, $\mathrm{F_{ref}}$, used as a proxy for the planet-occulted line profile. The idea is to assess which proxy of the planet-occulted stellar line best mitigates the POLDs induced by the stellar rotation. Therefore, for each of the simulations above, I compute their absorption spectrum using three different $\mathrm{F_{ref}}$: the disc-integrated spectrum $\mathrm{F_{out}}$, as it is commonly done in the literature; $\mathrm{F_{out}}$ shifted to the radial velocity of the planet-occulted stellar region in a given exposure ($\mathrm{F_{out}}(\mathrm{v_{rad}})$); and the local spectrum ($\mathrm{F_{loc}}\,(\mu = 1)$) from the stellar region occulted at the centre of the stellar disc (here corresponding to the centre of the transit T_0). Finally, I also include in the following figures the unaffected absorption spectrum computed for each simulation. This spectrum is computed with the exact planet-occulted spectrum at each exposure ($F_{loc}(t)$). Therefore, it should be equal to the absorption spectrum in the Sect. 3.1.1 provided that the spatial variation of $v_{eq}\sin(i_*)$ across the occulted stellar surface in a given exposure can be neglected.

Without the thermosphere

Figure 3.3 shows the resulting absorption spectra of the simulations of the transit of the planetary opaque body without atmosphere for the case with a $v_{eq}\sin(i_*) = 3\,\mathrm{km\,s^{-1}}$. This figure also shows the different spectra used to compute the absorption spectra to help understand and interpret these results. Figure 3.4 is the same for the case with a $v_{eq}\sin(i_*) = 20\,\mathrm{km\,s^{-1}}$. These figures only display the absorption spectra at two illustrative time steps of the transit: the centre of the transit (T_0) where the velocity shift of the planet-occulted line profiles is minimal and the second contact time (T_2, just after ingress) where the velocity shift of the planet-occulted line profiles is maximal. In these figures, F_{out} and $F_{out}(v_{rad})$ were multiplied by the ratio between the occulted surface and the surface of the star to bring them to the level of F_{loc} and make the comparison easier.

$F_{ref} = F_{loc}\ (\mu = 1)$ (green curve)

- At T_2, the absorption spectrum exhibits the most notable POLD both for the moderate and fast-rotating cases. It comes from the fact that the planet-occulted stellar regions have narrow line profiles that are shifted away from their rest wavelength due to stellar rotation. Meanwhile, the line profile of the reference spectrum is similarly narrow but remains centred on the rest wavelength. The POLD also increases as $v_{eq}\sin(i_*)$ increases. This is caused by the planet-occulted line profile, which is gradually drifting away from the line profile of $F_{loc}\ (\mu = 1)$, and is eventually normalised by the continuum of the latter. At this point, the POLD would consist of the complete spectral line profiles of both spectra.

- At T_0, on the contrary, as the impact parameter of the planetary orbit is zero, the planet-occulted line profile is naturally identical to the line profile in $F_{loc}\ (\mu = 1)$. Therefore, there is no POLD observed in the resulting absorption spectrum.

$F_{ref} = F_{out}$ (black curve)

- At T_2, for moderate $\mathrm{v}_{\mathrm{eq}}\sin(i_*)$ values, the POLD is comparable in shape and amplitude to the previous scenario because the line profile of $\mathrm{F}_{\mathrm{out}}$ only undergoes a slight broadening in comparison to $\mathrm{F}_{\mathrm{loc}}\,(\mu=1)$ and the planet-occulted line profile is barely shifted from its rest wavelength.
  For increasing $\mathrm{v}_{\mathrm{eq}}\sin(i_*)$, the POLDs' amplitudes increase as well but remain less extreme than in the previous case. Even if the planet-occulted line profile shifts farther from its rest wavelength it still overlaps with the wings of the broadened line profile of $\mathrm{F}_{\mathrm{out}}$, rather than with the flat continuum of $\mathrm{F}_{\mathrm{loc}}\,(\mu=1)$ as in the previous case. In the case of extremely fast-rotators, the disc-integrated line profile of $\mathrm{F}_{\mathrm{out}}$ would be flattened by strong rotational broadening and tend to a practically constant flux. The planet-occulted line profile would thus be normalised by a flat spectrum, similarly to the previous case with $\mathrm{F}_{\mathrm{loc}}\,(\mu=1)$ where it was normalised by the continuum, and the POLD would directly trace its line profile.

- At T_0, regardless of the $\mathrm{v}_{\mathrm{eq}}\sin(i_*)$ value, the POLD does not disappear but reaches its minimal value. The planet-occulted line profile is centred at the same wavelength as the disc-integrated line profile of $\mathrm{F}_{\mathrm{out}}$ and so the amplitude of the POLD is governed by the flux ratio between the cores of the two line profiles. The disc-integrated line profile being broadened by stellar rotation, this ratio increases with increasing $\mathrm{v}_{\mathrm{eq}}\sin(i_*)$, and so does the amplitude of the POLD.

$\mathbf{F}_{\mathbf{ref}} = \mathbf{F}_{\mathbf{out}}(\mathbf{v}_{\mathbf{rad}})$ (blue curve)

- In this case, at each exposure time, the shape of the resulting POLD is identical to the one in the absorption spectrum computed with $\mathrm{F}_{\mathrm{out}}$ at T_0 (dashed black curve), but the POLD is shifted according to the radial velocity of the planet-occulted stellar region.

The main conclusion that can be drawn from the test on the sky-projected spin-orbit angle is that the amplitude of the POLD diminishes as the angle increases (for a zero impact parameter). Indeed, by increasing the sky-projected spin-orbit angle, the planetary transit chord is modified. As a result, the planet transits stellar regions with lower radial velocities throughout the transit. For the same time step, the planet-occulted line profiles are thus less shifted. The amplitude of the resulting POLD is thus decreased as the wavelength departure between the planet-occulted line profiles and the unshifted reference spectrum (here either $\mathrm{F}_{\mathrm{out}}$ or $\mathrm{F}_{\mathrm{loc}}(\mu=1)$) is reduced.

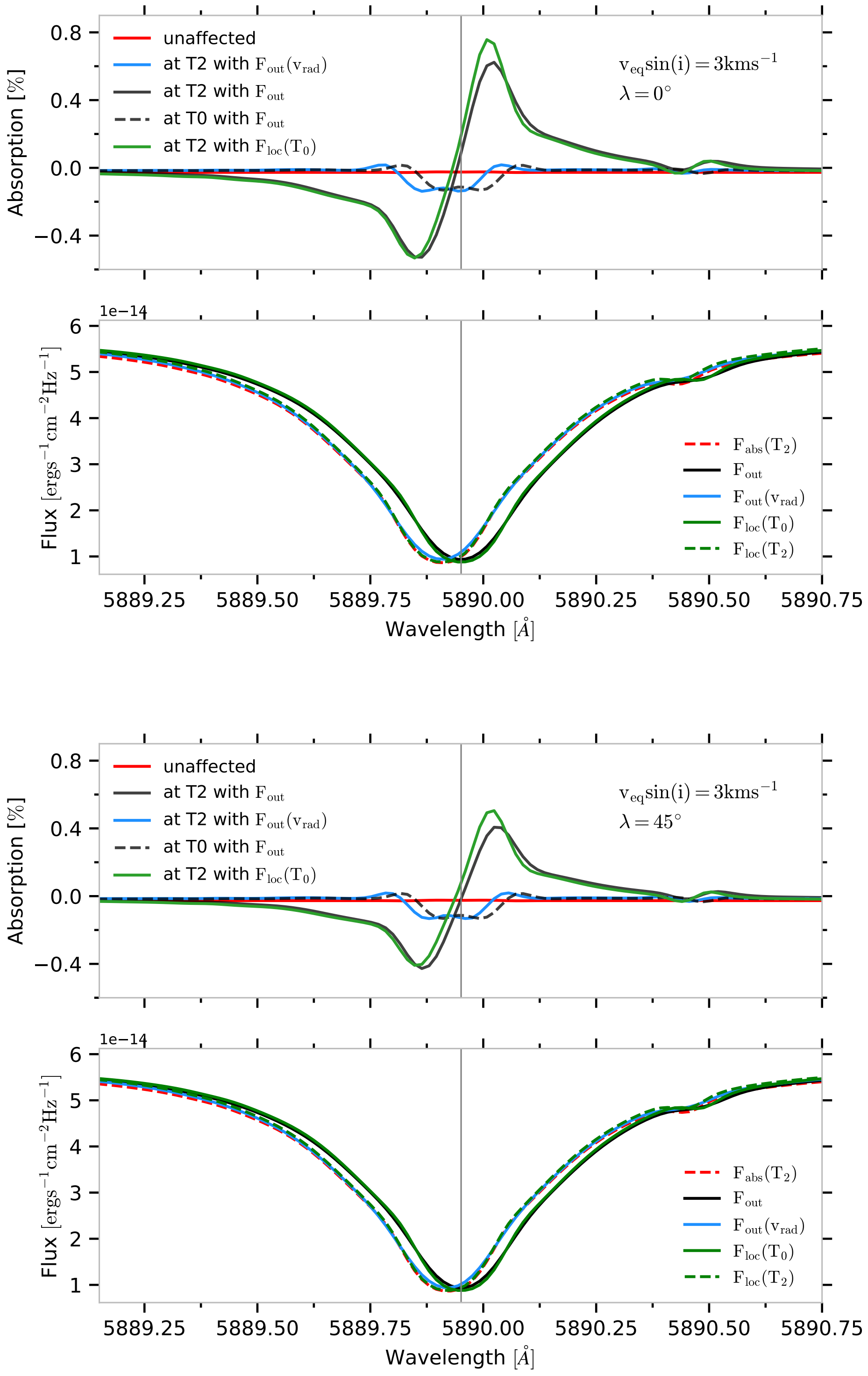

Fig. 3.3.: Theoretical absorption spectra of the generic planet without atmosphere as a function of wavelength in the stellar rest frame, computed with the different reference spectra from Sect. 3.1.2. The results are for the moderate-rotator case ($\mathrm{v_{eq}\sin(i_*)} = 3$ km $\mathrm{s^{-1}}$) and for the two planetary obliquities (cases 1 and 3). The vertical grey lines mark the transition wavelength of Na I D2. **Upper panels**: Theoretical absorption spectra. **Lower panels**: Quantities used to compute the absorption spectra.

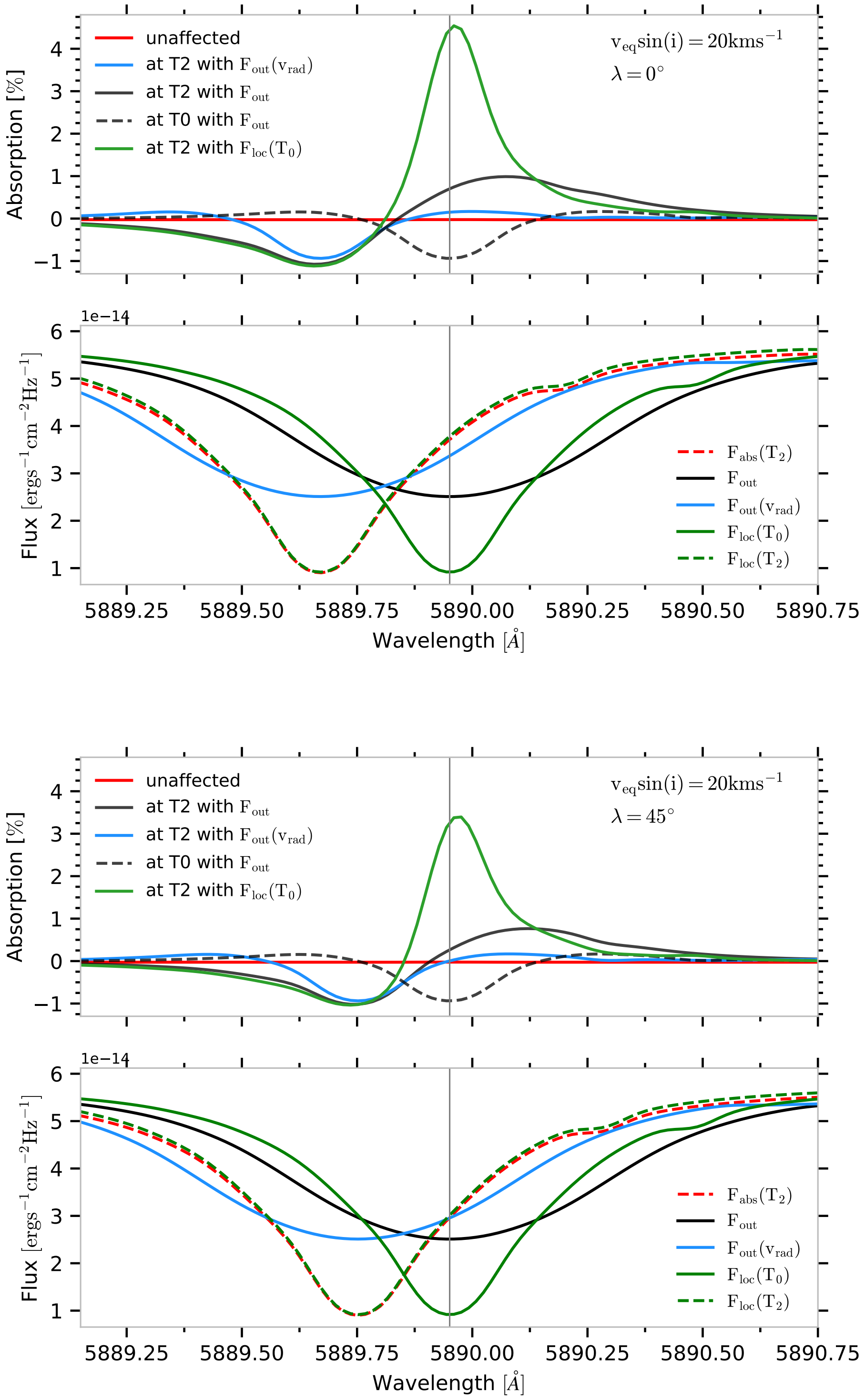

Fig. 3.4.: Theoretical absorption spectra of the generic planet without atmosphere as a function of wavelength in the stellar rest frame, computed with the different reference spectra from Sect. 3.1.2. The results are for the fast-rotator case ($v_{eq} \sin(i_*) = 20$ km s^{-1}) and for the two planetary obliquities (cases 2 and 4). The vertical grey lines mark the transition wavelength of Na I D2. **Upper panels**: Theoretical absorption spectra. **Lower panels**: Quantities used to compute the absorption spectra.

With the thermosphere

Figure 3.5 shows the resulting absorption spectra of the simulations of the transit of the planetary opaque body with an atmosphere containing neutral sodium atoms for the case with a $\mathrm{v_{eq}}\sin(i_*) = 3\,\mathrm{km\,s^{-1}}$. Similarly to Figs. 3.3 and 3.4, this figure also shows the different spectra used to compute the absorption spectra to help interpret the results. Figure 3.6 is the same for the case with a $\mathrm{v_{eq}}\sin(i_*) = 20\,\mathrm{km\,s^{-1}}$. In these figures, $\mathrm{F_{out}}$ and $\mathrm{F_{out}(v_{rad})}$ were multiplied by the ratio between the occulted surface and the surface of the star to bring them to the level of $\mathrm{F_{loc}}$ and make the comparison easier.

By comparing the unaffected absorption spectrum with the other absorption spectra, it appears clearly that for all of them, the atmospheric absorption signature is affected and sometimes can even be counterbalanced by the POLDs (see e.g. black curve middle panel of Fig. 3.6). Quite intuitively, the atmospheric signature is more affected by the POLDs when $\mathrm{v_{eq}}\sin(i_*)$ increases as their amplitude also increases, as was described earlier. However, this is not the only reason for the greater contamination. The overlap between the POLD and the atmospheric signature also plays a role. As the planet moves on its transit chord, its radial orbital velocity also varies. As the atmosphere moves with the planet, its absorption signature is shifted in wavelength in the absorption spectrum according to their radial orbital velocity throughout the transit. When the radial orbital velocity of the planet matches the radial velocity of the planet-occulted stellar surface, the POLD and the atmospheric signature overlap. When such situations occur, the atmospheric absorption signature is consequently more impacted by the POLDs.
The uppermost panel of Fig. 3.6 illustrates this aspect clearly as the absorption spectrum computed with $\mathrm{F_{out}}$ (black curve) has a completely different shape than the unaffected absorption spectrum. At the centre of the transit ($\mathrm{T_0}$), for the circular and aligned orbit that I used for these simulations, the planetary radial orbital velocity is null and thus, the atmospheric signature that is contained in the absorbed spectrum (green curve in the second uppermost panel of Fig. 3.6), is centred on the rest wavelength of the Na I D2 line. Furthermore, the stellar region occulted by the planet at this time also has a null radial velocity, and the peak of the POLD is thus also centred on the rest wavelength of the Na I D2 line (see the upper panel of Fig. 3.4). At this time step, the POLDs overlap with the atmospheric absorption signature and their impact is therefore significant.
The overlap is exact at $\mathrm{T_0}$ regardless of the $\mathrm{v_{eq}}\sin(i_*)$ value. For other time steps it is only partial, as can be seen in Figure 3.7. This figure shows the time evolution of the absorption spectrum as a function of wavelength computed using $\mathrm{F_{out}}$ as a reference. It helps to see how the planetary orbital track in the velocity-time space (dashed orange curve) can overlap with the track of the planet-occulted stellar line throughout a transit and explains why the atmospheric signature is more affected

in the case of the fast-rotator. It comes from the combination of two effects. Firstly, the POLDs are stronger and broader for the fast-rotator, as was already mentioned before. Secondly, because the change in the radial orbital velocity of the planet during the transit follows more the radial velocity variation of the occulted stellar surface than in the case of moderate-rotator, enhancing the overlap between the planetary signature and the POLDs. These 2D maps of the absorption spectrum also offer a way to identify the exposures where the atmospheric absorption signature is free from the effects of the POLDs.

For these specific simulations, the radial orbital velocity of the planet at T_2 is $\mathrm{v_{orb}}(\mathrm{T_2})$ = 14.4 $\mathrm{km\,s^{-1}}$. For the moderate-rotator, the radial velocity of the occulted stellar surface at T_2 is 2.6 $\mathrm{km\,s^{-1}}$ and 1.8 $\mathrm{km\,s^{-1}}$ for $\lambda_{\mathrm{pl}} = 0^\circ$ and 45°, respectively. For the fast-rotators it is equal to 17.3 $\mathrm{km\,s^{-1}}$ and to 12.3 $\mathrm{km\,s^{-1}}$ for $\lambda_{\mathrm{pl}} = 0^\circ$ and 45°, respectively.

Summary

There are a few key points to remember from this section :

- Due to the inherent rotation of stars, using $\mathrm{F_{out}}$ as a reference for the planet-occulted line profile when computing absorption spectra inevitably leads to spurious features that resemble emission and absorption (POLDs) that cannot be neglected.

- These POLDs get larger with increasing $\mathrm{v_{eq}}\sin(i_*)$ values. This is due to the line profiles of $\mathrm{F_{out}}$, which become broader and shallower and which gradually contrast with the planet-occulted line profile.

- The POLDs adopt the shape of the line profile of the planet-occulted stellar regions when the star rotates so rapidly that the line profile of $\mathrm{F_{out}}$ is practically flat and constant.

- When the evolution of the planetary radial orbital velocity throughout the transit is comparable to the evolution of the radial velocity of the stellar regions occulted by the planet, the POLD and the atmospheric absorption signature can overlap, which renders the detection and characterisation of the planetary atmosphere more complicated.

- All the different reference spectra that I tested induced some distortions in the absorption spectra. However, the amplitude of the POLDs was reduced

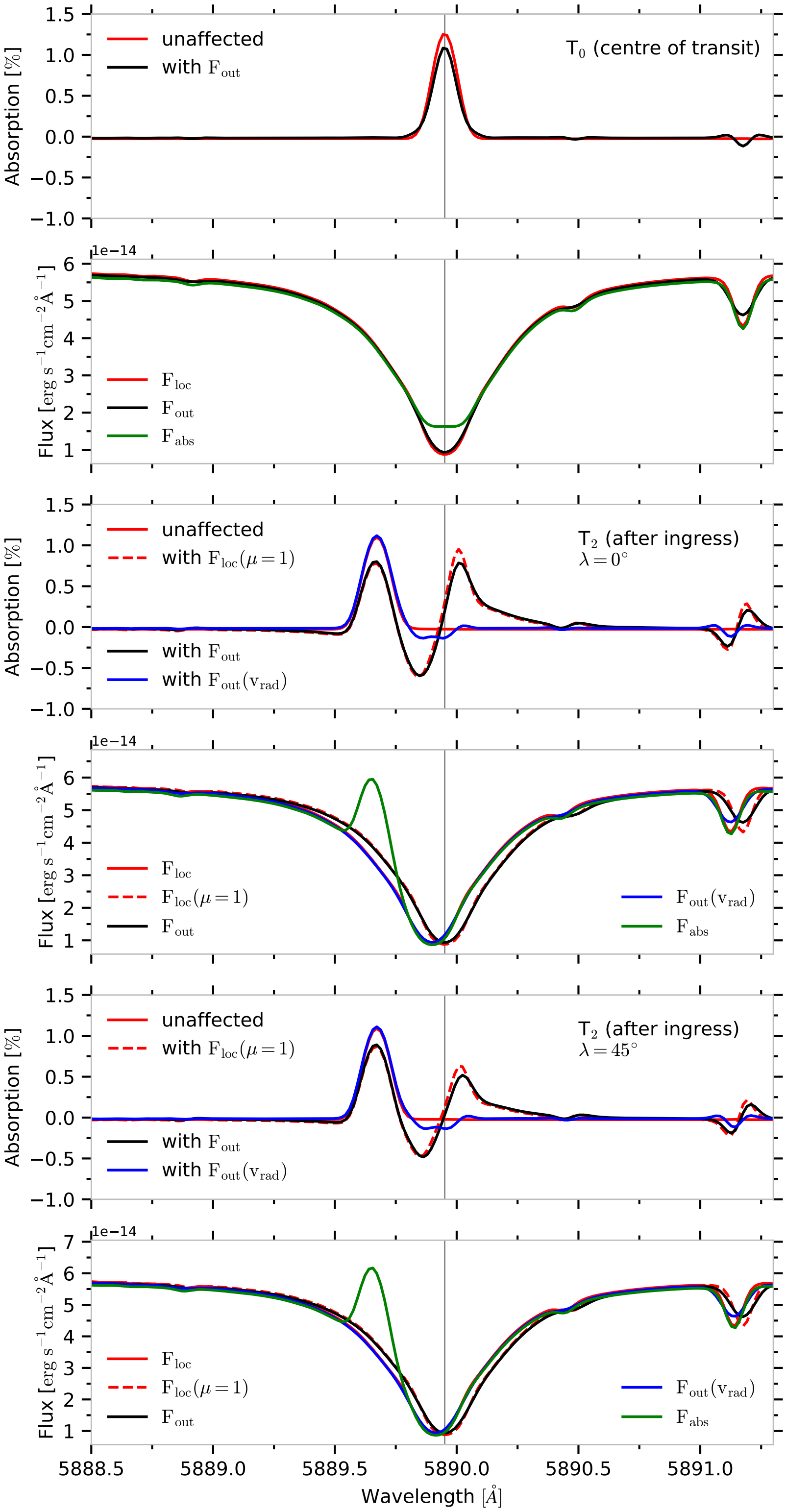

Fig. 3.5.: Theoretical absorption spectra of the generic planet with the atmosphere containing neutral sodium atoms, as a function of wavelength in the stellar rest frame, computed with the different reference spectra mentioned in Sect. 3.1.2 and for a $v_{eq} \sin(i_*) = 3 \ \mathrm{km\,s^{-1}}$. **Upper panels**: Absorption spectra. **Lower panels**: Quantities used to compute the absorption spectra. Naturally, for the case at T_0, the absorption spectra derived with $F_{loc}\ (\mu = 1)$ and with $F_{out}(v_{rad})$ are not displayed as they are equivalent to the unaffected absorption spectrum and to the case derived with F_{out}, respectively.

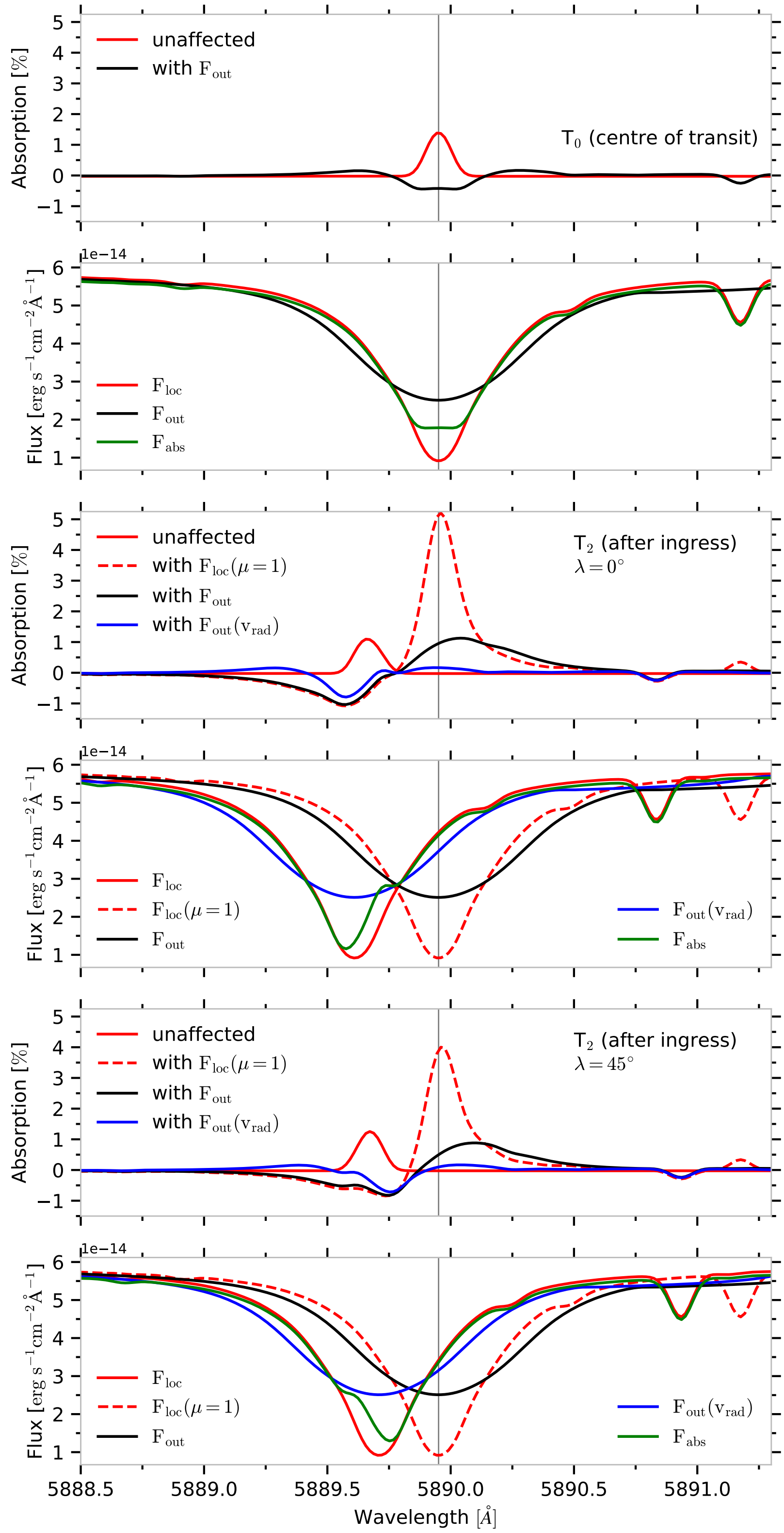

Fig. 3.6.: Theoretical absorption spectra with the atmosphere containing neutral sodium atoms, as a function of wavelength in the stellar rest frame, computed with the different reference spectra mentioned in Sect. 3.1.2 and for a $v_{eq}\sin(i_*) = 20\,\mathrm{km\,s^{-1}}$. **Upper panels**: Absorption spectra. **Lower panels**: Quantities used to compute the absorption spectra. Naturally, for the case at T_0, the absorption spectra derived with F_{loc} $(\mu = 1)$ and with $F_{out}(v_{rad})$ are not displayed as they are equivalent to the unaffected absorption spectrum and to the case derived with F_{out}, respectively.

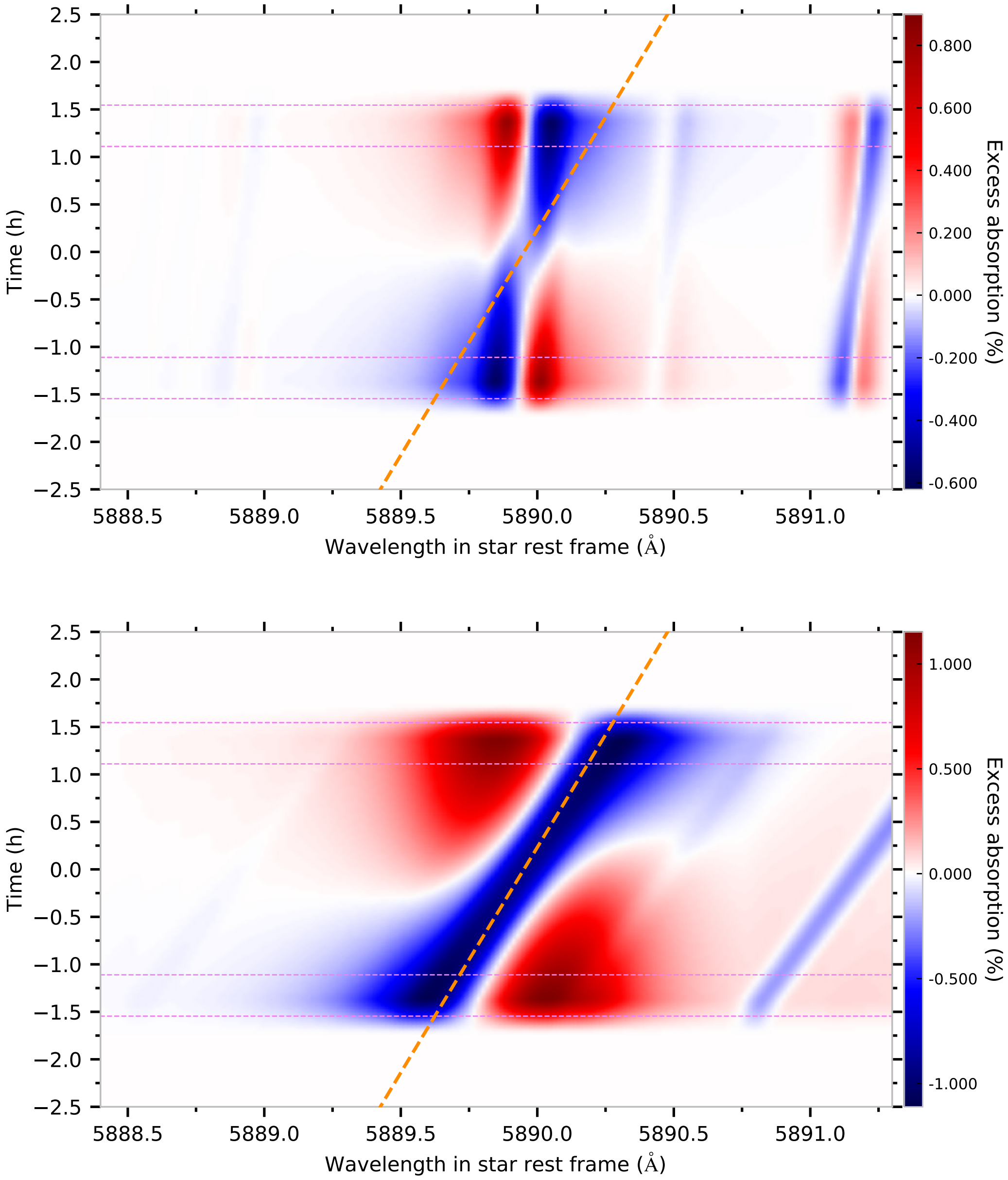

Fig. 3.7.: Absorption spectra of the planet without atmosphere around the Na I D2 line as a function of time and wavelength in the stellar rest frame. $\mathrm{F_{out}}$ was used as a reference to compute the absorption spectrum. **Upper panel**: with a $\mathrm{v_{eq}}\sin(i_*) = 3\,\mathrm{km\,s^{-1}}$ and $\lambda_{\mathrm{pl}} = 0°$. **Lower panel** : with a $\mathrm{v_{eq}}\sin(i_*) = 20\,\mathrm{km\,s^{-1}}$ and $\lambda_{\mathrm{pl}} = 0°$. The dashed orange line is the orbital track of the planet in the velocity-time space. The horizontal dashed violet lines show the contact times of the transit. The y axis shows the time from the centre of the transit.

when shifting these spectra to the radial velocity of the planet-occulted stellar surface. This suggests that $\mathrm{F_{out}(v_{rad})}$ might be a more appropriate choice over a correct but unshifted line profile.

3.1.3 Impact of centre-to-limb variations

In this section, I study the effect of centre-to-limb variations on planetary absorption spectra. To only account for this effect individually, the position in wavelength of the stellar lines does not vary locally over the stellar surface, unlike in Sect. 3.1.2, but their profiles are affected by CLV.
Contrarily to the Sect. 3.1.2, I only simulated two transits of our test planet (i.e. one without atmosphere and one with the atmosphere) as I fixed the stellar atmospheric model used to compute the stellar spectral grid. Indeed, while the exact variation of the local line profile across the stellar disc depends on the characteristics of the atmospheric model, the manifestation of the CLV is independent of that model.
Similarly to the previous section, I compare the derived absorption spectra as a function of the reference spectrum, $\mathrm{F_{ref}}$, used as a proxy for the planet-occulted line profile. The $\mathrm{F_{ref}}$ I used in this section are:

- $\mathbf{F_{out}}$: its line profile is made of the sum of all the local line profiles over the stellar surface, each affected by the CLV. Its line profile thus depicts a sort of average CLV effect. Its continuum is affected by a mean broadband limb darkening.

- $\mathbf{F_{loc}(\boldsymbol{\mu} = 1)}$: as it is merely affected by CLV, its line profile matches the planet-occulted line profile at transit centre ($\mathrm{T_0}$) in our simulation, but deviates from the local stellar line profiles towards the limbs.

Figure 3.8 shows the resulting absorption spectra of the simulations of the transit of the planetary opaque body with and without atmosphere at the time-step at the centre of the transit ($\mathrm{T_0}$) where the effect of CLV on the planet-occulted line profile is negligible. This figure also shows the different spectra used to compute the absorption spectra to help understand and interpret these results. Figure 3.9 shows the results of the same simulations at the time step just after ingress ($\mathrm{T_2}$), where the effect of CLV on the planet-occulted line profile is strongest. In these figures, $\mathrm{F_{out}}$ was multiplied by the ratio between the occulted surface and the surface of the star to bring it to the level of $\mathrm{F_{loc}}$ and make the comparison easier.
These figures also include the unaffected absorption spectrum computed for each simulation. This spectrum is computed with the exact planet-occulted spectrum at each exposure ($\mathrm{F_{loc}(t)}$). Therefore, it should be equal to the absorption spectrum in

the Sect. 3.1.1 provided that the spatial variation of CLV across the occulted stellar surface in a given exposure can be neglected.

Impact on the stellar line profiles

$\mathbf{F_{ref} = F_{out}}$:

- At T_0, the planet occults a region around the centre of the stellar disc. The effect of CLVs on the planet-occulted line profile is thus negligible. The line profile of F_{out}, visibly departs from the planet-occulted line profile in particular when comparing their wings. As can be seen in the absorption spectra, the POLD is thus stronger around the wavelength corresponding to the wings of the profiles. The shape of the atmospheric signature (which is centred and rather narrow) is not significantly altered by the POLD. However, by looking at the peak-to-continuum ratio of the absorption spectrum, it is clear that the amplitude of the atmospheric signature has decreased, which could lead to an underestimation of the actual Na I signal.

- At T_2, the planet-occulted line profile is also strongly affected by CLVs. This tends to reduce the discrepancy between the wings of the two line profiles compared to the case at T_0. The global shapes of the two line profiles are thus more similar, and the amplitude of the POLD in the absorption spectrum is attenuated. The atmospheric signal - apart from being shifted away from the POLD due to the planetary radial orbital velocity - is consequently less impacted.

$\mathbf{F_{ref} = F_{loc}(\mu = 1)}$:

- At T_0, the reference matches by definition the planet-occulted line profile. Therefore, no POLDs are induced in the absorption spectrum.

- At T_2, the reference and the planet-occulted line profile are the most different as the latter is strongly affected by CLV while the former is barely affected by it. This difference is noticeable in the absorption spectrum where the peak-to-continuum ratio of the POLD is the most significant regarding the simulation done for the spectral grid containing CLV. Both the shape and amplitude of the atmospheric signature are affected by the POLD, which can lead, similarly to the case with F_{out}, to underestimation and misinterpretation of the actual atmospheric Na I properties.

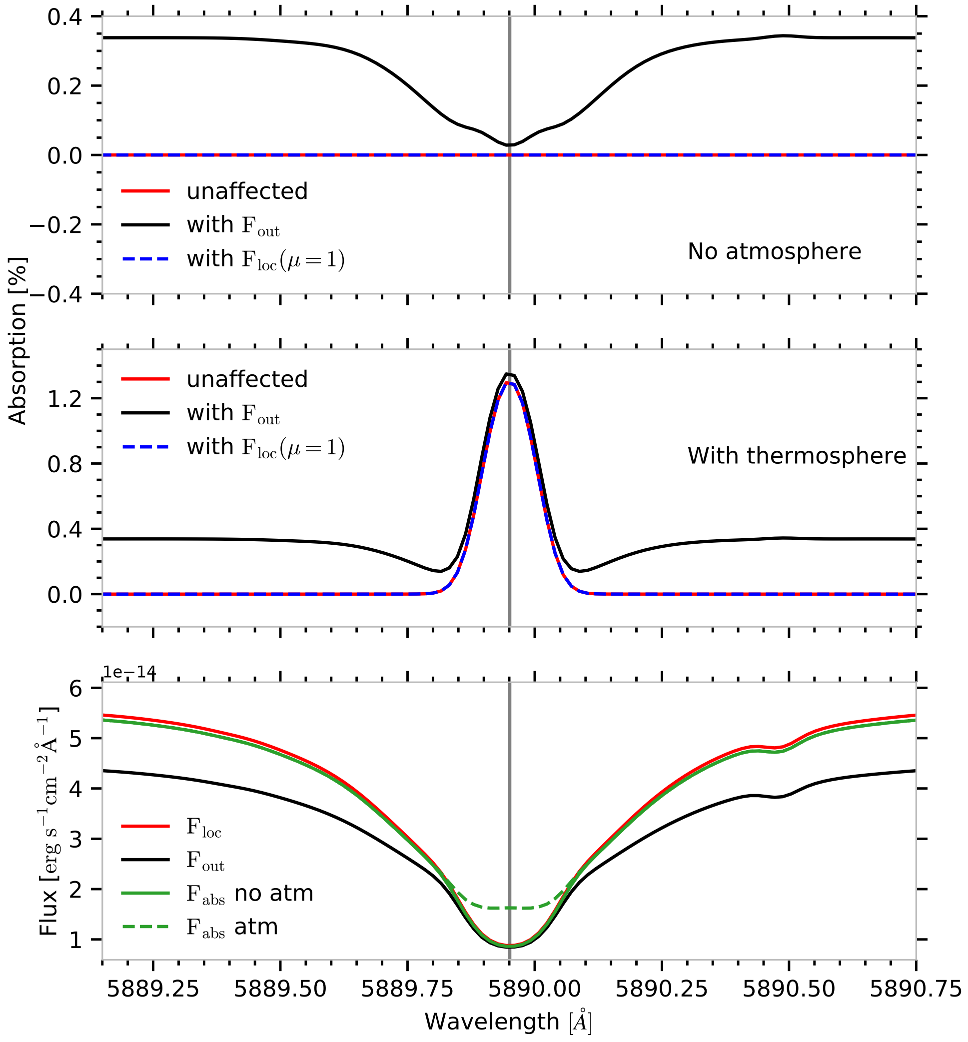

Fig. 3.8.: Theoretical absorption spectra at the centre of the transit (T_0) as a function of wavelength in the stellar rest frame for synthetic stellar spectra containing CLVs and computed with the different reference spectra mentioned in Sect. 3.1.3. **Upper panel**: Absorption spectrum of the planetary disc without atmosphere. **Middle panel**: Absorption spectrum of the planetary disc with the atmosphere containing neutral sodium atoms. **Lower panel**: Quantities used to compute the absorption spectra.

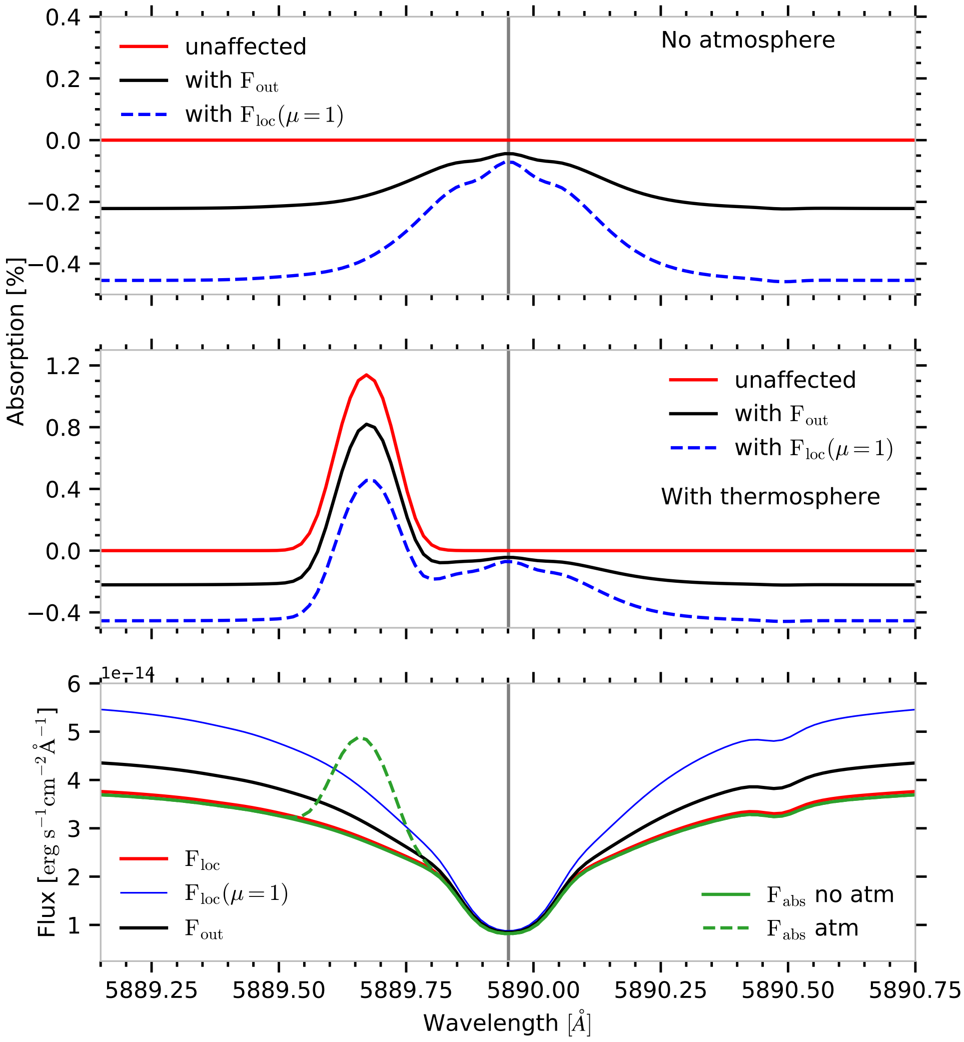

Fig. 3.9.: Theoretical absorption spectra after ingress (T_2) as a function of wavelength in the stellar rest frame, for synthetic stellar spectra containing CLVs and computed with the different reference spectra mentioned in Sect. 3.1.3. **Upper panel**: Absorption spectrum of the planetary disc without atmosphere. **Middle panel**: Absorption spectrum of the planetary disc with the atmosphere containing neutral sodium atoms. **Lower panel**: Quantities used to compute the absorption spectra.

A conclusion to this analysis is that the POLDs induced by CLVs in the absorption spectrum of transiting planets, while milder than those induced for moderate-to-fast stellar rotators, may reach values of 0.2 to 0.4 %.

For slow-rotating stars, the POLDs due to CLVs are a serious cause for contamination of the absorption spectra. They cannot be overlooked as they could easily result in misinterpretation of the actual observed atmospheric signature. For these stars, both $\mathrm{F}_{\mathrm{out}}$ and $\mathrm{F}_{\mathrm{loc}}(\mu = 1)$ create POLDs if used as a reference spectrum for the planet-occulted stellar line. The choice between them will thus depend on the position of the planet at a specific time step of the transit. When the planet occults regions near the limb, POLDs can be mitigated by using $\mathrm{F}_{\mathrm{out}}$ since its line profile, being influenced by CLV, corresponds more to the planet-occulted line profile. On the contrary, closer to the stellar disc centre, the use of $\mathrm{F}_{\mathrm{loc}}(\mu = 1)$ helps to better mitigate the POLDs, as the effect of CLV on the planet-occulted line profile becomes negligible.

Finally, the amplitude of the CLV-induced POLDs could be more or less important depending on the atmospheric model that is used (i.e. the simulated star) and on the stellar line of interest. The values of the amplitude of the POLDs shown here are thus only indicative. However, this single qualitative analysis still allows us to get a better understanding of the behaviour of these stellar contamination in planetary absorption spectra.

Impact on the stellar continuum

The impact of centre-to-limb variations is not limited to the line profiles of the stellar spectrum, as the continuum of the local spectra is not at a constant level across the stellar surface due to broadband limb darkening (BLD). For stellar regions closer to the limb, the continuum of the local spectra is uniformly decreased. This leads to contaminations that affect the overall absorption spectra, in addition to the POLDs which have a more local effect around the line profile's rest wavelength. The manifestation of this effect is visible in both Fig. 3.8 and Fig. 3.9 where the continua of the different absorption spectra are not systematically centred on 0.

$\mathbf{F}_{\mathrm{ref}} = \mathbf{F}_{\mathrm{out}}$:

To better understand the origin of this discrepancy, I re-express Eq. 3.1 assuming that the line profiles are uniform over the stellar disc and that only BLD is considered and acts as a multiplicative coefficient.

$$\frac{\mathrm{F}_{\mathrm{abs}}(\lambda, \mathrm{t})}{\mathrm{F}_{\mathrm{out}}(\lambda)} = \frac{\sum_k \mathrm{I}_{\mu=1}(\lambda)\ \mathrm{LD}_k(t)\ \Delta\Omega_k\ + \sum_l \left[1 - \mathrm{e}^{-\tau_l(\lambda)}\right]\ \mathrm{I}_{\mu=1}(\lambda)\ \mathrm{LD}_l(t)\ \Delta\Omega_l}{\sum_i \mathrm{I}_{\mu=1}(\lambda)\ \mathrm{LD}_i\ \Delta\Omega_i}, \tag{3.3}$$

after simplifying for $\mathrm{I}_{\mu=1}$ and neglecting BLD variations across the planet-occulted surface,

$$\frac{\mathrm{F}_{\mathrm{abs}}(\lambda, \mathrm{t})}{\mathrm{F}_{\mathrm{out}}(\lambda)} = \frac{\mathrm{LD}(t)\ \mathrm{S}_{\mathrm{pl}}(t)\ + \left[1 - \mathrm{e}^{-\tau_{atm}(\lambda)}\right]\ \mathrm{LD}(t)\ \mathrm{S}_{\mathrm{atm}}(t)}{\mathrm{S}_{*}^{\mathrm{LD}}}. \tag{3.4}$$

where S_{pl} and $\mathrm{S}_{\mathrm{atm}}$ are the stellar surfaces occulted by the planetary disc and the atmosphere, respectively, $\mathrm{S}_{*}^{\mathrm{LD}}$ is the BLD-weighted stellar surface, and τ_{atm} stands for the mean spectral optical depth in the atmosphere.

- At T_0, an overestimation of the continuum level of the absorption spectrum appears. The continuum of $\mathrm{F}_{\mathrm{out}}$ is made of the sum of the continua of all the local spectra across the stellar surface, which are each affected by a local BLD. The level of the continuum of $\mathrm{F}_{\mathrm{out}}$ thus decreases with respect to the continuum of $\mathrm{F}_{\mathrm{out}}$ from the purely uniform stellar emission case of Sect. 3.1.1. $\mathrm{S}_{*}^{\mathrm{LD}}$ is thus smaller than the actual stellar surface. Furthermore, the LD coefficient for the planet-occulted surface is equal to 1. The continuum of $\mathrm{F}_{\mathrm{abs}}/\mathrm{F}_{\mathrm{out}}$ is thus greater than the planet-to-star surface ratio, and the absorption spectrum is not centred around 0 after a simple subtraction of this latter ratio (see black curves in upper panels of Fig. 3.8).

- At T_2, an underestimation of the continuum level of the absorption spectrum appears. The planet-occulted surface is significantly down-weighted by BLD with an LD coefficient smaller than 1. Unlike the previous case, the continuum of the absorption spectrum is smaller than the surface ratio of the planet and the star (see black curves in upper panels of Fig. 3.9).

$\mathbf{F}_{\mathbf{ref}} = \mathbf{F}_{\mathrm{loc}}(\boldsymbol{\mu} = \mathbf{1})$:
In the same fashion as for Eq. 3.3, I write Eq. 3.1 as:

$$\frac{\mathrm{F}_{\mathrm{abs}}(\lambda, \mathrm{t})}{\mathrm{F}_{\mathrm{loc}}(\mu = 1; \lambda)} = \frac{\sum\limits_{k,k'} \mathrm{I}_{\mu=1}(\lambda)\ \mathrm{LD}_k(t)\ \Delta\Omega_{k,k'}\ + \sum\limits_{l,l'} \left[1 - \mathrm{e}^{-\tau_{l,l'}(\lambda)}\right]\ \mathrm{I}_{\mu=1}(\lambda)\ \mathrm{LD}_l(t)\ \Delta\Omega_{l,l'}}{\sum\limits_{j} \mathrm{I}_{\mu=1}(\lambda)\ \mathrm{LD}(\mu = 1)\ \Delta\Omega_j}, \tag{3.5}$$

After simplifying for $\mathrm{I}_{\mu=1}$, neglecting BLD variations across the planet-occulted surface and knowing that $\mathrm{LD}(\mu = 1) = 1$, we get

$$\frac{\mathrm{F}_{\mathrm{abs}}(\lambda, \mathrm{t})}{\mathrm{F}_{\mathrm{loc}}(\mu = 1; \lambda)} = \frac{\mathrm{LD}(t)\ \mathrm{S}_{\mathrm{pl}}(t)\ + \left[1 - \mathrm{e}^{-\tau_{atm}(\lambda)}\right]\ \mathrm{LD}(t)\ \mathrm{S}_{\mathrm{atm}}(t)}{\mathrm{S}_{\mathrm{pl}}}. \tag{3.6}$$

- At $\mathrm{T_0}$, similarly as for Sect. 3.1.3, the continuum of the reference equals by definition the one of the planet-occulted spectrum.
  Therefore, the continuum of the absorption spectrum is equal to 1.

- At $\mathrm{T_2}$, similarly as for the case with $\mathrm{F_{out}}$, an underestimation of the continuum level of the absorption spectrum appears, but stronger. As mentioned earlier, the planet-occulted stellar surface is strongly down-weighted by BLD close to the limb while, contrary to the case with $\mathrm{F_{out}}$, the continuum of the reference ($\mathrm{F_{loc}}(\mu = 1)$) is not affected by BLD. The continuum of the absorption spectrum is thus lower than one (see Eq. 3.1 of the uniform stellar emission case).

These equations show that limb darkening cannot be neglected in order to make absorption spectra comparable.
One way, often seen in the literature, to avoid the discrepancies caused by BLD is to place the continuum of the absorption spectra at a zero value. This is done by subtracting the measured continuum of the absorption spectrum ($\mathrm{LD(t)\ S_{pl}(t)/S_*^{LD}}$) directly at each time step.
This step alone, however, does not remove the BLD influence on the atmospheric signature, as can be seen in Eq. 3.4 and in Figure 3.10. This figure shows the absorption spectra with the atmosphere at the two time steps after subtracting the measured continuum. It is clear that the peak-to-continuum ratio of the atmospheric absorption signature is reduced compared to the one of the unaffected signature, as the BLD coefficient affecting the atmospheric signature was not corrected for. Nevertheless, Eq. 3.4 demonstrates how the BLD can be compensated for by multiplying the absorption spectrum with the ratio $\mathrm{S_*^{LD}/(LD(t)S_*)}$. This would guarantee that the absorption spectra of each time step are comparable (see also Mounzer et al. 2022).

Another way to place the continuum of the absorption spectra at a zero value (e.g. Casasayas-Barris et al. (2020, 2021, 2022)) is to normalise the out-of-transit and in-transit spectra to their continuum flux level before computing the absorption spectrum. However, there still remains a bias with this operation as I show through the following equations. The continuum of $\mathrm{F_{out}}$ can be written as :

$$\mathrm{F_{out}^{C} = LD_*\ S_*}, \tag{3.7}$$

and the continuum of $\mathrm{F_{in}(t)}$ as:

$$\mathrm{F_{in}^{C}(t) = LD_*\ S_* - LD_{pl}(t)\ S_{pl}}. \tag{3.8}$$

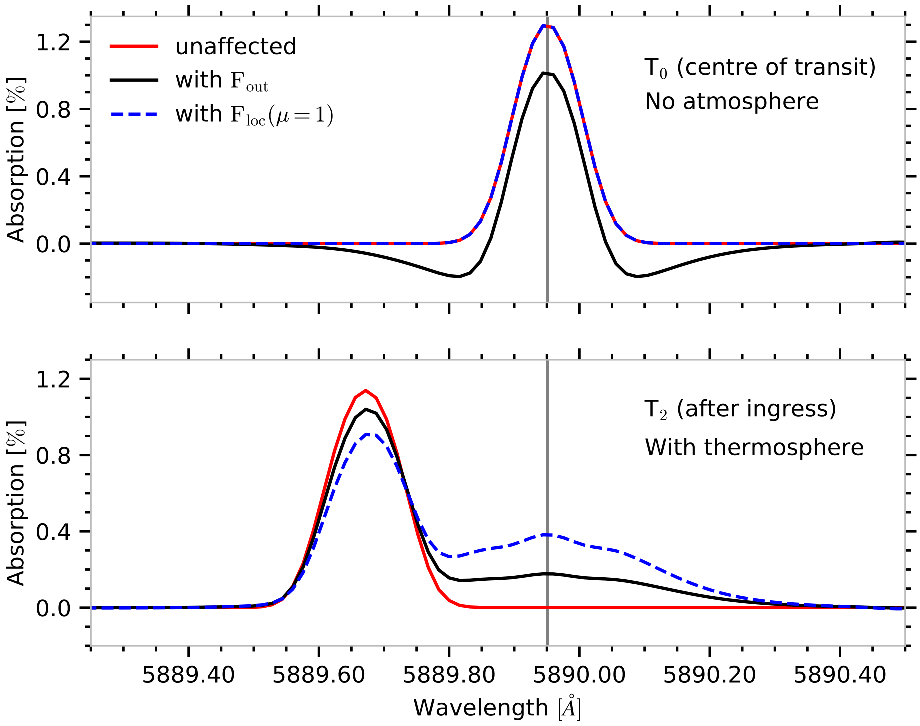

Fig. 3.10.: Middle panels of Figs. 3.8 and 3.9 after subtracting the measured continuum of the absorption spectra.

The normalised continuum of F_{out} is thus equal to 1 but the one of $F_{in(t)}$ is,

$$\begin{aligned}\overline{F_{in}(t)} =& \frac{LD_* \ S_* - \left[LD(t) \ S_{pl} + \left(1 - e^{-\tau_{atm}(\lambda)}\right) \ LD(t) \ S_{atm}\right]}{LD_* \ S_* - LD(t) \ S_{pl}} \\ =& 1 - \frac{\left(1 - e^{-\tau_{atm}(\lambda)}\right) \ LD(t) \ S_{atm}}{LD_* \ S_* - LD(t) \ S_{pl}}.\end{aligned} \tag{3.9}$$

The continuum of the absorption spectrum is effectively placed at a zero value when using normalised spectra. However, once again, the atmospheric absorption signature is subject to a time-variable factor due to the limb darkening of the planet-occulted stellar surface.

Even though the impact of BLD is less significant than the impact of the POLDs induced by CLV on the atmospheric absorption signature, it can still be relevant to consider this effect as being critical if looking for faint atmospheric absorption signatures. To conclude, I therefore promote the use of an adequate factor to correct for the effect of BLD on individual absorption spectra over the use of normalised spectra or subtraction of measured continuum.

3.2 Application to real exoplanet systems:

With the comprehensive analysis performed in the third section of Dethier & Bourrier (2023), the necessary bases were laid. We now have all the tools to understand why and how distortions can affect the absorption spectrum of a transiting planetary atmosphere. The next natural step for this study was to re-investigate real observed absorption spectra of two intriguing planetary systems to assess if more could be inferred than what had been previously published about them.

3.2.1 The controversial case of HD 209458 b

As mentioned at the beginning of the chapter, HD 209458 b is an interesting planetary system for several reasons, but in particular, because the detection of sodium in its atmosphere is indecisive. Historically, it was Charbonneau et al. (2002) who, after analysing HST STIS's transit observations of this system, first claimed the detection of atmospheric sodium around a planet. Later, Snellen et al. (2008) and Albrecht et al. (2009) confirmed this finding by analysing independent transit observations made from the ground with the Subaru's HDS spectrograph and UVES/VLT. Much more recently, Casasayas-Barris et al. (2020) confronted the synthetic absorption spectrum derived from their simulations of the planetary transit of HD 209458 b with observational datasets from the HARPS-N and CARMENES instruments. They demonstrated that the observed signatures in the Na I D2 and D1 in the absorption spectrum of HD 209458 b could be recreated by the transit of an opaque planetary body alone. Then, Casasayas-Barris et al. (2021) expanded on the analysis of Casasayas-Barris et al. (2020) by accounting for NLTE effects in the sodium lines formation in their synthetic stellar spectrum model and analysing transit observations from the ESPRESSO instrument. With this refined model, they could explain even better the observed signals around the sodium lines without the need to include an atmosphere around the simulated planet. These results further support that the features observed in the absorption spectrum of HD 209458 b can be entirely explained by planet-occulted line distortions induced by stellar rotation and CLVs.

Reproducing published results

The approach I used in Dethier & Bourrier (2023) with the EVE code is analogous to the approach used in Casasayas-Barris et al. (2020, 2021) when it comes to simulating a planetary transit. However, one major difference is that the EVE code is capable of including a realistic three-dimensional planetary atmosphere in the simulations. The absorption of the local stellar spectrum by the atmosphere is thus computed simultaneously to the opaque planetary body's absorption throughout the

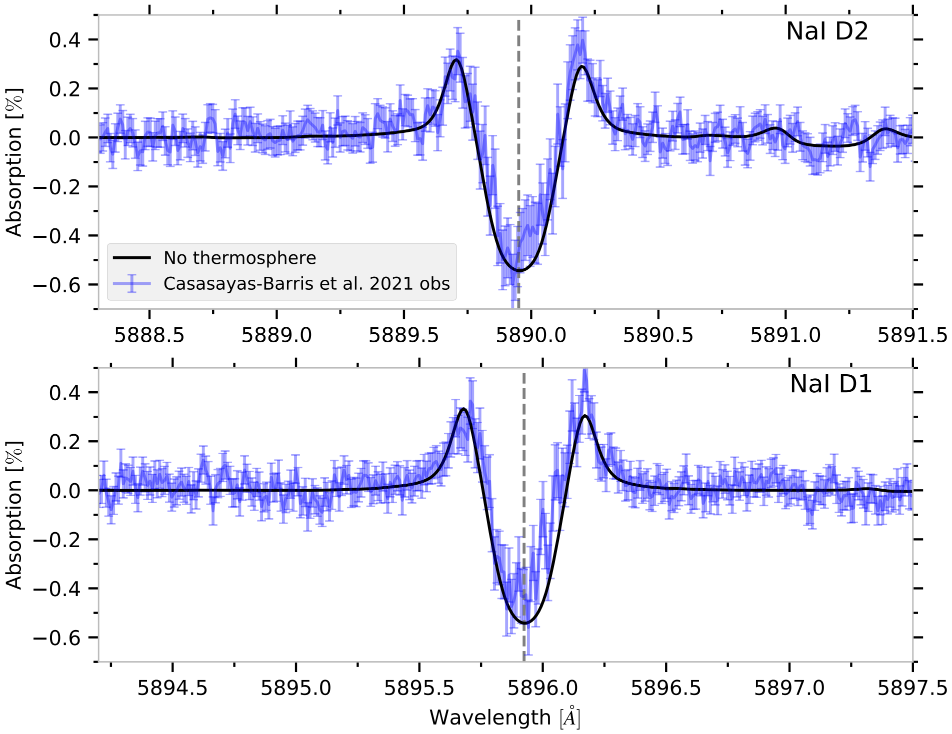

Fig. 3.11.: Mean of the theoretical absorption spectra of HD 209458 b between contact times T_2 and T_3 computed with the out-of-transit spectrum as a function of the wavelength in the planetary rest frame without atmosphere. The blue points are ESPRESSO data from Casasayas-Barris et al. (2021). **Upper panel**: Zoom on the Na I D2 line. **Lower panel**: Zoom on the Na I D1 line.

whole transit. With this approach, the atmospheric absorption signatures naturally appear in the absorption spectra (Sect. 2.4.1). The idea behind this chapter is twofold. Firstly, reproducing the absorption spectrum of HD 209458 b, presented in Casasayas-Barris et al. (2021). Secondly, investigating if the ESPRESSO observations could contain residual absorption by atmospheric sodium.

Table 5.1 lists the system parameters that were used for the transit simulations of HD 209458 b. The stellar model for HD 209458 was interpolated from MARCS models using the interpolation routine provided in the *Turbospectrum_NLTE* package (see Sect. 2.4.2). The stellar spectrum used in these simulations was generated using *Turbospectrum* and accounts for NLTE effects in the sodium lines formation. A solar sodium abundance is used.

Figure 3.11 shows the comparison between the observed mean absorption spectrum from Casasayas-Barris et al. (2021) and our synthetic absorption spectrum for HD 209458 b computed from simulations without a planetary atmosphere, and including CLV, stellar rotation and NLTE effects (for the Na I D2 and D1 lines). As in Figure 10 of Casasayas-Barris et al. (2021), the core of our simulated POLDs is slightly larger than the amplitude of the observed signature in the absorption spectrum around both Na I lines. Still, the simulated absorption spectrum of the sole planetary body of HD 209458 b, which only contains distortions induced by CLV and stellar rotation, is a good match with the observation. Using the same stellar parameters as Casasayas-Barris et al. (2021) and a similar approach of simulating planetary transits, I was able to reproduce an absorption spectrum that has, overall, the same behaviour as theirs[2].

Searching for additional signatures

Exploiting the full potential of the EVE code, I investigated if the slight gap between the simulated and observed absorption spectra could be filled with a planetary atmospheric absorption feature of sodium. Before diving straight into the fit, however, it is worth noting that the observed absorption spectrum exhibits a departure from the modelled absorption spectrum red-ward of the rest wavelength of the Na I D1 line. Meanwhile, this red-ward decrease is not visible around the Na I D2 line, which suggests that it is most likely not a planetary absorption signature but rather a spurious feature. Indeed, if it were, first, both features would be centred in the planet rest frame, and second, the depth of the feature would be larger around the D2 line than around the D1 line as the oscillator strength of the D2 line is about a factor two larger than the one of the D1 line.
Therefore, I decided to fit a planetary atmosphere absorption signature, considering only the absorption spectrum around the D2 line. For this fit, the temperature and radius of the thermosphere were fixed to 8000 K and 2.94 planetary radius (i.e. the Roche lobe), respectively. Trusting the stellar and planetary parameters from Casasayas-Barris et al. (2021), the only parameter that was varied was the density of neutral sodium atoms in the simulated atmosphere. I also chose to model the structure of the planetary atmosphere using a Parker wind description (Sect. 2.4.3). The best fit was reached with a value for the planetary atmospheric sodium density of $0.0007 \pm 0.0003\ \mathrm{at.\,cm^{-3}}$. Figure 3.12 shows the resulting absorption spectrum for the best-fit simulation. The atmospheric absorption feature absorbs upward as expected and fills the gap between the synthetic and observed absorption spectrum. Figure 3.13 shows the $\Delta\chi^2$ for the fit on the planetary atmosphere sodium density. As this figure shows, the simulation without atmosphere is still compatible with the observation within 2 to 3 σ of the best fit. Therefore, as I mentioned in the publication, the results of this work indicate the potential detection of sodium in

---

[2] To be comparable with Casasayas-Barris et al. (2020, 2021), all flux spectra were normalised by their continuum before computing the absorption spectra to have its continuum at zero. As explained in Sect 3.1.3, this action can induce biases. However, to ensure that it would not alter the following results, I compared the absorption spectra computed with and without the normalised spectra. I found a difference of 0.01 % in the peak-to-continuum ratio of the atmospheric absorption signature from the previous section, which I considered to be negligible.

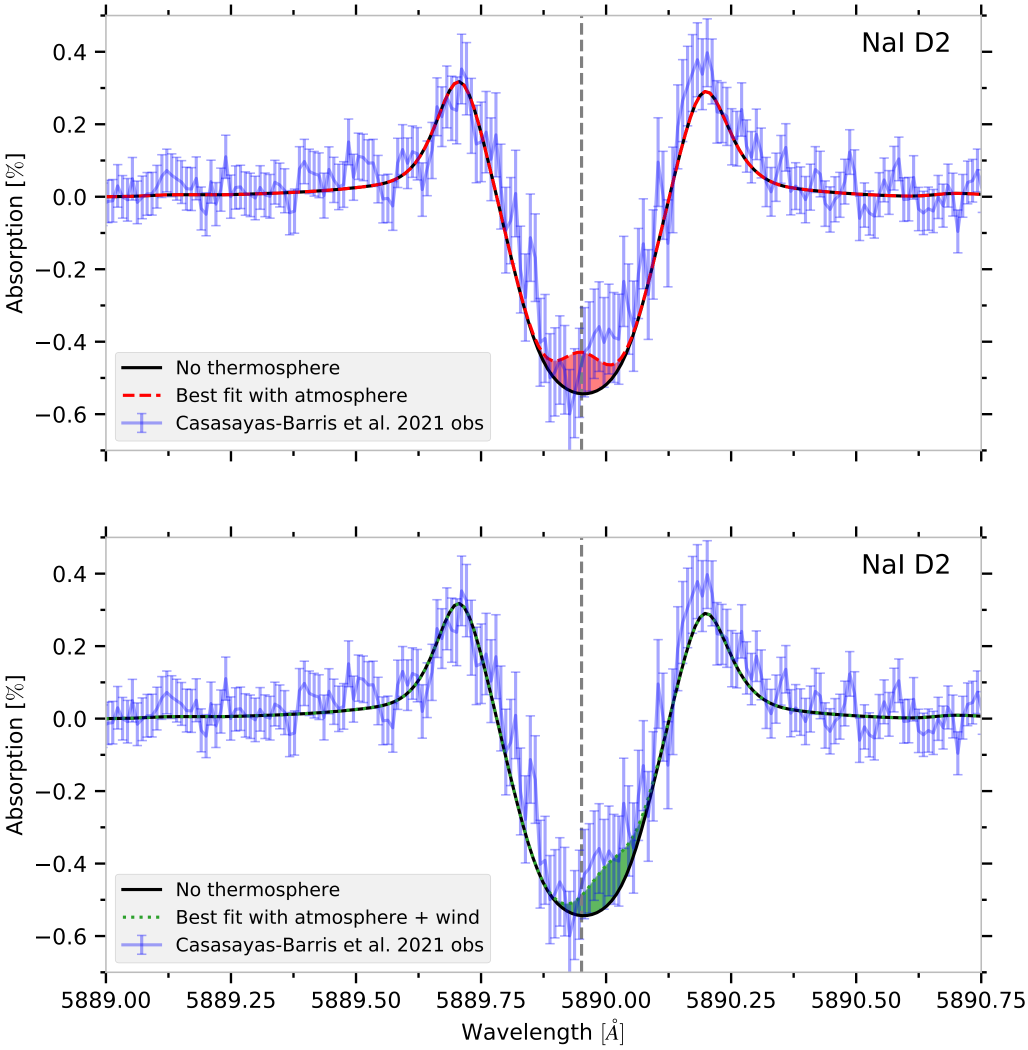

Fig. 3.12.: Mean of the theoretical absorption spectra of HD 209458 b between contact times T_2 and T_3 computed with the out-of-transit spectrum as a function of the wavelength in the planetary rest frame. The blue points are ESPRESSO data from Casasayas-Barris et al. (2021). **Upper panel**: simulated absorption spectrum without atmosphere and best fit simulation with atmosphere. **Lower panel**: simulated absorption spectrum without atmosphere and best fit simulation with atmosphere + nightside-to-dayside wind of 3 km s^{-1}.

the atmosphere of HD 209458 b, motivating for further observing campaigns of the system.

An alternative way to look at the absorption spectrum is to look at its temporal evolution during the transit. Figure 3.14 shows this evolution of the absorption spectrum as a function of time and wavelength for both the simulation with and without atmosphere. In the lower panel, the supplementary atmospheric absorption signature is visible, although faint, at the beginning and at the end of the transit, where the planetary orbital track and planet-occulted stellar line track do not overlap. Apart from these exposures, the width of the POLDs combined with the more significant overlap make the atmospheric absorption signature vanish. Finally, I investigated the possibility that the observed signature traces the presence of a wind in the atmosphere of the planet. Indeed, the gap between the observation and the simulation without atmosphere appears slightly redshifted, which could indicate a night-to-dayside wind. For this, I used the parameters of the best fit, and I included an additional night-to-dayside wind in the simulated atmosphere. By including a wind of 3 km s^{-1}, I was able to reproduce much better the tendency of the observed signature than without the wind (see the lower panel of Fig. 3.12). The computed $\Delta\chi^2$ with respect to the best fit without wind gives a value of ~ -6. This result further suggests and reinforces the potential detection of sodium in the atmosphere of HD 209458 b.

However, a night-to-dayside wind is usually not expected in such planetary systems. On the contrary, one expects a day-to-nightside wind, driven by the strong temperature gradient between the hot dayside and the colder nightside (Seidel et al. 2020). Again, more observations are needed to confirm if the behaviour of the observed signature repeats itself over time and is indeed the indication of sodium in the atmosphere of HD 209458 b.

Sodium abundance in the stellar model

In addition to the fit on the planetary atmosphere sodium density, I investigated two other possibilities to explain the observed absorption spectrum without the need for a planetary atmosphere. These possibilities concern the fact that the chosen stellar model could be inadequate in terms of sodium abundance. Firstly, in their Figure 10, Casasayas-Barris et al. (2021) demonstrated that the amplitude of the POLD around the Na I doublet lines increased when including NLTE effects in their stellar model. Moreover, modifying the sodium abundance, which affects the line depth, also impacts the amplitude of the POLD, potentially increasing it. Figure 3.15 shows the absorption spectrum for a simulation for the exact same planetary system without atmosphere except that no NLTE effects were included in the stellar model and that I adjusted the stellar sodium abundance to increase the amplitude of the

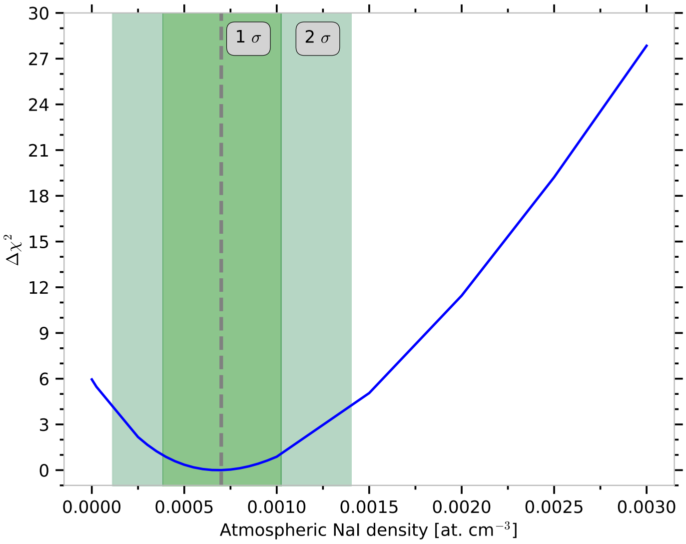

Fig. 3.13.: $\Delta\chi^2$ as a function of the planetary atmosphere density of Na I for the fit of HD 209458 b. The green shaded areas show the values of Na I densities within the 1 and 2 σ intervals of the minimum value of χ^2. The vertical grey dashed line shows the minimum value of χ^2. The data point of the case with the best fit atmosphere and a night-to-day side wind is not shown, but falls at approximately a value of -6.

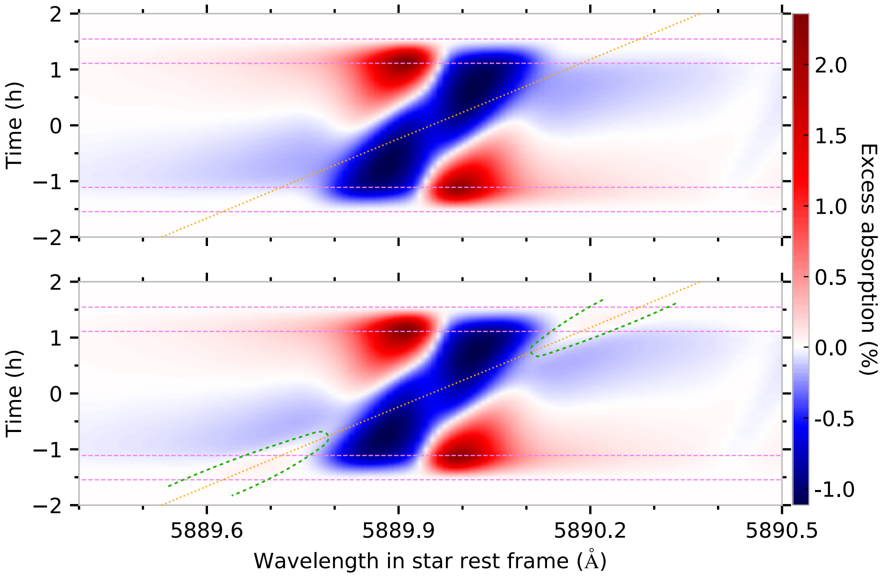

Fig. 3.14.: Theoretical absorption spectra of HD 209458 b around the Na I D2 line as a function of time and wavelength in the stellar rest frame. The simulated out-of-transit spectrum was used as reference. **Upper panel**: Without atmosphere. **Lower panel**: With the best-fit atmosphere. The dashed green lines highlight the regions where the atmospheric absorption signature is visible along the orbital track of the planet (dotted orange curves). The horizontal violet dashed lines show the contact times of the transit. The y axis shows the time from the centre of the transit.

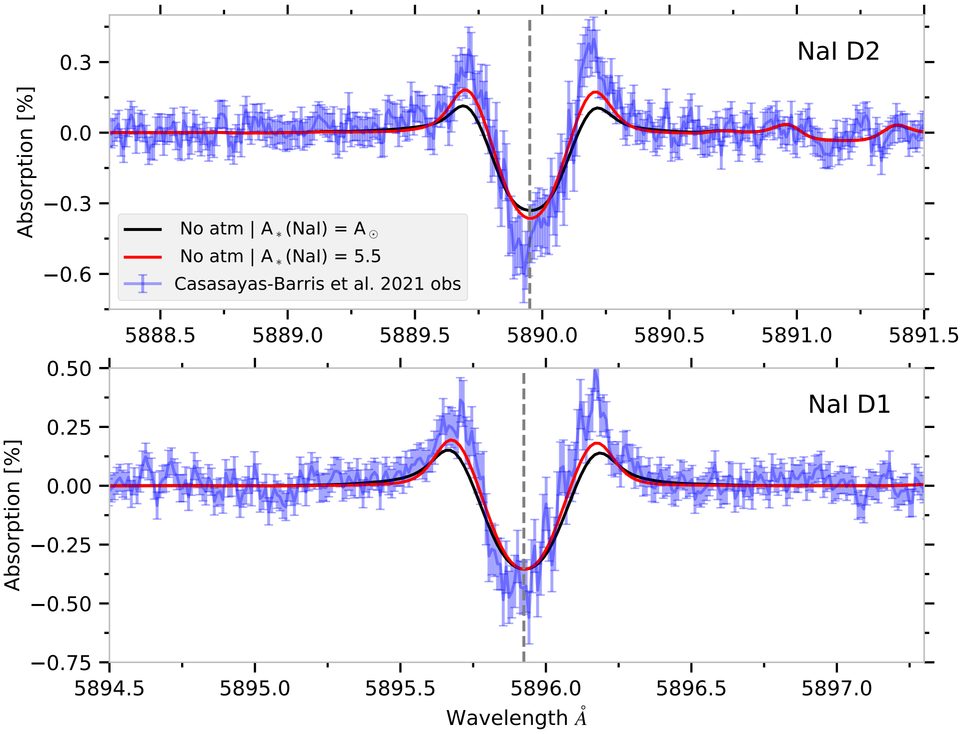

Fig. 3.15.: Theoretical mean absorption spectrum between contact times T_2 and T_3 of HD 209458 b computed with the out-of-transit spectrum as a function of the wavelength in the planetary rest frame without atmosphere. No NLTE effects are included in the stellar model, and I used a modified stellar Na I abundance from Solar ($A_\odot = 6.17$) to 5.5 to compute the synthetic stellar spectrum (which means there were about 4.6 times less sodium atoms in this stellar model than in the model using solar abundance). The abundance of element X is defined, relative to hydrogen, as $A(X) = 12 + \log_{10}\left(\frac{n(X)}{n(H)}\right)$.

POLD. The stellar model with a modified sodium abundance and no NLTE effects allows the simulated absorption spectrum to match better with the observation than the model with solar sodium abundance and no NLTE effects. However, the match is not nearly as good as for the model that includes NLTE effects. Moreover, the resulting disc-integrated spectrum for the model with modified stellar abundance strongly deviates from the observed one. In this case, modifying the stellar sodium abundance alone is thus not a plausible alternative to explain the amplitude of the signature observed in the absorption spectrum of HD 209458 b.

Secondly, upon visual inspection of the Figure A.3 of Casasayas-Barris et al. (2021) (see Figure 3.16), which shows the synthetic and observed F_{out}, it appears that all the stellar lines of the synthetic spectrum simulated with NLTE effects are too deep compared to the stellar lines of the observed spectrum. Moreover, the wings of the

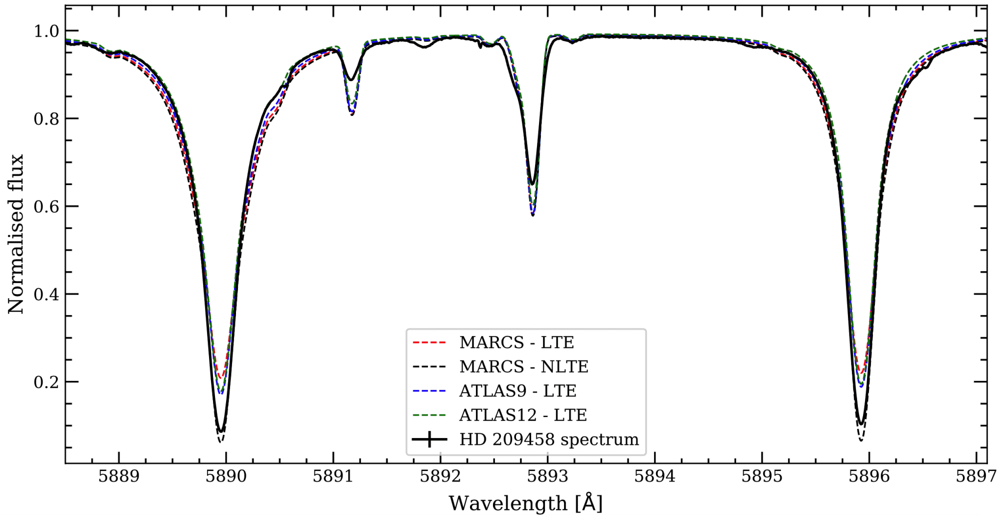

Fig. 3.16.: Observed and synthetic normalised disc-integrated spectra of HD 209458 as a function of wavelength. Taken from Figure A.3 in Casasayas-Barris et al. (2021)

observed Na I D2 and D1 line profiles are narrower than the simulated ones. One way to modify the depth of the disc-integrated stellar line profiles is to reduce the stellar abundance of the corresponding elements. Again, a smaller sodium abundance could reduce the depth of the local stellar lines and, as a result, modify the amplitude of the POLD, which could then match the observed distortion. This suggests that the synthetic stellar model might not reproduce correctly the local stellar line profiles and thus might play a role in the mismatch between the observed and synthetic absorption spectra.

I explored this possibility by reducing the sodium abundance in the stellar model with NLTE effects to verify if the disc-integrated line profile could better match the observation. Unfortunately, when reducing the sodium abundance, the wings of the synthetic Na I lines got narrower than the observed wings before the core of the synthetic lines could reach the level of the observed core. Moreover, the amplitude of the POLDs barely decreased even for the value of sodium abundance that allowed the wings of the synthetic and observed F_{out} to match.

These two investigations suggest that some stellar parameters could be not well constrained and/or that there might be some missing physics in the stellar model, such as 3D effects (e.g. convective patterns, (Dravins 1982; Bergemann et al. 2019; Gallagher et al. 2020)) and/or the fact that parts of the Na I line's core form in the stellar chromosphere, which is not accounted for in MARCS models (see, e.g. Figure 11 of Bruls & Rutten (1992) or Figure 5.32 of Tessore (2017)) .

In summary, before being able to make a definitive conclusion regarding the presence of neutral sodium in the atmosphere of HD 209458 b, there still remain improvements to make on multiple aspects. This includes more realistic stellar and planetary atmosphere models. Accurate measurements of stellar parameters such as $\mathrm{v_{eq}}\sin(i_*)$, temperature, log g and metallicity (the effects of the last three have not been discussed in this manuscript, but they primarily affect the stellar lines). Precise constraints on planetary parameters, such as the inclination and obliquity. Repeated transit observations with high-resolution spectrographs such as ESPRESSO, for example, and explorations of the data by coupling fits on the stellar and planetary models with codes such as *Turbospectrum* and EVE. Suppose the signature in the high resolution absorption spectrum of HD 209458 b around the sodium doublet eventually turns out to be totally explained by POLD. In that case, it is not physically incompatible with the low resolution detection by Charbonneau et al. (2002). Indeed, the detection at low resolution might trace the presence of dense optically thick layers of sodium, while the non-detection at high resolution might mean that sodium neutral atoms do not reach high atmospheric layers and/or are ionised before they become optically thin in higher layers (Vidal-Madjar et al. 2011).

3.2.2 The peculiar case of MASCARA-1 b

MASCARA-1 b (Talens et al. 2017) is a planetary system which presents a strong overlap between the planetary orbital track and the planet-occulted stellar line track for the whole second half of its transit. Casasayas-Barris et al. (2022) analysed in detail the absorption spectrum of this system using transit observations collected with the ESPRESSO instrument. They could not conclude on the detection of any atmospheric absorption signatures around the Na I D2 and D1 lines in part due to the contamination by the strong overlap mentioned before. They even investigated the individual effects of stellar rotation and of many orbital parameters on the POLDs, but unfortunately could never fully reproduce the observed absorption spectrum. In Dethier & Bourrier (2023), I investigated the absorption spectrum of MASCARA-1 b, which was published in their work, with EVE simulations to verify if an additional atmospheric absorption signature of sodium could help better explain the observations.

MASCARA-1 b is a very fast-rotator with a $\mathrm{v_{eq}}\sin(i_*)$ of approximately 100 km s^{-1} (see Table 3.3 which lists the system's parameters used in the present simulations) and from what I explained in Sect. 3.1.2, the POLDs in absorption spectra of such systems tend to directly trace the planet-occulted stellar line profiles. Interestingly, the observed absorption spectrum exhibited features that were always deeper than the simulated POLDs in Casasayas-Barris et al. (2022), suggesting that the local stellar lines should maybe be deeper to better reproduce the observed POLDs. Therefore, to verify that hypothesis, I played on two aspects: including NLTE effects in the sodium lines formation, which increases the depth of the sodium lines as

Tab. 3.3.: MASCARA-1's stellar and planetary properties.

Parameter	Value
Stellar :	
Radius ($R_\odot$)	$2.082^{+0.022}_{-0.024}$
Mass ($M_\odot$)	1.72 ± 0.07
T_{eff} (K)	$7\,554 \pm 150$
Metallicity [Fe/H]	0
$\log g$ (cm s^{-2})	4
Age (Gyr)	1.0 ± 0.2
$v_{\text{eq}} \sin(i_*)$ (km s^{-1})	$101.7^{+3.5}_{-4.2}$ †
Planetary :	
Radius (R_{Jup})	$1.597^{+0.018}_{-0.019}$
Mass (M_{Jup})	3.7 ± 0.9
Semi-major axis (au)	$0.040352^{+0.000046}_{-0.000049}$
i_{pl} (°)	88.45 ± 0.17††
Period (days)	$2.14877381^{+0.00000087}_{-0.00000088}$
Eccentricity	$0.00034^{+0.00034}_{-0.00033}$
Sky-projected spin-orbit angle (deg)	$69.2^{+3.1}_{-3.4}$ †††

Note. Values are taken from Talens et al. (2017); Hooton et al. (2022); Casasayas-Barris et al. (2022). Parameters that we vary in the study:(†, ††) Sect. 3.2.2 . (††,† † †) Sect. 3.3.1 set to 90 and 61, respectively.

shown in Casasayas-Barris et al. (2021); enhancing the sodium abundance in the stellar model to increase the depth of the sodium lines. Below, I present the three cases that I explored in Dethier & Bourrier (2023).

Case I: Nominal system's parameters of MASCARA-1 b and NLTE effects

Similarly to the case of HD 209458 b, I first reproduced the absorption spectrum of MASCARA-1 b using the nominal system's parameters published by Casasayas-Barris et al. (2022), a solar abundance of sodium in the stellar model and, in addition, including NLTE for sodium lines formation. In Figures 3.17 and 3.18, the resulting mean absorption spectrum and disc-integrated spectrum are compared to the observations published in Casasayas-Barris et al. (2022). These figures show that neither the disc-integrated spectrum nor the absorption spectrum correctly matches the observations. The synthetic disc-integrated line profiles are too shallow even with NLTE effects included, and the simulated POLDs are not deep enough and seem to be shifted blue-ward of the observed features in the absorption spectrum. This suggests that considering only NLTE effects is insufficient to explain the observed signature,

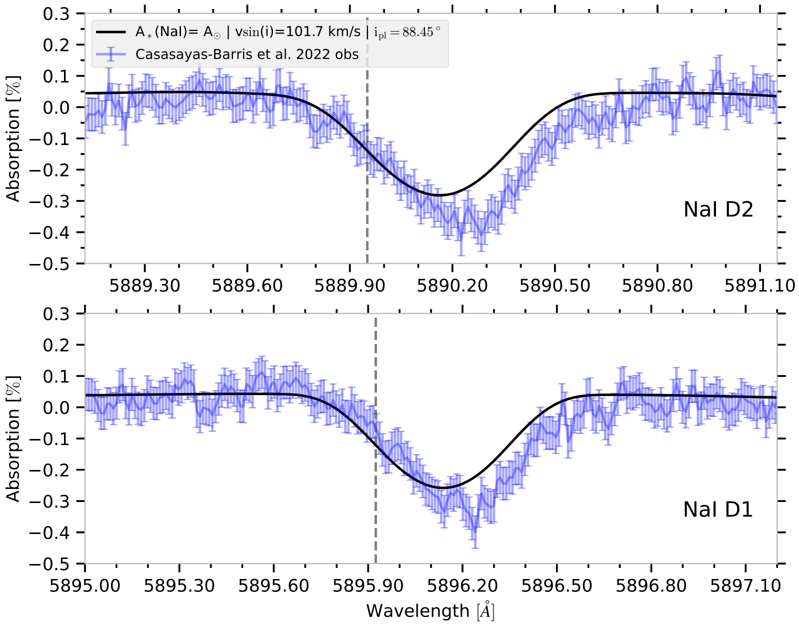

Fig. 3.17.: Mean absorption spectrum of MASCARA-1 b between contact times 2 and 3 without atmosphere, computed with the out-of-transit spectrum as reference, and plotted in the planetary rest frame for the case I. Blue points are ESPRESSO data from Casasayas-Barris et al. (2022).

unlike in the case of HD 209458 b. Increasing the stellar sodium abundance, therefore, could help get a better match overall.

Case II: Increased stellar abundance and a planetary atmosphere

In this second case, I increased the sodium abundance of the stellar model until the red wing of the simulated absorption spectrum matched the red wind of the observed absorption spectrum, as shown by the dashed red curve in Figure 3.19. The stellar sodium abundance used was $\mathrm{A}_*(\mathrm{Na\,I}) = 7.5$ while $\mathrm{A}_\odot(\mathrm{Na\,I}) = 6.17$. This means there are about 21 times more sodium atoms in this stellar model than in the model using solar abundance. Moreover, I also changed the $\mathrm{v_{eq}} \sin(i_*)$ to minus 1 σ of its nominal value so as to reach a better match with the core of the POLD. This decision is based on Figure 7 of Casasayas-Barris et al. (2022), which shows that for MASCARA-1 b, decreasing the $\mathrm{v_{eq}} \sin(i_*)$ widens the blue wing of the POLD around the sodium doublet lines, decreases its core, leaving its red wing untouched. This set-up, however, creates a gap between the blue wings of the simulated POLD and the observed absorption spectrum feature, with the blue wing of the POLD being deeper than the observed feature. Yet, this gap falls exactly where the planetary atmosphere is supposed to produce an absorption signature (indicated by the dashed grey vertical line). This led me to add an atmosphere containing neutral sodium

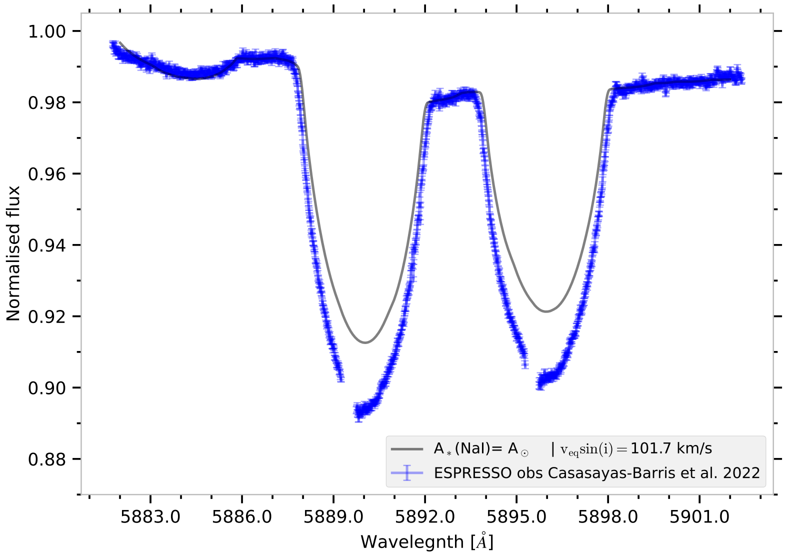

Fig. 3.18.: Observed and synthetic out-of-transit spectra of MASCARA-1 for the case I. Blue points are ESPRESSO data from Casasayas-Barris et al. (2022). The vertical grey line indicates the rest wavelength of the NaI D2 and D1 lines. The missing data points in the observations are remnants of the telluric and/or interstellar absorption correction.

atoms in the simulation to fit the overall absorption spectrum. The result of this fit is shown by the red curve in Figure 3.19 and was achieved for a thermosphere with a fixed temperature of 9 500K, a fixed radius of 3.23 planetary radius (Roche lobe radius), and a Na I density at this radius of 1×10^{-14} at. cm $^{-3}$. This approach demonstrates that by adjusting both the stellar and planetary properties, a good overall match of the absorption spectrum can be reached. Nevertheless, this result is obtained at the expense of a strong departure between the synthetic and observed disc-integrated sodium lines, as Figure 3.20 illustrates, due to a strong increase in the stellar sodium abundance.

Case III: Fit on $\mathrm{F}_{\mathrm{out}}$ and on the absorption spectrum

To solve the previous issue, I decided to make a two-steps fit. First of all, I fitted the disc-integrated spectrum and only after, I fitted the absorption spectrum, as the former directly intervenes in the calculation of the latter. Finally, I co-added the χ^2 values of each fit to determine the overall best fit. To fit the disc-integrated spectrum, there are two free parameters: the stellar sodium abundance and the stellar rotational velocity. The $\mathrm{v}_{\mathrm{eq}}\sin(i_*)$ is, however, only free to vary between three different values: nominal, nominal + 1σ, nominal + $2 \times 1\sigma$. This choice was made because I presumed that the fit I run on the spectral region containing only two strong lines (Na I D2 and D1 lines) cannot constrain better the $\mathrm{v}_{\mathrm{eq}}\sin(i_*)$ value than

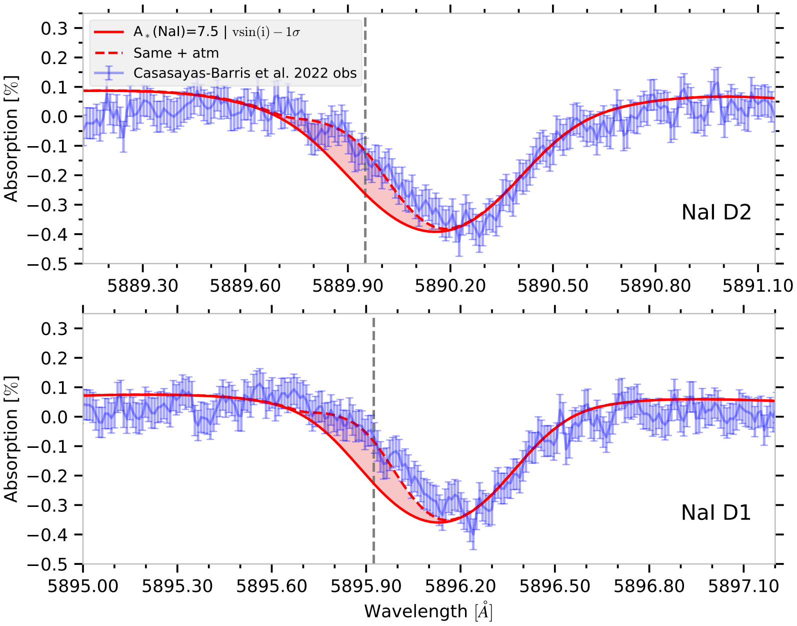

Fig. 3.19.: Mean absorption spectrum of MASCARA-1 b between contact times 2 and 3 without atmosphere, computed with the out-of-transit spectrum as reference, and plotted in the planetary rest frame for the case II. Blue points are ESPRESSO data from Casasayas-Barris et al. (2022). The vertical grey line indicates the rest wavelength of the NaI D2 and D1 lines.

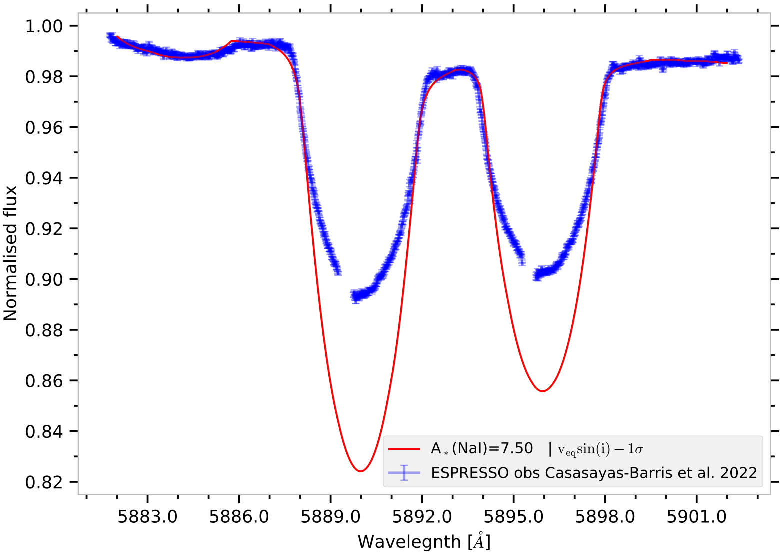

Fig. 3.20.: Observed and synthetic out-of-transit spectra of MASCARA-1 for the case II. Blue points are ESPRESSO data from Casasayas-Barris et al. (2022). The vertical grey line indicates the rest wavelength of the NaI D2 and D1 lines. The missing data points in the observations are remnants of the telluric and/or interstellar absorption correction.

the more complete techniques that were used in the literature, (for instance Hooton et al. 2022). Still, I only explored values of $\mathrm{v_{eq}}\sin(i_*)$ equal to, or larger than, the nominal value as smaller values did not help to improve the fit.
Then, I used the values around the minimum $\chi^2_{\mathrm{F_{out}}}$ to create the stellar spectral grids to use in the EVE code for simulating planetary transits. Furthermore, based on the findings of Casasayas-Barris et al. (2022) that decreasing $\mathrm{i_{pl}}$ causes a red-ward shift in the position of the POLDs, I decided to allow $\mathrm{i_{pl}}$ to vary in the simulations as the simulated POLDs appeared blue-shifted compared to the feature observed in the absorption spectrum (see Fig. 3.17). The planetary orbital inclination was thus varied between three values: nominal, nominal - 1σ, nominal - $2 \times 1\sigma$. Similarly as for $\mathrm{v_{eq}}\sin(i_*)$, I only use these specific values because I consider that the literature techniques to estimate the planetary orbital inclination are more complete and robust than the fit I run on the absorption spectrum in the spectral region of the sodium doublet lines. The values I use for $\mathrm{v_{eq}}\sin(i_*)$ and $\mathrm{i_{pl}}$ to get the best fit still remain within the error bars of Talens et al. (2017). This highlights that even slight variations of these parameters impact the simulated POLD to a detectable level.

The resulting simulated mean absorption spectrum and disc-integrated spectrum for the best fit are shown alongside the observed spectra in Figure 3.21 and Figure 3.22, respectively. The best fit is achieved with an $\mathrm{A_*(Na\,I)} = 6.865 \pm 0.002$[3], a $\mathrm{v_{eq}}\sin(i_*)$ equal to the nominal value $+2 \times 1\sigma$, and a $\mathrm{i_{pl}}$ equal to the nominal value - $2 \times 1\sigma$. The result of the chi-square analyses that we performed for the combined fit is shown in Figure 3.23. The figure displays the $\Delta\chi^2$ of the sum of the individual χ^2 from the fits on the disc-integrated spectrum ($\chi^2_{\mathrm{F_{out}}}$) and on the absorption spectrum ($\chi^2_{\mathcal{A}}$) as a function of stellar sodium abundance[4].

By performing a joint analysis of the disc-integrated and absorption spectrum of MASCARA-1, I concluded in Dethier & Bourrier (2023), that the feature around the Na I D2 and D1 lines in its observed absorption spectrum can be interpreted as POLDs induced from a planet, with no detectable sodium in its atmosphere, transiting a star with supra-solar sodium abundance. Figure 3.24 shows the temporal evolution of the absorption spectrum for the best fit. As can be seen, the planetary orbital track does not overlap with the planet-occulted line track for most of the first half of the transit. By focusing on this part of the transit of MASCARA-1 b, with repeated and precise enough observation, one could increase the chances to assess the presence, or not, of a potential sodium atmospheric feature as this is where the atmospheric absorption signature would be the least affected by the distortions.

---

[3] This means there are about 5 times more sodium atoms in this stellar model than in the model using solar abundance

[4] It is worth noting that because the disc-integrated spectrum is measured at very high SNR, stellar models cannot reproduce perfectly its complex shape; to avoid biasing the results I thus scaled the uncertainties on the disc-integrated spectrum to obtain a reduced chi-square equal to unity for its fit.

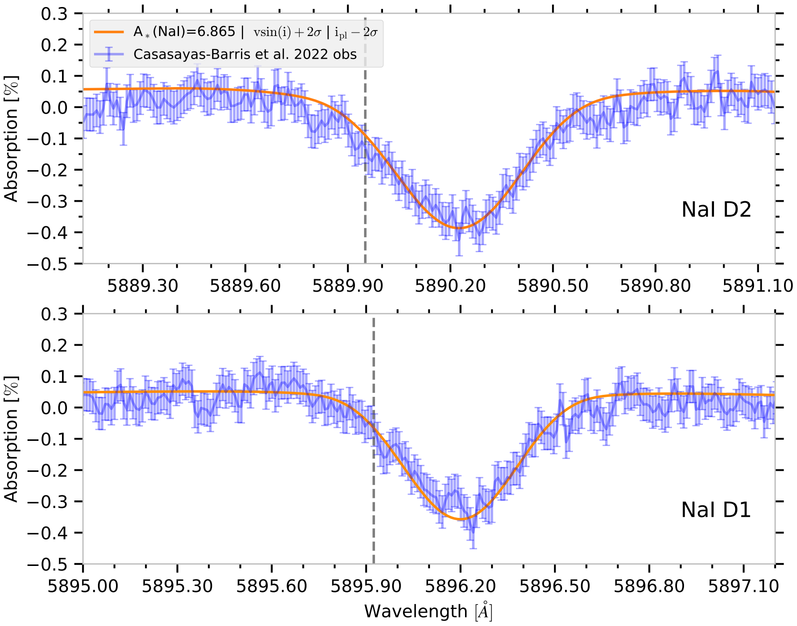

Fig. 3.21.: Mean absorption spectrum of MASCARA-1 b between contact times 2 and 3 without atmosphere, computed with the out-of-transit spectrum as reference, and plotted in the planetary rest frame for the case III. Blue points are ESPRESSO data from Casasayas-Barris et al. (2022). The vertical grey line indicates the rest wavelength of the NaI D2 and D1 lines.

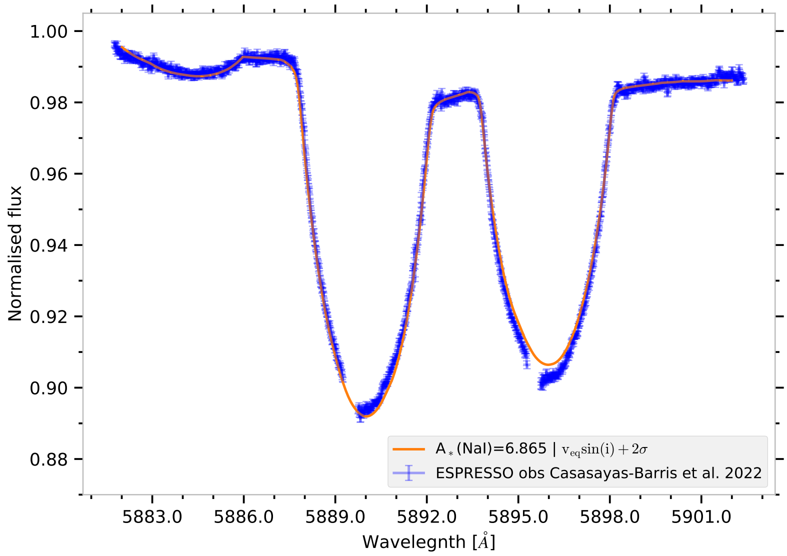

Fig. 3.22.: Observed and synthetic out-of-transit spectra of MASCARA-1 for the case III. Blue points are ESPRESSO data from Casasayas-Barris et al. (2022). The vertical grey line indicates the rest wavelength of the NaI D2 and D1 lines. The missing data points in the observations are remnants of the telluric and/or interstellar absorption correction.

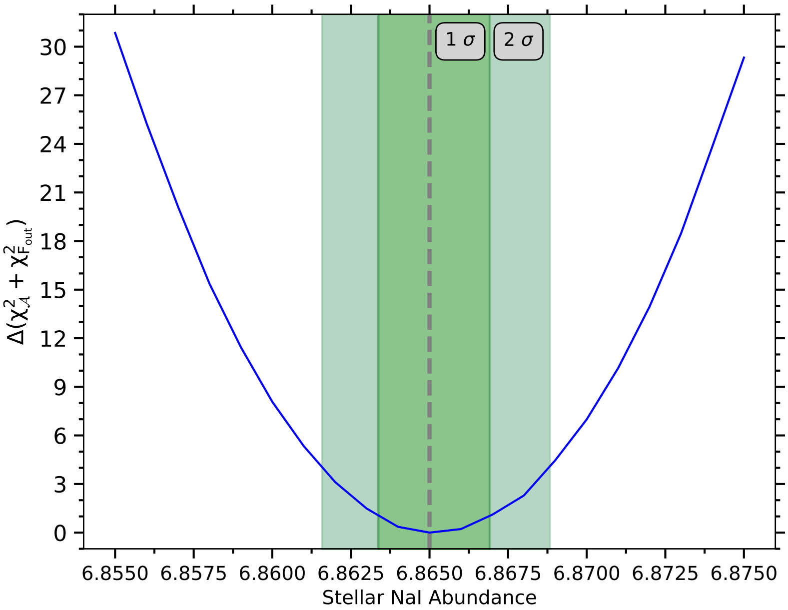

Fig. 3.23.: $\Delta_{(\chi^2_{\mathcal{A}}+\chi^2_{\mathrm{F_{out}}})}$ as a function of the stellar sodium abundance for the fit of MASCARA-1 b with $\mathrm{v_{eq}}\sin(i_*) + 2\times 1\sigma$ and $\mathrm{i_{pl}} - 2\times 1\sigma$. The green shaded areas show the values of stellar sodium abundance within the 1 and 2 σ intervals of the minimum value of $\chi^2_{\mathcal{A}} + \chi^2_{\mathrm{F_{out}}}$. The vertical grey dashed line shows the minimum value of χ^2

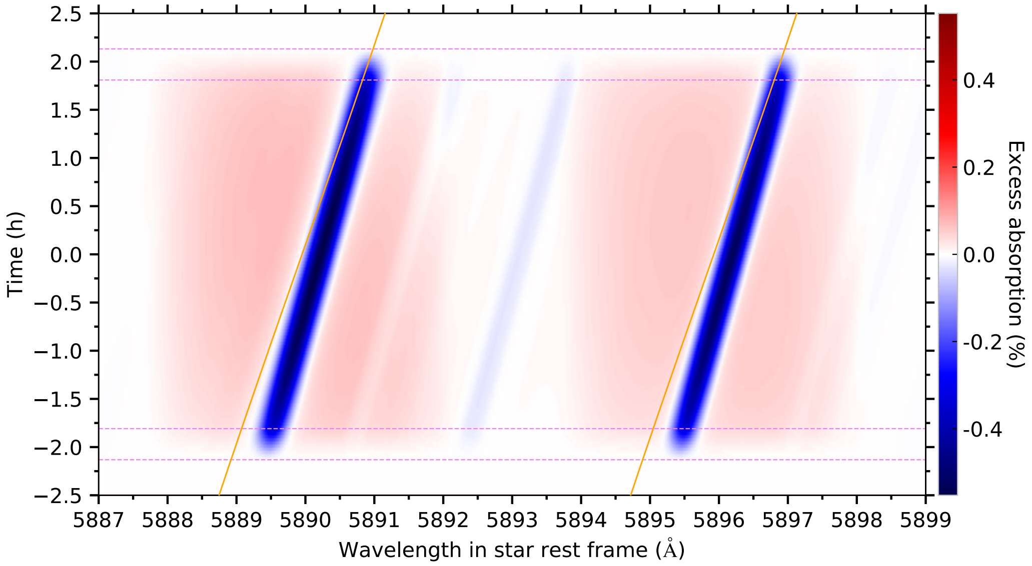

Fig. 3.24.: Theoretical absorption spectrum of MASCARA-1 b as a function of time and wavelength, computed with the out-of-transit spectrum as reference, and plotted in the stellar rest frame for the case III.

3.3 Veiled planetary atmospheric signatures

3.3.1 Overlapping planetary orbital and planet-occulted stellar line tracks

In this section, I study the hypothetical case where the orbital track of the planet (orange dashed curve Fig. 3.7) is aligned and overlaps with the track of the planet-occulted stellar line in the absorption spectrum throughout the whole transit. This happens when the radial orbital velocity of the planet equals the radial velocity of the occulted stellar surface at each exposure. MASCARA-1 b and HD 209458 b only present a partial overlap because of their specific orbital architecture and stellar rotational velocity. This means that at some exposures of their transit, the effect of the POLD is negligible on the planetary absorption signature. With good SNR, these exposures could be studied individually, and the atmospheric absorption signature would be detectable, allowing for more reliable interpretations of the atmospheric properties. This present case, however, illustrates that the stellar contamination can render totally undetectable the presence of an atmosphere. To achieve this configuration, I used the same system's parameters as those of MASCARA-1 b except for the sky-projected spin-orbit angle and the planetary orbital inclination, whose specific values can be found in Table 3.3. I also adjusted the planetary atmosphere parameters to reach an atmospheric absorption signature of about 0.3%.

Figure 3.25 shows the mean absorption spectra between contact times 2 and 3 with and without atmosphere resulting from simulations based on the set-up described above. Apart from a clear reduction of the core of the POLD, its global shape is unaltered by the presence of atmospheric sodium. This means that in the absence of a precise estimate of the pure contribution of the POLDs, it is impossible to presume any atmospheric signature from the absorption spectrum and even more to infer any properties of the planetary atmosphere. Unfortunately, Figure 3.26 shows that the temporal evolution of the absorption spectrum does not offer a better option for analysing the atmosphere, as its absorption signature is completely veiled by the POLDs at each exposure of the transit. However, it is worth noting that close-in planets are expected to have a thermosphere strongly heated by the high level of XUV stellar radiation due to their spatial proximity to their host. High temperatures can be the source of strong atmospheric dynamics, which could lead in some cases to a day-to-night-side wind with speeds of several km s^{-1} (e.g. Seidel et al. (2020)). These types of winds can shift the atmospheric absorption signature blue-ward of their rest wavelength. Thus, with a high enough wind speed, the atmospheric absorption signature could be shifted out of the planet-occulted stellar line track and become detectable. As an example to illustrate the effect of a day-to-night-side wind on the atmospheric absorption signature in the absorption spectrum of a transiting

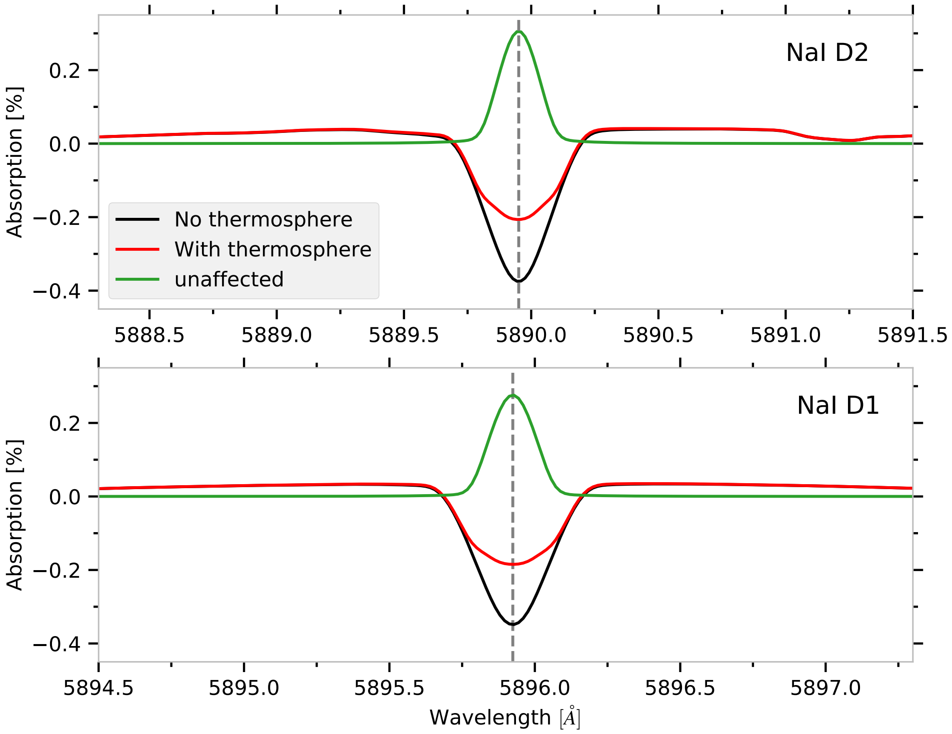

Fig. 3.25.: Theoretical mean absorption spectra between contact times T_2 and T_3 for the perfect overlap case computed with the out-of-transit spectrum, with and without sodium atmosphere as a function of the wavelength in the planetary rest frame.

planet, I added a 3 km s^{-1} day-to-night-side wind in the atmosphere of the previous simulation (typical speed value of day-to-night-side wind (Seidel et al. 2020)). The result of this simulation is shown in Figure 3.27, where the combination of the POLD and the atmospheric absorption signature now exhibits a profile skewed to the right, which hints at the presence of the atmosphere.

Configurations, where the planetary radial orbital velocity follows the radial velocity of the occulted stellar surface throughout the entire transit, may happen for close-in planets around fast rotating stars and for planets transiting slowly rotating stars at large orbital distances. This thus emphasises the importance of accounting for POLDs as accurately as possible when searching for atmospheres of temperate planets. Indeed, in such scenarios, while the POLDs might be fainter due to slower stellar rotation, the planetary atmospheric absorption signature will also be fainter as a consequence of lower stellar irradiation and more compact atmospheres.

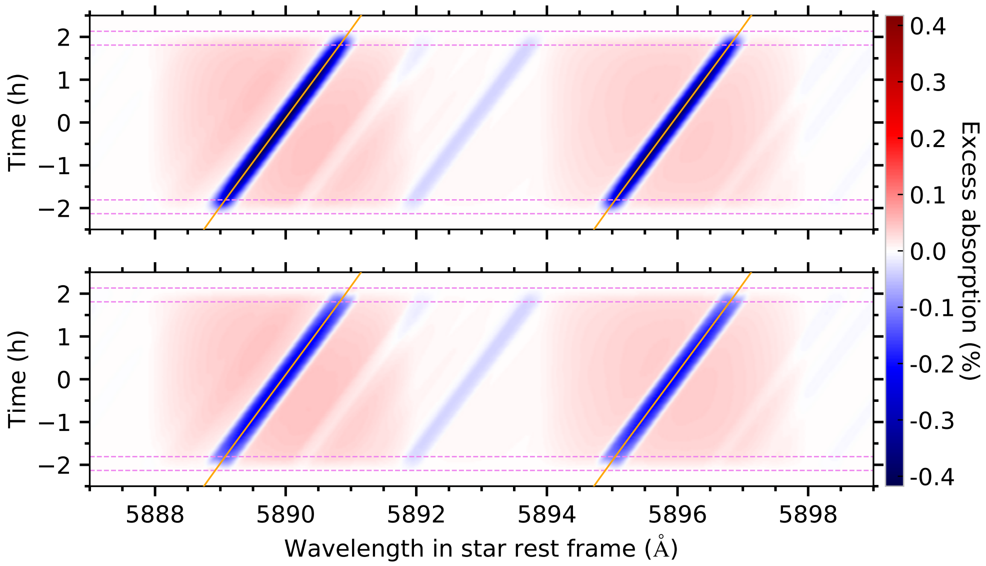

Fig. 3.26.: Theoretical absorption spectra for the perfect overlap case computed with the out-of-transit spectrum, around the Na I D2 and D1 lines as a function of time and wavelength in the stellar rest frame. **Upper panel**: without atmosphere. **Lower panel**: with atmosphere.

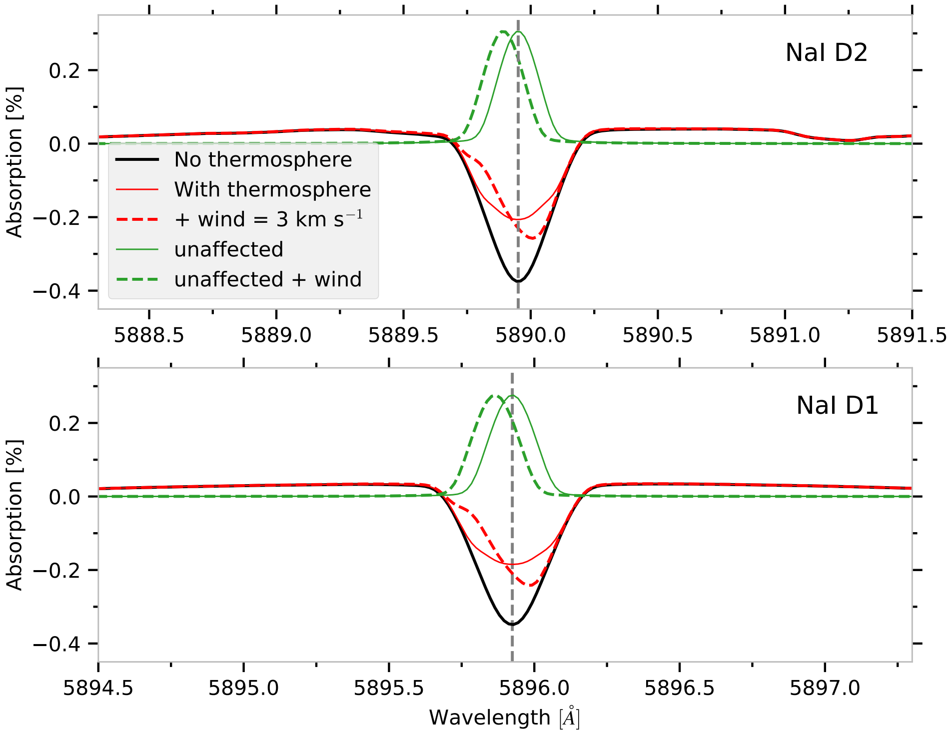

Fig. 3.27.: Theoretical mean absorption spectra between contact times T_2 and T_3 for the perfect overlap case computed with the out-of-transit spectrum, with and without sodium atmosphere as a function of the wavelength in the planetary rest frame. The dashed curves represent the absorption spectra computed from simulations that included a 3 km s^{-1} day-to-night-side wind in the thermosphere.

3.3.2 Hidden in the noise

The study of individual exposures and of the time evolution of the synthetic absorption spectra during the transits was simplified by the absence of noise in my simulations. However, real data sets are naturally contaminated by diverse noise sources and thus the temporal evolution of absorption spectra becomes much more challenging to faithfully analyse. A solution to this matter is to average the absorption spectra between T_1 and T_4 or T_2 and T_3 as was done in the previous sections, to enhance the signal-to-noise ratio (see also Sect. 2.2.1). This technique does, however, have a downside as it can induce a stronger blending of the POLD and the atmospheric signatures. Furthermore, all information on the temporal evolution of the signatures is lost, but it can still allow one to assess the presence of an atmospheric signature if is strong enough.

To see if an atmospheric signature could be lost in the 2D map but still visible in the mean absorption spectrum, I added noise to reach an SNR of 80[5] in the in-transit spectra of our previous simulations for HD 209458 b and, I increased the atmospheric signature. Figure 3.28 shows the results of this simulation. In this case, the atmospheric signal disappears in the 2D maps because of the noise but remains clearly identifiable in the mean of the absorption spectra.

3.4 Conclusion

Using the 3D forward-modelling code EVE along with the *Turbospectrum* code for spectral synthesis, I simulated planetary transit spectra of a typical hot Jupiter with neutral sodium atoms in its atmosphere under various stellar and planetary conditions to investigate the general behaviour of POLDs and their impact on its absorption spectrum. In a first step, I individually included stellar rotation, centre-to-limb variations and broadband limb darkening in my simulations to study their respective contributions to the POLDs and, thus, their influence on the detectability of an atmospheric signature. Additionally, for each individual stellar effect, I compared the absorption spectra computed with different spectra chosen as proxies for the planet-occulted stellar lines. Thanks to the forward modelling approach, I had access to the exact local planet-occulted spectrum. The latter allowed me to compute an unaffected absorption spectrum that I used as a benchmark to compare to the absorption spectra derived with these other proxies.

Below I list the main results of the study.

A key finding of this investigation is that, overall, without accurate assessments of

---

[5] The value was arbitrarily chosen to make the atmospheric signature disappear in individual exposures, but visible in the mean absorption spectrum.

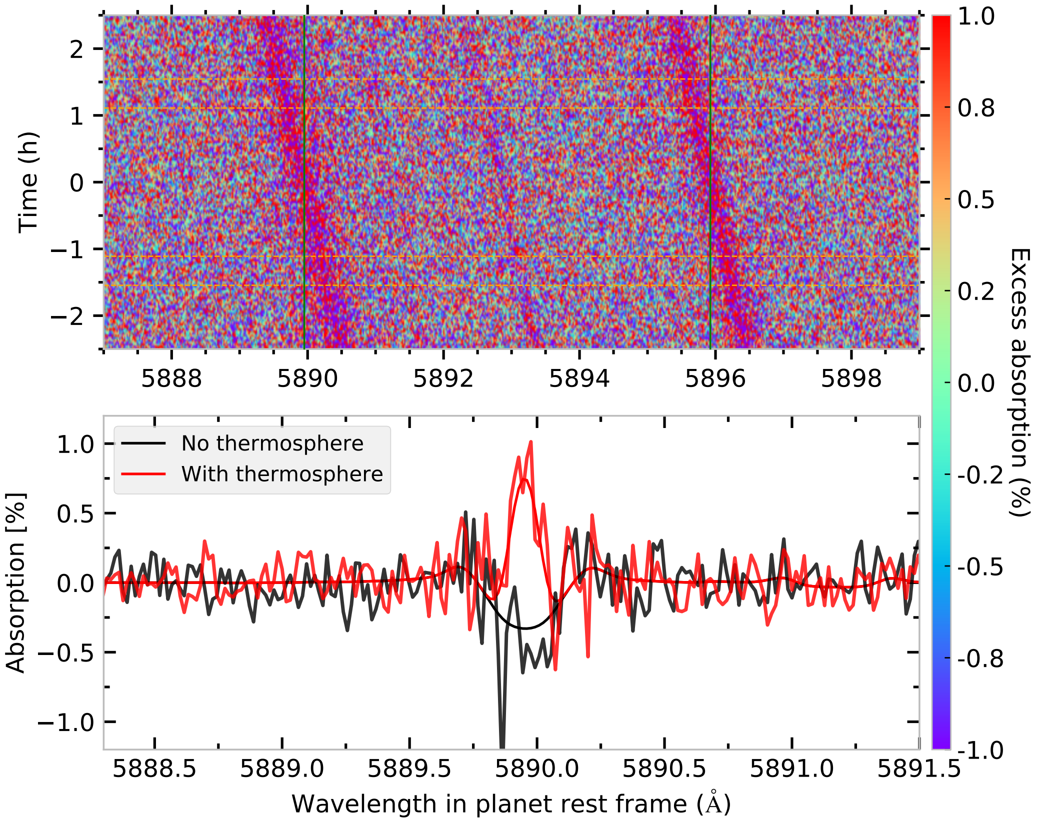

Fig. 3.28.: **Upper panel**: Theoretical absorption spectra of HD 209458 b around the Na I D1 and D2 lines, as a function of time and wavelength in the planetary rest frame with an atmosphere. **Lower panel**: Mean of the theoretical absorption spectra of HD 209458 b around the Na I D2 line computed with the out-of-transit spectrum between contact times 2 and 3, with and without sodium atmosphere as a function of the wavelength in the planetary rest frame. I added noise in the simulated in-transit spectra to reach a SNR of 80. The noise in the out-of-transit spectrum is neglected.

the planet-occulted stellar spectra, there is no universally adequate proxy to mitigate the impact of the POLDs induced by stellar rotation, CLVs and BLD.

- In the case of slowly rotating stars, the disc-integrated line profile remains a decent substitute for the planet-occulted stellar line profile unless strong CLVs are present.
- For moderate to fast-rotating stars (in this study, i.e. $\mathrm{v_{eq}}\sin(i_*) \gtrsim 3$ km s^{-1}), all the tested proxies induced POLDs in the absorption spectra.
- Rotation-induced POLDs are best minimised with proxies shifted by the radial velocity of the planet-occulted surface at each exposure.
- CLV-induced POLDs are best minimised with the local line profile at disc's centre as a proxy for planet-occulted regions close to the centre of the apparent stellar disc. However, they are best minimised with the disc-integrated spectrum as a proxy for planet-occulted regions close to the stellar limb.

Rotation-induced POLDs can reach amplitudes comparable to typical planetary Na I atmospheric absorption signatures. Their peak-to-peak amplitude increases with $\mathrm{v_{eq}}\sin(i_*)$. In the case of a null impact parameter, their peak-to-peak amplitude decreases with increasing planetary spin-orbit angles.

Generally, the POLDs induced by CLVs are smaller in amplitude compared to those resulting from moderate-to-fast stellar rotation. Nevertheless, they can reach several tenths of a percent, which is on the order of magnitude of typical Na I absorption signatures. CLVs, therefore, become a primary source for misinterpreting atmospheric absorption signatures for planets orbiting slowly rotating stars.

The impact of BLD on absorption spectra is smaller than the impact of CLVs, but it can still introduce a global bias. This global bias can be removed but necessitates the use of an adequately estimated multiplicative factor from limb darkening laws, (see for instance Kopal 1950; Klinglesmith & Sobieski 1970; Diaz-Cordoves & Gimenez 1992).

Atmospheric absorption signatures are more biased by the POLDs in exposures where the planetary radial orbital velocity is similar to the radial velocity of the occulted stellar surface. When the planetary radial orbital velocity follows the radial velocity of the occulted stellar surface during the entire transit, atmospheric absorption signatures can end up being completely hidden in the POLDs and become non-detectable. Eventually, with the knowledge I gained from studying stellar distortions in absorption spectra in the first part of this chapter, I re-addressed real transit observations of two interesting exoplanets, namely HD 209458 b and MASCARA-1 b.

I reproduced the absorption spectrum of HD 209458 b, presented in Casasayas-Barris et al. (2021), using EVE simulations to investigate the potential presence of an additional Na I absorption signature. I confirmed the findings of Casasayas-Barris et al. (2020, 2021) that the observed signatures around the Na I D2 and D1 lines in the absorption spectrum of HD 209459 b at high spectral resolution appear to be mainly composed of POLDs. However, I was able to reach a better fit between the simulated and observed absorption spectra by including an atmosphere containing sodium atoms around the transiting planet. This claim is, nevertheless, tentative and only hints at the possible detection of sodium in the atmosphere of HD 209458 b. To confirm this detection, it will be necessary to make a thorough investigation of the signal using a combination of precise stellar and planetary line profiles along with modelling tools such as EVE and repeated transit observations with high resolution spectrographs such as ESPRESSO.
Similarly, I simulated transits of MASCARA-1 b to investigate whether atmospheric absorption signatures of sodium could be hidden in ESPRESSO spectra published in Casasayas-Barris et al. (2022). I found that by adjusting the $\mathrm{v_{eq}} \sin(i_*)$, the stellar sodium abundance and the $\mathrm{i_{pl}}$, the asymmetric feature in the mean absorption spectrum around the Na I D2 and D1 lines can be entirely explained by a POLD with no need for a planetary atmosphere. To reach this conclusion, I combined a fit to the disc-integrated spectrum and to the absorption spectrum around the sodium doublet lines.

This study was conducted focusing on the Na I D2 and D1 lines, and of course, the absolute impact of POLDs might vary from one system to another and also from one spectral line to another. However, it gives a sense of the qualitative behaviour of POLDs in absorption spectra depending on various stellar and planetary parameters. It also shows the importance of gaining a better understanding of how POLDs affect the absorption spectrum when searching for the presence of a planetary atmosphere. Finally, it shows that using a global approach for transit simulations – i.e. fitting together the disc-integrated stellar lines and a combined model of the POLDs and planetary atmospheric absorption lines – can lead to more faithful planetary atmospheric constraints derived from absorption spectra as it allows for distinguishing planetary absorption signatures from stellar lines contaminations.

4

Local stellar spectrum of the He I triplet at 10830 Å

Transit observations focusing on detecting the absorption signature of planetary atmospheric helium have increased in recent years thanks to high resolution spectrographs observing in the infrared wavelengths. To illustrate this recent growing interest, Guilluy et al. (2023) presented an exhaustive list of planets that were the subject of studies focusing on detecting helium in planetary atmospheres (see their Table A.1.). They listed a total of 46 targets (or 55, if we include the targets of their sample), that have been studied since 2018.

Hydrogen and helium-rich atmospheres, under intense heating, are likely to undergo hydrodynamic escape, as they can, due to their lightweight nature, more easily reach high bulk velocities necessary to overcome the gravitational attraction of the planet. Heavier species can also be brought to the upper layers via collisions with the hydrogen atoms of the expanding atmosphere (Watson et al. 1981; Lammer et al. 2003; Vidal-Madjar et al. 2003). Considering a solar composition for planetary atmospheres gives a helium-to-hydrogen atoms ratio of $\sim 10/90$. Helium is thus a species that is expected to be predominantly found in the upper layers of an extended atmosphere. Consequently, planetary atmospheric helium has a high potential of producing strong absorption signatures during the transit of the planet (e.g. up to $\sim 7\%$ of excess absorption on WASP-107 b in Allart et al. (2019)) as it can occupy a broad region around the opaque planetary body. Helium is thus a valuable candidate element for studies of planetary absorption signatures in order to infer properties on the structure and dynamics of the high layers of a planetary atmosphere and, to some extent, on its state of escape (Seager & Sasselov 2000; Oklopčić & Hirata 2018; Lampón et al. 2020; Dos Santos 2022).
Observationally, infrared wavelengths offer the possibility to probe the atmospheric layers relevant to escape, namely the thermosphere and exosphere, as they encompass the spectral region around 10830 Å, where the He I triplet lines form (e.g. Allart et al. 2019). The particular state of the helium atom that allows these transitions is commonly referred to as the infrared metastable He I triplet. The metastable He I triplet is favourably found in planetary thermospheres as these layers usually have high temperatures and absorb the stellar XUV flux, which are needed for the formation mechanism of the metastable state (see more details below) (Oklopčić & Hirata 2018). Moreover, the probability of having helium atoms in the metastable

state within the interstellar medium is rather low. Therefore, the contamination by supplementary absorption lines from the interstellar medium in observations is negligible (Indriolo et al. 2009; Allart et al. 2019). This further establishes the metastable He I triplet lines as a crucial diagnostic to probe planetary atmospheres and makes helium a reliable element to consider for transit observations.

4.1 Modelling the local stellar line profiles of the He I triplet from observations

As I demonstrated in Chapter 3, it is essential to model correctly the absorption spectrum of a transiting planet in order to infer robust atmospheric properties. This includes modelling the planetary atmospheric absorption signature and predicting the possible bias introduced by the absorption of strong stellar lines by the planet. The latter requires modelling the planet-occulted-line distortions, which in turn requires a precise knowledge of the variations of the local stellar line profiles across the stellar surface (CLV and stellar rotation, see Chapter 3).

In stellar atmospheres, two mechanisms are usually proposed to explain the formation of the He I triplet metastable state (Andretta & Jones 1997). The first one is the photoionisation-recombination mechanism which is the dominant mechanism in high-altitude layers of the chromosphere that have temperatures below 10 000 K. The photoionisation of helium atoms is caused by the XUV flux short-ward of 504 Å coming from the above coronal regions. The helium ion then recombines with an electron and can deexcite to the metastable level. The other mechanism is via excitation of helium atoms to the metastable state by collisions with high energy electrons, which requires temperatures greater than 20 000 K, typically met in the transition region or the corona in the Solar atmosphere (Andretta & Jones 1997; Centeno et al. 2008; Sanz-Forcada & Dupree 2008; Leenaarts et al. 2016; Hintz et al. 2020).

Unfortunately, the MARCS models that I use as input of the *Turbospectrum* code to generate synthetic spectra only account for the photospheric layers of stellar atmospheres. I thus needed to find a way to include the He I lines of the triplet in the synthetic stellar spectrum generated by *Turbospectrum* in order to have an estimate of the local line profiles that will be absorbed by the transiting planet across the stellar spectral grid in EVE simulations.

4.1.1 Including the He I triplet lines

To circumvent this issue, I have added an isothermal, isodense chromospheric layer of helium atoms on top of the 2D stellar spectral grid representing the photosphere. I considered this layer to only contribute to absorption (here, I neglected emission from the chromospheric layer). Then, I included in the series of intensity spectra from *Turbospectrum* (emerging from the photosphere) the He I lines calculated analytically based on the temperature and density of the helium atoms in the layer.

Below, I introduce the analytical form of the line profile that I used to model the helium triplet lines. I denote the intensity spectra derived from *Turbospectrum* for the different positions on the stellar disc as I_{μ_i}. Based on the formalism introduced in App. A, the intensity coming from the photosphere and going through the considered chromospheric layer – neglecting emission from the helium atoms, assuming a Gaussian shape for the absorption profiles of the different triplet lines and thermal broadening only – can be written following standard notations (e.g. Chapter 2 of Rutten (2003)) as,

$$I_{\mu_i}^{\mathrm{He\,I}}(\lambda) = I_{\mu_i}(\lambda) \times \exp\left(-\sum_{m=1}^{3} \tau(\lambda, \lambda_{0,m})\right) \tag{4.1}$$

or

$$I_{\mu_i}^{\mathrm{He\,I}}(\lambda) = I_{\mu_i}(\lambda) \times \exp\left(-\sum_{m=1}^{3} \sigma(\lambda, \lambda_{0,m}, T) \times n \times L\right) \tag{4.2}$$

where λ indicates wavelength dependence and $\lambda_{0,m}$ are the rest wavelength of the m^{th} transition of the He I triplet. The density, length and temperature of the layer are given by n, L and T, respectively. σ is the absorption coefficient of the m^{th} transition.
It is given by,

$$\sigma(\lambda, T) = \frac{\pi e^2}{m_e c} f_{\mathrm{osc}} \underbrace{\frac{\lambda_0}{w\sqrt{\pi}} \exp\left[-\left(\frac{c}{\lambda_0}\frac{(\lambda-\lambda_0)}{w}\right)^2\right]}_{\phi(\lambda-\lambda_0)=\text{line profile function}} \tag{4.3}$$

with

$$w = \sqrt{\frac{2k_bT}{m}} \tag{4.4}$$

the thermal broadening, f_{osc} the oscillator strength of the transition, k_b the Boltzmann constant, m the mass of an helium atom, e the electron electric charge, m_e its mass and c the speed of light. This form of the equation is valid in cgs units[1].
Once each I_{μ_i} has been multiplied by the He I triplet line profiles, they are interpo-

---

[1] This form is also valid in SI units. Still, the introduction of additional constants would be necessary.

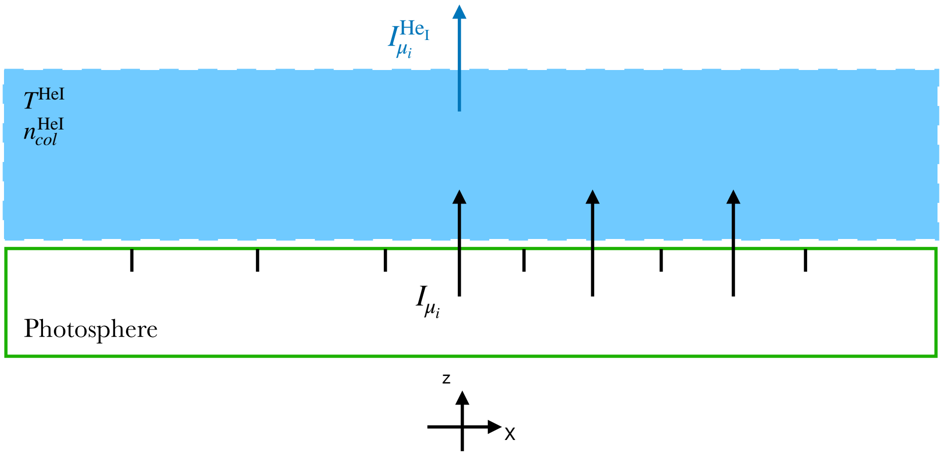

Fig. 4.1.: Sketch of the layer of helium atoms (in blue) above the photosphere (in green). The stellar grid is flat to represent the apparent stellar disc. The intensities are in the direction of the observer and perpendicular to the stellar surface. In this case, the length travelled inside the layer of helium atoms is not known. Instead, I use the column density in the fit.

lated over the whole stellar grid, then multiplied by the surface of a grid cell (to have flux units) and then shifted in wavelength according to the radial velocity of the grid cell they emerge from. The disc-integrated spectrum is computed by adding all the local fluxes (see Chapter 3 and App. B). Finally, after being convolved by an adequate instrumental response, the synthetic disc-integrated spectrum is compared to the observed disc-integrated spectrum.

This chromospheric helium lines model has been included in a fitting routine that compares the observed and simulated disc-integrated spectra and where the unique free parameters are the temperature and the column density of the helium atoms. Due to the degeneracy between L and n in Eq. 4.2, I chose to fit the column density, which is defined as $\mathrm{n_{col}} = n \times L$. Furthermore, the same value of temperature and column density is used for all the I_{μ_i}. When the best fit is achieved, I consider that the analytical local line profiles of the He I triplet used to build the synthetic disc-integrated line profiles are representative of the actual local line profiles. I can then use the stellar grid of synthetic local spectra that corresponds to the best fit as an input for transit simulations with EVE. Figure 4.1 shows a schematics of this basic model in which a layer of helium atoms is placed on top of the photosphere from which the intensities computed by *Turbospectrum* emerge perpendicularly to the stellar disc's surface.

4.1.2 Application to observations

I used this tool I developed in a publication dedicated to characterising atmospheric evaporation on diverse exoplanets called: *DREAM: III. A helium survey in exoplanets on the edge of the hot Neptune desert with GIANO-B@TNG* (Guilluy et al. 2023)[2]. The aim of this study was to characterise the evaporation of the atmospheres of a sample of nine Jupiter- and Neptune-sized exoplanets using transit observations of the high resolution spectrograph GIANO-B (Telescopio Nazionale Galileo Roque de los Muchachos La Palma) to target the absorption signature of the He I triplet at 10830 Å. The idea was to search for absorption signatures of the He I triplet and, if detected to a significant level, fit them with the code *p-winds* (Dos Santos et al. 2022) to assess the evaporation state of these planets and infer properties about their atmospheres. Before this fit could be done, there was a need to evaluate the possible bias due to planet-occulted line distortions of the He I triplet in the absorption spectra of the sample (Chapter 3).

Therefore, I used my routine to fit the observed disc-integrated helium triplet line profiles for the four targets with the highest $\mathrm{v_{eq}}\sin(i_*)$ values[3]. Once the best fit is reached, the derived synthetic spectrum at disc's centre was used to build a proxy for the local planet-occulted spectrum at each exposure of the planetary transits (proxy used in Eq. 3 of Guilluy et al. (2023)). This was done by multiplying the synthetic stellar intensity at disc's centre with a limb darkening coefficient – accounting for the planet-occulted stellar surface – evaluated at each specific observed exposure. Then, this quantity was shifted in wavelength according to the radial velocity of the occulted stellar region at each exposure. Finally, these synthetic local flux spectra were convolved with the adequate instrumental response.
Eventually, we compared the absorption spectra computed using this derived synthetic proxy of the planet-occulted spectrum with the absorption spectra computed with the observed out-of-transit spectrum (see Equations 3 and 4 in Guilluy et al. (2023)). This comparison between the results of Eq. 3 and Eq. 4 is shown in Figure A.3 in Guilluy et al. (2023) (see also App. C). We performed two types of comparison: for each exposure, we computed the difference between the results of Eq. 3 and Eq. 4, in the stellar rest frame (see left panels); and we directly compared the mean of the absorption spectra computed with each equation, in the planet rest frame (see right panels). From these comparisons, we found that the planet-occulted line distortions caused by stellar rotation (CLV is not modelled in the calculations of the local He I line profiles) are not significant compared to the dispersion of the data around the He I triplet lines. This led us to conclude that for this sample of observations, the disc-integrated line profile of the He I triplet was

---

[2] This publication can be found in App. C

[3] The planet-occulted line distortions are expected to be stronger for fast-rotators as explained in Chapter 3

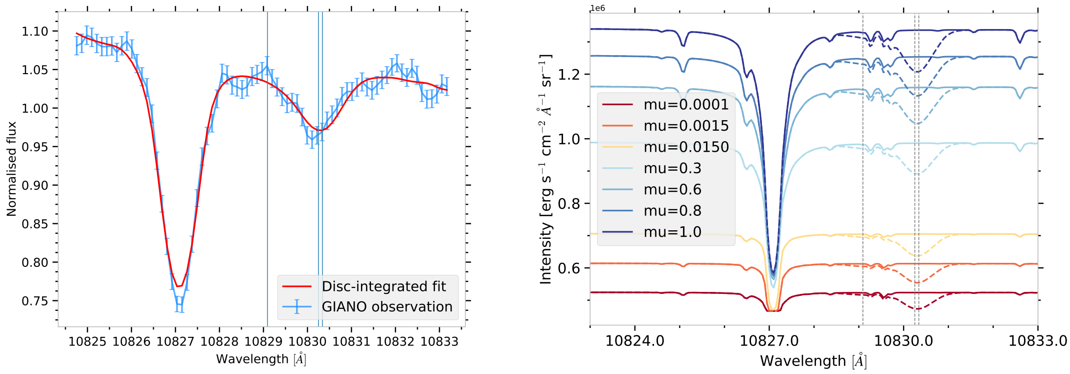

Fig. 4.2.: **Left panel**: Disc-integrated spectrum of HAT-P-33. The red curve shows the best fit to the observed disc-integrated spectrum in blue. **Right panel**: Spectral intensities at different positions on the stellar disc of HAT-P-33 computed with *Turbospectrum*. The dashed spectra are obtained after multiplying the intensity spectra by the analytical He I triplet line profiles derived for the best fit. The vertical lines show the transition wavelengths of the He I triplet lines. The strong line on the left is a Si I line. This line is not fitted.

an acceptable proxy of the planet-occulted line profiles to compute the absorption spectra around the He I triplet lines. The subsequent fits of the atmospheric helium absorption signatures with *p-winds* were therefore performed on the absorption spectra computed using the observed disc-integrated spectrum.

Figures 4.2 and 4.3 show the results for the best fit on the disc-integrated spectrum for the two targets of the sample with the highest value of $\mathrm{v_{eq}}\sin(i_*)$. They also display a series of synthetic intensity spectra at different positions on the stellar disc with the added He I triplet line profiles computed with the parameters of the best fit.

4.1.3 Towards a more realistic approach

While this model allows me to derive a first approximation of the local line profiles of the He I triplet from a fit on the observed disc-integrated spectrum, it remains rather basic and omits crucial physics. In particular, this model does not account for centre-to-limb variations of the He I line profiles, which can induce significant planet-occulted line distortions in the absorption spectrum of a transiting planet as demonstrated in Chapter 3.

In this section, I present an update of the model, which goes towards a more self-consistent modelling of the stellar He I triplet lines. As mentioned at the beginning of Sect. 4.1, models and observations of the helium lines suggest that, in stellar atmospheres, the metastable triplet forms mainly in two distinct regions (Vernazza et al. 1981; Andretta & Jones 1997; Centeno et al. 2008; Hintz et al. 2020). These two regions, with different properties, are crucial to understand the formation processes of these lines. Thus, the single-layer model of the previous section has

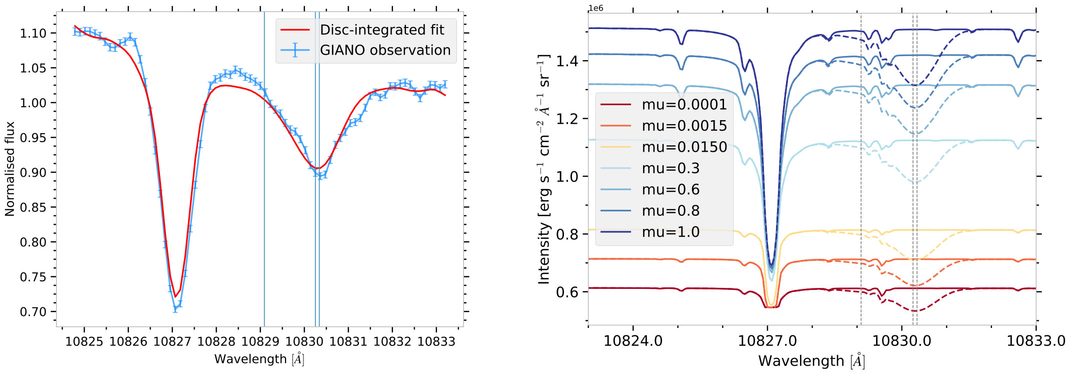

Fig. 4.3.: **Left panel**: Disc-integrated spectrum of HAT-P-49. The red curve shows the best fit to the observed disc-integrated spectrum in blue. **Right panel**: Spectral intensities at different positions on the stellar disc of HAT-P-49 computed with *Turbospectrum*. The dashed spectra are obtained after multiplying the intensity spectra by the analytical He I triplet line profiles derived for the best fit. The vertical lines show the transition wavelengths of the He I triplet lines. The strong line on the left is a Si I line. This line is not fitted.

been extended to a two-layers model. Furthermore, the problem is handled more thoroughly as the radiative transfer equation in these layers (of constant properties) is solved exactly, taking into account both emission and absorption contributions. Finally, I accounted for the change in the path length travelled by radiation inside each layer as a function of the position on the stellar disc. The latter is responsible for the centre-to-limb variation of the lines.

Emission contribution

The model I used in Guilluy et al. (2023) only accounts for the absorption of the radiation by the helium atoms but does not consider any emission from these atoms. However, unless the helium atoms are very cold in order not to emit any radiation, it is natural to consider that these atoms emit a minimum of radiation. Moreover, emission becomes dominant if the layer of formation of the lines is optically thick (see Eq. A.8), which can happen close to the stellar limb. When considering emission from the helium atoms, we not only need to consider the population of the lower level (l) of the metastable triplet, but also the populations of the excited level u. In our case, these energy levels correspond to the 2 ^{3}S and 2 ^{3}P states shown in Figure 1 in Oklopčić & Hirata (2018) for example. Considering these two energy levels and following Section 2.3.2 in Rutten (2003), the definition of the absorption coefficient times the number density of atoms is now given by,

$$\alpha = \sigma \times n = \frac{\pi e^2}{m_e c} f_{\text{osc}}(n_l - n_u \frac{g_l}{g_u})\phi. \tag{4.5}$$

The emission coefficient j multiplied by the number density of atoms in the upper energy level (n_u) is given by,

$$\eta = j \times n = \frac{\pi e^2}{m_e c} f_{\text{osc}}\, n_u \frac{g_l}{g_u} \frac{2hc}{\lambda_0^3} \phi \tag{4.6}$$

with g_l and g_u the statistical weights of the lower and upper energy levels, respectively[4]. h the Planck constant, and ϕ the Gaussian line profile. For simplicity, we consider that both the absorption and emission coefficients have the same line profile function. Using these two coefficients, we can now use Eq. A.7 to calculate the emerging intensity from the helium layers, with the source function S given by the ratio of Eq. 4.6 to Eq. 4.5.

There are, therefore, two different number densities per layer, one for the lower level of the metastable state and one for the upper level. However, the upper energy level $2\,^3$P is actually divided into three levels (namely, excited levels), that allow for the formation of each line of the He I triplet. In addition to the free parameters of the model presented in Sect. 4.1, we are left now with three more parameters, representing the populations of each individual excited level of the helium metastable state. To reduce the number of free parameters, I make the assumption that these three upper levels can be grouped into a single upper *superlevel*.
Under this approximation, we can write the total number density for the *superlevel* N_{sl} as,

$$N_{sl} = n_{u_1} + n_{u_2} + n_{u_3} \tag{4.7}$$

where the n_{u_i} are the number density of each excited level of the metastable state $2\,^3$P. I further assume that the individual population of each excited level,n_{u_i}, pertaining to the superlevel, follows the Boltzmann statistics. The latter assumption holds because each excited level is close in terms of energy (see Hubeny & Mihalas 2014, for a more in-depth discussion on superlevels). Therefore, the knowledge of the temperature and N_{sl} is sufficient to retrieve each individual n_{u_i}.

A two-layer model

To account for several layers in the model, the radiative transfer equation A.7 has to be generalised. Its solution for the intensity coming from the photosphere at a position μ_i and going through the N chromospheric layers in the direction of an observer, $I^{\text{He}\,\text{I}}_{N,\mu_i}$, is written,

$$I^{\text{He}\,\text{I}}_{N,\mu_i} = I^{ph}_{\mu_i} e^{-\tau_{tot}} + \sum_{j}^{N} S_j \left(1 - e^{-\tau_j}\right) e^{-\sum\limits_{k=j+1}^{N} \tau_k} \tag{4.8}$$

---

[4] Rutten (see 2003); Hubeny & Mihalas (see 2014, for more details),

with $I_{\mu_i}^{ph}$ the intensity exiting the photosphere from a position μ_i on the stellar disc. The total optical depth of the N layers is given by $\tau_{tot} = \sum_j^N \tau_j$. The source function and the optical depth of each layer are given by S_j and $\tau_j = \alpha_j l_j(\mu_i)$, respectively, with α_j the total absorption coefficient of the layer. As already stated, two distinct regions are considered to encompass the zone of formation of the helium triplet lines. Based on the temperature profile for the Solar atmosphere published in Figure 1 of Vernazza et al. (1981) (see also Fig. 2.11) or Figure 6 of Andretta & Jones (1997), we can determine constraints to evaluate the approximate length of each region as well as their temperature ranges. The lower region has temperatures ranging between ∼ 5000 K and 10000 K and a length of about 1500 km, corresponding to the chromosphere. The upper region has temperatures ranging between ∼ 20000 K and 30000 K and a length of about 300 km, which forms a plateau in the transition region, slightly above the chromosphere. Figure 4.4 illustrates the architecture of the two chromospheric layers that I considered above the photosphere.
In the case with two layers, Eq. 4.8 becomes:

$$\begin{aligned} I_{2,\mu_i}^{\mathrm{He\,I}} &= I_{\mu_i}^{ph} e^{-(\tau_1+\tau_2)} + S_1(1-e^{-\tau_1})e^{-\tau_2} + S_2(1-e^{-\tau_2}) \\ &= \underbrace{\left[I_{\mu_i}^{ph} e^{-\tau_1} + S_1(1-e^{-\tau_1})\right]}_{I_{1,\mu_i}^{\mathrm{He\,I}}} e^{-\tau_2} + S_2(1-e^{-\tau_2}) \end{aligned} \tag{4.9}$$

with the layer 1 and 2 being the innermost and outermost layer, respectively. This is the form I used in the numerical implementation of the model. I did not let the number of layers be a free parameter for the fitting routine, as this would strongly increase the number of free parameters.

Length of the path along a specific line of sight

Another key aspect to improve the model was to account for the variation of the length of the path travelled by radiation in each chromosheric layer as a function of the position on the stellar disc. Figure 4.5 shows a visual representation of how the length of the path can vary from the centre to the limb of the star for the case with two chromospheric layers. Based on the geometry presented in Fig. 4.4, we can derive the length of the path, $l_j(\mu_i)$, inside a layer j in the direction of a distant observer and from a position i on the stellar disc as,

$$l_j(\mu_i) = \sqrt{R_j^2 - x^2(\mu_i)} - \sqrt{R_{j-i}^2 - x^2(\mu_i)} \tag{4.10}$$

where R_j is the radius corresponding to the chromospheric layer j that is being traveled and R_{j-1} the radius corresponding to the underlying layer. $x(\mu_i)$ corresponds to the abscissa of the stellar cell from which I_{μ_i} is emerging from. This form of

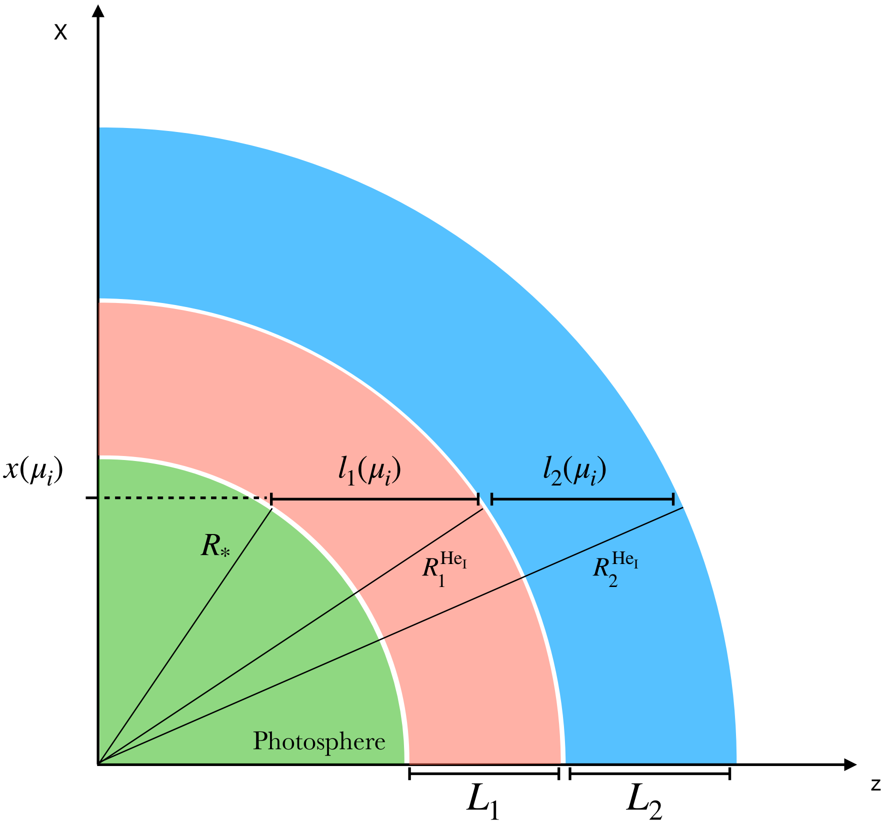

Fig. 4.4.: Sketch of the two additional atmospheric layers of helium atoms on top of the photosphere.

the equation is only valid for I_{μ_i} emerging from cells along the x axis (cells with an ordinate value of 0). A more general formula can be expressed as a function of $\mu_i = \sqrt{1-(x^2(\mu_i)+y^2(\mu_i))}$, where $x(\mu_i)$ and $y(\mu_i)$ are the coordinates of the stellar cell i in the Cartesian frame of reference centred on the stellar disc's centre. The formula is given, in units of stellar radius, by

$$\begin{aligned} l_j(\mu_i) &= \sqrt{R_j^2 - (x^2(\mu_i)+y^2(\mu_i))} - \sqrt{R_{j-i}^2 - (x^2(\mu_i)+y^2(\mu_i))} \\ &= \sqrt{R_j^2 - (1-\mu_i^2)} - \sqrt{R_{j-i}^2 - (1-\mu_i^2)}\ . \end{aligned} \tag{4.11}$$

With these modifications, the improved model now has four free parameters per layer: the width, the density of the lower level of the metastable He I state, the density of the upper superlevel of the metastable He I state and the temperature.

4.1.4 Test of the improved model

In this section, I present some tests of the latest version of the model. Firstly, I constructed a generic disc-integrated spectrum in the spectral region of the metastable He I triplet using the model with specific fixed values for each of the free param-

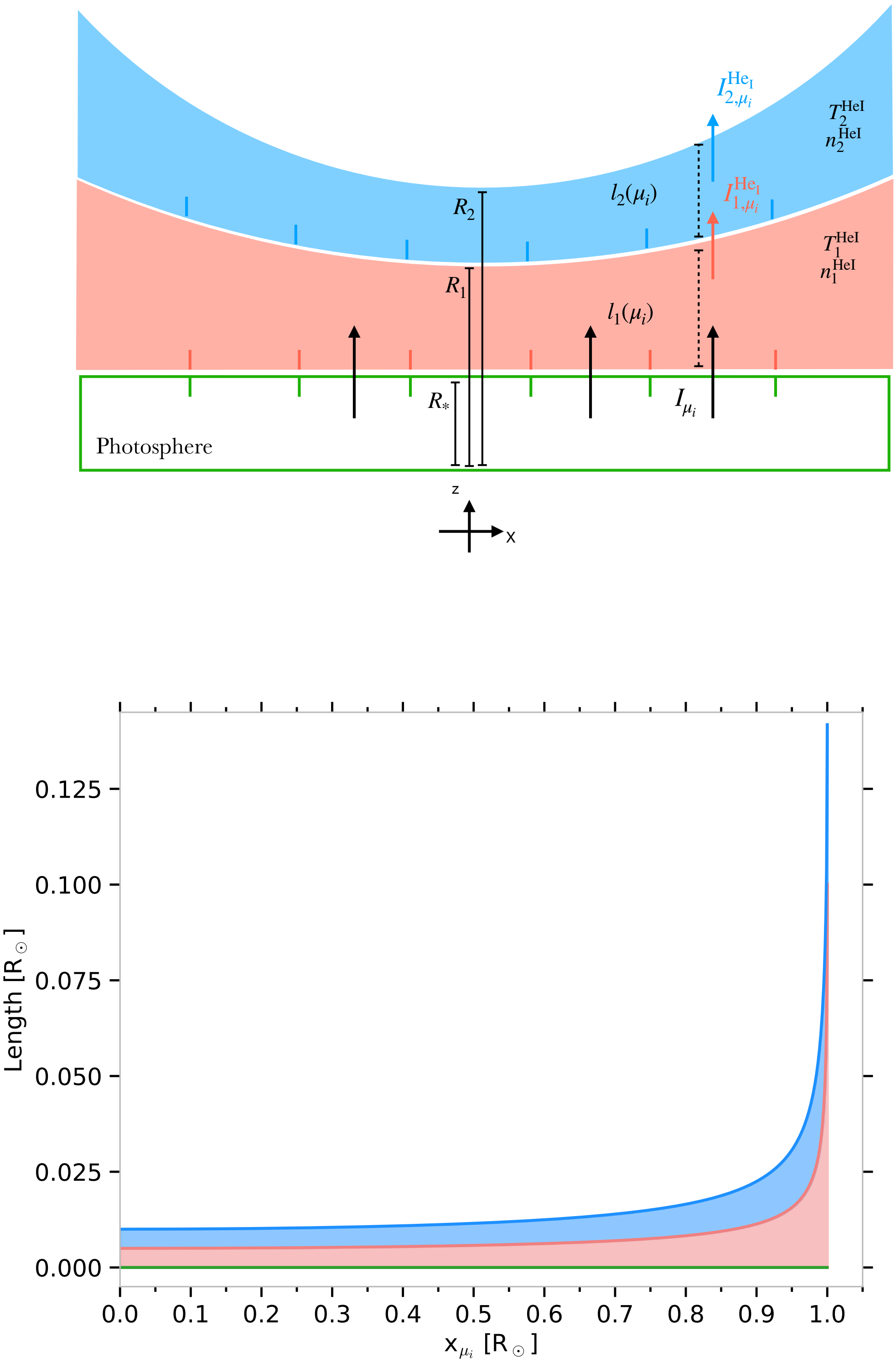

Fig. 4.5.: **Upper panel**: Schematic representation of the change in the length of the path travelled by radiation in the additional helium layers from Figure 4.4. **Lower panel**: Solution of Equation 4.11 for two layers of radii equal to 1.005 and 1.01 stellar radius for the lower and the upper layers, respectively. The solution of the equation for the upper layer was added to the solution for the lower layer. The result is only shown along a single stellar radius.

Tab. 4.1.: Parameters of the layers used for the model disc-integrated spectrum.

Parameter	Lower layer	Upper layer
Temperature (K)	7000	23000
Density lower level (cm^{-3})	2.0×10^{10}	5.0×10^{9}
Density superlevel (cm^{-3})	2.0×10^{9}	5.0×10^{8}
Radius (R_*)	1.001250	1.001295

Tab. 4.2.: Stellar and planetary properties.

Parameter	Value
Stellar :	
Radius ($R_\odot$)	1.0
Mass ($M_\odot$)	1.0
T_{eff} (K)	5000
Metallicity [Fe/H]	0
log g (cm s^{-2})	4.5
$v_{\mathrm{eq}} \sin(i_*)$ (km s^{-1})	5, 20 and 50
Planetary :	
Radius (R_{Jup})	1.138
Mass (M_{Jup})	1.123
Semi-major axis (au)	0.031
Inclination (deg)	90.0
Period (days)	2.2185752
Eccentricity	0.0
Sky-projected spin-orbit angle (deg)	0.0

Note. Values for the planetary radius, mass, orbital period and semi-major axis are taken from Bonomo et al. (2017) for the planet HD 189733 b, another well-known and studied exoplanet.

eters (the parameters are listed in Table 4.1). Then, I added noise to the generic disc-integrated spectrum to simulate an observation with a signal-to-noise ratio of 400 and 200. The stellar parameters used to generate the synthetic stellar spectral intensities are listed in Table 4.2. I also used a $v_{\mathrm{eq}} \sin(i_*) = 20$ km s^{-1}.

Secondly, I used the routine to fit the He I line profiles of these two model disc-integrated spectra. Figure 4.6 shows the two modelled disc-integrated spectra and the best fit of the He I triplet line profiles obtained with the routine. After the best fit is reached, I used the parameters derived from the best fits and the parameters used for the model disc-integrated spectra, in order to compute the spectral intensities for specific μ positions. Finally, I compared the intensities computed from the best-fits parameters with the intensities injected in the model to highlight the difference in the local line profiles of the He I triplet. In Figure 4.7 I show the difference in

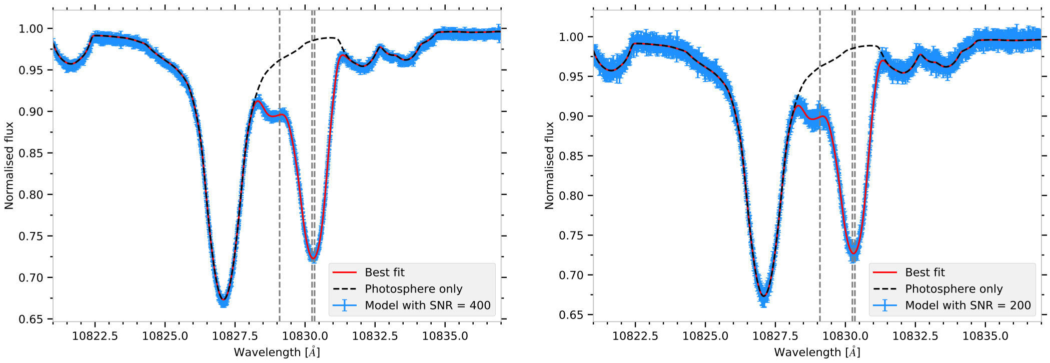

Fig. 4.6.: Disc-integrated spectra of our modelled star, computed from the best-fit parameters as a function of wavelength. **Left panel**: with an SNR of 400. **Right panel**: with an SNR of 200. The vertical lines indicate the transition wavelengths of the He I triplet lines.

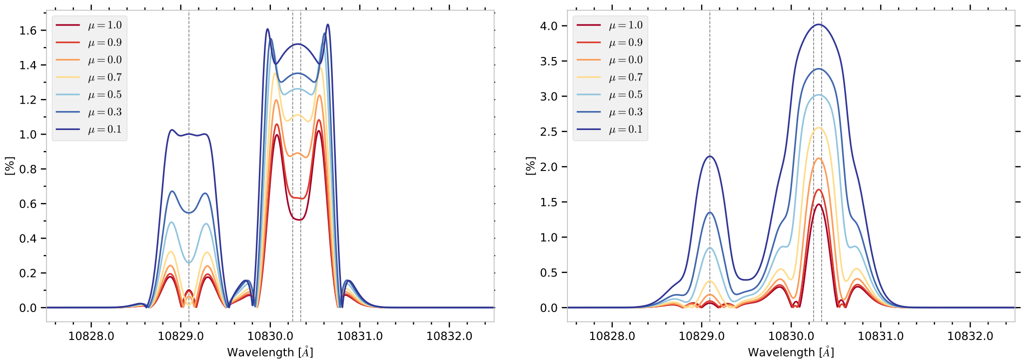

Fig. 4.7.: Difference in percentage between the intensities of the model and the intensities reconstructed from the best-fit parameters. **Left panel**: for a modelled disc integrated spectrum with a SNR = 400. **Right panel**: for a modelled disc integrated spectrum with a SNR = 200. The vertical lines indicate the transition wavelengths of the He I triplet lines.

percentage between the modelled intensities and the intensities reconstructed from the best fit values. We see that the largest difference is for the μ positions close to the limb. This is expected as those local line profiles give much less weight to the disc-integrated spectrum than the local line profiles close to the centre of the stellar disc. Consequently, the fit does not constrain the line profiles from close to the limb as well as it constrains the line profiles from closer to the stellar disc centre. However, even for μ values of 0.1, that is, for a position at a distance of 0.995 stellar radius from the centre of the disc, the maximum difference is around 1.6% and 4% for the case with an SNR of 400 and 200, respectively.

Finally, I injected these three spectral grids (the grid of the model star and one for the best fit for each SNR value) as inputs in the EVE code to run a transit simulation of a test planet in order to compare the distortions in the resulting absorption

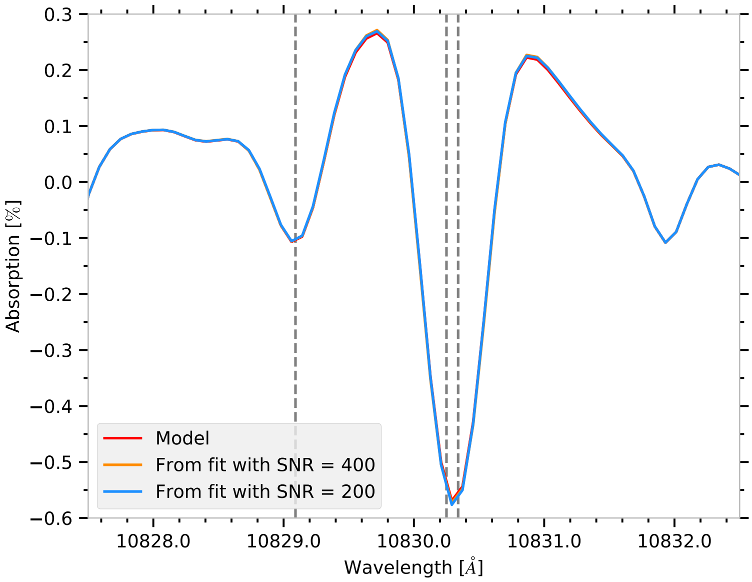

Fig. 4.8.: Mean absorption spectrum as a function of wavelength for the modelled star and the best-fit stellar grids. The vertical lines indicate the transition wavelengths of the He I triplet lines.

spectra. The parameters of the planet are listed in Table 4.2; no atmosphere was injected in the simulations. Figure 4.8 shows the mean absorption spectrum for the transit of our test planet for each of these three grids. The differences between the induced planet-occulted line distortions around the He I triplet are barely visible to the naked eye. This illustrates that my routine has allowed me to reconstruct the local line profiles of the He I triplet from the disc-integrated line profile with a precision good enough – less than 5% – not to introduce significant change in the absorption spectrum. I conclude that this routine shows promising potential to be used to give a first-order estimate of the POLDs in absorption spectra around the metastable He I triplet lines and that it could benefit the community.

4.2 Predicting POLDs around the He I infrared triplet

In this section, I wish to estimate the POLD induced around the metastable helium triplet lines in the absorption spectrum of a generic transiting planet. For this, I simulated a spectral grid using *Turbospectrum* and a MARCS model for a temperature of T = 5000 K, a log(g) = 4.5 and [Fe/H] = 0, which are approximately the stellar parameters of HD 189733, the host of a well-known exoplanet. I then added the He I triplet lines using the model presented in Sect. 4.1.3, setting fixed parameters of temperature, density and size of the layers. I created two model stars: one with shallow He I triplet lines and one with He I triplet lines almost as deep as the neighbour Si I line. For the shallow lines, I matched the line depth of the spectrum of HD 189733 published in Moutou et al. (2020) (see their figure 8). For the deep lines, I adjusted the parameters so that the He I lines depth approximately matched the Si I line depth, but I did not reproduce a specific system. For the deep lines, I used the same parameters as in Table 4.1 except for the density of the superlevel of the upper layer, which was set to 3.0×10^8 cm^{-3}. For the shallow lines, the density of the lower level was set to 7.0×10^9 cm^{-3} and 2.0×10^9 cm^{-3} for the lower and upper layer, respectively. The density of the superlevel was set to 7.0×10^8 cm^{-3} and 6.0×10^7 cm^{-3} for the lower and upper layer, respectively. The temperature and radius of the layers were the same as for the deep lines. Figure 4.9 shows the intensity spectra for a series of μ positions for the two model stars with shallow and deep He I lines.

From these two model stars, I created six synthetic stellar spectral grids by choosing three values of $\mathrm{v_{eq}}\sin(\mathrm{i}_*)$: 5, 20 and 50 km s^{-1}. The six disc-integrated spectra reconstructed from these grids are shown in Figure 4.10. Finally, I ran a transit simulation for a generic Jupiter-sized planet without atmosphere for each of these six synthetic stellar spectral grids and compared the resulting absorption spectra. The parameters of the system used for the simulations of the transiting planet are listed in Table 4.2. The resulting mean theoretical absorption spectra for the six models are shown in Figure 4.11. As expected, planet-occulted line distortions appear around the He I triplet lines. The distortions have a larger amplitude for the cases with deep He I triplet lines, as the local line profiles are also deeper. In the case with $\mathrm{v_{eq}}\sin(\mathrm{i}_*) = 50$ km s^{-1} the mean POLD is smaller in amplitude than for the case with $\mathrm{v_{eq}}\sin(\mathrm{i}_*) = 20$ km s^{-1}, but exposure-by-exposure the amplitudes of the POLD is larger as can be seen in Fig 4.12. This figure shows the temporal evolution of the absorption spectrum as a function of wavelength in the planetary rest frame of our generic planet for the six different cases. The mean POLD is larger for $\mathrm{v_{eq}}\sin(\mathrm{i}_*) = 20$ km s^{-1} because the individual POLDs follow approximately the radial velocity shift of the planet during the whole transit and are therefore aligned in the planetary rest frame. For $\mathrm{v_{eq}}\sin(\mathrm{i}_*) = 50$ km s^{-1}, the individual POLDs are not aligned in the planetary rest frame, and even though they have a larger amplitude, the mean tends to average out their amplitude. This result is, of course, not an absolute conclusion and pertains to the specific system I simulated.

From these simulations, we can better understand why in Guilluy et al. (2023) we determined that the POLDs were negligible. It is because the disc-integrated line profiles of the He I triplet were shallow for the targets we analysed, and so we can assume that the local line profiles were shallow as well and thus, as the upper panel of Fig. 4.11 illustrates, the amplitude of the POLDs was not significant.

As explained in Chapter 3, the absorption signatures of planetary helium might be more or less affected by the induced POLD depending on the overlap between the

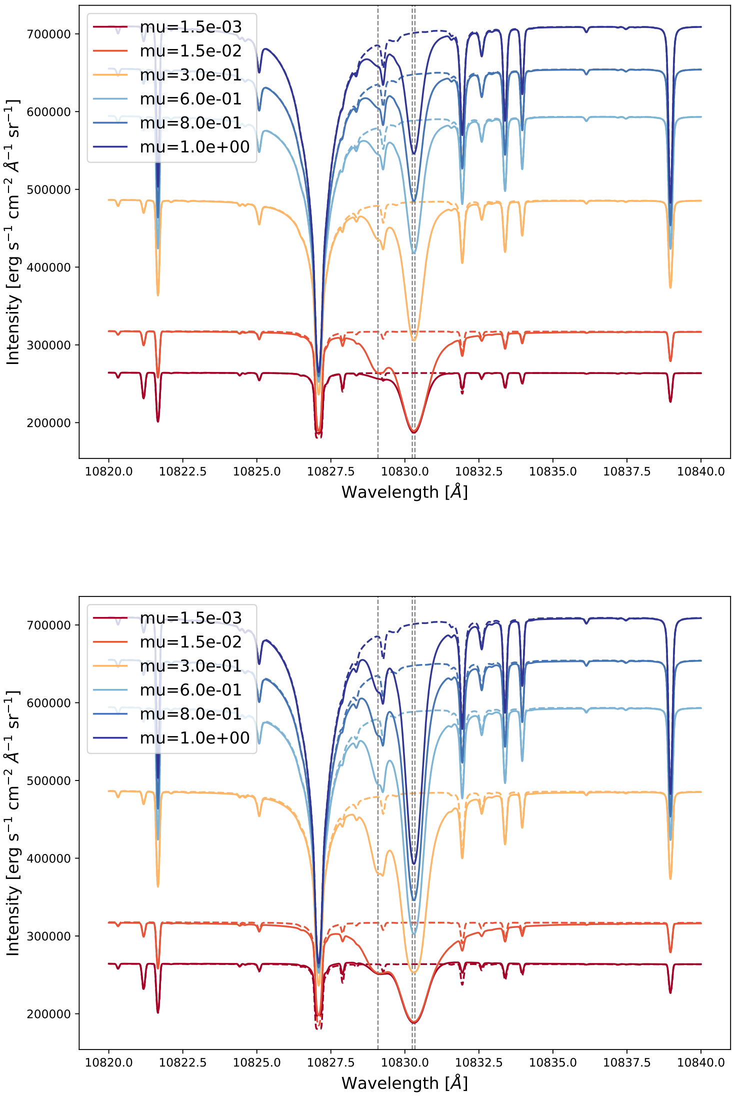

Fig. 4.9.: Spectral intensities for different positions on the stellar disc of the generic star derived with *Turbospectrum*. The dashed spectra are before the multiplication of the intensity spectra by the analytical He I triplet line profiles derived for the shallow (upper panel) and for the deep (lower panel) cases. The vertical grey dashed lines show the transition wavelengths of the He I triplet lines.

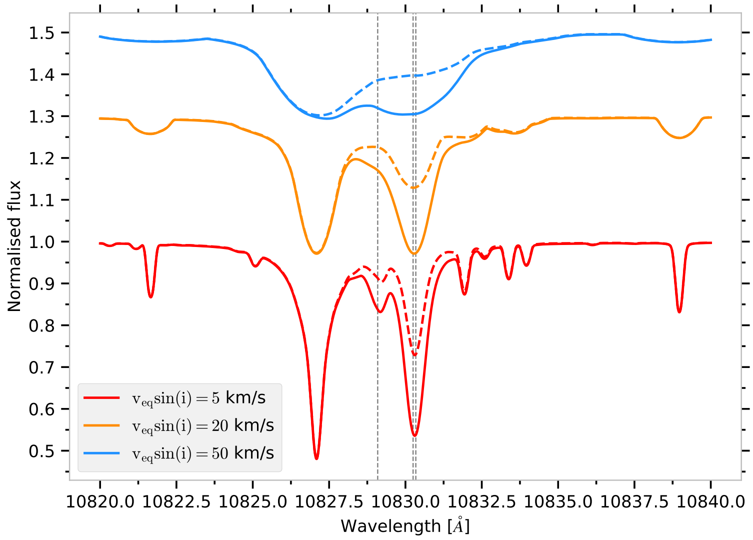

Fig. 4.10.: Theoretical disc-integrated spectrum of the generic star for the three values of $v_{eq}\sin(i_*)$ and the two line depths models. The dashed lines show the models with shallow helium lines. The blue and orange curves were manually shifted along the y axis for more clarity. The vertical lines indicate the transition wavelengths of the He I triplet lines.

planet's radial orbital velocity track and the radial velocity of the occulted stellar surface during the transit. The exact amplitudes of the POLDs are also going to vary from one system to another. These present results should thus serve as an example of what to expect from stellar contamination in the He I triplet lines.

Finally, the POLDs might be negligible for strong absorption signatures of helium of several percents. Nevertheless, they could still impact the wings of the atmospheric signature, where the absorption is weaker. In order to be thorough and avoid any source of bias in the derived atmospheric parameters of the planet, I again emphasise the importance of accounting for stellar lines variations in transit simulations.

4.3 Proposal for an observational campaign to detect planetary helium absorption

In the course of my thesis, I had yet to have the opportunity to apply and test the EVE code to observational data sets of young stars. Even though there is a large amount of data on classical and weak-line T Tauri stars available in the group I am part of, these data are not focused on detecting transiting planets and, therefore, were not exploitable with the EVE code. In order not to be limited to hypothetical exploration with the model, I studied the feasibility of detecting and interpreting planetary helium signatures with the EVE code around young stellar objects. This

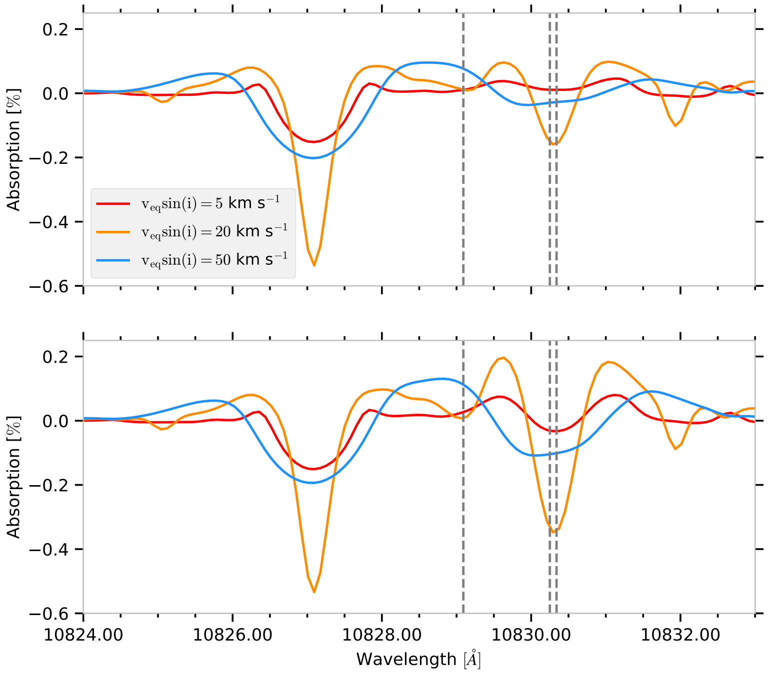

Fig. 4.11.: Mean theoretical absorption spectrum between contact times T_2 and T_3 without atmosphere as a function of wavelength in the planetary rest frame. **Upper panel**: for the shallow He I triplet lines case. **Lower panel**: for the deep He I triplet lines case. The grey vertical dashed lines show the transition wavelengths of the He I triplet lines.

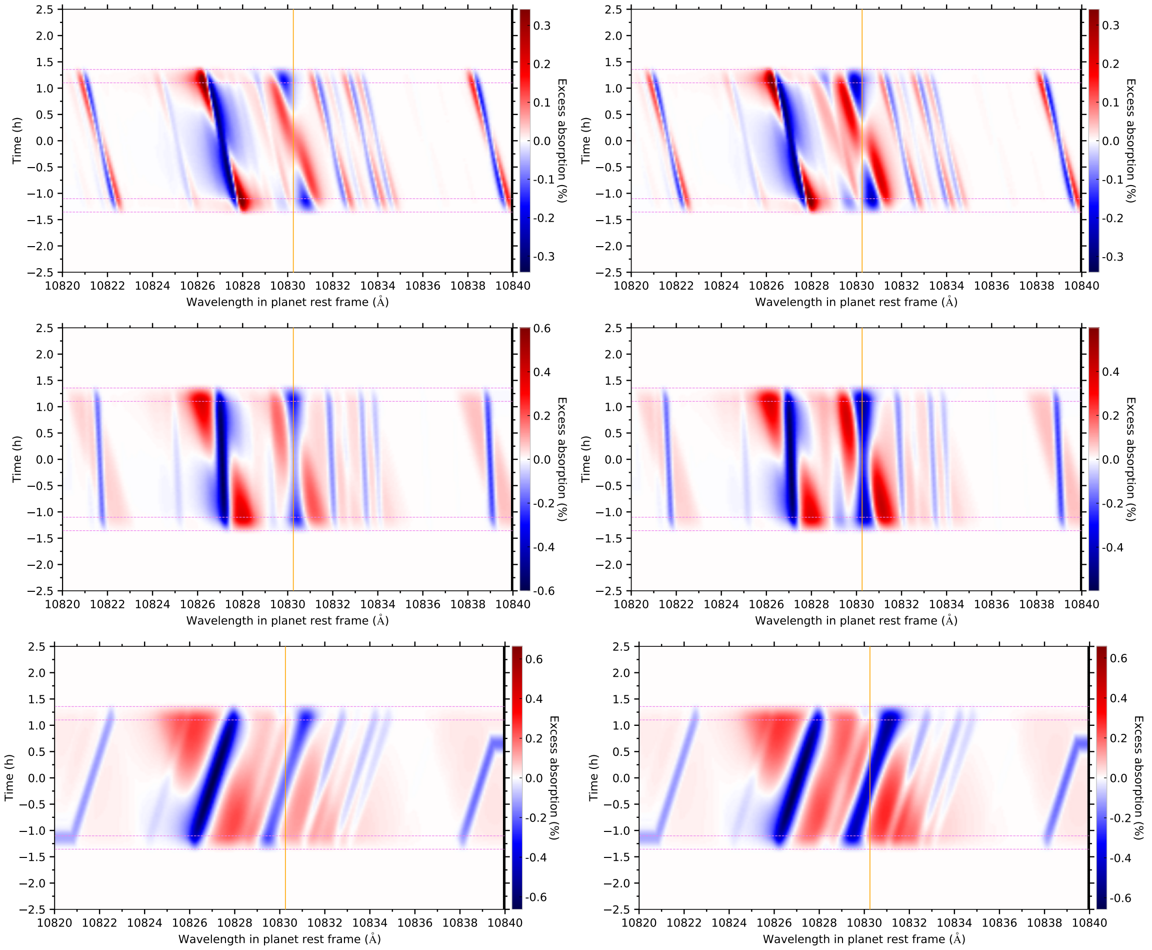

Fig. 4.12.: Theoretical absorption spectrum of the generic planet without atmosphere as a function of time and wavelength in the planetary rest frame. Left row: shallow He I triplet lines. Right row: deep He I triplet lines. Upper, middle and lower panels: $v_{eq} \sin(i_*)$: 5, 20 and 50 km s^{-1}, respectively.

involved writing a proposal to obtain transit observations of V 1298 Tau b (David et al. 2019), a planet in orbit around a weak-line T Tauri K-type star of about 23 Myr old. Based on the parameters of the system, we believed this planet to be a promising candidate to detect planetary atmospheric helium absorption.

I submitted this proposal in March 2022 to the Canada-France-Hawaii Telescope (CFHT). The objective was first to detect atmospheric absorption signatures in the He I infrared triplet at 10830 Å during the transit of the planet and then to study the dependence of this signature on the stellar activity.

The choice of this target was also motivated by a few attempts that had been made at detecting transit atmospheric absorption on this planetary system. Vissapragada et al. (2021) found no signs of excess He I absorption during the second half of the transit while Gaidos et al. (2022) found a decrease of the equivalent width of the He I triplet that, interestingly, started before the white light (photometric) transit and ended approximately at mid-transit. Both observations are, therefore, compatible and hint at an atmosphere that absorbs upstream of the planetary body. This unusual observation suggests that the escaping atmosphere may have an intriguing structure that could be caused by significant interactions between the star and the planet (e.g. Matsakos et al. 2015; Strugarek et al. 2019; Vidotto & Cleary 2020).

I had requested observation time at two different epochs, spaced about four months apart, to allow for changes in the star's activity. At each of these epochs, I asked for a series of observations of the star with SPIRou in spectropolarimetric mode spanning several days around the transit, in order to map and reconstruct the stellar surface magnetic field. Additionally, I requested observations of the planetary transit during each epoch to have contemporaneous stellar activity to the planetary signature. We could then have used this information to search for connections between stellar activity and the variations in atmospheric absorption signatures if detected and confirmed. The proposal received an encouraging feedback from the time allocating committee, citing its clear objectives, innovative approaches and interesting observation strategy. However, the two transits for which we requested observing time, fell during dark night periods. This meant that SPIRou was not mounted at that time on the CFHT and that observing time could not be scheduled and allocated.
I had estimated the ephemerides for the next two years. It revealed that there were no other forthcoming transits as adequate as those we had selected. We, therefore, plan to resubmit this proposal whenever a similar configuration as the one I described occurs.

A copy of the CFHT proposal can be found in Sect. D.

4.4 Conclusion

In this chapter I presented a model I developed to reconstruct the local metastable He I triplet stellar line profiles from the disc-integrated spectrum of a star. This was motivated by the fact that the metastable He I triplet lines cannot be modelled from MARCS photospheric models as these lines generally form in the chromosphere of stars. As I argue that planet-occulted line distortions should always be considered in the analyses of planetary transit absorption spectra, I developed this model to derive an estimate of the local line profiles of the He I triplet, which allows me to include these line profiles in the synthetic stellar spectral grids used as inputs in the EVE simulations. With this tool, EVE simulations can now account for the local variations of the He I triplet line profiles across the stellar disc and thus for the induced planet-occulted line distortions in the absorption spectra of the transiting planet.

The first version of this model was used in Guilluy et al. (2023) to estimate the POLD in a series of absorption spectra of diverse exoplanets. I have since then improved the model to account for more physics, which I explained throughout this Chapter. I plan to continue refining this model in terms of speed and physics. For example, another conceivable improvement that could be brought to the model in the future is to consider a similar approach as the one used in the *p-winds* code (Dos Santos et al. 2022) to compute the populations of the helium levels more coherently in the chromospheric layers based on the XUV flux of the star. The model could easily be modified to account for sub-layers within the two main layers in order to accommodate a non-constant density profile in the helium lines' formation region. Still, this version should be tested against loss of computing rapidity and to ensure it improves the results. The model could also be run on observations of the Sun for which we have access to both the disc-integrated and local spectra. This could help further validate the accuracy of the model.
The model I presented still lacks much physics, and there are studies that use more sophisticated models that include all the relevant physical processes to compute the He I triplet line formation in stellar atmospheres (see for example, Asensio Ramos et al. (2008); Hintz et al. (2020) and HAZEL2). Still, these sophisticated models demand, in general, heavy computational resources that are not always suited for fitting of observations. My goal, ultimately, is to make this tool light and available to the community so that others can use it to predict the POLDs they should expect in their absorption spectra. Although I made some strong assumptions in developing this tool, it captures the essential physics necessary to give first-order estimates of the POLDs around the He I triplet lines. In the future, it will help the exoplanet community to better interpret the helium absorption signatures, relevant for the study of planetary atmospheric escape.

5

Planets transiting T Tauri stars

The growing number of confirmed exoplanets suggests that a large proportion of stars actually host a planetary system (Borucki 2017). There is thus a keen interest in the community to try to explain how these planetary systems can form, seemingly so easily, in the circumstellar disc of gas and dust surrounding young stars (Baruteau et al. 2016). Interestingly, by looking at planetary systems statistics, e.g. exoplanet.eu, it appears that most planets detected so far have a semi-major axis that falls around or below 0.1 AU, with a significant portion of them having masses similar to the gas giants of our solar system. These statistics somewhat contrast with the architecture of the solar system as its closest planet, Mercury, has a semi-major axis of ∼0.38 AU and is about 10 000 times lighter than Jupiter.

Studying planets and their atmosphere right after their birth allows for an insight into their initial conditions and is complementary to the large number of studies on main-sequence stars' planets, which allow for comparisons with the solar system. Delving into the realm of nascent planets is a judicious approach to help build an exhaustive understanding of planetary systems' evolution. In this chapter, I address the issue of studying transiting nascent planets around young stellar objects.

It is commonly considered that a star forms after a nebulous pre-stellar core of gas and dust undergoes an external perturbation and condenses under its own gravitational force (Shu 1977; Motte et al. 1998; Andre et al. 2000; Roggero 2021). The centre of this condensing cloud starts to heat up under growing pressure and, by conservation of angular momentum, a rotating disc structure starts to form around the central core. After about one million years, most of the initial matter of the cloud has been accreted, ejected or has formed into the star and the rest has settled into the disc structure around the central core. This surrounding disc structure of gas and dust is often called a circumstellar or protoplanetary disc. At this moment, the star is considered to be born and becomes visible: it has entered what is referred to as the classical T Tauri star (cTTs) phase. After approximately a few million years, the star has accreted most of the circumstellar disc of gas and dust remaining from the original pre-stellar core. The star continues to contract and eventually leaves the pre-main sequence stage of its life and enters the main sequence stage.

These young stellar objects are very complex systems with many physical phenomena that happen in their close environment and that are not present on main-sequence stars. They usually have strong magnetic fields, typically around 1 to 3 kG (Donati & Landstreet 2009) against up to ~10 G for the Sun-as-a-star (Vidotto 2016). The magnetic field of cTTs is strong enough to disrupt the inner edge of the circumstellar disc. This creates accretion columns that channel the matter along the magnetic field lines onto the stellar surface where an accretion shock forms (Hartmann et al. 2016). The bases of these magnetospheric accretion columns deform the inner disc's edge into what is called a warp (Bouvier et al. 1999). These warps are mostly optically thick because of the dust they contain. The presence of these warps on the inner disc's edge is the cause of the observational phenomenon called dippers. Dippers usually occur at high inclination when the observer's line-of-sight is grazing the surface of the circumstellar disc and when the opaque warp, rotating with the disc, crosses its path, see, for example, Figure 6 and Figure 7 of Bodman et al. (2017). This phenomenon is the leading cause to explain the strong dips visible in the lightcurves of some young stellar objects (Bouvier et al. 1999; McGinnis et al. 2015; Bodman et al. 2017; Roggero et al. 2021; Roggero 2021).

The phenomenon of dippers occurs in a specific configuration and, therefore, seems to be unlikely. However, there have been statistical studies on samples of young stellar objects showing that between 20 to 40% of these objects are, in fact, in a dipper configuration (Alencar et al. 2010; McGinnis et al. 2015; Cody & Hillenbrand 2018; Wang et al. 2023). Furthermore, this configuration appears to be the most promising to hope to detect a planet transiting a classical T Tauri star. Indeed, as planets form in the circumstellar disc, chances are rather low that they exit the plane of the disc and enter on polar orbits for as long as the disc does not dissipate. Searching for transiting planets at low stellar inclination in such stars would likely be unfruitful. Likewise, searching for them at high stellar inclination would not offer more possibilities as the star is fully obscured by the disc in an edge-on view and, consequently, no transit is observable. Dippers thus seem to offer the best opportunities for hoping to catch any transiting planet and/or its escaping atmosphere, close to the inner disc's edge. It is worth mentioning that other phenomena, such as disc winds and stellar winds, stellar activity and accretion shocks, also take place in the vicinity of these objects and make them very complex to study. For a review on the physical phenomena taking place in the environment of cTTs see Hartmann et al. (2016). Accounting for all the star-disc interactions self-consistently is not an easy task and is out of the scope of this work. In this study, I focus only on the effect of the inner disc's warp on the planetary transit.

5.1 The impact of the inner disc's warp on absorption spectra

As I showed in the previous chapters, the stellar spectrum plays a major part in the study of transiting planets and in the characterisation of their atmosphere. However, if the inner disc's warp transits, a significant part of the stellar surface might be hidden. Therefore, the observed line profiles in the disc-integrated spectrum of the star are expected to be altered with respect to those of the unocculted disc-integrated stellar spectrum, similarly to brightness inhomogeneities – such as dark spots – which can change the observed disc-integrated stellar line profiles (Queloz et al. 2001; Boisse et al. 2009). Yet, as I explained in Chapter 3, this spectrum is an important term in the computation of planetary transit absorption spectra. It is therefore expected that the planet-occulted line distortions in absorption spectra are going to be affected by the presence of the inner disc's warp. The goal of this section is to explore a hypothetical case where a planet transits a star partially occulted by an inner disc's warp and to assess its impact on the resulting absorption spectrum.

5.1.1 Description of the model

To take into account the presence of the inner disc and the warp, I start by defining the x, y and z coordinates of a circle that represents the inner disc's edge. These coordinates are defined in the stellar frame of reference where the x y plane is the stellar equatorial plane and z is aligned with the stellar rotation axis.

$$\begin{aligned} x_*(\theta) =& R_I \cos(\theta) \\ y_*(\theta) =& R_I \sin(\theta) \\ z_*(\theta) =& 0, \end{aligned} \tag{5.1}$$

with R_I the inner radius of the disc and θ the azimuth angle. The disc's rotation axis is aligned with the star's rotation axis.

In order to define the value of each z coordinate or the height variation $h(\theta)$ of the warp along the inner edge of the disc, I use Eq. 1 of McGinnis et al. (2015), which is written as,

$$z_*(\theta) = \begin{cases} h_{\text{max}} \left| \cos\left(\frac{\pi(\theta-\phi_0)}{\phi_w}\right) \right|, & \text{if } -\frac{\phi_w}{2} \leq \theta \leq \frac{\phi_w}{2} \\ 0, & \text{otherwise,} \end{cases} \tag{5.2}$$

with h_{max} the maximum height of the warp, ϕ_0 the azimuthal position of the top of the warp and ϕ_w the azimuthal extension of the warp. The value of h_{max} is set to be 25% of the inner radius of the disc. This value is representative of the ratio measured for classical T Tauri stars as reported in Table 3 of McGinnis et al. (2015).

In this study, I chose $\phi_w = 180°$, which means that the warp is defined on half of the disc's inner edge. This value is typical for the extension of the warp as per McGinnis et al. (2015), although their finding suggests a broader extension on average. The maximum height of the warp is aligned with the line of sight when $\phi_0 = 0$.
Finally, using the inclination of the stellar rotation axis with respect to the line of sight of a distant observer, I convert the coordinates of the inner disc from the stellar reference frame to the observer's reference frame. The coordinates of a point on the inner edge of the disc in the observer's reference frame are written as,

$$\begin{aligned} x_{obs}(\theta) &= x_*(\theta)\sin(i_*) + z_*(\theta)\cos(i_*) \\ y_{obs}(\theta) &= y_*(\theta) \\ z_{obs}(\theta) &= -\,x_*(\theta)\cos(i_*) + z_*(\theta)\sin(i_*), \end{aligned} \tag{5.3}$$

with i_* the stellar inclination. From the simple geometric configuration shown in Figure 5.1, we can determine the maximum angle, $i_{*,max}$, at which we can observe the star without being hidden by the outer disc. It is given by,

$$i_{*,max} = \arctan(\frac{R_O}{H_O + R_*}) \tag{5.4}$$

with R_O and H_O, the outer radius and outer height of the circumstellar disc, respectively. In our case, with standard values of 100 AU for R_O, 10 AU for H_O and 2 solar radii for R_*, $i_{*,max} = 84.28°$. A ratio of 10 between the outer disc radius and its optically thick height is not an absolute value but is within reported measurements (Stapelfeldt et al. 1998; Villenave et al. 2020; Benisty et al. 2022). Our configuration also assumes that at grazing incidence, below the limiting angle ($i_* < 84.28°$), the disc remains optically thin. It is worth noting that the corresponding limit angle of $77°$ mentioned by McGinnis et al. (2015) and based on theoretical predictions by Bertout (2000), would require a semi-major axis of ~ 0.018 AU for the planet to have the same impact parameter as in the case with $i_* = 84.28°$. This semi-major axis value is still fairly acceptable as quite a number of exoplanets have been detected under 0.02 AU (exoplanet.eu). However, the outer disc might not always be an issue. Indeed, there have been observations of outer discs misaligned with the inner disc. For example, see Pinilla et al. (2018); Sicilia-Aguilar et al. (2020); Bohn et al. (2022). See also Roggero et al. (2021) who report stellar and disc inclination values that indicate misaligned outer discs. This implies that in some systems, the outer disc might not interfere with observations and that the star would be visible even at high inclination.
Figure 5.2 shows a sketch up to scale that represents the inclusion of the inner disc and the warp in the EVE code. The relevant parameters of the system are listed in Table 5.1.

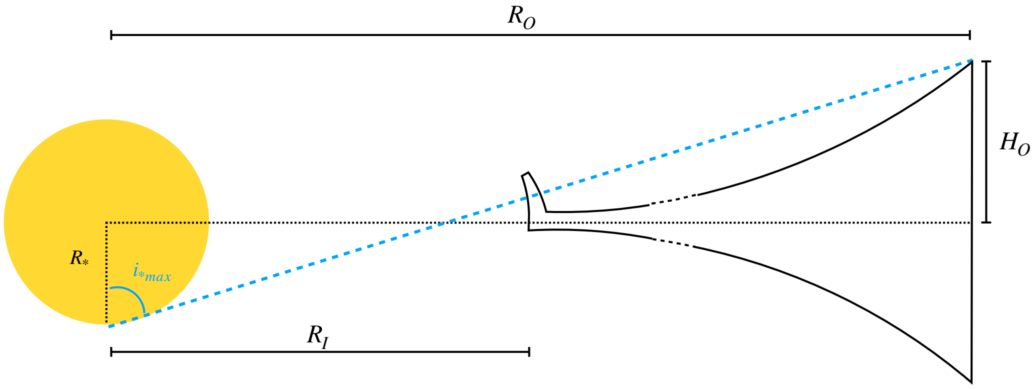

Fig. 5.1.: Geometrical configuration of a star and a circumstellar disc used to determine the maximal angle at which the star can be fully seen. This sketch is not to scale.

Tab. 5.1.: Stellar, disc and planetary properties of the generic system.

Parameter	Value	Parameter	Value	Parameter	Value
Stellar :		**Disc :**		**Planetary :**	
R_* ($R\odot$)	2	R_I (AU)	0.05	R_{pl} (R_{Jup})	1
M_* ($M_\odot$)	1	h_{max} (AU)	0.0125	M_{pl} (M_{Jup})	1
i_* (°)	84. 28	i_{disc} (°)	84.28	i_{pl} (°)	84.28
v_{eq} (km s^{-1})	20	R_O (AU)	100	Semi-major axis (AU)	0.04
		H_O (AU)	10	Period (days)	2.92
		ϕ_w (°)	180	λ_{pl} (°)	0

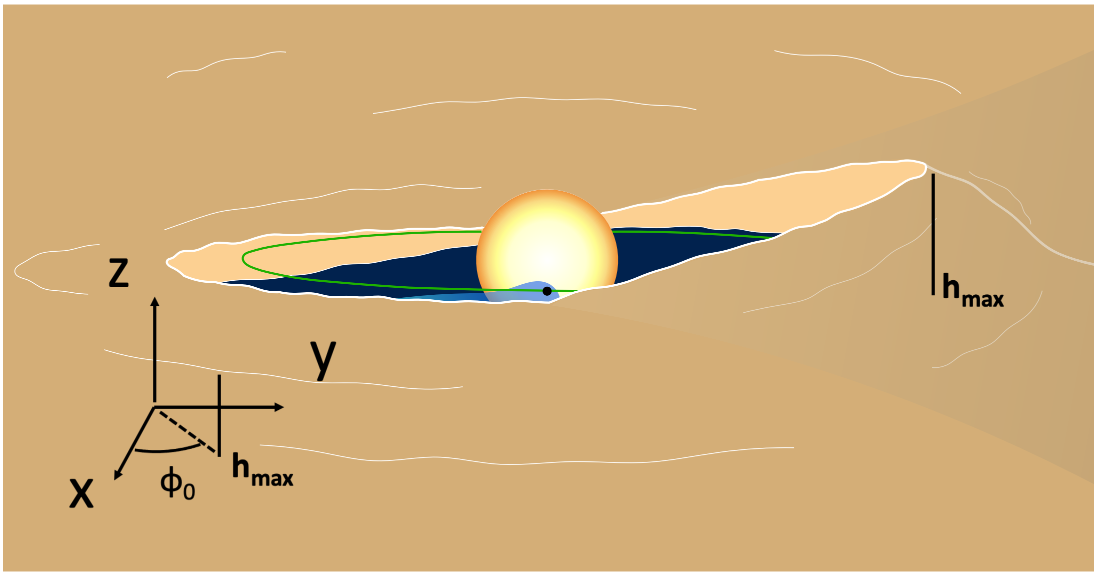

Fig. 5.2.: Sketch illustrating the inclusion of the inner circumstellar disc and the warp in the EVE code. The accretion column is not represented in this plot. The system is viewed under grazing incidence on the circumstellar disc with an inclination of 84.28°, the planetary orbit is in the plane of the disc, and the disc's rotation axis is aligned with the stellar rotation axis. $\phi_0 = 90°$ in this image. ϕ_0 is counted positively counterclockwise. This image is to scale and is zoomed on the inner regions of the disc.

5.1.2 Impact of the inner-disc's warp on POLD

A major change when including the presence of the inner disc's warp concerns, $\mathrm{F}_{\mathrm{out}}$, the disc-integrated stellar spectrum. Indeed, the warp occults a part of the star that is non-symmetrical with respect to the rotation axis of the star. This means that depending on the ϕ_0 value, there will be more or less of the red, respectively blue, shifted regions of the star that will be missing (see Figure 5.3). The Doppler-shifted lines emerging from these hidden regions will therefore not be accounted for in the disc-integrated spectrum. The lines in $\mathrm{F}_{\mathrm{out}}$ will thus exhibit a skewed and altered profile compared to the lines in the unocculted $\mathrm{F}_{\mathrm{out}}$ as can be seen in Figure 5.4. As $\mathrm{F}_{\mathrm{out}}$ intervenes directly in the computation of the absorption spectrum of a planetary transit, it is expected that the absorption spectrum is also affected by the presence of the disc.

To study the effect of the inner disc's warp on distortions of the absorption spectrum, I simulated the transit of a generic planet for four different orientations of the warp, namely $\phi_0 = 82.5, 85.0, 87.5$ and $90.0°$. The system parameters used for the simulations are listed in Table 5.1. The stellar grid spectrum used was computed for a temperature of 7500 K, a log g of 4 cm s^{-2} and a metallicity of 0. Figure 5.4 shows $\mathrm{F}_{\mathrm{out}}$ around the Na I D2 line for the four different positions of the warp. I use the Na I line again to be consistent with Chapter 3, but also because the Na I D2 line of the case without a warp exhibits a strong and overall symmetrical profile. It is thus

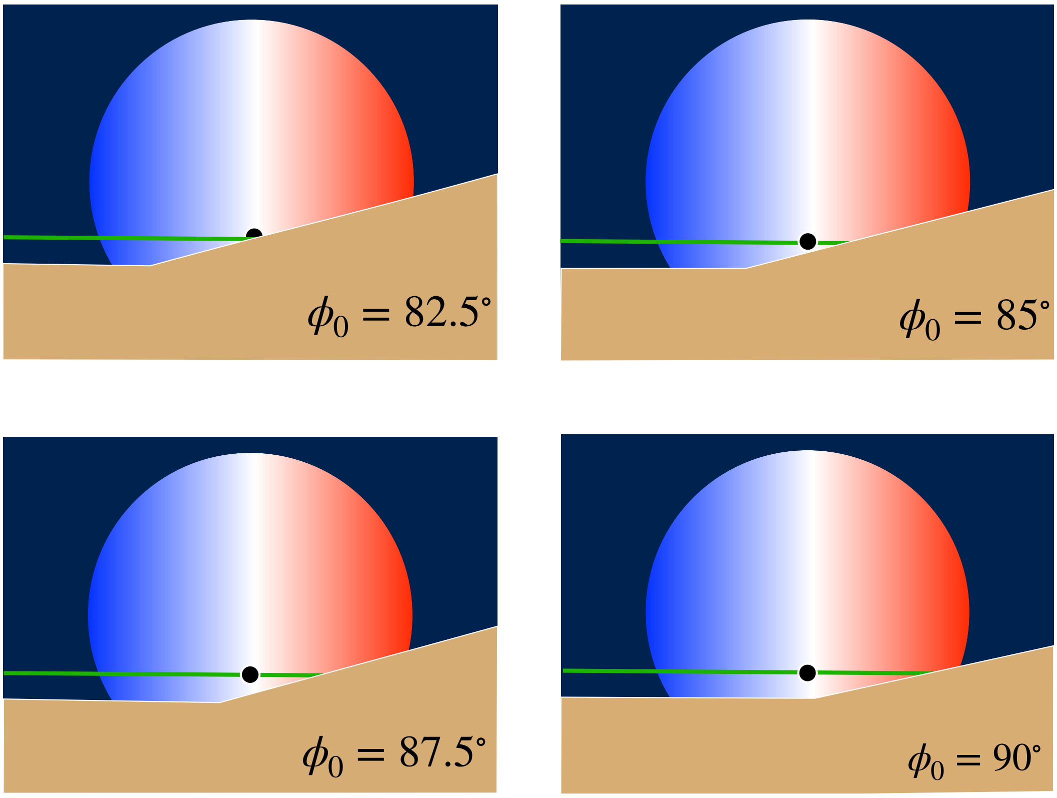

Fig. 5.3.: Close-up view of Figure 5.2 for $\phi_0 = 82.5, 85.0, 87.5$ and $90.0°$.

a good reference to highlight the changes in the line profile that the presence of the warp could induce. There is a visible decrease in the absolute flux level with respect to the case without a disc, which is expected as a large portion of the stellar surface is occulted. A visible change in their shape is also noticeable, but to understand the actual impact of the warp on the line profile and have a better idea of the difference between each case, it is more adequate to look at Figure 5.5.

This figure shows the difference between $\mathrm{F}_{\mathrm{out}}$ with and without the presence of the warp for the four ϕ_0 angles. The reddish curves correspond to when the warp occults more of the redshifted part of the star. For the case of $\phi_0 = 82.5°$, the difference is the strongest because the warp occults a larger surface of the star than any of the other cases (see Figure 5.3). The difference is also the most shifted redward for this case because more of the redshifted stellar surface is hidden than in the other cases; therefore, the disc-integrated line profile is missing a larger part of the redshifted local spectra. As the warp occults less the star for the other ϕ_0 angles, this difference attenuates and is less redshifted. Analogous observations are made when the warp occults more of the blue-shifted stellar surface (see blueish curves).

For a specific time step, the planet-occulted spectrum (the absorbed spectrum) is the same, independently of the position and of the presence of the warp or not (for as long as the warp does not occult parts of the planet-occulted stellar region). We

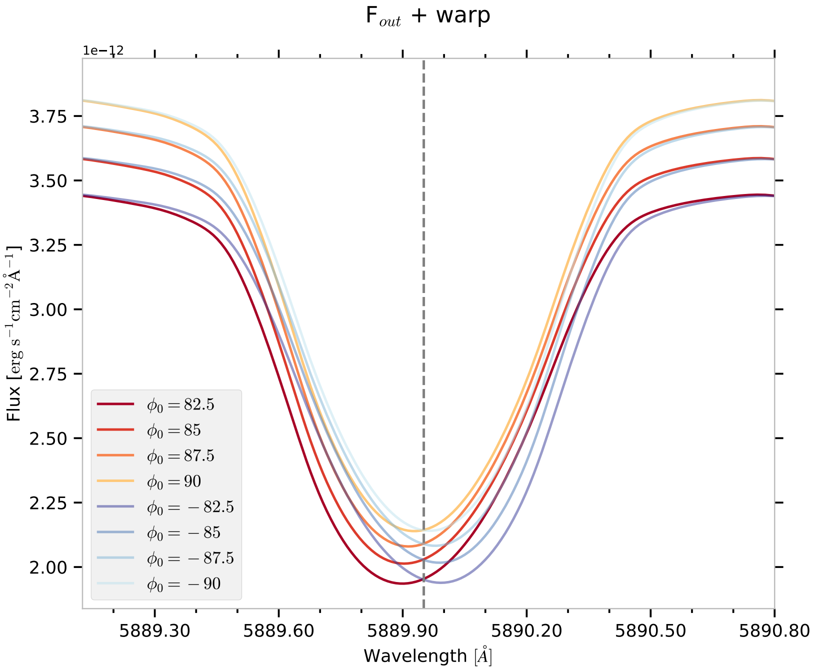

Fig. 5.4.: F$_{\text{out}}$ occulted by the inner disc's warp as a function of wavelength. The vertical dashed grey line shows the position of the rest wavelength of the Na I D2 line. The case without a disc is not displayed because its continuum level is too large compared to the other spectra, and the figure would be unclear.

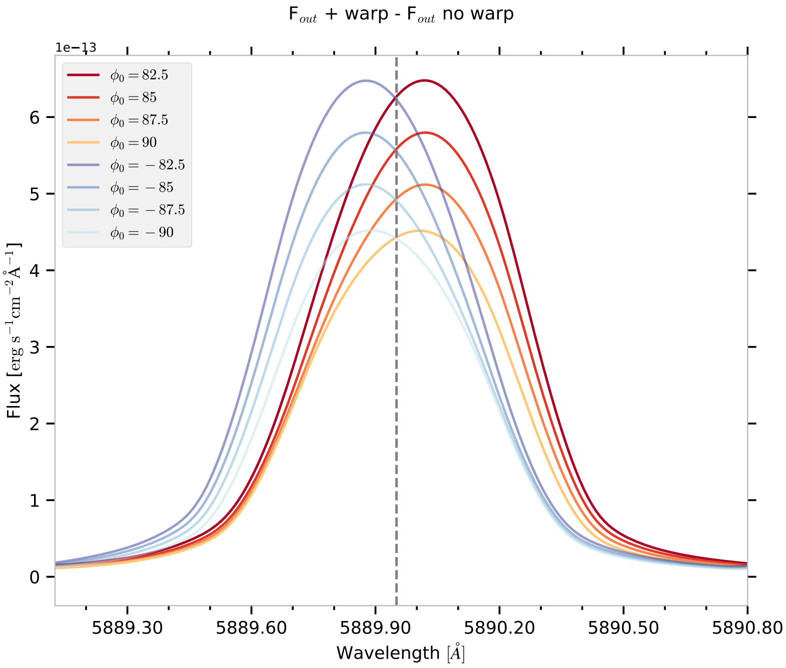

Fig. 5.5.: Flux difference between F$_{\text{out}}$ occulted by the inner disc's warp and F$_{\text{out}}$ without the warp, as a function of wavelength. The vertical dashed grey line shows the position of the rest wavelength of the Na I D2 line. All the continua were subtracted by hand to make the comparison between the different cases clearer.

can thus compare the absorption spectrum at one time step so that we can isolate the effect of the change in the line profile of F_{out} due to the warp. Figure 5.6 shows the absorption spectrum computed for the different cases a few time steps after T_2. The only difference with the case without the warp is thus in the line profile of F_{out}, and we can see that it has the effect of increasing the amplitude of the POLD in the absorption spectrum.

Another difference with respect to the case without a warp is that the duration of the visible planetary transit changes when the warp is included in the simulation, as for a certain number of exposures, the planet is behind the occulting warp. Figure 5.7 shows the lightcurves for the different cases. Figure 5.8 shows the temporal evolution of the absorption spectrum for each case. When computing the mean absorption spectrum, depending on the different positions of the warp, not all the same distortions are accounted for. Figure 5.9 shows the resulting mean absorption spectrum for the different cases. The mean POLD has a different overall shape compared to the case without the warp. In addition, it is worth noting that for cases with less visible exposures, one should expect lower SNR (this is not shown in these simulations). For the case at $\phi_0 = 82.5°$ (the one with the least visible exposures), the peak-to-peak amplitude of the POLD approximately doubles with respect to the case without the disc. Averaging the absorption spectra over the expected total duration of the planetary transit risks introducing additional bias, as exposures that do not contain planetary absorption could be included.

5.2 Motion of the inner-disc's warp

In the previous sections, I made the assumption that the inner disc's warp was static during the transit of our test planet. However, if we consider that the inner edge of the disc is at a radius equal to the co-rotation radius, then this assumption cannot be easily satisfied. It implies that, depending on the stellar rotation period, the warp could move significantly during the planetary transit. Having the inner edge of the disc at the co-rotation radius is not uncommon in accreting T Tauri stars (D'Angelo & Spruit 2012; Stauffer et al. 2015; Alencar et al. 2018). This will naturally have an impact on the line profiles of the disc-integrated stellar spectrum, which will thus vary in time. It means that the usual technique I have used throughout this work to compute the absorption spectra of transiting planets is less straightforward in such cases. Indeed, the out-of-transit spectrum is not a relevant quantity anymore. Depending on the rotation period of the inner disc, the stellar disc-integrated line profiles can change during the out-of-transit exposures duration. Averaging the spectra of the out-of-transit exposures could lead to further bias in the line profiles. Furthermore, the line profiles of the disc-integrated spectrum

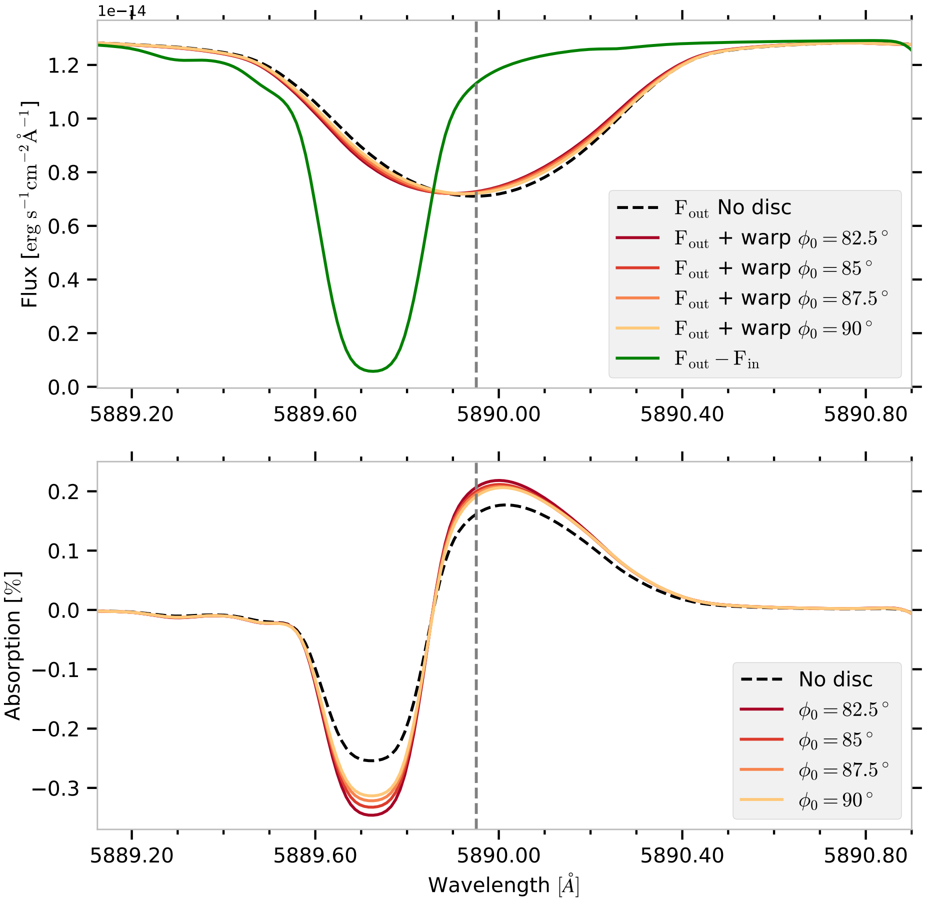

Fig. 5.6.: Absorption spectra of the generic case for different positions of the warp. **Upper panel**: planet-occulted spectrum after T_2 and F_{out} as a function of the series of the ϕ_0 angles. **Lower panel**: absorption spectra after T_2 as a function of the series of positive ϕ_0 angles. For the lower panel, the respective continua of the absorption spectra were subtracted to make them comparable. For the upper panel, the F_{out} were multiplied by the ratio between the planet-occulted surface and the unocculted stellar surface to make them comparable.

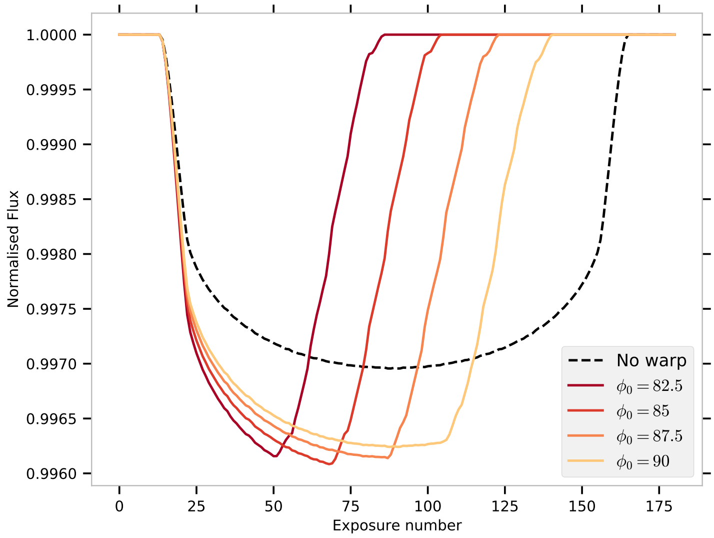

Fig. 5.7.: Lightcurve of the transit of the generic planet for the different ϕ_0 angles. The lightcurve was computed from 5882 Å to 5902 Å. The apparent step features are caused by the stellar and planetary grids that were slightly too coarse, but it does not change the result and interpretations. The flux is normalised to its out-of-transit value (i.e. occulted by the warp but not by the planet).

outside of the transit could be different from those of the unocculted (by the planet) disc-integrated spectrum during the transit, which makes it non-useful for absorption spectra computation. A possible solution to this issue would be to directly fit to the observations a model like EVE including a moving warp during the transit. Each out-of-transit and in-transit exposure should be fitted in order to determine the position of the warp during the transit of the planet. That way, with an adequate stellar model, we could reconstruct the disc-integrated line profiles during the transit of the planet and compute absorption spectra for all the in-transit exposures. I have adapted the EVE code so that at each time step, it can compute the position of the inner disc's warp based on its architecture and angular velocity. The code then computes the projection of the warp onto the stellar surface and absorbs all the spectra from the cells behind the warp.

Assuming that the warp is at the co-rotation radius, if we change the stellar rotation period, the inner disc radius will also be modified as per Kepler's third law of planetary motion. This means that the projection of the inner disc's warp onto the stellar surface changes if the rotational period of the star is modified. It is thus interesting to study the effect of the warp on planetary transits as a function of the stellar rotational period for the dippers configuration.

I chose four different stellar rotational velocities for the following examples, which are $\mathrm{v_{eq}}\sin(i_*)$: 6.75, 10.00, 20.00 and 30.00 km s^{-1}. With a stellar radius of two solar radii, it gives rotational periods of about P_*: 15, 10, 5 and 3 days, respectively.

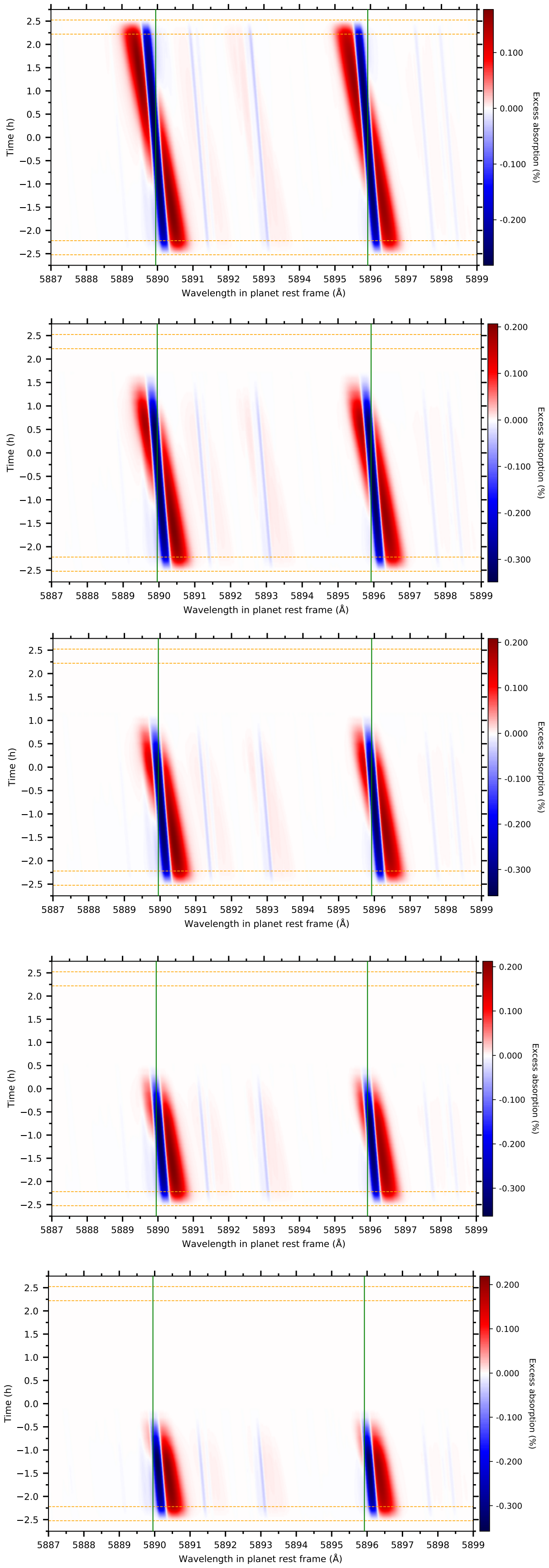

Fig. 5.8.: Theoretical absorption spectrum of the generic planet without atmosphere as a function of time and wavelength in the planetary rest frame for the different positions of the warp. **Upper panel**: no warp. **Upper middle panel**: $\phi_0 = 90°$. **Middle panel**: $\phi_0 = 87.5°$. **Lower middle panel**: $\phi_0 = 85°$. **Lower panel**: $\phi_0 = 82.5°$.

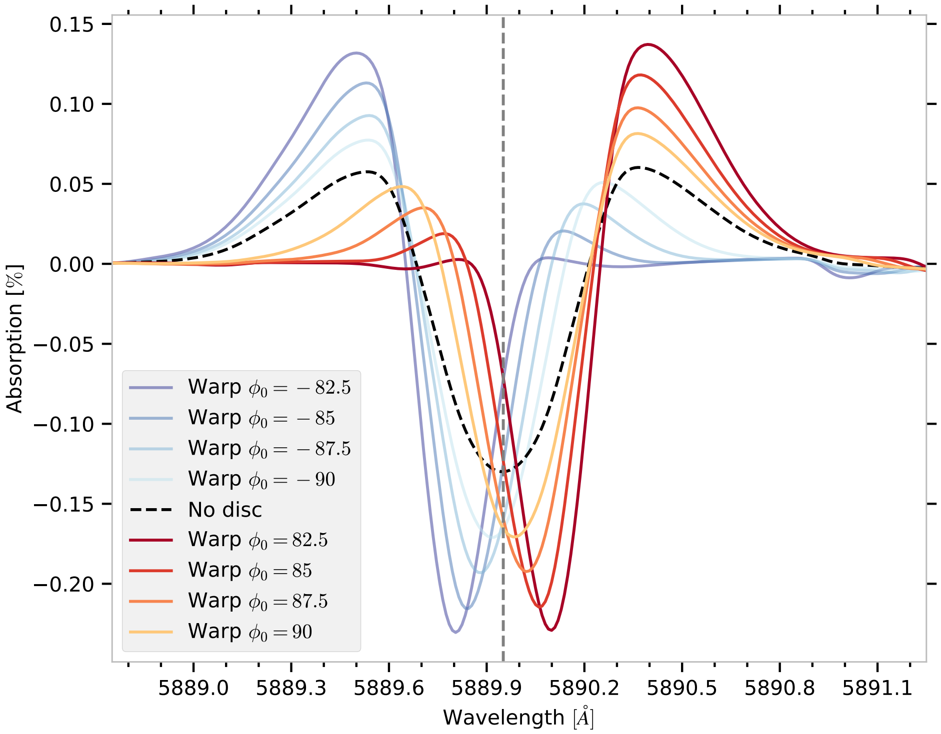

Fig. 5.9.: Mean theoretical absorption spectra of the generic planet for different positions of the warp as a function of wavelength in the planetary rest frame. The vertical dashed grey line shows the position of the rest wavelength of the Na I D2 line. The means are calculated over exposures when the planet in not hidden by the warp and is fully in transit.

These values are representative of typical rotation period values for classical T Tauri stars (Bouvier et al. 2014; McGinnis et al. 2015; Rebull et al. 2020; Roggero et al. 2021).

Considering Keplerian rotation of the inner disc and that its mass is negligible compared to the stellar mass, we get values for the inner radius of the disc (i.e. co-rotation radius) of about: 0.119, 0.092, 0.058, 0.044 AU. I also chose to keep a constant ratio between the height of the warp and the disc's inner radius ($h_{max}/R_I = 1/4$, Sect. 5.1.1). It means that the height of the warp increases with the disc's inner radius. This is acceptable because for an inner disc's edge that is further from the star, the magnetic field lines that allow the accretion column to form go higher above the rotation plane of the disc (Hartmann et al. 1994). Also, as the matter at the base of the accretion columns, which forms the warp, is further from the stellar surface, the dust can survive longer in the accretion column (Nagel & Bouvier 2020). In Figure 5.10, I show the projection of the inner disc's warp onto the stellar surface for these four different rotational periods, at phases $\phi_0 = 0$ and $90°$. In Figure 5.11, I show the variation of the Si I[1] line at 10827 Å during the entire rotation cycle of the inner disc for the case with $P_* = 5$ days. The variation is illustrated in terms of the spectral position of the minimum and of the half-maxima values inside the line. The difference between the half-maxima values represents the full width at half maximum. This figure gives an idea of how the line profile is deformed because of the occultation of the star by the warp during one rotation cycle.

To estimate the chances of having a detectable planetary transit in the dipper configuration, I simulated a series of approximately 72 planetary orbital periods for each inner-disc rotational period introduced above with a time step of 0.1 hour. Apart from the parameters discussed in the paragraph above, I kept the values of the other parameters introduced in Table 5.1. For each time step, I computed the percentage of the stellar surface occulted by the inner disc's warp. For the time steps when the planet was transiting, I checked if the planet was visible or hidden by the warp. The simulations started at the T_0 of the planet and for a $\phi_0 = 90°$.
The results of these simulations are shown in Figures 5.12. and 5.13. They only show the results over a duration of 50 days, that is about 18 planetary transits. These simulations have shown that 41, 41, 39 and 36 of the 72 simulated transits were detectable with the presence of an inner disc's warp, for P_* =15, 10, 5 and 3 days, respectively. The occurrence of the configuration in which both the planet and the warp are transiting simultaneously and the planet is detectable is rather rare. Therefore, with all the approximations that I made to construct the inner disc's warp, I can say, from these simulations, that a planet in transit in a system that includes an

---

[1] I chose to simulate the effect in this line as it exhibits a symmetrical profile. The spectral grid used was computed for a temperature of 4000 K, a log g of 4 cm s^{-2} and a metallicity equal to 0. These are typical values for classical T Tauri stars.

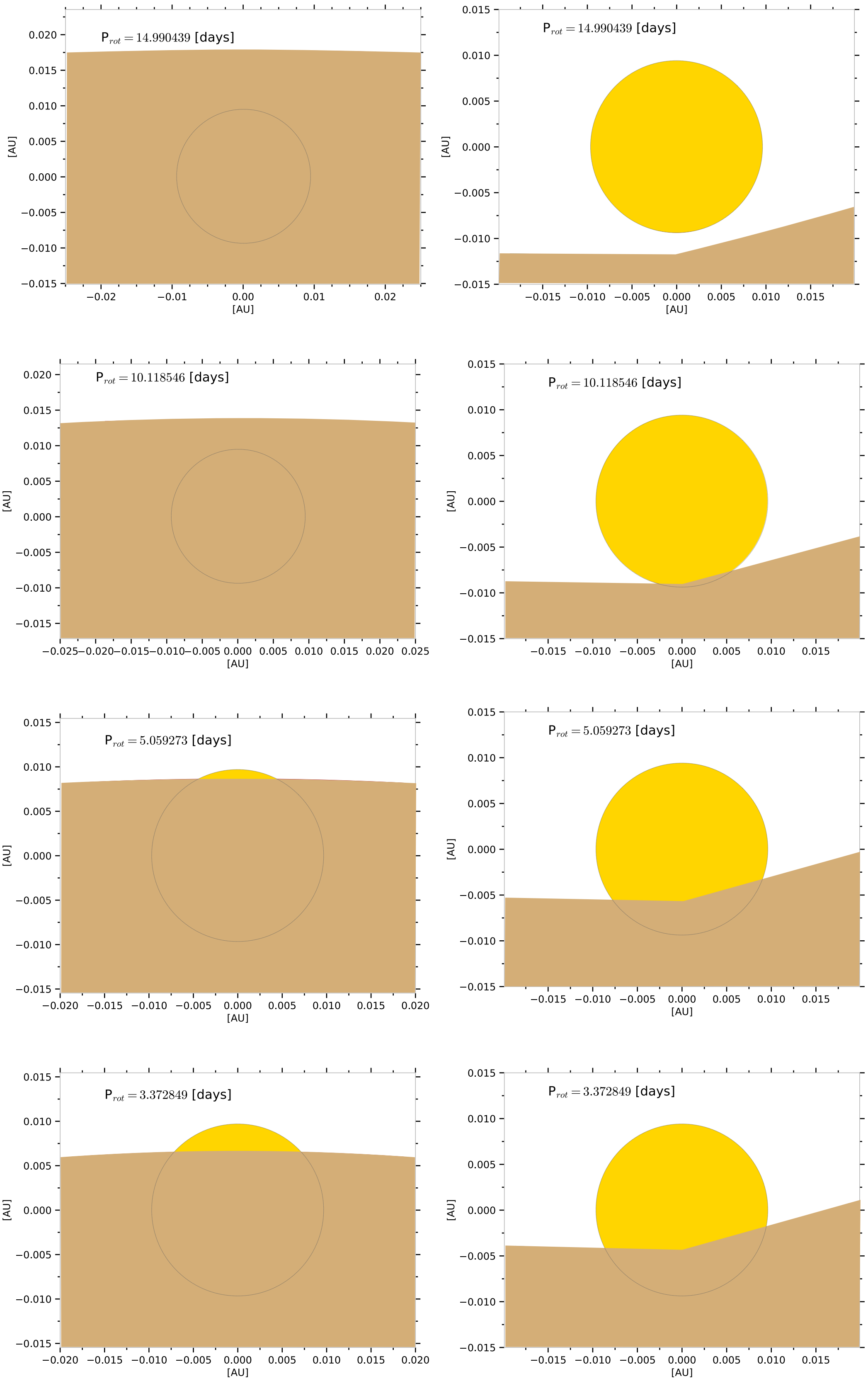

Fig. 5.10.: Warp-occulted stellar surface as a function of the rotation period of the star for the generic system. **Left panels**: ϕ_0, the position of the top of the warp was set to $0°$. **Right panels**: ϕ_0, the position of the top of the warp was set to $90°$.

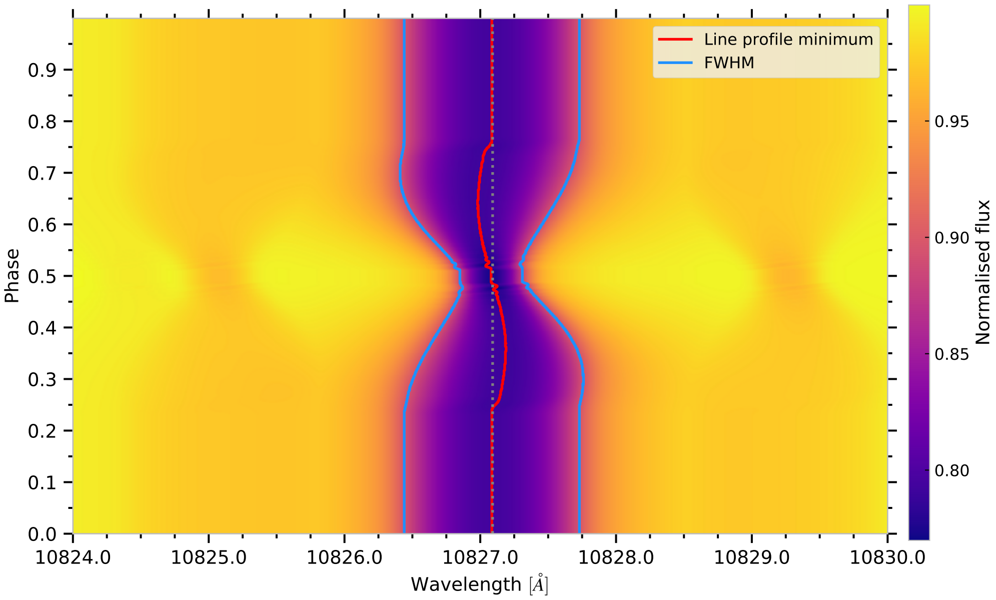

Fig. 5.11.: Evolution of the disc-integrated Si I line profile at 10827.091 Å during one rotation cycle of the warp with $P_* = 5$ days. The red curve shows the position of the minimum of the Si I line profile. The blue curves show the position of the half maxima of the line profile and represent the full width at half maximum of the Si I line profile. The colormap represents the normalised flux. Here, phase 0.5 corresponds to a $\phi_0 = 0°$ for the warp.

inner disc's warp, is detectable in about 50% of the transits. This, of course, holds for a warp with an azimuthal extension of 180° and the statistics might change with a different extension. The detectability of planetary transits in young stellar systems is, of course, affected by other aspects of classical T Tauri stars that I have not accounted for. The values of the statistics I gave are thus only indicative and would most probably diminish in more realistic simulations.

5.3 Conclusion

Young stellar objects are great laboratories to study nascent exoplanets and learn more about their conditions at the time of their formation. However, these objects are usually embedded in a circumstellar disc of gas and dust, which complicates the study of their planets with the transit method. There is, nevertheless, a window of action to study transiting planets in such stars. By observing the star at high inclination with a grazing incidence to the disc, one could hope to catch a transiting planet in the plane of the disc. In such configurations, the LOS grazing the outer regions of the disc is often intercepted by a deformation of the inner regions of the disc called a warp, causing a periodic occultation of the star and, thus, dips in their lightcurves. A star seen under these conditions is referred to as a dipper.

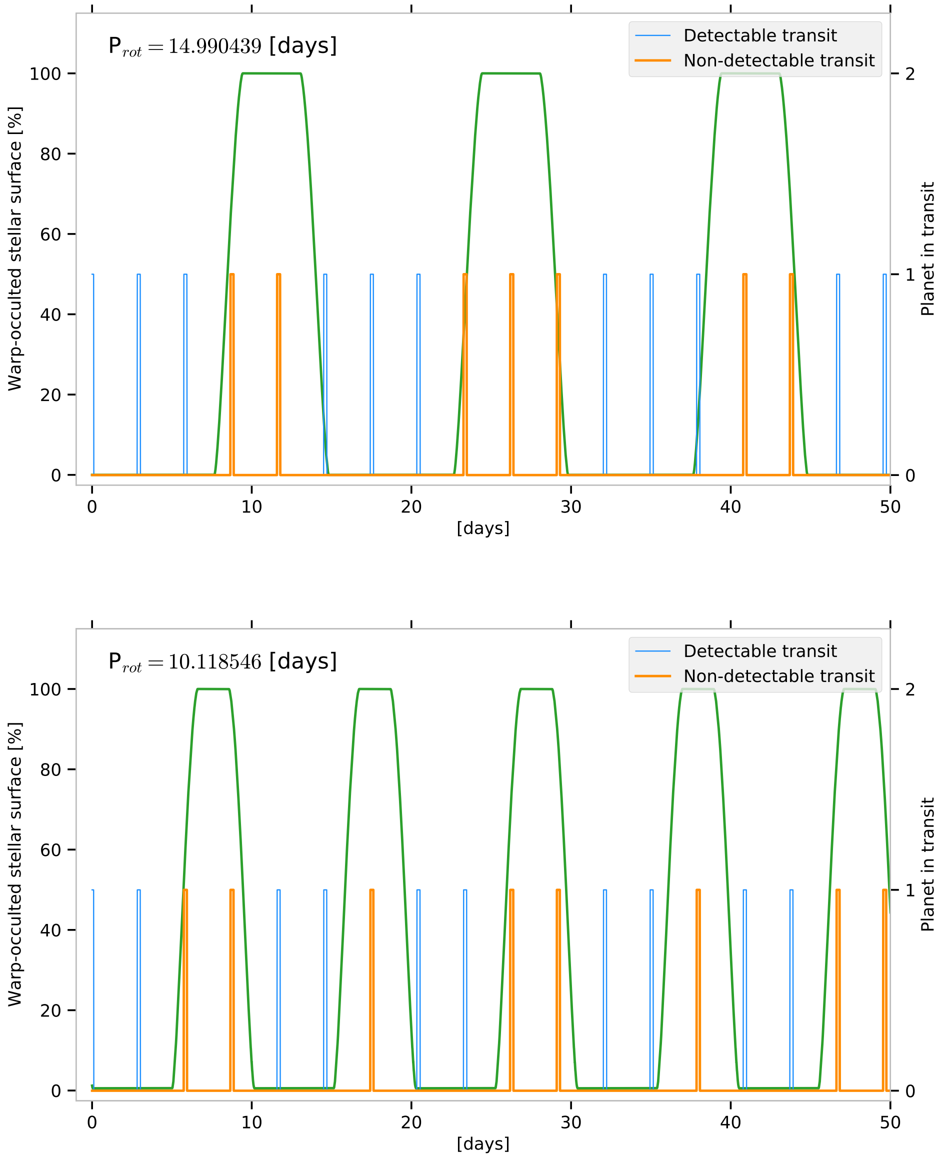

Fig. 5.12.: Percentage of the stellar surface occulted by the inner disc as a function of time for the rotation periods of 15 and 10 days. Overlaid are the transits of the planet, with values of one when the planet is transiting and zero when it is out of transit

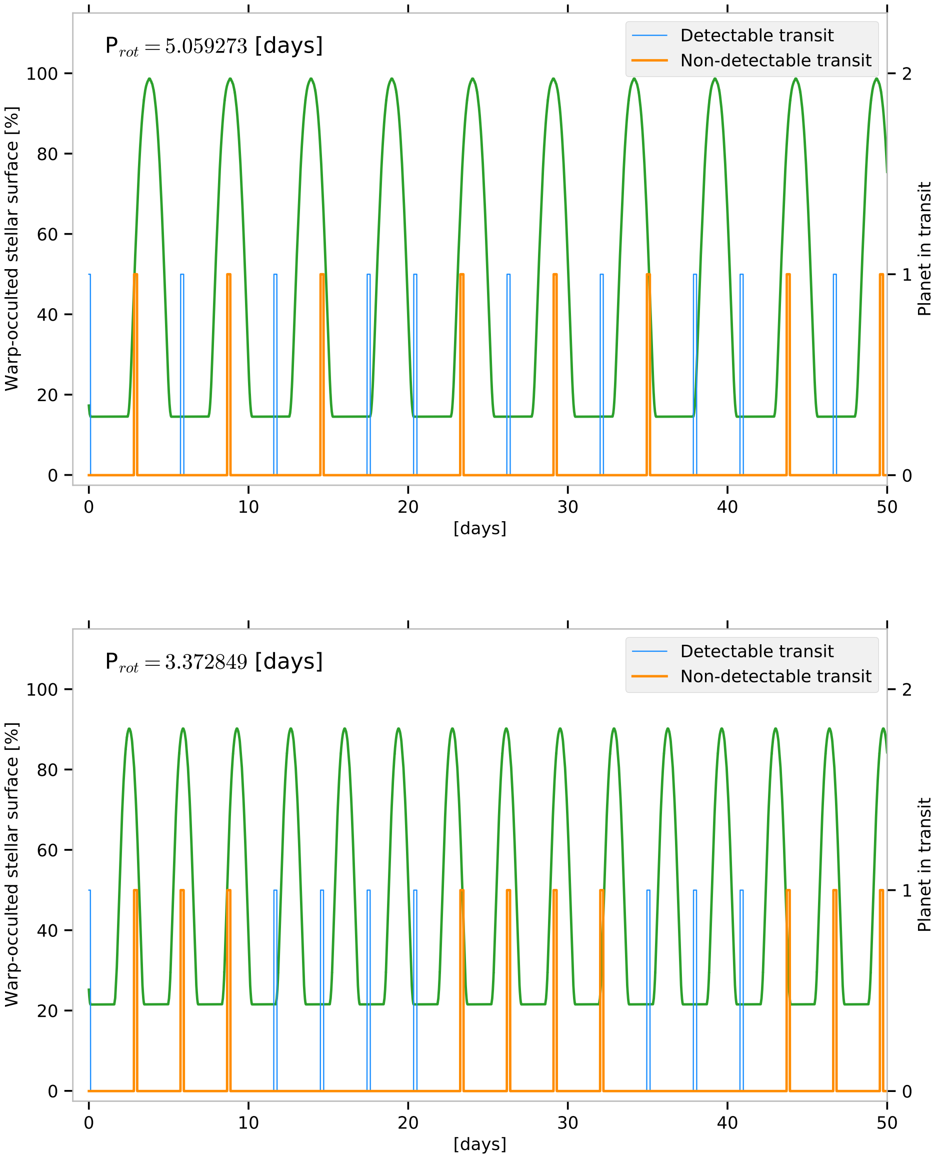

Fig. 5.13.: Same as Figure 5.12 for the rotation periods of 5 and 3 days.

I have adapted the EVE code to model dipper stars and to study the impact of an inner warp on planetary transits. In particular, the rotation of the warp during the planetary transit is taken into account. I have shown that the inner disc's warp can impact the absorption spectra of transiting planets. Mainly because the line profiles of the out-of-transit spectrum – used in the computation of transit absorption spectra – are deformed by the occulting warp. Consequently, the planet-occulted line distortions, which can affect absorption spectra, increase due to this deformation. This may hinder the potential characterisation of an atmospheric absorption signature in such observations. I have also discussed the fact that the warp, which is frequently found at the co-rotation radius, rotates significantly during the transit of close-in planets. This renders the analysis of planetary transit observations more complicated because the line profiles of the disc-integrated spectrum vary significantly over a rotation cycle of the warp. Computing a reference out-of-transit spectrum becomes irrelevant in such cases and the strategy of observation must be adapted.
The statistics I presented indicate that about 50% of planetary transits are detectable in the presence of a warp. However, these statistics are bound to change due to the delicate interplay between stellar rotation, warp geometry and planetary orbital architecture. Indeed, as McGinnis et al. (2015) showed, not only does the position of the top of the warp change over time, its height and azimuthal extension can be variable (by up to 10-20%) on a timescale of days. The occulted stellar surface by the warp can thus change significantly from one transit to the other, adding complexity to these types of studies. A more thorough exploration of these two parameters is foreseen, which should give new values for our statistics.

This exploratory study could greatly benefit from observations monitoring stellar objects in dipper configuration with high temporal cadence such as those presented in McGinnis et al. (2015). Using a methodology like the one presented in McGinnis et al. (2015) to fit the position and shape of the warp as a function of time to the observed lightcurve seems a suited approach. Once the warp's position and shape are constrained by high temporal cadence photometry, they can be injected in the EVE code to study contemporaneous high resolution, high temporal cadence spectroscopic observations of the system. Because of the motion of the warp, we need to adapt the way we analyse these high resolution spectroscopic transit observations. A single, mean, out-of-transit spectrum is not relevant and the out-of-transit observed exposures should be kept unaveraged. Using the EVE code with a warp model constrained by photometry and a robust stellar spectrum model would allow for an exposure-by-exposure fit that would allow us to reconstruct the unocculted (by the planet) in-transit disc-integrated spectra to be used in the computation of the absorption spectra of the transiting planet. The choice of the spectroscopic lines to study for transiting planets and their atmospheres is also important. In cTTs, there are strong lines that are affected by the star-disc interactions. For example, strong emission lines from hydrogen transitions due to the accretion shock. The metastable

He I triplet lines are also tracers of the inner disc physics, showing a redshift due to the matter infalling in accretion columns and a blueshift because of the disc winds (Edwards et al. 2006; Kurosawa et al. 2011; Hartmann et al. 2016; Roggero 2021). This emphasises the need for accurate knowledge of the spectrum of the host star and its variability, as H and He are common tracers of atmospheric escape. Whether or not it is realistic to attempt to detect transiting exoplanets around cTTs is too early to conclude. The observing strategy suggested above has yet to be tested, but it highlights the need for detailed observational and computational approaches adjusted punctually to each observed system.

6

Conclusion and perspectives

The research I conducted in this thesis takes place in a broader context that focuses on characterising exoplanets and understanding their long-term evolution. The community is driven by the desire to understand and find answers to why exoplanetary systems are so diverse and sometimes so different from our own solar system. The study of exoplanets could also help us answer one of the most elusive questions: What makes Earth so favourable for hosting life as we understand it?
Understanding exoplanets – their formation, evolution and properties – inevitably goes through the study of their atmospheres, which are windows into the past, current and future state of these planets. An unambiguous characterisation of these atmospheres is thus a critical aspect in the study of exoplanetary systems. My thesis work was motivated by the recent highlighting of the potential presence of residual stellar contamination in the absorption spectra of transiting planets and their atmospheres, one of our main spectroscopic diagnostics. Specifically, it was motivated by the need to properly identify the origin of these contaminations and account for their associated distortions in order to avoid introducing bias in the derived atmospheric properties. To address this intriguing problem, I used the planetary transits code named EVaporating Exoplanets (EVE) and upgraded it to precisely account for stellar contaminations. Ultimately, the improvements I brought to this code enable more accurate interpretations of the absorption signatures that a planetary atmosphere imprints in transit spectroscopy observations.

Towards a better characterisation of exoplanet atmospheres

The transit spectroscopy method is one of the most advanced techniques to analyse exoplanetary atmospheres. It relies on observing the star during the transit of a planet to identify any change in the observed spectrum, indicating the signature of absorption by the planetary atmosphere. Traditionally, to extract these signatures, the spectra collected during the transit are directly divided by the spectrum of the star collected outside the transit. However, in recent years, it has been demonstrated that such methodology is subject to residual contaminations from the stellar spectrum. Indeed, computing absorption spectra in such ways induces spurious features that we call planet-occulted line distortions or POLDs. These contaminations originate from the non-uniformity of the stellar spectrum over the apparent stellar surface, which causes the planet to absorb locally varying stellar spectra throughout its transit. These POLDs sometimes take the form of absorption and emission features and have the potential to significantly affect the atmospheric absorption signature of the planet, ultimately leading to misinterpretations. If those stellar effects are not treated correctly in planetary transit simulations, there is a risk of deriving erroneous atmospheric properties.

In the framework of my thesis, I used and expanded the capabilities of the EVE code. This code generates realistic synthetic stellar spectra during exoplanet transits, accounting for the 3D geometry of the system's architecture and atmospheric structure. The EVE code has the advantage of being able to compute the absorption of the local stellar spectra during the transit both by the planet and the atmosphere simultaneously. In turn, it produces synthetic planetary transit observations that are directly comparable to real observations. However, a refined handling of the local variations of the spectra across the stellar disc was required in order for the code to naturally account for the POLDs. To address this matter, I have coupled the EVE code with a spectral synthesis code that generates accurate synthetic local stellar spectra. This adaptation ensures that the simulated planet absorbs the correct local stellar spectrum at each time step of the transit.

With this improvement, I was able to study in great details the stellar contaminations induced in absorption spectra by the local variations of the stellar spectrum over the apparent stellar surface, namely, the stellar rotation and centre-to-limb variation. The study I presented in Chapter 3 has allowed for a deeper understanding of the behaviour of POLDs and their individual impact on atmospheric absorption signatures. I have demonstrated the usefulness of a global approach when simulating planetary transit, especially by re-investigating observational datasets of two well-known and peculiar exoplanets.

Using the full potential of the global modelling approach of the EVE code, I have drawn new conclusions about these two systems. For the first one, HD 209458 b, I have shown possible evidence for the presence of sodium atoms in the atmosphere of the planet. For the second system, MASCARA-1 b, I have shown that POLDs could entirely explain the observed absorption spectrum and that there was no detectable signature of atmospheric sodium in the observations. These sorts of studies would greatly benefit from good quality observations and advanced stellar spectrum modelling. Future exploration of the three-dimensional effects of the stellar atmosphere could be tested to see if different interpretations of the observed signature would come out. Also, extending stellar models to account for chromospheric contributions in specific stellar lines that are notorious for partly forming under chromospheric conditions, such as the core of the Na I doublet lines, could help further refine the results. Our approach should explore and include other stellar phenomena to complement what I have presented. For example, differential stellar rotation, convective blueshift and stellar surface inhomogeneities such as spots. These phenomena are potential contributors to the POLDs because they affect local stellar spectra in a way akin to CLV and stellar rotation.

The work I presented in this chapter will serve as a base to understand how and why planet-occulted line distortions form in absorption spectra, but also to understand their behaviour and their impact on atmospheric absorption signatures. With the new generation of high-resolution spectrographs such as ESPRESSO/VLT, NIRPS at La Silla and ANDES/ELT, POLDs will become a dominant source of contamination in planetary transit absorption spectra. A similar approach to the one I have used in this chapter to analyse atmospheric absorption signatures ought to be more systematically used in order not to introduce further bias.

One of the scientific objectives of the newest space observatory, the James Webb Space Telescope, is actually to observe transiting exoplanets and study their atmospheres. The JWST is equipped with spectrographs that observe the planets under low to medium spectral resolution. A relevant question to ask is: will absorption spectra under lower resolution also be significantly affected by planet-occulted line distortions? The expertise I developed during my thesis is ideally suited to tackle this interrogation. A natural extension of my thesis work is then to investigate the effects of stellar rotation and CLV in such observations in a similar fashion as the one presented in Chapter 3. These two studies will be complementary and relevant as medium and low resolution spectroscopy give access to the denser parts of a planetary atmosphere.

Finally, I have been involved in different collaborations thanks to the expertise I developed on planetary transit simulations. For instance, I was involved in the publication *HEARTS VIII. Nondetection of sodium in the atmosphere of the aligned planet KELT-10b* by M. Steiner (Steiner et al. 2023). The authors asked me to simulate the mean absorption spectrum for a typical transit of the planet KELT - 10 b in the spectral region of the sodium doublet. We aimed to compare the absorption spectrum they reconstructed from HARPS observations to the synthetic absorption spectrum of the opaque body of KELT-10 b to better discriminate between POLDs and actual planetary signatures. The synthetic absorption spectrum I computed is displayed in the Figure 7 of the paper.
I also worked with Ph.D. student Adrien Masson from LESIA, observatoire de Paris, to analyse absorption spectra he reconstructed from SPIRou observations for HD 189733 b in the region of the He I triplet at 10830 Å.
I am collaborating with Ph.D. student Dany Mounzer from the Geneva observatory to interpret ESPRESSO transit observations of HD 189733 b in the spectral region of the sodium doublet. These two last collaborations are still ongoing works.
I am currently collaborating with a Master's student from the Geneva observatory to examine the sodium signatures from the transit observations of the targets of the

DREAM I study (Bourrier et al. 2023). In this study, we will use a similar approach as the one used in Dethier & Bourrier (2023) to analyse HD 209458 b's and MASCARA-1 b's observations. That is, fit the observed out-of-transit spectrum in the Na I doublet spectral region. Then, use the EVE code to simulate the transits of the planets for each target and search for possible atmospheric signatures of sodium. As part of this collaboration, I have co-supervised an undergraduate student whose task was to use a routine I developed to fit the Na I doublet lines in the observed out-of-transit stellar spectrum of the sample of targets.

A simplified, yet efficient, modelling of helium lines

The infrared triplet lines of helium near 10830 Å have proved to be excellent tracers of high altitudes expending layers of planetary atmospheres. Because of this, a significant proportion of the exoplanet community has been focusing on studying the signature of helium in transiting planets. As I presented in Chapter 3, the atmospheric absorption signatures of transiting planets are subject to residual stellar contaminations, and helium is no exception. To simulate realistic synthetic transit observations and account for these contaminations, it is necessary to have an accurate knowledge of the local stellar spectrum.

Unfortunately, current publicly available models of stellar atmospheres, like the one I used throughout this work, do not account for the He I triplet lines. Indeed, the metastable state of helium atoms that allows for these lines to form requires physical conditions that are typically met in the chromospheric regions of stellar atmospheres, while these stellar atmosphere models focus on the photosphere. To address this issue, I presented, in Chapter 4, a model that allows one to reconstruct the local metastable He I triplet stellar lines from a fit to the observed disc-integrated spectrum of a star. The computed local stellar spectra can be used directly in the EVE code to fill its stellar grid, allowing the code to make more accurate predictions of the POLDs in the He I triplet lines. I used a version of this model in a publication intended to characterise atmospheric evaporation on diverse exoplanets (Guilluy et al. 2023). Specifically, through the use of the model, we evaluated the POLDs to assess their impact on the absorption spectra of the targets of the study before any further exploration of the absorption signatures was conducted.

Because accurate modelling of POLDs is essential in planetary transit simulations, this helium lines formation model must be improved further. The latter is also motivated by the growing number of observations and studies focusing on these lines in the context of exoplanet atmospheres characterisation. Ideally, the helium lines formation should be treated in detail in stellar models that include both the photosphere and the chromosphere. However, these kinds of models are not as generalised as the pure photospheric models which makes them difficult to use in practice (e.g. Hintz et al. 2020). A natural improvement to the model would then be to treat more self-consistently the processes adding up to the helium triplet lines formation. For instance, taking into account the stellar XUV flux in the computation of the population of the metastable helium triplet levels in a similar way as in Oklopčić & Hirata (2018) and used in the *p-winds* code (Dos Santos et al. 2022). This is a promising perspective of my work, as an interface between EVE and *p-winds* exists.

In its current version, the model has already shown its capabilities. As I plan to make it publicly available, it will serve as a light tool to give a first estimate of the POLDs that are to be expected in absorption spectra reconstructed from transit observations. The end goal is to derive more trustworthy properties from the observed helium absorption signatures.

Studying transiting planets in classical T Tauri stars

Because the state of a planetary atmosphere continuously evolves throughout its whole lifetime, it is important to study planets at all ages. While planets around stars of a similar age to the Sun have been discovered en masse, planets around young stars have been more successful at evading detection. The most fruitful technique for planetary detection, up to now, is the transit technique. Still, its relevance for studying planets orbiting young stars might need to be investigated. Indeed, among the many physical phenomena inherent to young stars and that complexify their study, one stands out for hindering the detection of transiting planets in these systems. Young stars are still surrounded by a circumstellar disc of gas and dust, which is the birthplace of planets. Depending on the geometrical configuration of the system, the disc might fall in the observer's line-of-sight, hiding potential transiting planets.

In Chapter 5, I addressed the case of dippers, a specific configuration in which planets could potentially be observed transiting the host star. In these objects, the line-of-sight of the observer has a grazing incidence with respect to the disc and is periodically blocked by a deformation of the inner disc, called a warp, induced by the magnetospheric accretion from the inner disc onto the stellar surface.

In this chapter, I first present the disc and warp model that I used to adapt the EVE code to the environment of young stars. I then study the impact of the occulting warp on the POLDs in the absorption spectra of a hypothetical transiting planet. I showed how the warp deforms the line profiles of the disc-integrated stellar spectrum, which in turn modifies the POLDs, compared to a case without a disc and warp. Finally, I explore the effect of the periodic motion of the warp on the detectability of a transiting planet in such systems.

In the systems studied in this chapter, the stellar disc-integrated spectrum changes constantly due to the periodic occultation by the warp. The use of a unique out-of-transit spectrum to compute the absorption spectra of a transiting planet, thus, becomes irrelevant. Instead, one would need to be able to reconstruct the disc-integrated spectrum outside of, but also during, the transit of the planet. This can be achieved by fitting the observations at each time step so that the position of the warp and the disc-integrated spectrum (without the occultation by the planet) can be predicted during the transit of the planet. To facilitate this approach, a key strategy would be to combine high resolution spectroscopic observations with high temporal cadence photometric monitoring of the star. The former allows for an accurate knowledge of the variability of the stellar spectrum and for detecting any change in the stellar spectral lines that could indicate absorption by a transiting planet and its atmosphere. The latter gives the possibility to constrain the shape and position of the inner disc's warp as a function of time (see McGinnis et al. 2015). The shape of the warp can significantly change between rotation cycles, e.g. McGinnis et al. (2015) and Figure 3 of Alencar et al. (2018), underlining the necessity for simultaneous photometry and spectroscopy. In its current version, the EVE code is technically adapted to perform analysis of such observations.

So far, the disc and its warp have been considered opaque. Still, the mixture of dust and gas present in the disc has its own optical properties. As a consequence, the edges of the warp might not be fully opaque at the wavelengths scrutinised. In turn, the transiting warp could induce spectral signatures in the absorption spectrum of the planet and possibly alter the POLDs in a way never envisioned before. Fortunately, the versatile nature of the EVE code makes it possible to introduce a better description of the disc, including opacity effects.

Another aspect of young stars to consider is their typically high level of XUV flux compared to main-sequence stars (Johnstone et al. 2015). Under such conditions, one might expect extended planetary atmospheres in these systems. An extended planetary atmosphere of helium, for example, could increase the detectability of the planet. If the atmosphere is strongly extended due to the high level of XUV flux, it could transit without the need for the planetary body to transit (Ehrenreich et al. 2012). This could create detectable signatures and increase the range of semi-major axes at which a transit is detectable, therefore enlarging the range of relevant stellar inclinations. The EVE code is already suited for such exploration, thanks to its coupling with the *p-winds* code. One missing ingredient for such exploration is the XUV flux, which is a quantity that is complex to collect for distant stars. However, a starting point is the recently published XUV flux of the young star V1298 Tau by Maggio et al. (2023), who have agreed to collaborate with us.

Due to possible strong interactions with the stellar magnetosphere and winds – by-products of the star-disc interaction – the absorption signature of the transiting atmosphere might be different from expected (e.g. Matsakos et al. 2015; Strugarek et al. 2019; Vidotto & Cleary 2020). In the SPIDI project[1], of which I am part of, we are developing numerical models of the close environment of young stars and the radiative signatures associated with it (Pantolmos et al. 2020; Tessore et al. 2023). It is, therefore, reasonable to think that the signatures of an evaporating atmosphere could be detectable in this complex environment, as the signatures of the star-disc interaction are more and more constrained.

The approach I used in this chapter could seem heuristic, but with the ever more efficient instruments, telescopes and advanced modelling tools, the observations and study of young stellar objects will be facilitated. The EVE code shall be suited and ready to take on the challenge of confirming transiting planets in young stars.

The community working on exoplanet transit observations, especially in high resolution spectroscopy, has started to account more and more for stellar contaminations in their analyses of absorption spectra (see e.g. Yan et al. 2017; Yan & Henning 2018; Casasayas-Barris et al. 2020, 2021, 2022; Zhang et al. 2022, and others). The expertise I developed in simulating exoplanetary transit absorption spectra during my thesis has allowed me to start new collaborations with other groups. These collaborations emphasise the usefulness of the global approach I helped build with the adaptations I brought to the EVE code. The community's interest for tools that allow for estimates of the stellar contamination in planetary transit absorption spectra is tangible. Finally, accounting for POLDs in absorption spectra analysis should become systematic and customary. The work I presented intends to give the basis for such endeavour, with the ultimate objective to better characterise the atmospheres of distant worlds.

---

[1] `https://spidi-eu.org`

A

Radiative transfer equation

This appendix introduces the formalism to the equation of radiative transfer used in this manuscript (see also Gray (2005)). Let us consider a slab of matter of length L composed of a single type of particles with a density ρ in $\mathrm{g\,cm^{-3}}$, an absorption coefficient κ in units of $\mathrm{cm^2\ g^{-1}}$ and an emission coefficient j in units of $\mathrm{erg\ s^{-1}\,Hz^{-1}\ sr^{-1}\ g^{-1}}$ (see Figure A.1). The absorption and emission coefficients are considered constant along the slab. If I is a radiation traveling through the element of matter, then the change in radiation through an element dl of the slab is written as,

$$dI = -\kappa\rho I dl + j\rho dl. \tag{A.1}$$

To know what is the radiation exiting the slab in a specific direction, we need to integrate this equation from l_1 to l_2 the boundaries of the slab. First, knowing that

$$\tau_{out} = \int_{l_1}^{l_2} \kappa\rho dl, \tag{A.2}$$

let us write the following change of variable,

$$d\tau = \kappa\rho dl, \tag{A.3}$$

where τ is the optical depth of the element of the slab. The boundaries become τ_{in} and τ_{out}.
The equation becomes

$$\begin{aligned} dI &= -I d\tau + j\frac{d\tau}{\kappa} \\ \frac{dI}{d\tau} &= -I + \frac{j}{\kappa} \\ \frac{dI}{d\tau} &= -I + S, \end{aligned} \tag{A.4}$$

with S named the source function of the slab. Then we can write

$$\begin{aligned} \frac{dI}{d\tau} + I &= S \\ e^{\tau} \times \left(\frac{dI}{d\tau} + I\right) &= e^{\tau} \times S \\ \frac{d}{d\tau}(I \times e^{\tau}) &= e^{\tau} \times S. \end{aligned} \tag{A.5}$$

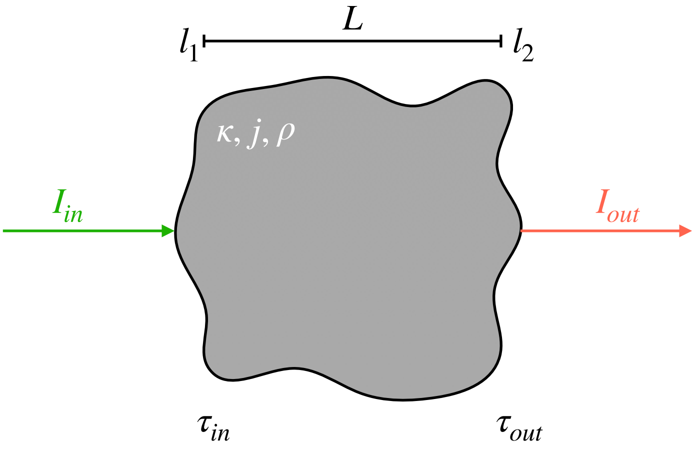

Fig. A.1.: Slab of matter composed of a single type of particles.

Now let's integrate as follows

$$\begin{aligned}\int_{\tau_{in}}^{\tau_{out}} d(I \times e^{\tau}) &= \int_{\tau_{in}}^{\tau_{out}} e^{\tau} \times S d\tau \\ [I \times e^{\tau}]_{\tau_{in}}^{\tau_{out}} &= [e^{\tau} \times S]_{\tau_{in}}^{\tau_{out}} \\ I_{out} \times e^{\tau_{out}} - I_{in} \times e^{\tau_{in}} &= e^{\tau_{out}} \times S - e^{\tau_{in}} \times S,\end{aligned} \tag{A.6}$$

considering $\tau_{in} = 0$ as the radiation just entered the medium at l_1, the equation becomes,

$$\begin{aligned}I_{out} \times e^{\tau_{out}} &= I_{in} + S \times (e^{\tau_{out}} - 1) \\ I_{out} &= \underbrace{I_{in} \times e^{-\tau_{out}}}_{\text{absorption component}} + \underbrace{S \times (1 - e^{-\tau_{out}})}_{\text{emission component}}\end{aligned} \tag{A.7}$$

with I_{in} the radiation entering the slab of matter and with I_{out} the radiation exiting the slab of matter.

In the case of an optically thick slab, $\tau_{out} >> 1$ and Equation A.7 reduces to,

$$I_{out} \simeq S \tag{A.8}$$

for an optically thin slab, $\tau_{out} << 1$ and Eq. A.7 becomes,

$$\begin{aligned}I_{out} &\simeq I_{in} - \tau_{out} I_{in} + S \times (1 - 1 + \tau_{out}) \\ I_{out} &\simeq I_{in} + \tau_{out} (S - I_{in})\end{aligned} \tag{A.9}$$

B

Definition of the stellar flux in the EVE code

Following Hubeny & Mihalas (2014), the general definition of the flux of radiation is given in units of erg cm^{-2} Å^{-1} s^{-1} and is written,

$$F(\vec{\lambda}) = \oint I(\lambda, \vec{n})\ \vec{n}\ d\Omega \tag{B.1}$$

where $I(\lambda, \vec{n})$ is the specific intensity, $\vec{n}$ its direction and $d\Omega$ is a unit solid angle. Let us consider the flux crossing the surface of a star of radius R_* with a Cartesian referential centred on the star's centre and the z direction being the direction of the line of sight of an external observer. The unit solid angle is given by $d\Omega = dS/R_*^2$, with dS the unit surface of the star. If we consider only the flux in the direction of the observer, Eq. B.1 can be written

$$F(\lambda, z) = \oint I(\lambda)\ \cos(\theta)\ d\Omega \tag{B.2}$$

where θ is the angle between the direction of propagation, $\vec{n}$, of $I(\lambda, \vec{n})$ and the line of sight of the observer (parallel to the z axis).

In the EVE code, the apparent surface of a star is represented by a disc of radius equal to the radius of the star. This disc is then discretised by a uniform two-dimensional square grid. So, the unit stellar surface dS is approximated by its projection onto the plane of the sky and is equal to the square surface, S_i, of a grid cell. The intensities generated by the code *Turbospectrum* are computed in the direction of the observer at specific position on the stellar disc. In the EVE code the flux at the surface of the star is computed in a discrete form as the sum of local fluxes – intensity emerging in a specific grid cell – at the surface of the star. The flux is written,

$$\mathrm{F}_{\mathrm{out}}(\lambda) = \sum_{i=1}^{n} \mathrm{F}\ (\lambda, \mu_i, v^i_{\mathrm{rad}}) = \sum_{i=1}^{n} \mathrm{I}\ (\lambda, \mu_i, v^i_{\mathrm{rad}})\Delta\Omega_i = \sum_{i=1}^{n} \mathrm{I}\ (\lambda, \mu_i, v^i_{\mathrm{rad}}) \frac{S_i}{R_*^2}\ , \tag{B.3}$$

with n, the total number of cells in the grid. In Eq. B.3, F $(\lambda, \mu_i, v^i_{\mathrm{rad}})$ is the flux out of each grid cell, affected by CLV and stellar rotation, which is the product of the local intensity and of the solid angle subtended by a surface element at the surface of the star.

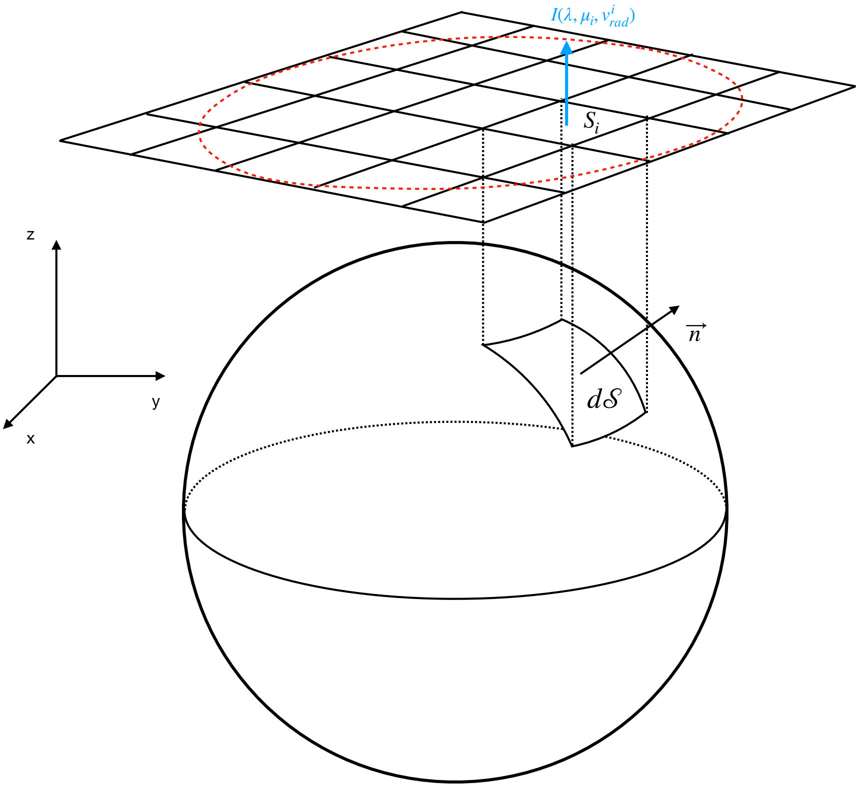

Fig. B.1.: Schematic representation of the stellar grid in the EVE code.

C

Publications

A&A 674, A86 (2023)
https://doi.org/10.1051/0004-6361/202245705

Astronomy & Astrophysics

Combined analysis of stellar and planetary absorption lines via global forward-transit simulations

W. Dethier[1] and V. Bourrier[2]

[1] Univ. Grenoble Alpes, CNRS, IPAG, 38000 Grenoble, France
e-mail: `william.dethier@univ-grenoble-alpes.fr`
[2] Observatoire Astronomique de l'Université de Genève, Chemin Pegasi 51b, 1290 Versoix, Switzerland

Received 16 December 2022 / Accepted 12 April 2023

ABSTRACT

Context. Transit spectroscopy of exoplanets has led to the detection of many species whose absorption signatures trace their atmospheric structure and dynamics. Improvements in resolution and sensitivity have, however, revealed biases induced by stellar lines occulted by the transiting planet.

Aims. We characterise the planet-occulted line distortions (POLDs) in absorption spectra that arise from proxies used for the occulted stellar lines and investigate the impact of stellar rotation, centre-to-limb variations, and broadband limb-darkening.

Methods. We used the EVaporating Exoplanets (EVE) code to generate realistic stellar spectra during the transit of exoplanets, accounting for the 3D geometry of the system's architecture and atmospheric transit, as well as for spectral variations over the stellar disc. The absorption spectra were calculated using approaches drawn from the literature and compared to the expected signal.

Results. The POLDs from stellar rotation are dominant for moderate to fast rotating stars, reaching amplitudes comparable to atmospheric signals, but they can be mitigated by shifting the stellar line proxies to the radial velocity of the planet-occulted region. Centre-to-limb variations become dominant for slow rotators and are more easily mitigated at the stellar limb. We re-interpret the ESPRESSO data of two iconic systems and confirm that the sodium signature from HD 209458 b mainly arises from POLDs. However, we unveil a possible contribution from the planetary atmosphere that warrants further observations. For MASCARA-1 b, we did not find evidence for atmospheric sodium absorption and we can fully explain the observed signature by a POLD for super-solar stellar sodium abundance.

Conclusions. We studied POLDs dependency on star and planet properties, and on the proxy used for planet-occulted lines. Distinguishing planetary absorption signatures from POLDs is challenging without access to accurate estimates of the local stellar spectrum and system orbital parameters. We propose a way to mitigate POLDs and improve atmospheric characterisation, by using simultaneous forward modelling of both the star and the planet to simulate the global observed signatures.

Key words. planets and satellites: atmospheres – methods: numerical – techniques: spectroscopic – stars: atmospheres – planets and satellites: individual: HD 209458 b – planets and satellites: individual: MASCARA-1 b

1. Introduction

Today's telescopes are capable of collecting and delivering observational data to such a high level of precision that we are able to detect the absorption of the stellar light caused by the atmosphere of a planet transiting its host star. Atomic species contained in the planetary atmosphere yield narrow absorption signatures in specific spectral lines that are in excess of the broadband absorption caused by clouds and hazes. To isolate this excess absorption, the standard technique consists of comparing stellar spectra measured outside of the transit, representative of the disc-integrated stellar spectrum ($F_{\rm out}$) and spectra measured during the transit with a high temporal cadence ($F_{\rm in}$). The difference between the out-of-transit and in-transit spectra yields the local stellar spectrum absorbed by the planet and its atmosphere (see Fig. 1). Normalising this absorbed spectrum ($F_{\rm abs}$) by a reference spectrum for the occulted star, yields the so-called absorption spectrum ($\mathcal{A}$), which is the counterpart of the transmission spectrum. It is expected to only contain the planetary absorption lines, as follows:

$$\mathcal{A}(\lambda, t) = \frac{F_{\rm abs}(\lambda, t)}{F_{\rm ref}(\lambda, t)}. \tag{1}$$

The nomenclature 'transmission spectrum' that is also used in the literature can be derived from the absorption spectrum as $\mathcal{T}(\lambda, t) = 1 - \mathcal{A}(\lambda, t)$. The definition of the reference spectrum, however, has a huge impact on the content of the absorption spectrum. Ideally, we should define the reference as the local spectrum of the region of the stellar surface occulted by the planet in a given observing exposure. In practice, however, this local spectrum is difficult to determine and, instead, the spectrum of the disc-integrated star is used as a reference. When this approximation is not valid, the extracted absorption spectrum is contaminated by residual stellar spectral lines and can be misinterpreted. As an example, Charbonneau et al. (2002) claimed the first detection of an exoplanet atmosphere by analysing transit observations of the Hot Jupiter HD 209458 b collected by HST STIS spectrograph. They interpreted absorption signatures in the absorption spectra as being due to sodium atoms in the planetary atmosphere. Similar signatures were observed by Snellen et al. (2008) and Albrecht et al. (2008) in Subaru's HDS spectrograph and UVES/VLT data, apparently supporting their planetary origin. However, Casasayas-Barris et al. (2020, 2021) challenged this claim through a detailed analysis of the absorption spectra of HD 209458 b collected with HARPS-N, CARMENES, and ESPRESSO. They revealed that the Na I signatures observed

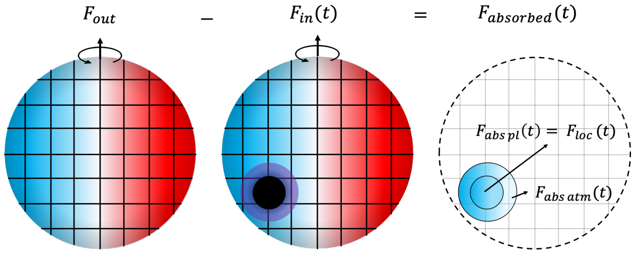

Fig. 1. Visual representation of the difference between F_{out} and $F_{\mathrm{in}}(t)$ during the transit of a planet with an atmosphere. The result is the stellar spectrum that has been absorbed by the planet and its atmosphere at a specific time. The blue and red colours represent the Doppler shift in wavelength caused by the stellar rotation.

during the transit of HD 209458 b could be explained by its occultation of the local stellar lines, without the need for an atmosphere. Indeed, the variations in shape and position of the planet-occulted stellar lines along the transit chord create spurious features in absorption spectra when they are normalised by the disc-integrated stellar line (Yan et al. 2017; Casasayas-Barris et al. 2020, 2021; Borsa et al. 2021).

A major limitation to the accurate calculation of absorption spectra is the so-called Rossiter–McLaughlin effect that is due to the planet crossing a rotating star (Rossiter 1924; McLaughlin 1924). The spectrum from a local region of the stellar hemisphere rotating towards (respectively, away from) the observer is indeed blue-shifted (respectively, red-shifted) according to the stellar rotational velocity projected on the line of sight (LOS). The exact Doppler-shift of a given planet-occulted region thus depends on both the stellar rotational velocity and the location of the transit chord, that is, the sky-projection of the orbital trajectory of the planet onto the stellar surface. Therefore, even if the spectrum used as reference for the planet-occulted region has the correct line profile, it should still be shifted to the correct spectral position to avoid biasing the absorption spectrum. Moreover, even if all regions of the stellar photosphere emitted the same line profile, the disc-integrated stellar lines would still be shallower and wider than the local stellar lines for a star that is rotating fast enough. In that case, using the disc-integrated lines as reference for the planet-occulted lines, even shifted at the correct spectral position, would result in abnormal signatures in the absorption spectrum (Louden & Wheatley 2015; Casasayas-Barris et al. 2020, 2021; Borsa et al. 2021).

Another limitation resides in centre-to-limb variations (CLVs) of the local stellar line profile. For an observer on Earth, the line profile from a region of the stellar photosphere arises from photons emerging from the underlying stellar atmospheric layers in the direction of the LOS. However, the photons forming the core and wings of stellar lines originate from different altitudes in the stellar atmosphere. The observed line profile thus changes in shape between the centre of the stellar disc and its limb. At the centre, photons from both deep and shallow atmospheric layers reach the observer. Close to the limb, only the photons from the upper atmospheric layers reach the observer. For more details, we refer, for example, to Fig. 1 of Vernazza et al. (1981), Fig. 6 of Tessore et al. (2021), Allende Prieto et al. (2004), and Pietrow et al. (2023). As the planet moves between the limbs of the star and its centre during transit, the line profile coming from the occulted stellar regions will change in shape accordingly. If the CLVs are strong, using the disc-integrated spectrum or the local spectrum at disc centre as a reference for stellar limb regions will therefore bias the absorption spectrum (Czesla et al. 2015; Yan et al. 2017; Casasayas-Barris et al. 2020).

Stellar rotation and CLVs can bias the absorption spectrum of a planet even in the absence of an atmosphere, as the spurious signatures these effects can create (which we propose calling planet-occulted line distortions, POLDs) arise solely from the local occultation of stellar lines by the planetary disc. An additional limitation arises, however, when the planetary atmosphere contains species absorbing in the same transitions as the occulted stellar lines. The planetary track in the velocity-phase space will follow the orbital trajectory of the planet, while the signatures arising from occulted stellar lines will form a track that follows the radial velocity of the stellar surface regions occulted by the planet along the transit chord. Since host stars typically rotate with velocity on the order of 1 km s^{-1}, while close-in planets have orbital radial velocities of the order of tens of km s^{-1} at ingress and egress, those two tracks are usually well separated and the stellar track can be masked. In some cases, however, the two tracks can overlap and the features arising from poorly-corrected occulted stellar lines cannot simply be masked.

In earlier studies of exoplanet transits, these limitations were often neglected or overlooked, especially the effects of stellar rotation. This is mainly because the orbital and stellar tracks were blended due to the lower resolution of spectrographs used at that time (Charbonneau et al. 2002; Snellen et al. 2008; Sing et al. 2008; Vidal-Madjar et al. 2011; Spake et al. 2018) or due to the choice of techniques to define and analyse the absorption spectra (Redfield et al. 2008). Although it is worth mentioning that corrections of limb darkening were included in analyses of absorption spectra early on, for example Charbonneau et al. (2002), Sing et al. (2008). However, the advent of high-resolution ground-based spectrographs made possible the measurement of absorption spectra with higher spectral resolution and temporal cadence. It became possible to isolate planetary from stellar absorption lines and to account for their motion in velocity-phase space, reflecting the variation of the planet's radial velocity during transits. Individual absorption spectra can then be aligned in the planetary rest frame, which helps avoid blurring and allows for them to be cumulated to improve the detectability of atmospheric signatures (Wyttenbach et al. 2015).

Progressively, the community has further become aware of the issues arising from an inaccurate definition of the planet-occulted stellar spectrum to normalise absorption spectra (Louden & Wheatley 2015; Barnes et al. 2016; Yan et al. 2017; Casasayas-Barris et al. 2017) and observation-oriented corrections of the stellar rotation effect on absorption spectra were proposed (Borsa & Zannoni 2018). Some studies still use the measured disc-integrated stellar spectrum as a reference and set it to the spectral position of the local planet-occulted line. This approach remains valid as long as stellar rotation and CLVs are small enough not to substantially alter the disc-integrated line profile compared to the local one (Wyttenbach et al. 2020; Mounzer et al. 2022). Others use stellar atmospheric models to compute a disc-integrated stellar spectrum representative of the measured one. By including CLVs and stellar rotation in their model, they can simulate theoretical absorption spectra comparable to actual observed absorption spectra and better interpret the stellar and planetary signatures they contain (Yan et al. 2017; Casasayas-Barris et al. 2020, 2021, 2022; Borsa et al. 2021). This last approach, however, requires precise knowledge of the target star's rotational velocity and of how its local spectrum is affected by CLVs. Both characteristics are not straightforward to determine, and our goal in this study is thus to investigate the accuracy of this approach in retrieving the correct planetary atmospheric signal. More precisely, we use forward three-dimensional (3D) simulations of a transiting planet with specific planetary properties, with and without an atmosphere, and include various effects in the simulated local stellar spectrum. Knowing the exact content of the resulting theoretical absorption spectra then allows us to determine how the measured ones can be biased by various extraction methods.

Throughout this paper, we focus on the absorption signature from sodium atoms in the atmosphere of exoplanets. This species has been detected several times in different exoplanets and its absorption signature typically reaches amplitudes on the order of 1% (Nikolov et al. 2016; Wyttenbach et al. 2017; Casasayas-Barris et al. 2018; Chen et al. 2018; Jensen et al. 2018; Deibert et al. 2019; Hoeijmakers et al. 2019; Seidel et al. 2019). The Na I signals are therefore subject to contamination by the aforementioned effects and make an ideal case-study for investigating their impact.

In Sect. 2, we begin by introducing the setup of our code. We also explain how we define the theoretical planetary system and stellar synthetic spectrum. Finally, we detail how we determined the different relevant quantities used to compute absorption spectra from the planet and its putative atmosphere. In Sect. 3, we then study the impact of different stellar effects and extraction methods on the retrieved planetary absorption spectra. Finally, in Sect. 4, we investigate how these biases affect two known exoplanets that have interesting orbital configurations and atmospheric properties.

2. Methods

This section is dedicated to showing how we simulated synthetic observations of a transiting planet with the EVaporating Exoplanets (EVE) code (Bourrier & Lecavelier des Etangs 2013; Bourrier et al. 2015, 2016) and how we used its end products to extract the synthetic absorption spectra of a transiting planet and its 3D upper atmosphere.

2.1. Framework of the EVaporating Exoplanet code

These spectra can be computed with a high spectral resolution and temporal cadence. The code takes into account geometrical effects associated with the 3D nature of the planetary orbit. Moreover, it uses a detailed description of the stellar spectrum variation over the stellar surface to compute realistic spectra. The code can simulate a 3D planetary atmosphere described by temperature, density, and velocity profiles. This allows us to compare simulated absorption spectra to observations of a transiting planet collected with high-resolution spectrographs to infer the planetary and stellar properties. In the following, we provide an abridged description of how the relevant physical phenomena are taken into account in the code. For a more detailed description, we refer, for instance, to the supplementary material of Allart et al. (2018).

2.1.1. Synthetic stellar spectrum

To simulate the absorption spectra of a transiting planet, it is crucial to accurately define the stellar spectrum it absorbs at each time-step. Indeed, as the planet moves during the transit it hides different regions of the stellar surface, whose local spectral profiles differ from each other due to stellar rotation and CLVs.

To account for these effects, the code models the host star as a disc discretised by a 2D uniform square grid of length equal to the stellar diameter. The intensity spectrum coming from each stellar cell can be set to a constant profile or interpolated from a series of input spectra. As an observer is sensitive to radial velocities, the spectra from each stellar cell are shifted in wavelength according to the sky-projected rotational velocity of the star. In the following, we use the property $v_{\mathrm{eq}} \sin(i)$ to quantify the stellar rotation, where i is the angle between the star's rotation axis and the LOS and v_{eq} is the star's equatorial rotational velocity. Finally, the spectra are scaled by the effective stellar surface of the grid cell to yield a grid of local flux spectra over the stellar surface.

To define stellar intensity spectra accounting for CLVs, we used the non-Local Thermodynamic Equilibrium (NLTE) version of Turbospectrum code for spectral synthesis[1] (Plez 2012; Heiter et al. 2021; Larsen et al. 2022; Magg et al. 2022) and related routines[2]. This code takes as its inputs: the MARCS photospheric models (Gustafsson et al. 2008)[3], spectral line lists from, for example, the VALD3 database[4] (Ryabchikova et al. 2015), and precomputed NLTE departure coefficients to simulate the synthetic stellar spectra. We generated intensity spectra for a series of μ values[5] following a logarithmic distribution. This allowed us to reach a finer spatial sampling of the stellar limb, where the observed stellar line profiles are altered the most by CLVs.

Figure 2 compares the local and disc-integrated stellar spectra around the Na I D2 line, when accounting for the various effects mentioned above. In case (a) the local lines have the same spectral profile and position over the whole stellar disc. The disc-integrated spectrum thus has the same profile. In case (b) the local lines keep the same spectral profile over the stellar disc, but we set the stellar rotational velocity to a value of $v_{\mathrm{eq}} \sin(i) = 10\,\mathrm{km\,s^{-1}}$. The local line profiles at different μ positions along the stellar equator are thus shifted according to the local radial velocity of the stellar surface. In this case, the disc-integrated spectrum displays rotationally broadened line profiles. In case (c) there is no stellar rotation but CLVs are considered, that is that the local lines remain at the same spectral position but change in shape as a function of μ over the stellar disc. The corresponding disc-integrated spectrum displays line profiles with altered shapes compared to case (a). Case (d) shows the combined effects of CLVs and stellar rotation ($v_{\mathrm{eq}} \sin(i) = 10\,\mathrm{km\,s^{-1}}$). Both the shape and velocity shift of the local lines change as a function of the position on the stellar disc. The disc-integrated spectrum displays rotationally-broadened line profiles with altered shapes compared to the previous cases[6].

The comparison of the local and disc-integrated line profiles makes it clear that they differ as soon as strong CLVs or stellar rotation is taken into account. This illustrates why using an incorrect reference for the stellar spectrum absorbed by the planet during its transit when computing the absorption spectrum can induce strong biases.

---

[1] `https://github.com/bertrandplez/Turbospectrum_NLTE`

[2] `https://keeper.mpdl.mpg.de/d/6eaecbf95b88448f98a4/`

[3] `https://marcs.astro.uu.se`

[4] `http://vald.astro.uu.se`

[5] For a star of radius equal to 1, $\mu = \sqrt{1 - (x^2 + y^2)}$ with (x, y) the coordinates of a point on the stellar disc in the Cartesian referential centred on the stellar disc. $\mu = 1$ at the centre of the stellar disc and 0 at the edge of the stellar disc.

[6] In cases (c) and (d), the local lines that form close to the limb exhibit a flat bottom. As the LOS approaches the limb, the column density of the stellar atmosphere increases. Consequently, the contribution to the intensity of the lines' source function increases, which results in a flat bottom profile in the synthetic spectra generated by `Turbospectrum`.

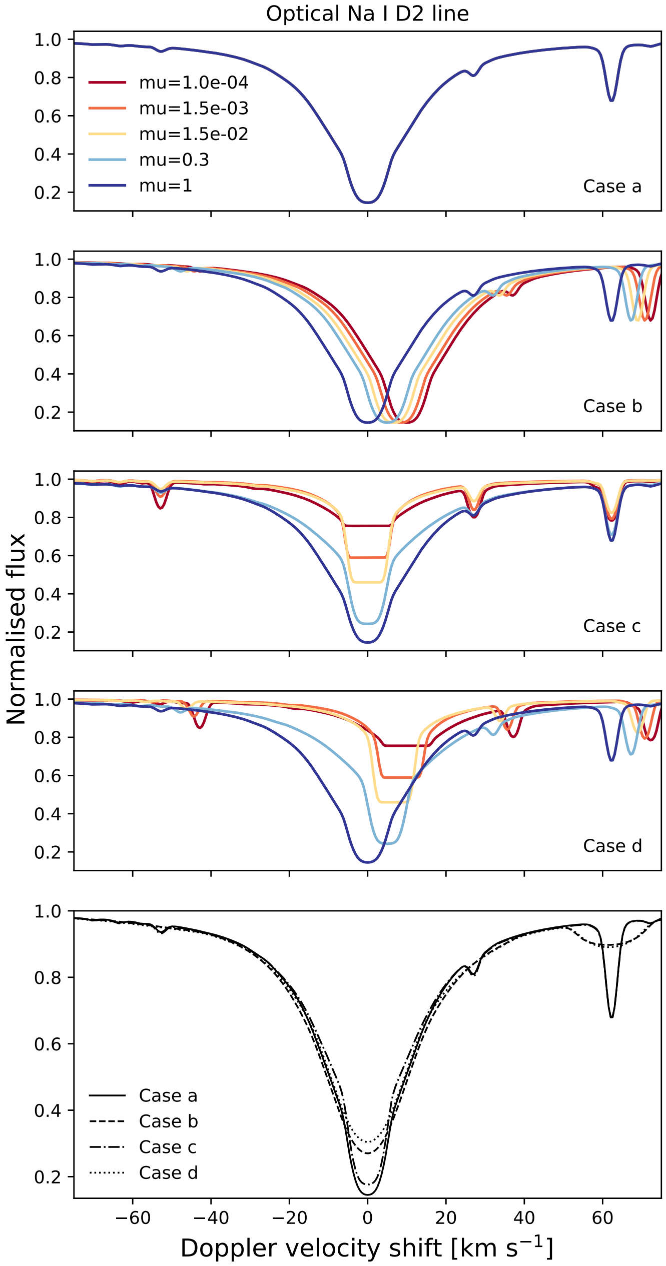

Fig. 2. Local (four upper panels) and disc-integrated (bottom panel) Na I D2 line profile at 5889.95 Å in the air, for a model star simulated with EVE under various conditions. *Case a*: constant local line profiles over the stellar disc. *Case b*: impact of fast stellar rotation on local line profiles. *Case c*: impact of CLVs on local line profiles. *Case d*: impact of CLVs and fast stellar rotation on local line profiles. Only a few red-shifted local spectra are shown for the sake of clarity in cases c and d. Local intensity spectra were taken for μ positions along the stellar equator to sample larger radial velocities.

2.1.2. Planetary atmospheric profiles

Once the stellar spectral grid has been defined, the code simulates the planet as an opaque disc, which absorbs equally at all wavelengths, surrounded by a 3D uniform cubic grid representing the thermosphere. The EVE code can further account for a collision-less exosphere above this grid, using a Monte-Carlo particle description. In this study, we limit our simulations to the thermosphere, as it is sufficient to illustrate our arguments.

The code computes the temperature, density, and velocity of gas within the thermosphere using 1D vertical profiles, which are distributed throughout the 3D grid assuming spherical symmetry. These profiles are used later in the simulation to compute the spectral optical depth of the thermosphere and, subsequently, to calculate the in-transit spectra.

We assumed that the thermosphere undergoes a hydrodynamical expansion following a Parker wind description (Parker 1958). To compute the thermospheric profiles, we used the relations described, for instance, in Lamers & Cassinelli (1999) and Oklopčić & Hirata (2018) that are adapted from Parker (1958) that had initially been developed for the solar wind. For example, see Eqs. (4) and (6) of Oklopčić & Hirata (2018).

The atmospheric profile derived from these equations is assumed to remain constant over time. This formalism allows us to derive a density profile within the thermosphere that is common to all simulated species. For a given species, we then assumed that its density profile can simply be scaled from the common profile via a chosen density value at a reference altitude, which can be set directly or derived from a known mass loss rate. The density profile of a specific species for an isothermal thermosphere is thus derived as follows from Eq. (7) of Oklopčić & Hirata (2018),

$$\rho_{\rm sp}(r) = \rho_{\rm sp}(r_{\rm top}) \exp\left[2r_{\rm s}\left(\frac{1}{r} - \frac{1}{r_{\rm top}}\right) - \frac{v^2(r) - v^2(r_{\rm top})}{2v_{\rm s}^2}\right], \quad (2)$$

where $\rho_{\rm sp}(r_{\rm top})$ is the density of the species at the top of the thermosphere, $r_{\rm s}$ the radius of the sonic point, where the planetary wind becomes supersonic, $v(r)$ is the velocity profile of the species, $v_{\rm s}$ is the speed of sound in the thermosphere. While thermospheric profiles are more complex in reality, we consider our approach sufficient to assess the first-order impact of CLVs and stellar rotation on the atmospheric absorption spectra of transiting planets.

2.1.3. Synthetic observations

The end products of EVE simulations are synthetic time-series of stellar spectra affected by the planet and its atmosphere. The first observable is the disc-integrated spectrum of the host star, computed in the code as the sum of the local spectra from all the cells of the 2D stellar square grid and in units of a specific flux:

$$F_{\rm out}(\lambda) = \sum_{i=1}^{n} {\rm F}\,(\lambda, \mu_i, v_{\rm rad}^i) = \sum_{i=1}^{n} {\rm I}\,(\lambda, \mu_i, v_{\rm rad}^i) \times \Delta\Omega_i\,, \quad (3)$$

with n as the total number of cells discretising the stellar disc. Then, $\sum_{i=1}^{n} {\rm F}\,(\lambda, \mu_i, v_{\rm rad}^i)$ is the specific flux coming from the ith cell on the stellar disc; ${\rm I}(\lambda, \mu_i, v_{\rm rad}^i)$ is the specific intensity emitted from the ith cell on the stellar disc, with the dependence on μ_i indicating that the CLVs (including broadband limb darkening) affect the spectrum coming from the ith stellar cell; $v_{\rm rad}^i$ is the radial velocity of the ith stellar cell with respect to a static distant observer; λ represents the wavelength dependency of the intensity; and $\Delta\Omega_i$ is the solid angle subtended by the surface of the ith cell at the distance of the stellar surface, defined as the ratio between the surface of the ith cell and the square of the stellar radius. To obtain $F_{\rm out}$ at any other distance, d, than the stellar radius, we need to perform the following calculation: $F_{\rm out}(d) = F_{\rm out} \times R_*^2/d^2$.

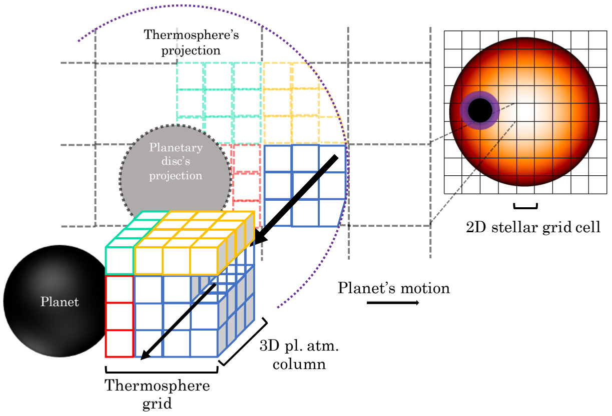

Fig. 3. Simplified sketch of the code's architecture for the computation of the absorption of the stellar spectrum during the transit of the planet and its atmosphere. Different colours for the thermosphere grid cells mean that their projections fall on different stellar cells. The black arrows represent the stellar light coming out of the stellar surface. We only show a small fraction of the simulated atmosphere for clarity.

Once the out-of-transit spectrum is computed, the code moves the planet on a predefined 3D orbital track, sampled with a high temporal and spatial resolution. The simulated transit starts as soon as the atmospheric limb occults the stellar disc, and EVE can then compute disc-integrated stellar spectra ($F_{\rm in}$) that accounts for planetary absorption.

This step is done by further discretising the stellar cells at the resolution of the planetary atmospheric grid and identifying the columns parallel to the LOS that arise from this refined stellar grid and cross the thermosphere. The code determines the LOS-positions of sub-cells that fall within the thermosphere, computes their optical depth in each column (Sect. 2.1.2), and, finally, calculates the resulting absorption of the stellar spectrum at the base of the column. In-transit spectra ($F_{\rm in}$) are finally computed similarly as the out-of-transit spectrum by summing over local spectra from all stellar cells as:

$$F_{\rm in}(\lambda, {\rm t}) = \sum_{i=1}^{n} {\rm I}\left(\lambda, \mu_i, v^i_{\rm rad}\right) \sum_{j=1}^{m} {\rm e}^{-\tau_{i,j}(\lambda,{\rm t})} \times \Delta\Omega_{i,j}\ , \tag{4}$$

where the j index runs over the sub-cells of a specific stellar cell at index, i; $\tau_{i,j}$ is the spectral optical depth of the thermospheric column occulting the stellar sub-cell (i, j). It is equal to 0 ($e^{-\tau_{i,j}} = 1$) when there is no atmosphere or planetary opaque body in front of the stellar sub-cell (i, j). It tends to infinity ($e^{-\tau_{i,j}} = 0$) for all wavelengths when the cell is behind the planetary disc. It also tends to infinity only for specific wavelengths when the sub-cell is behind a part of the atmosphere that is optically thick. This depends on the structure of the whole thermosphere and the optical properties of the species it contains. Figure 3 shows a sketch of the thermosphere absorbing the stellar flux during the transit to help visualise the architecture of the code.

At the end of a simulation, the code outputs a series of stellar spectra with high spectral and temporal resolution, which contain the absorption of the stellar light by the planet and its atmosphere during the transit. To simulate realistic synthetic observations, the code first convolves the spectra with the chosen instrumental response, then it averages the spectra over a lower-resolution wavelength table matching the instrument, and, finally, it averages the spectra within the chosen temporal windows (e.g. to match the observing cadence of a given dataset).

2.2. Computing the absorption spectrum

In the previous section, we have shown the different ingredients the code uses to simulate synthetic observational datasets of a transiting planet. In the following, we show how we used these synthetic observations to extract, for each time-step, the atmospheric and planetary absorption signatures. The local spectrum that is absorbed ($F_{\rm abs}$) by the planet and its atmosphere is computed as the difference between $F_{\rm out}$ and $F_{\rm in}$ (see Fig. 1):

$$\begin{aligned} F_{\rm abs}(\lambda, t) &= F_{\rm out}(\lambda) - F_{\rm in}(\lambda, t) \\ &= \underbrace{\sum_k {\rm I}\left(\lambda, \mu_k, v^k_{\rm rad}\right) \sum_{k'} \Delta\Omega_{k,k'}}_{F_{\rm abs\ pl}} \\ &\quad + \underbrace{\sum_l {\rm I}\left(\lambda, \mu_l, v^l_{\rm rad}\right) \sum_{l'} \left[1 - {\rm e}^{-\tau_{l,l'}(\lambda)}\right] \times \Delta\Omega_{l,l'}}_{F_{\rm abs\ atm}}, \end{aligned} \tag{5}$$

where the k index accounts for the stellar cells partially or fully occulted by the planetary disc at a time, t. The l index accounts for the stellar cells partially or fully occulted by the thermosphere at a time t. Indices k' and l' run only over stellar sub-cells that are occulted by the planetary body and the thermosphere columns, respectively. To isolate the absorption spectrum, $\mathcal{A}(\lambda, t)$ (see Eq. (1)), of the planetary atmosphere in a given exposure, we should then divide $F_{\rm abs}$ by the local spectrum integrated over the stellar surface occulted by the planet ($F_{\rm loc}$, see Fig. 1). A reasonable approximation for short exposure times is that the spatial scale of stellar lines variations induced by CLVs and stellar rotation is small over the stellar surface occulted by the planet during an exposure. The stellar line profiles of $F_{\rm loc}$ are then the same as those contained in $F_{\rm abs}$, so that dividing $F_{\rm abs}$ by $F_{\rm loc}$ removes the spectral variations due to the stellar lines in the resulting absorption spectrum[7]. However, in practice, it is difficult to determine the local planetary-occulted spectrum, since only the disc-integrated stellar lines can be observed.

A reference spectrum $F_{\rm ref}$ must thus be defined as a proxy for $F_{\rm loc}$. For example, most studies use the disc-integrated spectrum, $F_{\rm out}$. Yet, as we explain in Sect. 2.1.1, $F_{\rm out}$ may not be representative of local stellar spectra because its line profiles are formed by a sum of the CLVs and stellar rotation over the stellar surface. An alternative is to use theoretical spectra from models of stellar atmospheres, but their accuracy is also limited by the lack of observational constraints on the spatially resolved stellar surface. Even if it is possible to determine an accurate proxy for the profile of the local planet-occulted stellar line, it can be critical to shift it at the correct position for a given planet-occulted stellar region, which requires a good knowledge of the stellar rotation and planetary trajectory. The choice for $F_{\rm ref}$ thus has a huge impact on the retrieved absorption spectrum from the planetary atmosphere.

---

[7] In the following analysis, we chose this approximation and neglected the spatial variations of the intensity profile over the regions occulted by the planet in a given simulated exposure, focusing on the impact of variations along the full transit chord.

A forward model such as the EVE code allows us to generate theoretical absorption spectra with an exact knowledge of the absorption lines from the planetary atmosphere and of the local stellar spectra occulted by the planet. By processing the theoretical spectra in the same way as observational data, using various proxies for F_{ref}, we can thus evaluate their impact on the retrieval of the planetary lines. In the figures of the following sections, we show the 'unaffected' absorption spectrum computed with the exact F_{loc} from the simulations as a point of comparison.

3. Stellar and orbital contamination in absorption spectra

In this section, we show how the absorption signature retrieved from absorption spectra depends on the spectral profile chosen as proxy for the planet-occulted spectrum. As a test case to study the biases in the measured absorption spectra, we chose to simulate the transits of HD 209458 b (Henry et al. 2000; Charbonneau et al. 2000), a typical and well-studied Hot Jupiter for which the detection of atmospheric sodium has been challenged due to stellar contamination (Casasayas-Barris et al. 2020, 2021). We used the EVE code to produce synthetic spectra of HD 209458 during the planetary transit. First, we simulated the transit of the planet without sodium in its atmosphere to investigate the spurious signatures created by stellar contamination. We then performed the same simulations with a thermosphere containing neutral sodium atoms (Sect. 2.1.2), to investigate how the stellar signature can bias the planetary one. The simulations were performed using two different synthetic stellar grids: spectral profiles affected by rotation (cf. case b Sect. 2.1.1); spectral profiles affected by CLVs (cf. case c Sect. 2.1.1). We chose to study these effects separately to clearly identify the impact of their contamination on the atmospheric absorption spectrum. For each effect, we also explored different definitions for the reference spectrum. We simulated a planetary thermosphere made of ∼90% of hydrogen and ∼10% of helium. Neutral sodium was included as a trace species, with an abundance of ∼0.0001% (0.000007 ppm) (Nikolov et al. 2018), with respect to the total thermospheric density. This composition yields a mean atomic mass of ∼1.30746 units of atomic mass. The absolute density of the thermosphere was scaled so that its excess atmospheric absorption signature peaks at approximately ∼1% in the Na I D2 and D1 doublet, which is typical of the measured Na I absorption signature of Hot Jupiters (e.g. Wyttenbach et al. 2017; Casasayas-Barris et al. 2018; Seidel et al. 2019). Table 1 lists the parameters we used for the simulated system.

3.1. Impact of stellar rotation

We explored two different stellar rotational velocities ($v_{\mathrm{eq}} \sin(i) = 3\,\mathrm{km\,s^{-1}}$ and $20\,\mathrm{km\,s^{-1}}$) and two different sky-projected spin–orbit angle ($\lambda = 0$ and 45°). We note that the impact parameter also influences the orbital track of the planet and its projected trajectory across the stellar surface, so that high values of the impact parameter and spin–orbit angle can, for example, lead the planet to transit only the blue or red-shifted part of the stellar disc. In our present simulations, however, we set the impact parameter to 0 to isolate the net effects of stellar rotation and spin–orbit angle.

We compared the absorption spectra retrieved through three different ways of defining F_{ref}: with the disc-integrated spectrum F_{out}, as is commonly done in the literature; with F_{out} shifted to the radial velocity of the stellar region occulted by the planet in a given exposure, and with the local stellar line profile ($\mathrm{F}_{\mathrm{loc}}\,(\mu = 1)$) from the stellar region that would be occulted at the centre of the stellar disc (here corresponding to the centre of the transit T_0). The retrieved absorption spectra are compared with the unaffected absorption spectrum calculated with the local stellar profile ($F_{\mathrm{loc}}(t)$) from each planet-occulted region. Here, we focus on absorption spectra calculated at two representative time-steps: the centre of the transit (T_0) and the second contact (T_2, just after ingress).

Table 1. HD 209458's stellar and planetary properties.

Parameter	Value
Stellar	
Radius ($R_\odot$)	$1.155^{+0.015}_{-0.016}$
Mass ($M_\odot$)	1.119 ± 0.033
T_{eff} (K)	6065 ± 50
Metallicity [Fe/H]	0.00 ± 0.05
$\log g$ ($\mathrm{cm\,s^{-2}}$)	$4.361^{+0.007}_{-0.008}$
Age (Gyr)	4.0 ± 2.0
$v_{\mathrm{eq}} \sin i$ ($\mathrm{km\,s^{-1}}$)	$4.228 \pm 0.007^{(\dagger)}$
Planetary	
Radius (R_{Jup})	$1.359^{+0.016}_{-0.019}$
Mass (M_{Jup})	$0.682^{+0.015}_{-0.014}$
Semi-major axis (au)	$0.04707^{+0.00046}_{-0.00047}$
Period (days)	$3.52474859 \pm 0.00000038$
Inclination (deg)	$86.71 \pm 0.05^{(\dagger\dagger)}$
Sky-projected spin–orbit angle (deg)	$1.58 \pm 0.08^{(\dagger\dagger\dagger)}$

Notes. Values are the same as those used or derived in Casasayas-Barris et al. (2020), except for the rotational velocity of the star and sky-projected spin–orbit angle of the planet, taken from Casasayas-Barris et al. (2021). Parameters that we vary in the study: $^{(\dagger)}$ Sect. 3 set to 3 and 20; $^{(\dagger\dagger)}$ Sect. 3 set to 90; $^{(\dagger\dagger\dagger)}$ Sect. 3 set to 0 and 45.

3.1.1. Without the thermosphere

Figure 4 shows the results of simulations with only the planetary disc simulated during the transit. Figure A.1 shows the quantities used to compute the absorption spectra to help understand these results. With $v_{\mathrm{eq}} \sin(i) \rightarrow 0$ the local planet-occulted line profile tends to be equal to both $F_{\mathrm{loc}}\,(\mu = 1)$ and F_{out}, since the Doppler-shift of the planet-occulted regions and the broadening of the disc-integrated lines are then negligible. All other effects being ignored, POLDs are negligible for slow rotators and using F_{out} as reference to compute absorption spectra is a valid approximation. We discuss below the cases of moderate to fast rotators.

At T_2, the case where $F_{\mathrm{loc}}\,(\mu = 1)$ is used as reference to compute the absorption spectrum (green curves) has the strongest POLD regardless of the value of the stellar rotational velocity. This is because the planet-occulted stellar lines are narrow and shifted away from their rest wavelength by stellar rotation, while the line profile of $F_{\mathrm{loc}}\,(\mu = 1)$ is similarly narrow but remains centred on the rest wavelength. The POLD becomes stronger with increasing $v_{\mathrm{eq}} \sin(i)$, as the planet-occulted line profile separates more and more from the line profile of $F_{\mathrm{loc}}\,(\mu = 1)$, and the former ends up being normalised by the continuum of the latter – at which point the POLD is made of the full spectral profiles of both lines. At T_0, on the other hand, as the planet has a null impact parameter, the planet-occulted line

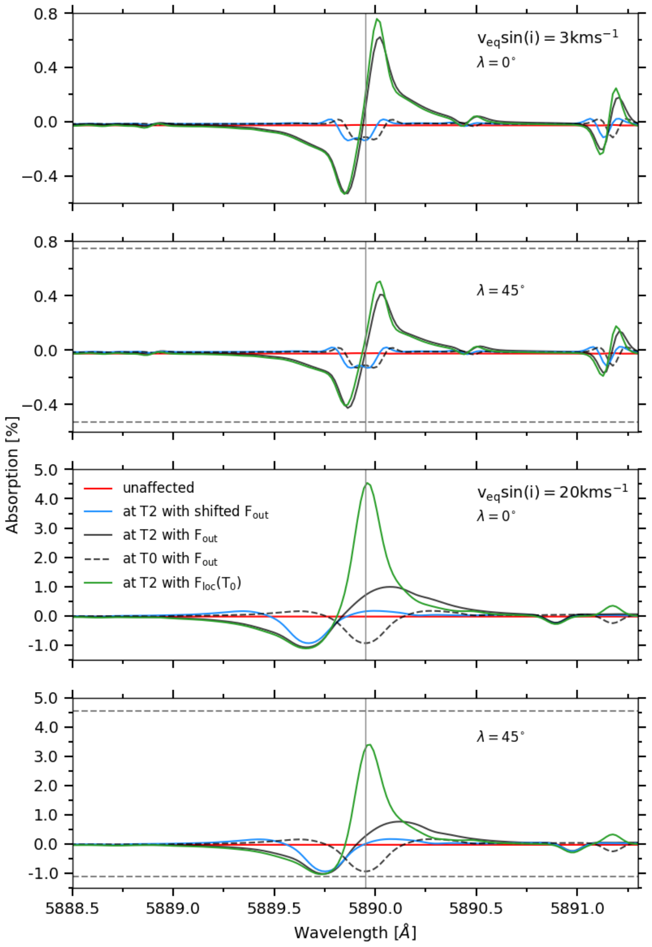

Fig. 4. Excess absorption spectra without thermospheric sodium, as a function of wavelength in the stellar rest frame, computed with the different reference spectra mentioned in Sect. 3.1. We display results for two $v_{\rm eq}\sin(i)$ values as well as for two sky-projected spin–orbit angles. The vertical grey lines mark the transition wavelength of Na I D2. For comparison the horizontal dashed grey lines mark the highest and lowest values of the POLD, obtained for $\lambda = 0°$.

profile is naturally equal to the line profile in $F_{\rm loc}\,(\mu = 1)$ and the absorption spectrum does not exhibit any POLD.

We now discuss the case for which $F_{\rm out}$ is used as reference without being shifted at the position of the planet-occulted line (black curves). We first consider the exposure at T_2. For moderate values of $v_{\rm eq}\sin(i)$, the POLD is similar to the case with $F_{\rm loc}\,(\mu = 1)$ because the planet-occulted line profile remains close to its rest wavelength and the line profile of $F_{\rm out}$ is only slightly broadened compared to $F_{\rm loc}\,(\mu = 1)$. When $v_{\rm eq}\sin(i)$ increases, the peak-to-peak amplitude of the POLD increases but remains smaller than the case with $F_{\rm loc}\,(\mu = 1)$ used as reference. This is because the planet-occulted line shifts farther from its rest wavelength but remains in the wings of the broadened disc-integrated line of $F_{\rm out}$, rather than the flat continuum of $F_{\rm loc}\,(\mu = 1)$. The POLD is maximum and tends towards the same profile as the planet-occulted profile, similarly to the case with $F_{\rm loc}\,(\mu = 1)$ used as reference, in the case of fast rotators when the disc-integrated line profile is flattened by broadening and the occulted line profile is normalised by a nearly constant flux.

For a given $v_{\rm eq}\sin(i)$ the amplitude of the POLD decreases when the planet-occulted line shifts closer to its rest wavelength (which corresponds to the centre of the disc-integrated line profile), as the flux in $F_{\rm out}$ gets more similar to the flux in the occulted line core. The POLD is thus minimal at the centre of the transit (T_0) for an aligned orbit, but its amplitude is not null and is controlled by the flux ratio between the occulted and disc-integrated line cores (>1 since the disc-integrated line is rotationally broadened) and thus increases with larger $v_{\rm eq}\sin(i)$.

The case for which $F_{\rm out}$ is used as reference, but shifted at the position of the planet-occulted line results in the same POLD as the absorption spectrum at T_0 computed with $F_{\rm out}$ (i.e. the dashed black curve), but shifted to the radial velocity of the planet-occulted stellar region.

Increasing the sky-projected spin–orbit angle changes the orbital track over the stellar surface, such that the planet occults regions with lower radial velocity throughout the transit. For the same time-step, the shift of the planet-occulted line profiles is smaller. Their spectral distance to an unshifted reference spectrum ($F_{\rm out}$ or $F_{\rm loc}(\mu = 1)$) is reduced and the resulting POLD is of smaller amplitude.

3.1.2. With the thermosphere

Figures 5 and 6 show the results obtained with a thermosphere included in our simulation, for $v_{\rm eq}\sin(i) = 20$ and $3\,\mathrm{km\,s^{-1}}$, respectively. As expected, we see in these figures that the unaffected atmospheric absorption signature is shifted according to the radial orbital velocity of the planet at the time of the considered exposures (i.e. at T_2 and T_0). Also, we notice that the POLD can to some extent compensate the atmospheric absorption signature. This is accentuated when there is an overlap between these signatures; for example, at the centre of the transit (T_0) where both the stellar radial velocity and the radial orbital velocity of the planet are null (for the circular, aligned orbit assumed in our simulations). As we show in Sect. 3.1.1, the POLD increases in amplitude when $\mathrm{v_{eq}}\sin(\mathrm{i})$ increases. The atmospheric absorption signature is thus less affected for lower $v_{\rm eq}\sin(i)$.

We also note that for the same reasons as explained in the paragraphs above, at T_0, the absorption spectrum derived with $F_{\rm loc}\,(\mu = 1)$ is the same as the unaffected case. The same goes for the absorption spectrum derived with both $F_{\rm out}$ and the shifted $F_{\rm out}$.

The overlap between the atmospheric absorption signature and the POLD can happen at various positions along the transit chord depending on the radial orbital velocity of the planet. For example the radial orbital velocity of our test planet at T_2 is $v_{\rm orb}(T_2) = 14.4\,\mathrm{km\,s^{-1}}$. For the case with $v_{\rm eq}\sin(i) = 3\,\mathrm{km\,s^{-1}}$, the radial velocity of the corresponding occulted stellar region is $2.6\,\mathrm{km\,s^{-1}}$ and $1.8\,\mathrm{km\,s^{-1}}$ for $\lambda = 0°$ and $45°$, respectively. In both cases, the atmospheric signature is almost entirely disentangled from the POLD and is weakly affected for all choices of $F_{\rm ref}$. On the contrary, for the case with $v_{\rm eq}\sin(i) = 20\,\mathrm{km\,s^{-1}}$, the radial velocity of the occulted stellar region is $17.3\,\mathrm{km\,s^{-1}}$ and to $12.3\,\mathrm{km\,s^{-1}}$ for $\lambda = 0°$ and $45°$, respectively. In this case, the atmospheric signature is shifted close to the POLD and is strongly contaminated.

3.1.3. Conclusion

In conclusion, using the disc-integrated line profiles of a star in rotation as a proxy for the planet-occulted stellar line profiles results in spurious emission-like and absorption-like features in absorption spectra. As $v_{\rm eq}\sin(i)$ increases, the amplitudes of the simulated POLDs increase because the broadened, shallower disc-integrated stellar line profiles differentiate more and more from the local planet-occulted line profiles. In the case

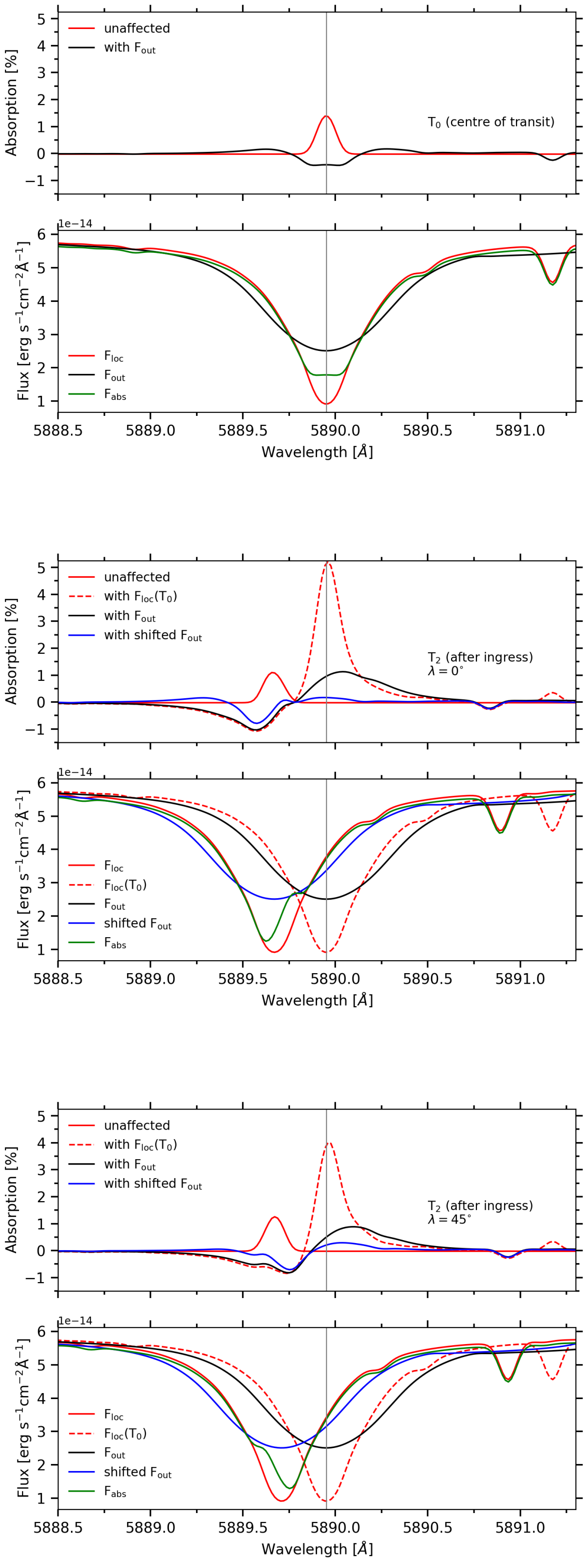

Fig. 5. Excess absorption spectra with thermospheric sodium, as a function of wavelength in the stellar rest frame, computed with the different reference spectra mentioned in Sect. 3.1 and for a $v_{eq}\sin(i) = 20\,\mathrm{km\,s^{-1}}$. *Upper panels*: excess absorption spectra. *Lower panels*: quantities used to compute the absorption spectra. Here, F_{out} was multiplied by the ratio between the occulted surface and the surface of the star to bring it to the level of F_{loc} and make the comparison easier. We show results for different time-steps (T_2 and T_0) and sky-projected spin–orbit angles (0 and 45°).

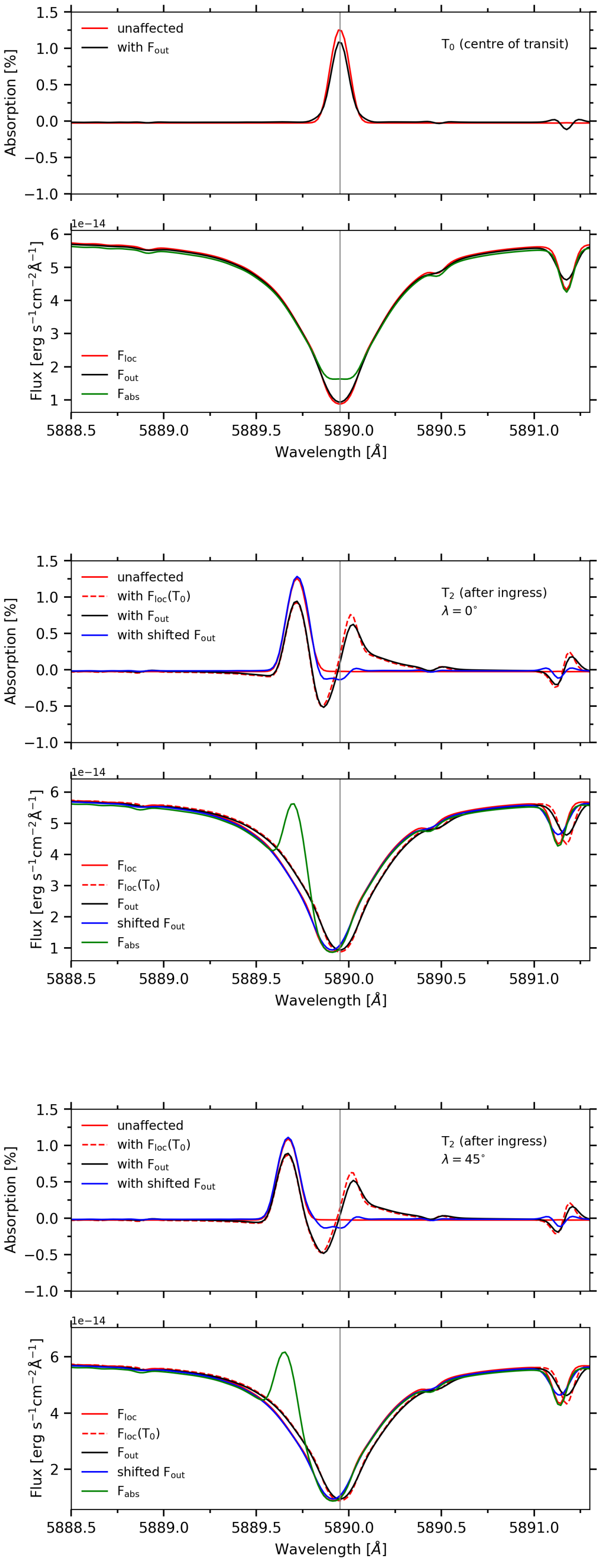

Fig. 6. Excess absorption spectra with thermospheric sodium, as a function of wavelength in the stellar rest frame, computed with the different reference spectra mentioned in Sect. 3.1 and for a $v_{eq}\sin(i) = 3\,\mathrm{km\,s^{-1}}$. *Upper panels*: excess absorption spectra. *Lower panels*: quantities used to compute the absorption spectra. Here, F_{out} was multiplied by the ratio between the occulted surface and the surface of the star to bring it to the level of F_{loc} and make the comparison easier. We show results for different time-steps (T_2 and T_0) and sky-projected spin–orbit angles (0 and 45°).

of very fast rotators, the POLD tends to directly reproduce the planet-occulted stellar line profiles. Even for small $v_{\rm eq}\sin(i)$, the amplitude of the POLD can be on the order of magnitude of typical atmospheric absorption signatures. When the orbital track of the planet overlaps with the planet-occulted stellar line track in radial velocity-phase space, it becomes difficult to disentangle planetary atmospheric absorption signatures from the POLD. No matter the line profile that is used for $F_{\rm ref}$, it will induce POLDs if it is not shifted to the radial velocity of the planet-occulted stellar lines. It can therefore be more adequate to use a shifted $F_{\rm out}$ as a reference spectrum rather than the correct but unshifted line profile. A larger spin–orbit angle reduces the overall amplitude of the POLD as the planet occults stellar regions with lower radial velocity during its transit.

3.2. Centre-to-limb variations

For these simulations, the synthetic local stellar line profiles were influenced by CLVs, but no rotational velocity was included. We compared the absorption spectra retrieved through two different ways of defining $F_{\rm ref}$: with the disc-integrated spectrum $F_{\rm out}$, whose spectral line profile is a combination of the CLVs over the entire stellar disc and whose continuum is affected by a mean broadband limb darkening; with $F_{\rm loc}(\mu = 1)$, from the stellar region that would be occulted at the centre of the stellar disc, which matches the planet-occulted line profile at transit centre (T_0) in our simulation, but deviates from the local stellar line profiles towards the limbs due to the CLVs. Figure 7 shows the results of the simulations with and without the thermosphere for the time-step at the centre of the transit (T_0). Figure 8 shows the results of the same simulations for the time-step just after ingress (T_2).

3.2.1. Impact on the stellar line profiles

When using $F_{\rm out}$ as reference, POLDs are created at both time-steps. At T_0, where the planet is at the centre of the stellar disc, the planet-occulted line profile is not influenced by CLVs, and differs the most from the line profile of $F_{\rm out}$, especially in the wings. At T_2, both the planet-occulted and disc-integrated stellar line profiles are affected by CLVs. Their wings, in particular, are closer in shape which tends to mitigate the amplitude of the POLD in the absorption spectrum. When using $F_{\rm loc}(\mu = 1)$ as reference, POLDs are created only at T_2, where the planet-occulted line profile from the stellar limb is the most affected by CLVs. At T_0 the reference matches by definition the planet-occulted line profile.

We conclude that although the POLDs created by CLVs are smaller than those caused by moderate-to-fast stellar rotator, they can still reach 0.2–0.4%. In the case of a slowly rotating star, these POLDs can therefore lead to misinterpretation of the actual atmospheric signature. In this case, there is no better choice for a reference spectrum between $F_{\rm out}$ and $F_{\rm loc}(\mu = 1)$. When the planet occults regions close to the limb, it is better to use $F_{\rm out}$ as its line profile is also affected by CLVs and is thus closer to the planet-occulted line profile. However, closer to the stellar disc centre, it is better to use $F_{\rm loc}(\mu = 1)$ as the effect of CLVs on the planet-occulted line profile becomes negligible.

3.2.2. Impact on the stellar continuum

In addition to the spurious signature in the line profiles, we also note an underestimation (resp. overestimation) of the continuum level of the absorption spectra computed with $F_{\rm out}$ at a time-step of T_2 (resp. T_0). This is due to broadband limb-darkening (BLD), which uniformly reduces the continuum of the local stellar spectrum closer to the stellar limb. When accounting for this effect in the definition of the stellar grid, the resulting $F_{\rm out}$ is affected by an average BLD and its continuum level decreases compared to the continuum of a purely uniform stellar emission case.

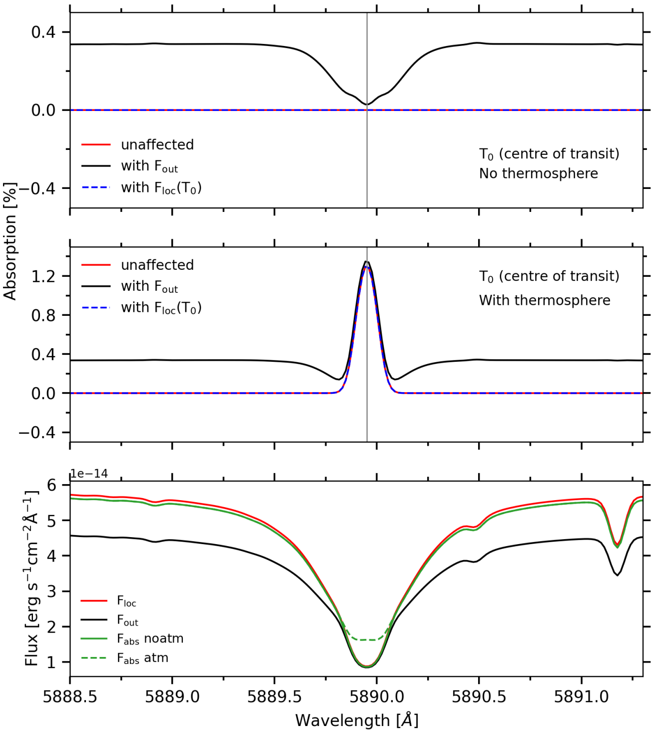

Fig. 7. Atmospheric absorption spectra at the centre of the transit as a function of wavelength in the stellar rest frame, for synthetic stellar spectra containing CLVs. *Upper panel*: absorption spectrum of the planetary disc only. *Middle panel*: absorption spectrum of the planet with a thermosphere. The black dashed curves were computed using $F_{\rm out}$. Blue dashed curves were computed using $F_{\rm loc}(T_0)$. *Lower panel*: quantities used to compute the absorption spectra. We multiplied $F_{\rm out}$ by the ratio between the occulted surface and the surface of the star to bring it to the level of $F_{\rm loc}$ and make the comparison easier.

Making the approximation that only BLD affects the stellar spectrum (i.e. the local line profile is uniform over the stellar disc) and that it takes the form of a multiplicative coefficient, we write Eq. (1) as:

$$\frac{F_{\rm abs}(\lambda,t)}{F_{\rm out}(\lambda)} = \frac{\sum\limits_{k,k'} \mathrm{I}_0(\lambda)\,\mathrm{LD}_k(t)\,\Delta\Omega_{k,k'} + \sum\limits_{l,l'}\left[1-\mathrm{e}^{-\tau_{l,l'}(\lambda)}\right]\mathrm{I}_0(\lambda)\,\mathrm{LD}_l(t)\,\Delta\Omega_{l,l'}}{\sum\limits_{i}\mathrm{I}_0(\lambda)\,\mathrm{LD}_i\,\Delta\Omega_i}, \tag{6}$$

After simplifying for I_0 and neglecting BLD variations across the planet-occulted surface, we get

$$\frac{F_{\rm abs}(\lambda,t)}{F_{\rm out}(\lambda)} = \frac{\mathrm{LD}(t)\,\mathrm{S}_{\rm pl}(t) + \left[1-\mathrm{e}^{-\tau_{atm}(\lambda)}\right]\mathrm{LD}(t)\,\mathrm{S}_{\rm atm}(t)}{S_*^{\rm LD}}. \tag{7}$$

where the pl and atm subscripts refer to the stellar regions occulted by the planetary disc and the thermosphere respectively,

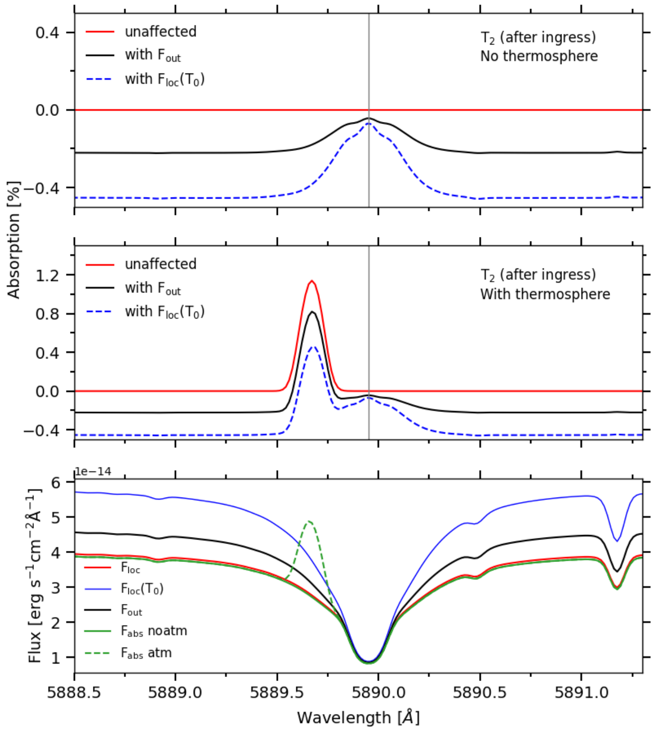

Fig. 8. Atmospheric absorption spectra at the time-step after ingress as a function of wavelength in the stellar rest frame, for synthetic stellar spectra containing CLVs. *Upper panel*: absorption spectrum of the planetary disc only. *Middle panel*: absorption spectrum of the planet with a thermosphere. The black dashed curves were computed using $F_{\rm out}$. Blue dashed curves were computed using $F_{\rm loc}(T_0)$. *Lower panel*: quantities used to compute the absorption spectra. We multiplied $F_{\rm out}$ by the ratio between the occulted surface and the surface of the star to bring it to the level of $F_{\rm loc}$ and make the comparison easier.

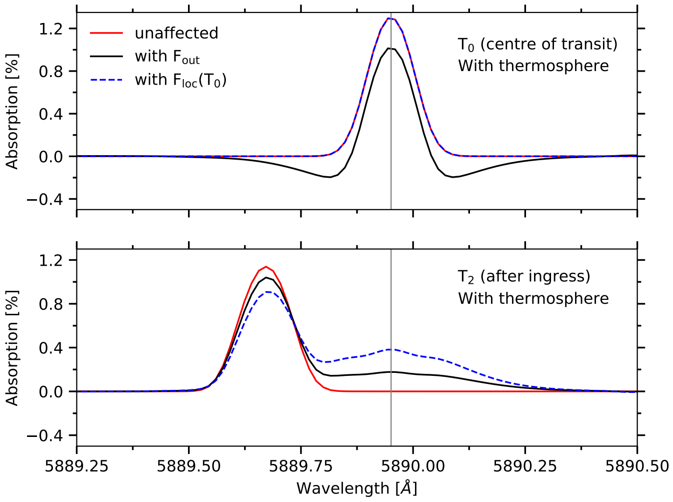

Fig. 9. Zoom on the middle panels of Figs. 7 and 8 after manually shifting the continuum of the absorption spectra to 0.

$S_*^{\rm LD}$ stands for the BLD-weighted stellar surface, and τ_{atm} stands for the mean spectral optical depth in the atmosphere.

At T_0, the planet-occulted surface in $F_{\rm abs}$ is not affected by BLD (LD = 1), while $S_*^{\rm LD}$ is smaller than the stellar surface. The continuum of $F_{\rm abs}/F_{\rm out}$ is thus greater than the planet-to-star surface ratio. In contrast at T_2, near the stellar limb, the planet-occulted surface in $F_{\rm abs}$ is strongly down-weighted by BLD (LD < 1), so that the continuum of $F_{\rm abs}/F_{\rm out}$ is lower than the planet-to-star surface ratio. First, this shows the need to properly account for limb-darkening to make absorption spectra comparable. Subtracting the known planet-to-star surface ratio is not sufficient, as we can see in the above simulation where the continuum of $F_{\rm abs}/F_{\rm out} - S_{\rm pl}/S_*$ will be respectively larger and lower than zero at T_0 (Fig. 7) and T_2 (Fig. 8). In the literature, absorption spectra are set to a null value outside of the planetary absorption lines by subtracting the measured continuum ($\mathrm{LD}(t)\ S_{\rm pl}(t)/S_*^{\rm LD}$) from Eq. (7). However, it is clear by looking at Eq. (7) that this operation is not sufficient to remove the effect of BLD on the atmospheric absorption signature. On the contrary, Eq. (7) (see also Mounzer et al. 2022) illustrates how we can correct for BLD by multiplying the absorption spectrum with $S_*^{\rm LD}/(\mathrm{LD}(t) S_*)$, thus ensuring that all absorption spectra are equivalent. We note that this correction can be applied before or after subtracting for the measured continuum. Figure 9 shows the absorption spectra of the same simulation as Sect. 3.2.1 after we shifted their continuum to 0. This figure shows that the ratio between the continuum and the peak of the atmospheric absorption signature does not match the one of the unaffected signature, as we did not correct for the BLD coefficient ratio introduced above.

Although the effect of BLD is smaller than the CLV effect on the retrieved atmospheric line profile, it can become significant when searching for faint signatures and thus needs to be accounted for as described above. We note that the standard practice (e.g. Casasayas-Barris et al. 2020, 2021, 2022) of normalising the out-of-transit and in-transit spectra to the same flux level before computing the absorption spectrum does not remove this bias (see Appendix B). We thus emphasise the importance of not normalising flux spectra to the same level and not simply correcting absorption spectra for their measured continuum, but instead accounting for the effect of BLD in individual absorption spectra with the correction factor given above.

4. Application to exoplanet systems

Now that we better understand how the occultation of stellar lines by a transiting planet can bias the absorption spectrum of its atmosphere, we can study the case of two planetary systems of particular interest in detail.

4.1. Controversial case of HD 209458 b

4.1.1. Context

Charbonneau et al. (2002) analysed transit observations collected by the HST STIS spectrograph and claimed the detection of sodium atoms in the atmosphere of HD 209458 b. This detection was corroborated by Snellen et al. (2008) and Albrecht et al. (2008) after studying Subaru's HDS spectrograph and UVES/VLT data. More recently, Casasayas-Barris et al. (2020) studied in details the absorption spectra of transits of HD 209458 b using observations collected with HARPS-N and CARMENES. Based on a similar methodology to ours, these authors simulated transits of a planetary body corresponding to HD 209458 b. They first computed a disc integrated spectrum (i.e. $F_{\rm out}$), using the tool `Spectroscopy Made Easy` (Valenti & Piskunov 1996) along with line lists from the VALD database, and accounting for CLVs and stellar rotation. Then, for a series of positions corresponding to the observed exposures they computed the synthetic local spectra absorbed by the planet and subtracted it from F_{out} to derive in-transit spectra that they used to compute absorption spectra.

They showed that the transit of HD 209458 b's opaque continuum could reproduce the observed features, without the need for sodium absorption from the atmosphere. However, there remained a difference between their model and the observations, which led Casasayas-Barris et al. (2021) to analyse absorption spectra of HD 209458 b collected by ESPRESSO using a refined model. By including non-local thermodynamic equilibrium (NLTE) effects in their synthetic stellar spectra, they were able to match better the observed absorption feature in the Na I D2 line. This supports the conclusion that the apparent absorption signatures of HD 209458 b in the Na I D1 and D2 spectral lines can entirely be explained by POLDs induced by CLVs and stellar rotation. However, Casasayas-Barris et al. (2021) did not investigate whether the observations could still trace the presence of atmospheric Na I absorption from the planet.

4.1.2. Reproducing published results

The aim of this section is to investigate whether the feature observed during the transit of HD 209458b could be explained by a combination of POLDs and atmospheric absorption or only by POLDs including NLTE effects alone (as proposed by Casasayas-Barris et al. 2021). To do so, we simulated transits of HD 209458 b with the EVE code, following the approach described in Sect. 2.

Our first step was to reproduce the same absorption spectrum as Casasayas-Barris et al. (2021), that is, by including NLTE effects in the stellar spectrum and simulating a transit of a bare planet. To define the spectral grid of HD 209458, we used the interpolation routine provided in the `Turbospectrum_NLTE` package[8] to interpolate a MARCS photospheric model corresponding to a temperature of 6065 K, a $\log g$ of 4.361 cm s^{-2}, and a metallicity [Fe/H] of 0. We then used `Turbospectrum` to compute a series of intensity spectra emerging from this stellar atmosphere model and thus accounting for broad-band limb darkening and CLVs. The shift in wavelength of the local spectra due to stellar rotation was added subsequently to each grid cell in `EVE`. We simulated a series of exposures during the transit of an opaque disc with the radius of HD 209458 b. The timestep of the simulation was set to a typical exposure time of two minutes for a bright star observed with ESPRESSO, and the spectral resolution and instrumental response correspond to this instrument.

Table 1 shows the parameters of the system that we used for the simulations. To be comparable with Casasayas-Barris et al. (2020, 2021), all flux spectra were normalised to the same continuum and absorption spectra were computed as $\frac{F_{\mathrm{in}}(t)-F_{\mathrm{out}}}{F_{\mathrm{out}}}$[9]. We caution that while this step is commonly applied in the literature to set the continuum of absorption spectra to 0, it can be the source of bias (Sect. 3.2.2). To make sure that this step would not change our conclusions, we computed the difference between the peak of the atmospheric signature and the continuum of the mean absorption spectrum. We found that normalising spectra beforehand only increases the absorption by 0.01%, and thus that this bias is negligible in the present case.

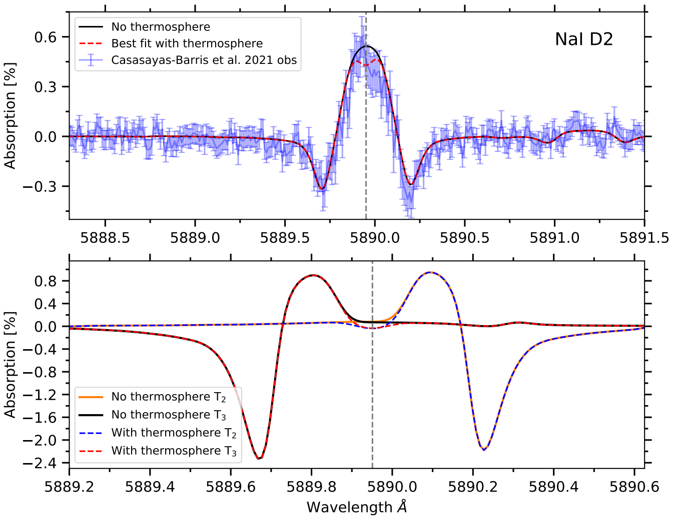

Fig. 10. Theoretical absorption spectra of HD 209458 b computed with the out-of-transit spectrum as a function of the wavelength in the planetary rest frame with and without sodium atmosphere. The blue points are ESPRESSO data from Casasayas-Barris et al. (2021). *Upper panel*: mean of the theoretical absorption spectra between contact times T_2 and T_3. *Lower panel*: theoretical absorption spectrum at contact times T_2 and T_3.

4.1.3. Searching for additional signatures

As can be seen in Fig. 10, the simulation with NLTE alone provides a good match to the observed absorption spectrum, similarly to Casasayas-Barris et al. (2021). However, we note that there still remains a gap between the simulation and the observation, which might be explained by the absorption signature from planetary sodium. By taking a closer look at the absorption spectrum around the Na I D1 line (see Fig. C.1), we see a deviation from the simulated POLD in the red wing of the measured profile, which is not present in the D2 line. This deviation is unlikely to be of planetary origins because it is not centred in the planet rest frame and because, considering that the D2/D1 oscillator strength ratio is about two, we would expect an even deeper absorption signature in the D2 line than in the D1 line. We thus consider the deviation in the D1 line to be spurious, and used the D2 line alone to fit a planetary atmospheric signature. The temperature and radius of the thermosphere were fixed to 8000 K and 2.94 planetary radius (i.e. the Roche lobe), respectively. We found that the best fit is obtained for a thermosphere with a sodium density at the top of 0.0007 ± 0.0003 at cm^{-3} (see the corresponding absorption spectrum in Fig. 10). Although a model with no thermospheric sodium is consistent with the data within 2σ from the best fit, our results hint at the possible presence of sodium in the atmosphere of HD 209458 b. Precise stellar models and repeated observations with ESPRESSO or other suited high-resolution spectrographs, along with a coupled exploration of the stellar and planetary models with codes such as EVE will be necessary to confirm this result.

Figure 11 shows the 2D map of excess absorption spectra for the simulation with NLTE alone and for the best-fit simulation with atmospheric sodium. These maps are built to show the time evolution of the absorption spectrum as a function of wavelength during the transit, allowing a direct visualisation of the putative signature along the planetary orbital tracks and planet-occulted stellar line tracks. In the upper panel, showing the simulation without Na I in the thermosphere, we notice the typical POLDs induced by stellar rotation (Sect. 3.1). In the

---

[8] Written by Thomas Masseron and available for download at `https://github.com/bertrandplez/Turbospectrum_NLTE`

[9] Instead of $\frac{F_{\mathrm{out}}-F_{\mathrm{in}}(t)}{F_{\mathrm{out}}}$ as in previous sections. In the following figures, absorption is thus associated with negative values as opposed to figures in the Sect. 3.

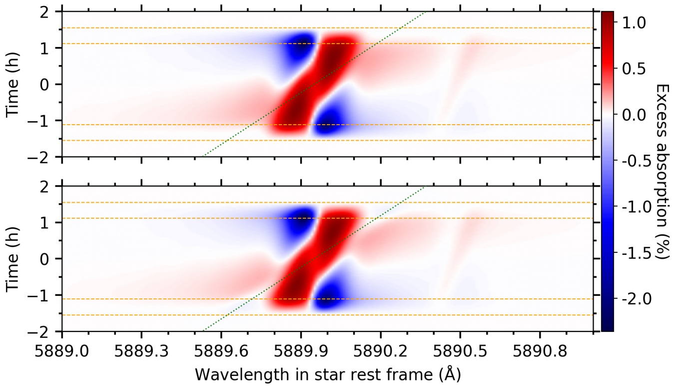

Fig. 11. Theoretical absorption spectra of HD 209458 b around the Na I D2 line, as a function of time and wavelength in the stellar rest frame. The simulated out-of-transit spectrum was used as reference. *Upper panel*: without a thermosphere. *Lower panel*: with a thermosphere containing neutral sodium atoms. The atmospheric absorption signature follows the orbital track of the planet represented by green curves. The horizontal orange dashed lines show the contact times of the transit. The y-axis shows time from the centre of the transit.

lower panel, the additional contribution from the thermosphere is slightly visible along the orbital track of the planet, particularly at the beginning and end of the transit. Even though the planetary atmospheric and the POLD tracks are relatively well disentangled for this system, the width of the POLD is such that they contaminate the atmospheric signature during most of the transit, especially around T_0. It is thus not straightforward to isolate the pure atmospheric signature, for example, by masking the POLD. Furthermore, in real observations disentangling the two features would be made harder by noise. In cases such as that of HD 209458b, it thus remains useful to interpret the mean absorption spectrum rather than individual exposures, to detect a possible atmospheric signature thanks to the increased signal-to-noise ratio (S/N) at the expense of the loss in the temporal evolution of the signal and of a stronger blending between the POLD and atmospheric signature. This highlights the need to better understand how POLDs bias the absorption spectrum when searching for the presence of a planetary atmosphere.

Finally, we investigated changing the Na I stellar abundance in our synthetic stellar model, as it modifies the depth of the stellar lines and thus the amplitude of the POLD. Casasayas-Barris et al. (2021) showed that including NLTE effects increases the amplitude of the POLD around the Na I doublet lines. We thus wanted to assess whether a change in the Na I stellar abundance could lead to the same result as including NLTE effects. We were able to get a better agreement with the observed absorption spectrum using a synthetic stellar model without NLTE and an adjusted Na I abundance (Fig. D.1), but the match is not as good as that obtained by Casasayas-Barris et al. (2021), where NLTE effects are included. Furthermore, changing the stellar Na I abundance also changes the depth of the disc-integrated stellar line. In this simulation, the stellar abundance was such that the synthetic disc-integrated stellar line departs from the observed one. Modifying the stellar abundance of the planet-occulted line is therefore not a likely alternative to explain the observed absorption spectrum in the case of HD 209458 and it highlights the need to fit together the POLD and disc-integrated lines, or at least use a prior on the abundance derived from the fit to the disc-integrated spectrum when fitting the POLD.

4.2. The peculiar case of MASCARA-1 b

In the case of HD 209458 b, the atmospheric absorption signature that we simulated could be distinguished from the POLD in most exposures, as both signatures follow separate tracks in velocity-phase space that only cross at transit centre (see Fig. 11). However, some orbital and stellar configurations can be such that the orbital and planet-occulted tracks overlap during most of the transit. This typically happens for planets on aligned and circular orbits with orbital radial velocity at ingress and egress on the order of the sky-projected stellar rotational velocity (Sects. 3 and 4.3).

Casasayas-Barris et al. (2022) studied ESPRESSO transit observations of such a system, MASCARA-1 b (Talens et al. 2017), and could not assess the presence of an atmospheric Na I signature due to the overlap between the orbital and planet-occulted tracks. The authors however explored the effects of stellar rotation and orbital parameters in the Na I doublet, finding that their simulated POLD, being too shallow, could never fully explain the observed signature.

Expanding on their analysis, we note that the large stellar rotational velocity yields a broad and shallow disc-integrated line profile, so that the POLD directly traces the planet-occulted line profile, as explained in Sect. 3.1. Deeper planet-occulted stellar line profiles would thus induce stronger POLDs that could help explain the absorption spectrum produced by Casasayas-Barris et al. (2022). Interestingly, both increasing the stellar abundance of Na I and accounting for NLTE effects in the synthetic stellar sodium lines (Casasayas-Barris et al. 2021) increase their depth. We first included NLTE effects in our synthetic stellar model and then explored the effect of Na I stellar abundance, setting the EVE transit simulations[10] as described in Sect. 2.

First, we used the nominal stellar parameters from Table 2 and a solar abundance. We see in the upper panel of Fig. 12, which shows the mean absorption spectra of MASCARA-1 b around the Na I D2 line, that the simulated POLDs are not strong enough to match the observed signature. This is in part due to the fact that the stellar line profiles are not deep enough for a solar abundance, as can be seen in Fig. 13. A visual inspection of the absorption spectrum by Casasayas-Barris et al. (2022) (Fig. 12) shows that it is asymmetrical in the planetary rest frame. This is an interesting feature considering that the putative absorption by the planetary atmosphere would fall in the blue wing of the signature. Furthermore, we know from the discussions in previous sections of this paper that an atmospheric absorption signature would peak in the other direction than the POLD. First, we found that the core and red wing of the observed signature can be reproduced by the POLD induced by deeper occulted lines, with $A_{*}(\mathrm{Na\,I}) = 12 + \log_{10}\left(\frac{n(\mathrm{Na\,I})}{n(\mathrm{H})}\right) = 7.5$ (middle panel of Fig. 12, dashed red curve). We note that we modified the $v_{\mathrm{eq}}\sin(i)$ value by -1σ to get a better match. Using this stellar abundance, we found a good match to the blue wing of the observed signature after adding a thermosphere in the simulation (red curve, middle panel of Fig. 12) with a temperature of 9500 K, a radius of 3.23 planetary radius (Roche lobe radius), and a Na I density at this radius of 1×10^{-14} at cm $^{-3}$. Unfortunately the stellar sodium abundance necessary to reproduce the absorption spectrum yields a strong mismatch between the simulated and observed disc-integrated spectra (Fig. 13), highlighting

---

[10] The stellar spectrum of MASCARA-1 was generated following the same steps as in Sect. 4.1, using a MARCS model with a temperature of 7500 K, a $\log g$ of 4 cm s^{-2} and a metallicity [Fe/H] of 0. Table 2 shows the system parameters used in the simulation.

Table 2. MASCARA-1's stellar and planetary properties.

Parameter	Value
Stellar	
Radius ($R_\odot$)	$2.082^{+0.022}_{-0.024}$
Mass ($M_\odot$)	1.72 ± 0.07
$T_{\rm eff}$ (K)	$7\,554 \pm 150$
Metallicity [Fe/H]	0
$\log g$ (cm s^{-2})	4
Age (Gyr)	1.0 ± 0.2
$v_{\rm eq} \sin i$ (km s^{-1})	$101.7^{+3.5}_{-4.2}$ $^{(\dagger)}$
Planetary	
Radius ($R_{\rm Jup}$)	$1.597^{+0.018}_{-0.019}$
Mass ($M_{\rm Jup}$)	3.7 ± 0.9
Semi-major axis (au)	$0.040352^{+0.000046}_{-0.000049}$
Inclination (deg)	$88.45 \pm 0.17^{(\dagger\dagger)}$
Period (days)	$2.14877381^{+0.00000087}_{-0.00000088}$
Eccentricity	$0.00034^{+0.00034}_{-0.00033}$
Sky-projected spin–orbit	
Angle (deg)	$69.2^{+3.1}_{-3.4}$ $^{(\dagger\dagger\dagger)}$

Notes. Values are taken from Talens et al. (2017); Hooton et al. (2022); Casasayas-Barris et al. (2022). Parameters that we vary in the study: $^{(\dagger)}$, $^{(\dagger\dagger)}$ Sect. 4.2; $^{(\dagger\dagger),(\dagger\dagger\dagger)}$ Sect. 4.3 set to 90 and 61 respectively.

again the need to account for both local and global stellar lines in such simulations.

We thus decided to model those lines together, co-adding the $\chi^2_{\rm F_{out}}$ and $\chi^2_{\mathcal{A}}$ from the independent fits to the disc-integrated spectrum and the absorption spectrum. The synthetic disc-integrated line, fitted using our model stellar grid, is controlled by the Na I stellar abundance and the stellar rotational velocity. For the latter we only used three values (nominal, nominal + 1σ, nominal + 2σ), considering that the fit to the two sodium lines will not constrain the stellar rotational velocity better than the literature fit to the full stellar spectrum. The synthetic absorption spectrum, fitting using EVE transit simulations, is controlled by the Na I stellar abundance, the stellar rotational velocity, and the orbital inclination. We varied the latter parameter because Casasayas-Barris et al. (2022) showed that the POLD position is sensitive to its value within the error bar (red-shifting for decreasing inclinations), but only tested three values (nominal, nominal – 1σ, nominal – 2σ) based on the assumption that it is better constrained by transit photometry. The best-fit was found for $A_*(\mathrm{Na\,I}) = 12 + \log_{10}\left(\frac{n(\mathrm{Na\,I})}{n(\mathrm{H})}\right) = 6.865 \pm 0.002$, $v_{\rm eq}\sin(i)$ nominal $+2\sigma$, and $i_{\rm pl} - 2\sigma$ (see the lower panel of Fig. 12 for the simulated absorption spectrum and Fig. 13 for the disc-integrated spectrum).

We can thus conclude from a combined fit to the disc-integrated and absorption spectrum of MASCARA-1 b in the Na I D2 and D1 lines that the observed signature can be explained by a POLD with super-solar sodium abundance and no trace of planetary sodium absorption.

4.3. Fully veiled planetary atmospheric signature

In the subsections above, we show that an overlap between the atmospheric absorption signature and the POLD can affect the overall absorption spectrum of a transiting planet. The two systems we study here only present a partial overlap due to their

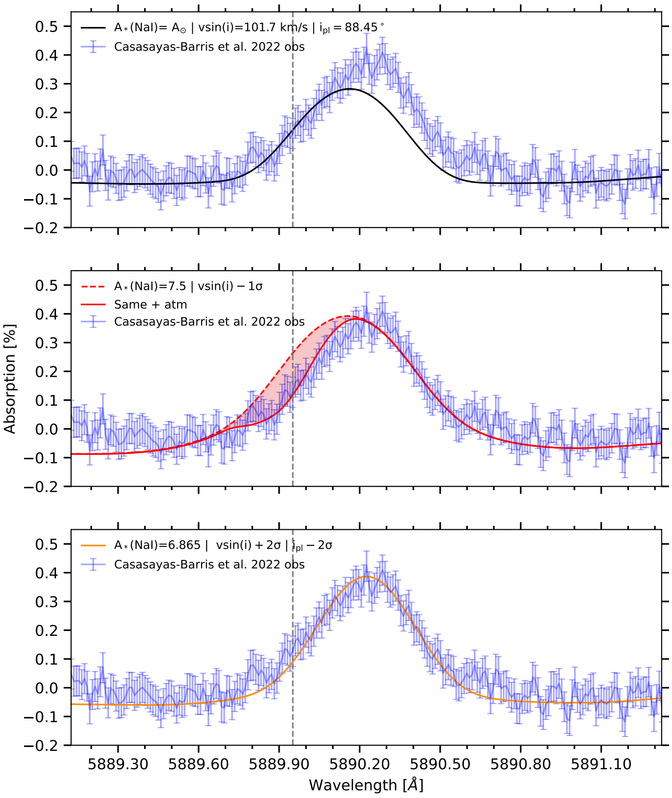

Fig. 12. Average absorption spectrum of MASCARA-1 b between contact times 2 and 3, computed with the out-of-transit spectrum as reference, and plotted in the planetary rest frame. Blue points are ESPRESSO data from Casasayas-Barris et al. (2022), red profiles show EVE simulations. The vertical grey line indicates the rest wavelength of the NaI D2 line. *Upper panel:* computed without planetary atmosphere using literature parameters and a solar abundance for the star. *Middle panel:* computed without planetary atmosphere (dashed red curve) for a modified $v_{\rm eq}\sin(i)$ and stellar Na I abundance, and with atmospheric sodium (solid red curve). The shaded area shows the atmospheric contribution to the absorption spectrum. *Lower panel:* computed without atmosphere, for a modified $v_{\rm eq}\sin(i)$, orbital inclination, and stellar Na I abundance yielding the best match to both the disc-integrated and absorption spectra.

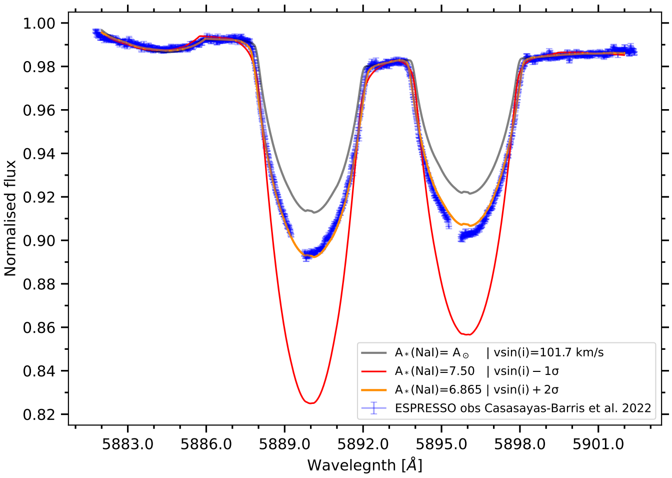

Fig. 13. Observed and synthetic out-of-transit spectra of MASCARA-1. The grey profile shows $F_{\rm out}$ computed with the nominal literature parameters. The red profile shows $F_{\rm out}$ from the best-fit to the absorption spectrum including atmospheric sodium absorption (see middle panel of Fig. 12). The orange profile shows $F_{\rm out}$ derived for the best fit to the disc-integrated and absorption spectra.

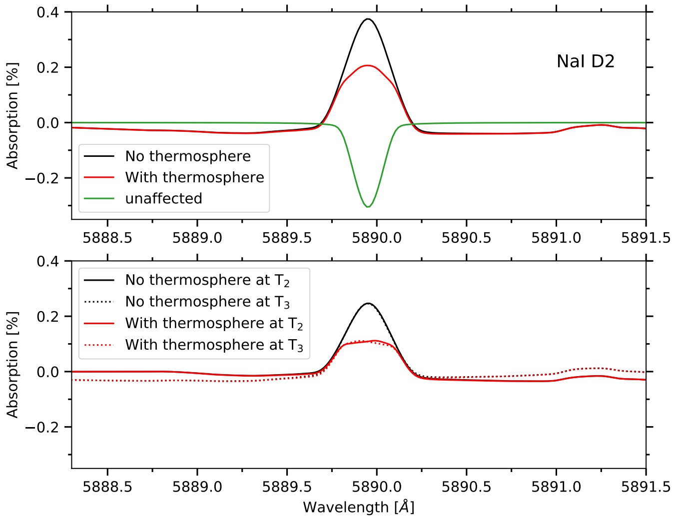

Fig. 14. Theoretical absorption spectra of the perfect overlap case computed with the out-of-transit spectrum, with and without sodium atmosphere as a function of the wavelength in the planetary rest frame. *Upper panel*: mean of the theoretical absorption spectra between contact times T_2 and T_3. *Lower panel*: theoretical absorption spectra at contact times T_2 and T_3.

orbital architecture and the rotation of their host star, making it possible to at least identify the presence of an atmospheric signature – if it is indeed present. Here, we explored the case where the orbital and planet-occulted stellar line tracks perfectly overlap. We studied the profile of the atmospheric signature merged with the POLD in the mean absorption spectrum of such a system to assess whether the presence of the former can be identified.

To investigate this scenario, we performed simulations using the parameters of the MASCARA-1 system, but adjusting the sky-projected spin–orbit angle and the planetary orbital inclination (Table 2) so that the orbital radial velocity matches the radial velocity of the occulted stellar surface throughout the whole transit. We performed simulations for a planet whose thermosphere contains or not neutral sodium. The thermosphere was simulated in the same way as for the previous sections and the parameters were tuned to reach an atmospheric absorption signature of ~0.3%.

Figure 14 shows the mean of excess absorption spectra between contact times 2 and 3, after being aligned in the planetary rest frame. Except for a decrease in the core of the POLD, the absorption spectrum remains similar whether we include sodium in the thermosphere or not. Thus, it is not possible to determine from the mean absorption spectrum the presence of an atmospheric absorption signature unless we have an accurate, independent knowledge of the planet-occulted stellar lines.

This particular configuration could happen for a close-in planet with a high radial orbital velocity around a fast-rotating star. For such close-in planets the thermosphere is expected to be heated by the higher levels of XUV flux, inducing strong dynamics that could render detectable its absorption signature. In particular, a day-to-night-side wind of a few km s^{-1} (e.g. Seidel et al. 2020) would shift the thermospheric absorption signature blue-ward of the orbital track (see Fig. E.1). With sufficient velocity the thermosphere could then absorb outside of the POLD and be disentangled.

We also note that the overlap between orbital and planet-occulted tracks can also occur for planets transiting slowly rotating stars at large orbital distances, due to their lower radial orbital velocity. At 0.2 AU the orbital radial velocity at ingress for a Jupiter-mass planet orbiting a Sun-mass star is of the order of a few km s^{-1}. At 1 AU for the Earth, this value is ~0.13 km s^{-1}. Although the POLD would be fainter for a slowly rotating star and smaller planets, this will also be the case of their absorption signature due to the lower stellar irradiation and more compact atmospheres. We thus highlight the need to account for planet-occulted stellar lines as accurately as possible in future searches for the atmospheric signatures of temperate planets.

5. Conclusions

The study of exoplanetary atmospheres was initiated less than a decade after their discovery. The spectrographs and techniques used to detect and analyse their absorption signatures during transits are continuously improving. However, it remains challenging to interpret transit signatures in terms of their atmospheric composition and dynamics. This is partly due to the distortions of absorption spectra (POLD) induced by the occultation of local stellar lines by the planetary disc along the transit chord. In this study, we use the 3D forward-modelling code EVE to simulate transit spectra of a typical hot Jupiter with the goal of investigating the impact of POLDs on the absorption signature from sodium in its atmosphere. The forward-modelling approach allows us to control the impact of each element we added in our simulations. In contrast to working with observations, we were able to find out the local spectrum occulted by the planet at each time-step and use it as a reference to characterise POLDs through comparisons with absorption spectra that were unaffected by any stellar effects. Specifically, we explored how the POLDs and, thus, the detectability of an atmospheric signature are influenced by stellar rotational velocity, broadband limb-darkening, centre-to-limb variations, and, more generally, by the spectrum chosen as a proxy for the planet-occulted stellar lines. We tested common proxies used in the literature, such as the out-of-transit spectrum, in the star rest frame and Doppler-shifted at the position of the occulted stellar regions; the local spectrum at the centre of the stellar disc; the local spectra occulted by the planet in each exposure, without accounting for their Doppler shift. One of our main conclusions is that, barring correct estimates of the planet-occulted stellar spectra, there is no universal proxy to mitigate the POLDs. Estimates of the planet-occulted spectra must be defined depending on the orbital and stellar properties, and on the transit phase. The results of our study provide useful information to this aim.

For slowly rotating stars, the disc-integrated line is not broadened by rotation and is a good proxy for the planet-occulted line in the absence of strong CLVs. For moderate to fast-rotating stars, POLDs are created in the absorption spectra for all proxies of the planet-occulted line and can be of the order of magnitude of typical Na I atmospheric absorption signatures. The peak-to-peak amplitude of the POLD increases with $v_{\rm eq}\sin(i)$ and decreases with the planetary spin–orbit angle. To mitigate the POLDs, it is better to shift the line proxy by the radial velocity of the occulted stellar surface region. In particular, POLDs affect atmospheric absorption signatures the most when the orbital track of the planet overlaps with the planet-occulted stellar line track in radial velocity-phase space (i.e. at time-steps where the planetary radial orbital velocity is close to the radial velocity of the occulted stellar surface). We studied the case in which the two tracks overlap perfectly. In that case, the POLD and atmospheric signatures are completely degenerate and the shape of the absorption spectrum remains similar for simulations with and without atmosphere. We note that this configuration can be achieved both for a close-in planet orbiting a fast rotating star, but also for planets transiting slowly rotating stars at large orbital distances. In the latter case, the POLD is expected to be fainter but so would be the atmospheric signatures. We thus emphasise the importance of accounting for POLDs in future observation of transiting temperate planets.

The POLDs created by CLVs are smaller than those caused by moderate-to-fast stellar rotation ($v_{\rm eq}\sin(i) \gtrsim 3\,{\rm km\,s^{-1}}$). However, CLV-induced POLDs can still reach a few tenth of % and, thus, they can also be on the order of magnitude of Na I atmospheric absorption signatures. In the case of slowly rotating stars, these POLDs can thus be the dominant source of bias in misinterpreting absorption spectra. Interestingly, while the local spectrum at the centre of the stellar disc is the better proxy for nearby occulted regions, the out-of-transit spectrum can be a more adequate proxy for planet-occulted regions close to the stellar limb because its profile is partly shaped by CLVs. Although its impact is smaller than CLVs, broadband limb darkening can bias absorption spectra if out-of-transit and in-transit spectra are not reset to their correct relative flux, which is typically the case in studies that normalise all stellar spectra to the same continuum or studies that simply shift the measured continuum to zero. This bias can be removed by using a simple multiplicative factor, and we encourage its application in future studies.

After exploring the origins and impacts of POLDs in spectra of theoretical planets, we exploited our results to use the EVE code to re-interpret the absorption spectra of two hot Jupiters of interest. We simulated transits of HD 209458 b to investigate whether the Na I signature measured in high-resolution ESPRESSO spectra by Casasayas-Barris et al. (2020, 2021) could be explained by a combination of POLDs and atmospheric absorption. This planet is of particular importance as it is the first for which a claim of atmospheric detection was made (Charbonneau et al. 2002), only to be attributed recently to a POLD by Casasayas-Barris et al. (2020), based on the analysis of the sodium signature at a high resolution. We confirm the findings of the latter authors, namely, that the observed signature mainly arises from a POLD. Nevertheless, our combined fit hints at the additional contribution from sodium in the atmosphere of HD 209458 b. To validate this conclusion, a comprehensive exploration based on accurate stellar and planetary lines, detailed codes such as EVE, and repeated transit observations with ESPRESSO or other suitable high-resolution spectrographs, is required. We then simulated transits of MASCARA-1 b to investigate whether we could detect atmospheric absorption in ESPRESSO spectra, which Casasayas-Barris et al. (2022) could not identify due to the strong overlap between the planet-occulted and orbital tracks. The asymmetric mean absorption spectrum can be fitted with a combination of POLDs and atmospheric Na I absorption, but the required local stellar lines yield a strong mismatch between the simulated and observed disc-integrated spectra. A combined fit to the disc-integrated and absorption spectra in the Na I D2 and D1 lines show that the observed signature can be explained by a POLD with super-solar sodium abundance and no planetary sodium absorption.

The interpretation of exoplanets absorption signatures in high-resolution transit spectra is not straightforward. A precise knowledge of the planetary system and importantly of the local stellar spectra occulted by the planet is crucial to disentangle planetary signatures from stellar lines contamination. While analysing the 2D velocity-phase maps of absorption spectra offers the possibility to separate the planet-occulted and orbital tracks, individual exposures are usually too noisy to do so. In such cases we showed that the average in-transit absorption spectrum can still be used to identify the presence of atmospheric signatures, if the impact of the POLDs is correctly understood. Forward-modelling codes such as EVE can simulate stellar spectra during an exoplanet transit, accounting simultaneously for local stellar line absorption by the planet and its atmosphere. They are helpful tools to address the challenges of interpreting exoplanet absorption signatures and to avoid biases that arise when correcting absorption spectra for stellar contamination independently. We thus advocate a global approach to derive planetary atmospheric constraints from absorption spectra, which consists of fitting together the disc-integrated stellar line and a combined model of the POLDs and planetary absorption lines.

With the upcoming generation of high-resolution spectrographs such as ANDES/ELT, contamination from POLDs, stellar activity and variability, or even stellar spots will become a dominant source of noise in many datasets of transiting planets. More than ever, accounting accurately for the impact of the stellar lines occulted by the planets will be decisive in characterising their atmosphere.

Acknowledgements. We thank the referee and editor for their precious and relevant advice that allowed to us to improve our study. We dearly thank Dr. Nuria Casasayas-Barris for her help, especially for the observational data of ESPRESSO for HD 209458 b and MASCARA-1 b transits she kindly shared with us and that allowed us to compare our models to. We thank Michal Steiner for sharing with us the ESPRESSO out-of-transit spectrum of MASCARA-1 and that was used in Casasayas-Barris et al. (2022). We also dearly thank Dr. Jérôme Bouvier for his mindful advice and feedback during the development of this study. This work has made use of the VALD database, operated at Uppsala University, the Institute of Astronomy RAS in Moscow, and the University of Vienna. This work has made use of the Turbospectrum code for spectral synthesis. This project has received funding from the European Research Council (ERC) under the European Union's Horizon 2020 research and innovation program (grant agreement No 742095 ; SPIDI : Star-Planets-Inner Disk-Interactions; `http://www.spidi-eu.org`). This work has been carried out within the framework of the NCCR PlanetS supported by the Swiss National Science Foundation under grants 51NF40182901 and 51NF40205606. This project has received funding from the European Research Council (ERC) under the European Union's Horizon 2020 research and innovation programme (project SPICE DUNE, grant agreement No 947634).

References

Albrecht, S., Snellen, I., de Mooij, E., & Le Poole, R. 2008, Proc. Int. Astron. Union, 4, 520
Allart, R., Bourrier, V., Lovis, C., et al. 2018, Science, 362, 1384
Allende Prieto, C., Asplund, M., & Fabiani Bendicho, P. 2004, A&A, 423, 1109
Barnes, J. R., Haswell, C. A., Staab, D., & Anglada-Escudé, G. 2016, MNRAS, 462, 1012
Borsa, F., & Zannoni, A. 2018, A&A, 617, A134
Borsa, F., Allart, R., Casasayas-Barris, N., et al. 2021, A&A, 645, A24
Bourrier, V., & Lecavelier des Etangs, A. 2013, A&A, 557, A124
Bourrier, V., Ehrenreich, D., & Lecavelier des Etangs, A. 2015, A&A, 582, A65
Bourrier, V., Lecavelier des Etangs, A., Ehrenreich, D., Tanaka, Y. A., & Vidotto, A. A. 2016, A&A, 591, A121
Casasayas-Barris, N., Palle, E., Nowak, G., et al. 2017, A&A, 608, A135
Casasayas-Barris, N., Pallé, E., Yan, F., et al. 2018, A&A, 616, A151
Casasayas-Barris, N., Pallé, E., Yan, F., et al. 2020, A&A, 635, A206
Casasayas-Barris, N., Palle, E., Stangret, M., et al. 2021, A&A, 647, A26
Casasayas-Barris, N., Borsa, F., Pallé, E., et al. 2022, A&A, 664, A121
Charbonneau, D., Brown, T. M., Latham, D. W., & Mayor, M. 2000, ApJ, 529, L45
Charbonneau, D., Brown, T. M., Noyes, R. W., & Gilliland, R. L. 2002, ApJ, 568, 377
Chen, G., Pallé, E., Welbanks, L., et al. 2018, A&A, 616, A145

Czesla, S., Klocová, T., Khalafinejad, S., Wolter, U., & Schmitt, J. H. M. M. 2015, A&A, 582, A51
Deibert, E. K., de Mooij, E. J. W., Jayawardhana, R., et al. 2019, AJ, 157, 58
Gustafsson, B., Edvardsson, B., Eriksson, K., et al. 2008, A&A, 486, 951
Heiter, U., Lind, K., Bergemann, M., et al. 2021, A&A, 645, A106
Henry, G. W., Marcy, G. W., Butler, R. P., & Vogt, S. S. 2000, ApJ, 529, L41
Hoeijmakers, H. J., Ehrenreich, D., Kitzmann, D., et al. 2019, A&A, 627, A165
Hooton, M. J., Hoyer, S., Kitzmann, D., et al. 2022, A&A, 658, A75
Jensen, A. G., Cauley, P. W., Redfield, S., Cochran, W. D., & Endl, M. 2018, AJ, 156, 154
Lamers, H. J. G. L. M., & Cassinelli, J. P. 1999, Introduction to Stellar Winds (Cambridge University Press)
Larsen, S. S., Eitner, P., Magg, E., et al. 2022, A&A, 660, A88
Louden, T., & Wheatley, P. J. 2015, ApJ, 814, L24
Magg, E., Bergemann, M., Serenelli, A., et al. 2022, A&A, 661, A140
McLaughlin, D. B. 1924, ApJ, 60, 22
Mounzer, D., Lovis, C., Seidel, J. V., et al. 2022, A&A, 668, A1
Nikolov, N., Sing, D. K., Gibson, N. P., et al. 2016, ApJ, 832, 191
Nikolov, N., Sing, D. K., Fortney, J. J., et al. 2018, Nature, 557, 526
Oklopčić, A., & Hirata, C. M. 2018, ApJ, 855, L11
Parker, E. N. 1958, ApJ, 128, 664
Pietrow, A. G. M., Kiselman, D., Andriienko, O., et al. 2023, A&A, 671, A130
Plez, B. 2012, Astrophysics Source Code Library [`record ascl:1205.004`]
Redfield, S., Endl, M., Cochran, W. D., & Koesterke, L. 2008, ApJ, 673, L87
Rossiter, R. A. 1924, ApJ, 60, 15
Ryabchikova, T., Piskunov, N., Kurucz, R. L., et al. 2015, Physica Scripta, 90, 054005
Seidel, J. V., Ehrenreich, D., Wyttenbach, A., et al. 2019, A&A, 623, A166
Seidel, J. V., Ehrenreich, D., Pino, L., et al. 2020, A&A, 633, A86
Sing, D. K., Vidal-Madjar, A., Désert, J. M., Lecavelier des Etangs, A., & Ballester, G. 2008, ApJ, 686, 658
Snellen, I. A. G., Albrecht, S., de Mooij, E. J. W., & Le Poole, R. S. 2008, A&A, 487, 357
Spake, J. J., Sing, D. K., Evans, T. M., et al. 2018, Nature, 557, 68
Talens, G. J. J., Albrecht, S., Spronck, J. F. P., et al. 2017, A&A, 606, A73
Tessore, B., Pinte, C., Bouvier, J., & Ménard, F. 2021, A&A, 647, A27
Valenti, J. A., & Piskunov, N. 1996, A&AS, 118, 595
Vernazza, J. E., Avrett, E. H., & Loeser, R. 1981, ApJS, 45, 635
Vidal-Madjar, A., Sing, D. K., Lecavelier des Etangs, A., et al. 2011, A&A, 527, A110
Wyttenbach, A., Ehrenreich, D., Lovis, C., Udry, S., & Pepe, F. 2015, A&A, 577, A62
Wyttenbach, A., Lovis, C., Ehrenreich, D., et al. 2017, A&A, 602, A36
Wyttenbach, A., Mollière, P., Ehrenreich, D., et al. 2020, A&A, 638, A87
Yan, F., Pallé, E., Fosbury, R. A. E., Petr-Gotzens, M. G., & Henning, Th. 2017, A&A, 603, A73

Appendix A: Quantities used to compute the absorption spectra in Fig. 4

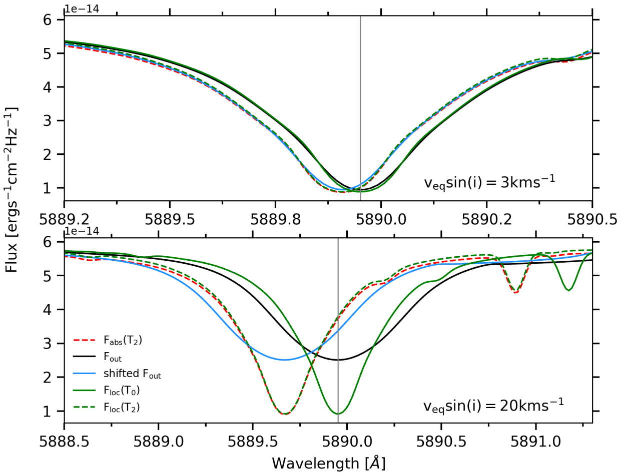

Fig. A.1. Quantities used in Sect. 3.1 to compute the absorption spectra at T_2 without the thermosphere (see Fig. 4). Here, we multiplied F_{out} by the ratio between the occulted surface and the surface of the star to bring it to the level of F_{loc} and make the comparison easier.

Appendix B: Effect of normalising F_{out} and $F_{in}(t)$ on the absorption spectra

As mentioned in Sect. 3.2.2, normalising the out-of-transit and in-transit spectra to the same flux level before computing the absorption spectrum does not remove the bias induced by BLD. Indeed, the continuum of F_{out} and $F_{in}(t)$ can be expressed in the following form respectively

$$F^{C}_{out} = LD_{*}\ S_{*}, \tag{B.1}$$

$$F^{C}_{in}(t) = LD_{*}\ S_{*} - LD_{pl}(t)\ S_{pl}. \tag{B.2}$$

The normalised continuum of F_{out} is thus equal to 1 but for $F_{in(t)}$ we get

$$\begin{aligned}\overline{F_{in}(t)} =& \frac{LD_{*}\ S_{*} - \left[LD(t)\ S_{pl} + \left(1 - e^{-\tau_{atm}(\lambda)}\right)\ LD(t)\ S_{atm}\right]}{LD_{*}\ S_{*} - LD(t)\ S_{pl}} \\ =& 1 - \frac{\left(1 - e^{-\tau_{atm}(\lambda)}\right)\ LD(t)\ S_{atm}}{LD_{*}\ S_{*} - LD(t)\ S_{pl}}.\end{aligned} \tag{B.3}$$

So, in this case, the continuum of the absorption spectrum is set to 0, but we see that the atmospheric signature is altered by a time-variable factor due to the limb-darkening of the planet-occulted region.

Appendix C: HD 209458 b absorption spectrum:

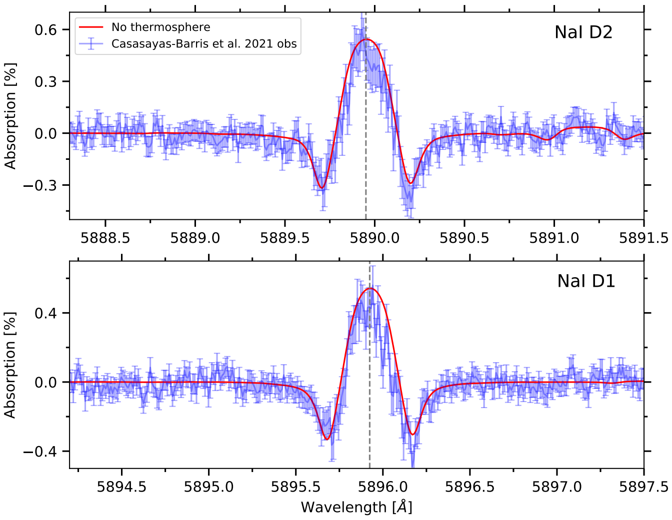

Fig. C.1. Theoretical mean absorption spectrum between contact times T_2 and T_3 of HD 209458 b computed with the out-of-transit spectrum as a function of the wavelength in the planetary rest frame without sodium atmosphere. The blue points are ESPRESSO data from Casasayas-Barris et al. (2021). *Upper panel*: Zoom on the Na I D2 line. *Lower panel*: Zoom on the Na I D1 line.

Appendix D: Stellar NaI abundance in HD 209458 stellar model:

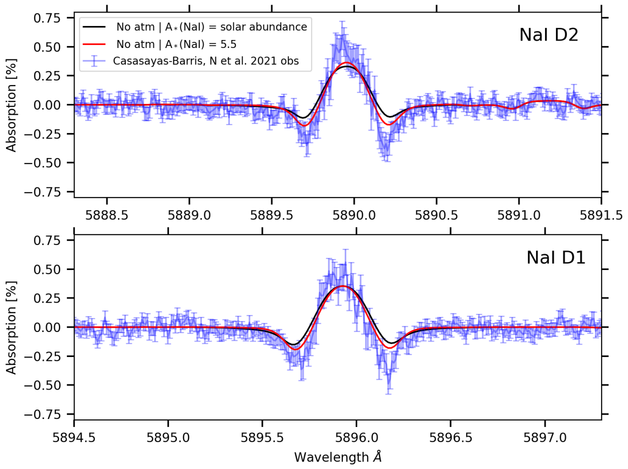

Fig. D.1. Theoretical mean absorption spectrum between contact times T_2 and T_3 of HD 209458 b computed with the out-of-transit spectrum as a function of the wavelength in the planetary rest frame without sodium atmosphere. We used a modified stellar Na I abundance from Solar (6.33) to 5.5 to compute the synthetic stellar spectrum such as $A_{*}(\mathrm{Na\,I}) = 5.5 = 12 + \log_{10}\left(\frac{n(\mathrm{Na\,I})}{n(\mathrm{H})}\right)$.

Appendix E: Atmospheric winds:

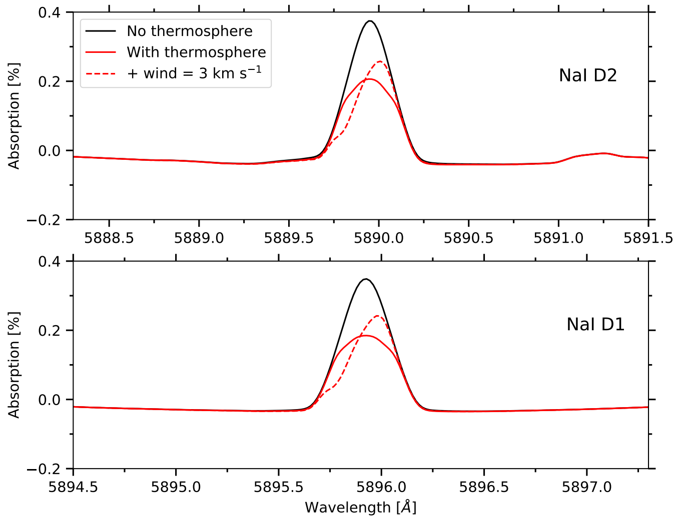

Fig. E.1. Theoretical mean absorption spectra between contact times T_2 and T_3 of the perfect overlap case computed with the out-of-transit spectrum, with and without sodium atmosphere as a function of the wavelength in the planetary rest frame. In addition to the simulations in Sect. 4.3, we included a day-to-nightside wind of 3 km s^{-1} in the thermosphere. *Upper panel*: Zoom on the Na I D2 line. *Lower panel*: Zoom on the Na I D1 line.

Appendix F: Absorption spectra of MASCARA-1 b for Na I D1 line

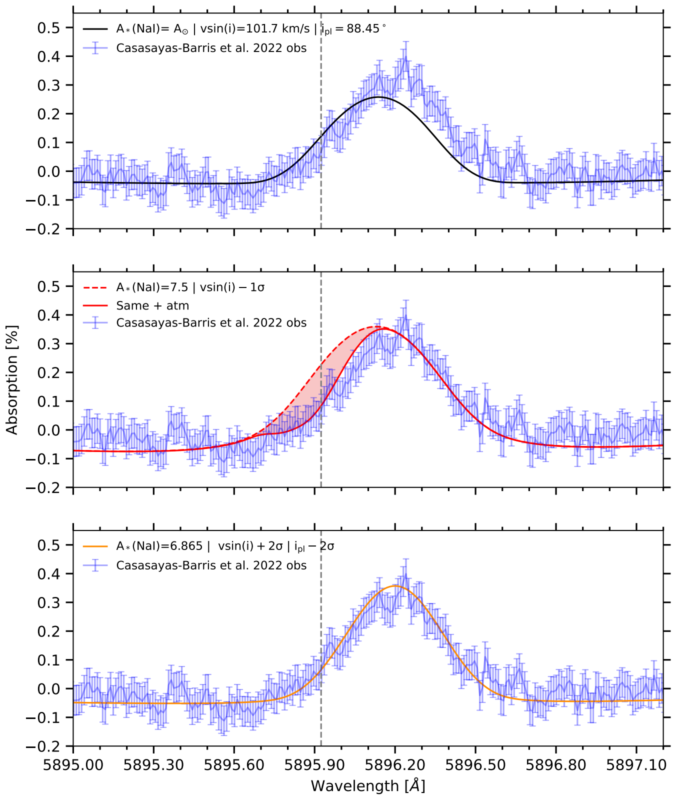

Fig. F.1. Average absorption spectrum of MASCARA-1 b between contact times 2 and 3, computed with the out-of-transit spectrum as reference, and plotted in the planetary rest frame. Blue points are ESPRESSO data from Casasayas-Barris et al. (2022), red profiles show EVE simulations. The vertical grey line indicates the rest wavelength of the Na I D1 line. *Upper panel:* Computed without planetary atmosphere using literature parameters and a solar abundance for the star. *Middle panel:* Computed without planetary atmosphere (dashed red curve) for a modified v_{eq} sin(i) and stellar Na I abundance, and with atmospheric sodium (solid red curve). The shaded area shows the atmospheric contribution to the absorption spectrum. *Lower panel:* Computed without atmosphere, for a modified v_{eq} sin(i), orbital inclination, and stellar Na I abundance yielding the best match to both the disc-integrated and absorption spectra.

Astronomy & Astrophysics manuscript no. 46419corr
July 19, 2023

DREAM

III. A helium survey in exoplanets on the edge of the hot Neptune desert with GIANO-B at TNG

G. Guilluy[1], V. Bourrier[2], Y. Jaziri[2] , W. Dethier[3], D. Mounzer[2], P. Giacobbe[1], O. Attia[2], R. Allart[4⋆], A. S. Bonomo[1], L. A. Dos Santos[5], M. Rainer[6], A. Sozzetti[1]

(Affiliations can be found after the references)

Received date ; Accepted date

ABSTRACT

Context. The population of close-in exoplanets features a desert of hot Neptunes whose origin remains uncertain. These planets may have lost their atmosphere, eroding into mini-Neptunes and rocky super-Earths below the desert. Direct observations of evaporating atmospheres are essential to derive mass-loss estimates and constrain this scenario. The metastable He i triplet at 1083.3 nm represents a powerful diagnostic of atmospheric evaporation because it traces the hot gas in extended exoplanet atmospheres while being observed from the ground. In addition, it is located at the bright near-infrared stellar continuum and is very weakly affected by interstellar medium (ISM) absorption.

Aims. We carried out a homogeneous He i transmission spectroscopy survey, targeting a selected sample of nine planets along the different edges of the desert, to interpret the absorption line profile with evaporation models and to better understand the role of photoevaporation in the desert formation.

Methods. We observed one transit per planet using the high-resolution, near-infrared spectrograph GIANO-B mounted on the Telescopio Nazionale Galileo telescope. We focused our analysis on the He i triplet, based on a comparison of the in-transit and out-of-transit observations, and we computed high-resolution transmission spectra. We then employed the 1D *p-winds* model to calculate the planetary thermospheric structures and to interpret the observed transmission spectra.

Results. We found no signatures of planetary absorption in the He i triplet in any of the investigated targets. We thus provided 3 σ upper-limit estimations on the thermosphere absorption, temperature and mass loss, and combined them with past measurements to search for correlations with parameters such as the stellar mass and XUV flux, which are thought to be key drivers in the formation of the He i triplet.

Conclusions. These results strengthen the importance of performing homogeneous surveys and analyses in bringing clarity to He i detections and (thereby) to plausible Neptunian desert origins. Our findings corroborate literature expectations that state the He i absorption signal is correlated with the stellar mass and the received XUV flux. However, when translated in terms of mass-loss rates, these trends seem to disappear. Thus, further studies are essential to shed light on this aspect and to better understand the photoevaporation process.

Key words. planets and satellites: atmospheres – techniques: spectroscopic - methods: observational - infrared: planetary systems

1. Introduction

The population of close-in exoplanets ($P \lesssim 30$ days) features a dearth of Neptune-size planets on very short orbits ($P \lesssim 4$ days). This so-called "Neptunian desert" (e.g., Lecavelier Des Etangs 2007; Davis & Wheatley 2009; Szabó & Kiss 2011; Beaugé & Nesvorný 2013) is not an observational bias, as close-in Neptunes are easy to detect via both transits and radial-velocity measurements. Debate around the key driver mechanisms at the origin of the desert, which are linked to the formation, migration, and atmospheric evolution of close-in planets, is still ongoing. Photoevaporation (e.g., Owen & Lai 2018; Owen 2019) and high-eccentricity orbital migration followed by tidal interaction with the star (e.g., Matsakos & Königl 2016) are the most likely explanations to date, but their interplay remains to be explored. Among questions that need to be addressed are the range of mass and period over which these processes are at play and whether they also shape the Neptunian "savanna" that is represented by a lighter deficit of Neptune-size planets at longer periods and lower irradiation, as highlighted by Bourrier et al. (2023).

Investigating this complex puzzle is the goal of the Desert-Rim Exoplanets Atmosphere and Migration (DREAM) program. In DREAM I (Bourrier et al. 2023), we measured the orbital architectures of a large sample of exoplanets spanning the borders of the Neptunian desert and savanna. This work revealed a high fraction of misaligned orbits, strengthening the importance of high-eccentricity orbital migration for close-in planets. Architecture measurements from DREAM I were included in a large statistical study of spin-orbit angles in DREAM II (Attia et al. 2023). This work confirmed the major role of tides in shaping the overall distribution of close-in planets' orbital architectures, except for a substantial fraction of planets on polar orbit that appears resilient to tidal realignment and further support the importance of disruptive dynamical processes. A subsample of the systems in DREAM I were observed in transit as part of a campaign our team led with

---

[⋆] Trottier Postdoctoral Fellow

the GIARPS observing mode (GIANO-B+HARPS-N) at the Telescopio Nazionale Galileo (TNG) telescope, to measure their Rossiter-McLaughlin effect in optical HARPS-N data and to analyze the planetary atmospheric spectra in near-infrared GIANO-B data. The objective of this third paper in the DREAM series is to search these GIANO-B data for absorption by helium escaping the upper atmosphere of these planets, bringing constraints on their mass loss and the role of atmospheric escape in the formation of the desert.

Strong high-energy X-rays and extreme ultraviolet (XUV) stellar radiation can lead to an expansion of the upper atmospheric layers and the substantial escape of gas into space (e.g., Vidal-Madjar et al. 2003; Lammer et al. 2003; Tripathi et al. 2015). While hot Jupiters are generally stable against this photoevaporation, hot Neptunes have lower gravitational potential that makes them more vulnerable (e.g., Lecavelier des Etangs et al. 2004; Owen & Wu 2017). The upper atmospheric layers of these planets have traditionally been probed via transit spectroscopy in the ultraviolet (UV), by monitoring the change in absorption during transit of the stellar Lyα line. The H I exospheres of hot Jupiters yield absorption signatures in the stellar Lyα that are ten times deeper than the lower atmosphere (Lecavelier des Etangs et al. 2012; Ehrenreich et al. 2012), and this absorption level is even higher for the exospheres of warm Neptunes (e.g., Ehrenreich et al. 2015; Lavie et al. 2017; Bourrier et al. 2018) – and possibly even for mini-Neptunes (e.g., dos Santos et al. 2020b; Zhang et al. 2023). However, UV observations can only be performed from space, and the stellar Ly-α line is contaminated by geocoronal emission and absorbed by the interstellar medium (ISM) absorption. While geocoronal emission can be reliably subtracted in the data reduction, there is nothing that can be done for the ISM absorption, so that only the wings of the line are usable when probing escaping atmospheres. In this way, gas dynamics in regions closer to the planet itself, at the wind-launching radius, remains obscured with Ly-α observations (e.g., Murray-Clay et al. 2009; Owen et al. 2023) leading to low-precision mass-loss rates, as we observe the gas when it has already escaped in the exosphere. Additionally, Ly-α studies have only been performed on a few systems due to ISM absorption, which prevents observing stellar Ly-α lines beyond ~50 pc. Accessing the thermosphere, the upper atmospheric layer below the exosphere, represents a way to overcome these limitations.

As it is very weakly affected by interstellar absorption and it can be observed from the ground the He I triplet at λ ~1083.3 nm (vacuum wavelength) has been recently identified as a robust alternative for tracing atmospheric expansion and evaporation (e.g., Seager & Sasselov 2000; Oklopčić & Hirata 2018). The first detection of a helium thermosphere was obtained by Spake et al. 2018 with the Wilde Field Camera 3 (WFC3) of the Hubble Space Telescope (HST). The He I feature was not spectrally resolved due to the low-resolution of the data, however, further observations at high-resolution with CARMENES (Allart et al. 2019) allowed for the absorption lines to be spectrally resolved and to derive atmospheric properties, showing that the helium tracer can probe the planet thermosphere and occasionally the exosphere. To date, He I has been searched for in the upper atmospheres of about 40 planets which (see Table A.1).

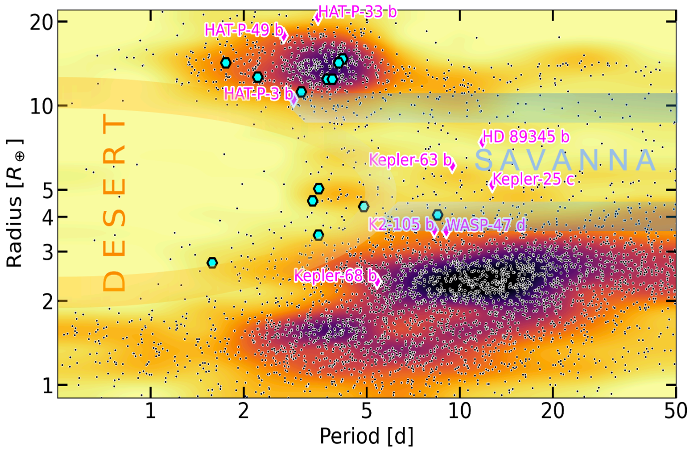

Fig. 1. Two-dimensional distribution of exoplanets as a function of their radius and period from the NASA Exoplanet Archive (Akeson et al. 2013). Magenta and pink diamonds represent DREAM III and Allart et al. (2023) -a work that we took as a reference for our analysis- targets, respectively. The approximate boundaries of the desert and savanna are highlighted.

These observations have led to He I absorption or upper limits estimations. However, the non-homogeneity in both observing methodology, and data reduction technique may mask possible trends in the data, thus making it difficult to find a clear correlation with the parameters (e.g., stellar mass, XUV irradiation) that are believed to drive the detection (or non-detection) of the He I triplet (e.g., Fossati et al. 2022).

Despite the several helium studies, the parameters that are considered to be important in triggering the He I detection are currently under debate. For instance, Oklopčić & Hirata 2018 proposed that planets orbiting K-type stars should be promising targets for showing evaporating or escaping helium atmospheres. This is because K-type stars emit a high amount of stellar XUV emission, which is responsible for He I atoms ionization from the ground state (which can then recombine into the metastable state) and a low stellar mid-ultraviolet emission, which reduces the ionization of metastable He I atoms (Oklopčić & Hirata 2018). However, the discovery of a strong helium signature for a gas-giant planet orbiting an F-star (Czesla et al. 2022), highlighted that also other planets orbiting stars with different spectral energy distribution (SED) can exhibit large helium outflow regardless of the stellar spectral type. More studies are thus essential to shed light on which are the mechanisms and parameters important in the He I detection.

The sample we analyze in DREAM III is part of a pilot survey of nine planets located at the different edges of the Neptunian desert and savanna. The sample is described in Sect. 2, and its near-infrared (nIR) observations with the GIANO-B high-resolution spectrograph are presented in Sect. 3. We detail the data reduction procedures in Sect. 4, and the interpretation of the helium absorption observations in Sect. 5. We then present our findings in Sect. 7, followed by our conclusions in Sect. 8.

2. Sample

Our survey consists of nine planets along the transitions defining the Neptunian desert and savanna. Their low densities ($\rho_{\rm pl}$<3.5 g cm^{-3}) and bright host stars (J<10.7) favor observations of their atmosphere in the nIR. The planet and star parameters adopted in this work are presented in Table A.2. Below, we describe the main features of interest for these planets, which led to their inclusion in our survey. We would like to stress that no helium studies were reported in the literature for these investigated planets.

Hot Jupiter HAT-P-3b. Its strong irradiation is expected to induce a large mass loss. The small radius of HAT-P-3b is indicative of a metal-enriched composition (Chan et al. 2011), which could be the result of atmospheric escape over the last 2.6 Gyr. Hydrogen would be lost preferentially, making helium a particularly interesting tracer for this planet. HAT-P-3b orbits a K-star, thus according to Oklopčić (2019), it is likely to show metastable helium absorption. DREAM I reports a polar orbit for this planet and, if confirmed, dynamical simulations will be needed to understand whether the present-day architecture is a result of a disruptive dynamical history (with partial evaporation of its volatile content) or a primordial misalignment between the protoplanetary disk and the star.

Hot Jupiter HAT-P-33b. The extreme irradiation and very low density ($0.134^{+0.053}_{-0.042}$ g cm^{-3}, Wang et al. 2017) of this highly inflated planet are expected to induce a large mass loss. Turner et al. (2017) measured an excess depth during transit in the R-band, which contains the Hα transition, suggesting that the planet may be undergoing hydrodynamical escape. The misalignment of the system, due to the inclination of the host star, suggests that HAT-P-33 b underwent a high-eccentricity migration, and thus it possibly migrated close to the star long after its formation, which would change its atmospheric history compared to an early-on migration and erosion.

Ultra-hot-Jupiter HAT-P-49b. It is a gas giant exoplanet discovered orbiting a bright (V = 10.3) slightly evolved F-star (Bieryla et al. 2014). Its extreme irradiation, due to its proximity to the host star (a=0.0438±0.0005 au, Bieryla et al. 2014), is expected to induce a large mass loss. According to the analysis presented in DREAM I, the planet is probably on a polar orbit, supporting a disruptive dynamical origin or evolution for the system, whose architecture was unaffected by tidal interactions with the shallow convective envelope of the host star (DREAM II).

Warm super-Neptune HD89345b. This planet is five times more irradiated than the evaporating super-Neptune WASP-107b, yet it survived atmospheric escape for 9.4 Gyr (e.g., Van Eylen et al. 2018). HD 89345b stands at the transition between stable Jupiter-mass planets and hot Neptunes that entirely lost their atmosphere and this is thus an essential piece in the puzzle that is the origin of the desert. HD 89345b is located on a misaligned orbit (DREAM I) right within the savanna (see Fig. 1). The present-day misalignment could trace both a primordial formation of the system, arising from the tilt of the early star or protoplanetary disk, or the planet could have migrated more recently, exiting a Kozai resonance with an outer companion (e.g., Bourrier et al. 2018; Attia et al. 2021). This second scenario would imply that HD 89345b arrived near the star at the end of its main-sequence lifetime, changing our view of its irradiative history and our interpretation of its inflation (Yu et al. 2018) and hydrodynamical escape.

Warm sub-Neptune K2-105b. It remains unclear why sub-Neptunes appear to be more resilient than warm Neptunes to the processes that created the desert (Owen 2019). K2-105b stands at the transition between these two populations and is predicted to have an atmosphere accounting for up to 10% of its total mass (Narita et al. 2017). Detecting the presence of this atmosphere and measuring its mass loss could bring constraints on the interior of the planet; if its evolution was controlled by atmospheric escape, it is estimated to have retained its envelope only if its core mass is greater than 6 M$_\oplus$(Narita et al. 2017). DREAM I reported a possibly misaligned orbit which, if confirmed, might support a turbulent dynamical history and the planet's late arrival into its close-in orbit. However, the presence of other targets may indicate a primordial inclination of the star or protoplanetary disk, as K2-105b is far away from its host stellar companion to experience tidal interactions.

Warm Neptune Kepler-25c. It is close to a resonant periodic configuration with a companion planet, which is known to be the final state of a system that undergoes migration within the protoplanetary disk (Migaszewski & Goździewski 2018). Kepler-25c should thus be evaporating since its formation 11 Gyr ago (Marcy et al. 2014), yet its low density ($0.588^{+0.053}_{-0.061}$ g cm^{-3}, Mills et al. 2019) indicates the presence of a H/He envelope.

Warm Neptune Kepler-63b. It is a gas giant exoplanet with a radius between Neptune and Saturn. The orbital period is around 9.4 days, leading to an equilibrium temperature of about 900 K (Mallonn et al. 2022). The planet is in a polar orbit around a young Sun-like star (Sanchis-Ojeda et al. 2013, DREAM I), thus offering the possibility to assess how evaporation shapes a Neptune's atmosphere in its early life. Its radius and insolation are similar to those of the other Neptunian targets, but it is much younger (200 Myr vs 10 Gyr) and still possibly undergoing vigorous escape.

Hot sub-Neptune Kepler-68b. With a density of $3.32^{+0.86}_{-0.98}$ g cm^{-3}(Gilliland et al. 2013), it is considered a candidate ocean planet (Zeng & Sasselov 2014) possibly topped by a moderate H/He envelope (Howe et al. 2014). Detecting He would offer insights on the mysterious nature of this sub-Neptune, representative of the transition between rocky planets and gas giants (Lopez & Fortney 2014).

Warm sub-Neptune WASP-47d. The WASP-47 planetary system is composed of at least four planets, a hot Jupiter (WASP-47 b; P = 4.159 days, Bryant & Bayliss 2022) with an inner super-Earth (WASP-47 e; P = 0.7896 days, Bryant & Bayliss 2022), a close-orbiting outer Neptune (WASP-47 d; P = 9.031 days, Bryant & Bayliss 2022), and a long-period giant planet (WASP-47 c; P = 588.4 days, Vanderburg et al. 2017; Bryant & Bayliss 2022). WASP-47 d is near a 2:1 resonance with the inner Hot Jupiter WASP-47b. It has a similar radius and insolation of K2-105b but is three times less massive. Their comparison could provide valuable insight into evaporation processes on sub-Neptunes.

3. Observations

We observed the systems in our sample with the nIR echelle spectrograph GIANO-B installed on the 3.6 m Telescopio Nazionale Galileo (TNG) telescope. The observations were performed with the GIARPS configuration and were carried out with the nodding acquisition ABAB (Claudi et al.

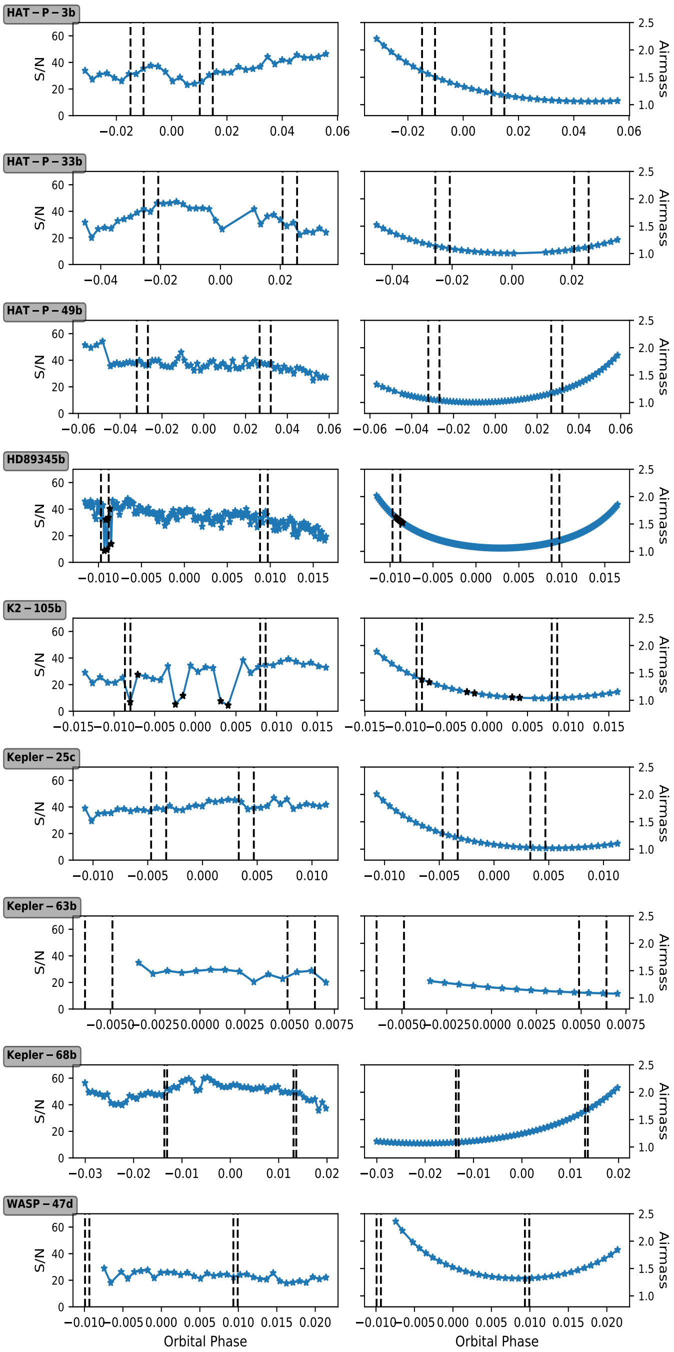

Fig. 2. S/N in the region of interest (1082.2-1085.5 nm)(left panel) and airmass (right panel) measured during the GIARPS observations. The vertical dashed lines mark the t_1, t_2, t_3, and t_4 contact points (from left to right). Black stars indicate the discarded AB couples for low S/N.

Table 1. Log of TNG-GIANO-B observations.

Target	Night	S/N$_{\mathrm{AVE}}$	am$_{\mathrm{min}}$-am$_{\mathrm{max}}$	N$_{\mathrm{obs}}$	Exposure time [s]
HAT-P-3b	2020-01-30	34	1.1-2.2	34	600.0
HAT-P-33b	2019-12-04	35	1.0-1.5	34	600.0
HAT-P-49b	2020-07-30	37	1.0-1.9	72	300.0^{+}
HD89345b	2020-02-02	34	1.1-2.0	176	100.0
K2-105b	2020-01-18	27	1.0-1.9	32	600.0
Kepler-25c	2019-06-14	40	1.0-2.0	38	600.0
Kepler-63b	2020-05-13	27	1.1-1.3	14	600.0
Kepler-68b	2019-08-03	50	1.1-2.1	66	300.0
WASP-47d	2021-07-30	23	1.3-2.4	34	600.0

Notes. time-averaged S/N in the spectral region containing the HeI triplet (1082.2–1085.5 nm).
($^{+}$) First four exposures at 600s.

2017). Therefore, while the targets were observed in one nodding position along the slit (A and B), the sky spectra were gathered simultaneously with the other one, thus providing an accurate reference for subtracting the thermal background and telluric emission lines.

GIANO-B covers the Y, J, H, and K spectral bands (0.95-2.45 μm) in 50 orders at a resolving power of R∼50,000. For this analysis, we focus on order #39, where the helium triplet falls. We collected a transit observation for each investigated target. The only exception is HAT-P-3b, as due to bad weather conditions, we collected two nights of observation, namely UT 14 April 2019 and UT 30 January 2020, but the first visit was excluded from our analysis since observations had to be stopped just before the transit. A log of the observations is reported in Table 1. Figure 2 shows the variation in the signal-to-noise ratio (S/N) for order #39 and the variation in airmass for each exposure. Due to the lack of a sufficient number of collected images, we had to discard Kepler-63b from our analysis. Moreover, K2-105b's and HD89345b's observations were affected by GIANO-B auto-guide problems and by the presence of clouds, so we decided to discard the AB couples of exposures which exhibit a very low S/N.

4. Data analysis

Extended or evaporating atmospheres can be detected through an excess absorption by metastable helium in the planet transmission spectrum. In the following section, we discuss the steps we performed in order to reduce the raw GIANO-B data, extract individual transmission spectra, and calculate average in-transit spectra in the planet rest frame.

4.1. Initial data reduction

The raw spectra were dark-subtracted, flat-corrected, and extracted (without applying the blaze function correction) using the GOFIO pipeline (Rainer et al. 2018). In addition, GOFIO yields a preliminary wavelength calibration (defined in vacuum) using U-Ne lamp spectra as a template. We used the ms1d spectra, with the echelle orders separated and the Barycentric Earth Radial Velocity (BERV) correction applied, the spectra are defined in the terrestrial rest frame.

Since the U-Ne is acquired at the end of the night to avoid the persistence of the saturated signal of some emission lines on the detector polluting the scientific observations, the mechanical instability of GIANO-B makes the wavelength solution determined by GOFIO insufficient in terms of accuracy. We corrected for this by aligning all the GIANO-B spectra to the telluric reference frame via spline-interpolation based on the retrieved shifts obtained by cross-correlating with a time-averaged spectrum used as a template (Brogi et al. 2018; Guilluy et al. 2019, 2020; Giacobbe et al. 2021). We thus aligned the spectra to the reference frame of the Earth's atmosphere, which is also assumed as the frame of the observer (neglecting any ∼10

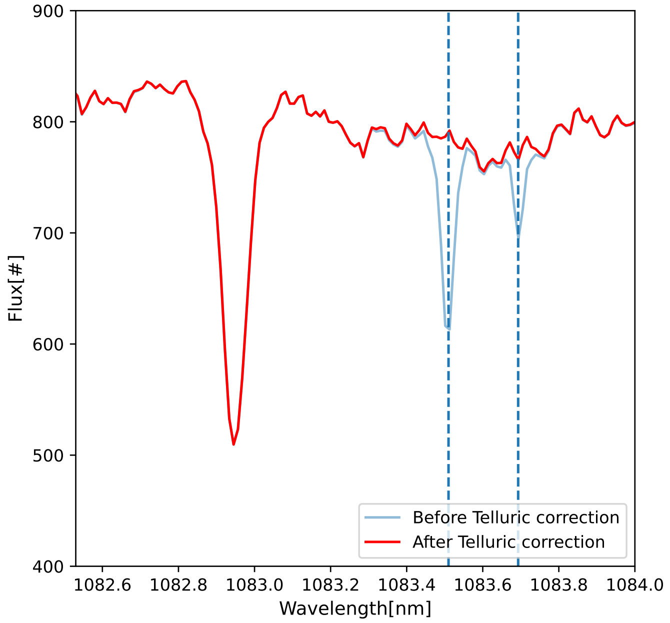

Fig. 3. Example of a time-averaged spectrum before (in blue) and after the telluric lines removal (in red). Dashed vertical lines highlight the position of two H_2O telluric lines, i.e., 1083.51 nm and 1083.69 nm, in the region around the He I triplet. These two lines are corrected in the red spectrum.

m s^{-1} differences due to winds). We then used the atmospheric transmission spectrum generated via the ESO Sky Model Calculator[1] to refine the initial GOFIO wavelength calibration.[2]

4.2. Transmission spectroscopy

We performed the transmission spectroscopy, applying the steps described below to each transit and target independently and considering the system parameters listed in Table A.2.

4.2.1. Telluric correction

First, we performed a detailed correction for telluric contamination. We used the `Molecfit` ESO software (Smette et al. 2015; Kausch et al. 2015) to correct for the transmission telluric lines (Allart et al. 2017). As this is the first time that `Molecfit` has been applied to GIANO-B data, we report the adopted parameters in Table A.3 .

`Molecfit` is based on a combination of two different sources: an atmospheric standard profile (MIPAS), and a Global Data Assimilation System (GDAS) profile. `Molecfit` gives the merging of these two profiles as input for a line-by-line radiative transfer model (LBLRTM). We considered the precipitable water vapor in our transmission model, and selected a fixed grid to merge the two atmospheric models, namely, the variations in temperature, pressure, humidity, and abundance of H_2O from 0 to 120 km are described with a fixed number of layers (50). Meanwhile, LBLRTM returns the telluric spectrum. We considered one observation at a time,and we initially performed the model fitting on selected spectral intervals inside the order #39 showing a well-determined continuum level, a good number of telluric lines, and a few or zero stellar lines. Based on the best-fit parameters derived by `Molecfit,` we then generated a telluric spectrum for the entire spectral order and we corrected the science spectrum. An example of telluric removal is shown in Fig. 3.

In the spectral region of interest, there are three OH emission lines that fall near the He I triplet (at ~1083.21 nm, ~1083.24 nm, and ~1083.43 nm, vacuum wavelengths). As the observations were gathered with the nodding acquisition mode that allows for the subtraction of the thermal background and emission lines (see Sect. 4.1), there is no need to correct for telluric emission lines. However, due to seeing variations during the observing nights, the A-B subtraction can leave some residuals at the wavelengths of the OH lines. We thus masked the correspondent wavelengths.

4.2.2. Alignment into stellar rest frame.

We then shifted the spectra in the stellar rest frame by accounting for the stellar radial velocity, $V_\star$, in the telluric reference system. This is given by:

$$V_{\star/\oplus} = \sum_i K_{\star i}[cos(\nu_i + \omega_i) + e_i cos(\omega_i)] + V_{\rm sys} + V_{\rm bar}, \quad (1)$$

where we account for the velocity of the observer induced by the rotation of the Earth and by the motion of the Earth around the Sun, namely: the barycentric Earth radial velocity, $V_{\rm bar}$, the stellar reflex motion induced on the host star by each planet i in the system (i.e. $K_{\star i}[cos(\nu_{\rm i} + \omega_{\rm i}) + e_{\rm i} cos(\omega_{\rm i})]$, where $\nu_{\rm i}$ is the true anomaly obtained from the eccentric anomaly via the Kepler's equation, in this way we directly account for the eccentricity which is significative for some of our targets, e.g., HAT-P-33b, HD89345b), $\omega_{\rm i}$ is the argument of periastron, $e_{\rm i}$ is the eccentricity, and $K_{\star i}$ is the stellar radial-velocity semi-amplitude, and the systemic velocity of the star-planets system with respect to the barycentre of the Solar System ($V_{\rm sys}$).

4.2.3. Transmission spectra calculation.

For every considered target, we divided each spectrum[3] by its median value, thus obtaining the normalized spectra, $\tilde{\rm F}_{\rm i}$. We then built a master stellar spectrum, $S_{\rm out}(\lambda)$, by averaging the out-of-transit spectra (i.e., with an orbital phase smaller than $\rm t_1$ or greater than $\rm t_4$), and derived individual transmission spectra, $T_{\lambda,\rm i}$, by dividing each spectrum by $S_{\rm out}(\lambda)$, that is, $\rm T_{\lambda,i}=\tilde{F}_i(\lambda)/S_{out}(\lambda)$ -1. Finally, we linearly interpolated transmission spectra in the planet rest frame, as follows:

$$V_{\rm pl_j/\star} = -\sum_i K_{\star i}[cos(\nu_i + \omega_i) + e_i cos(\omega_i)] - K_{\rm pl_j}(cos(\nu_j + \omega_j) + e_j cos(\omega_j)), \quad (2)$$

---

[1] `https://www.eso.org/observing/etc/bin/gen/form?INS.MODE=swspectr+INS.NAME=SKYCALC`

[2] When the telluric lines are not strong enough, the re-alignment into the telluric rest frame may not work properly, as in the case of Kepler-68b. Thus, we preferred to discard this step in the analysis for this specific target.

[3] We did not consider some spectra which exhibited much lower S/N compared to the other exposures or outliers near the position of the He I triplet -see Fig.A.2 for details.

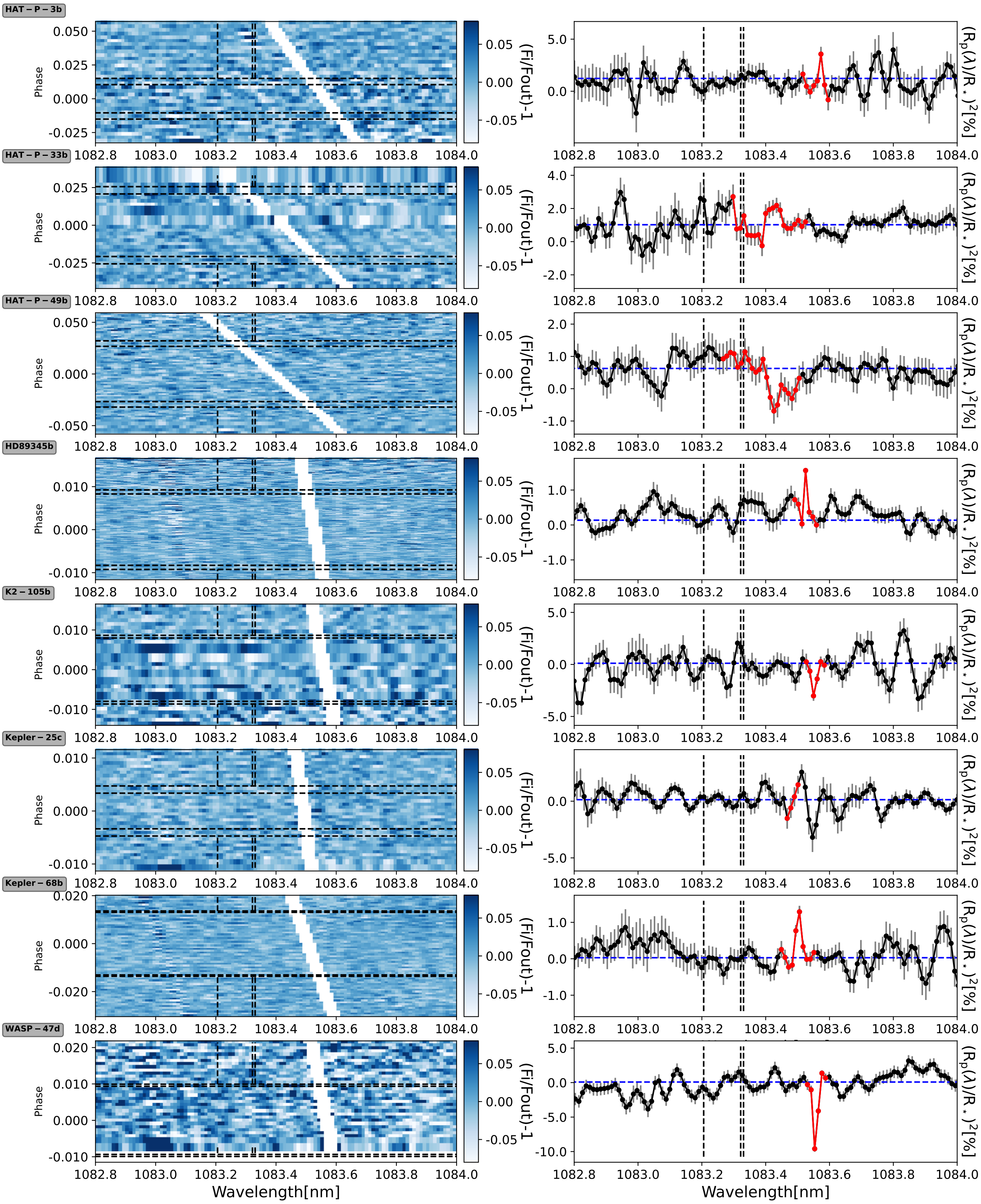

Fig. 4. Transmission spectra ($T_{\lambda,i}=\tilde{F_i(\lambda)}/S_{out}(\lambda)$ -1) shown in tomography in the planetary rest frame in the region of the He I triplet, as a function of wavelength and planetary orbital phase (left). The contact points t_1, t_2, t_3, and t_4 are marked with horizontal black lines. The regions affected by OH^- contamination are masked. Mean-transmission spectrum for each observed transit (right). The horizontal blue line is the white-light radius $(R_{pl}/R_\star)^2$. The mean transmission spectra have an inverted sign compared to $\tilde{F_i(\lambda)}/S_{out}(\lambda)$ -1 as the radius is expressed instead of absorption. Black vertical lines indicate the position of the He I lines. Red line marks the spectral regions affected by OH^- emission. For some planets, some residuals are left at the position of the Si line (∼1083 nm). This is due to the depth of the line which can give rise to difficulties in the spectral extraction (see e.g., Krishnamurthy et al. 2023)

.

where $K_{\mathrm{pl_j}}$ is the computed planet radial-velocity semi-amplitude (see Table A.2) of the considered target j). The 2D maps of the transmission spectra in the planet rest frame are shown in the left panels of Fig. 4.

The usual method to search for faint planetary atmospheric signatures is to average in-transit transmission spectra in the planet rest frame and thus boost the S/N. However, the naive calculation of transmission spectra performed above neglects the change in broadband flux level of in-transit flux spectra, due to the occultation of regions with varying flux intensity by the opaque planetary disk. For example, limb-darkening, if unaccounted for, biases the retrieved atmospheric absorption signal toward smaller values at phases close to the stellar limb, as compared to the stellar disk center. We thus followed the approach presented in Mounzer et al. (2022) that had been re-adapted from Wyttenbach et al. (2020) to compute the in-transit transmission spectra:

$$\left(\frac{R_{\mathrm{pl}}(\lambda,t)}{R_\star}\right)^2 = \frac{LD_{\mathrm{mean}}}{LD(t)} \frac{F_{\mathrm{out}}(\lambda) - (1-\delta(t))F_{\mathrm{i}}(\lambda,t)}{F_{\mathrm{local}}(\lambda,t)}, \qquad (3)$$

where $F_{\mathrm{i}}(\lambda,t)$ is each observed spectrum at phase t, $1-\delta(t)$ is the broadband ("white-light") transit light curve, $\delta(t)$ is the transit depth, $LD(t)$ and LD_{mean} represent the stellar limb darkening at the position of the transiting planet and the disk-averaged limb-darkening, respectively[4]. We used the Python *batman* code (Kreidberg 2015) and the system parameters from Table A.2 to calculate the white-light transit light curve and the limb-darkening coefficients (see Fig. A.1). $F_{\mathrm{local}}(\lambda)$ is the normalized local stellar spectrum (see Sect. 6) occulted by the planet at phase t. We applied Eq. 3 only to fully in-transit orbital phases (i.e., obtained between the t_2 and t_3 contact points), while ingress, and egress were not considered here. Indeed LD, and occulted stellar surface are not well known at the limbs. If we neglect the RM effect and center-to-limb (CLV) variations, the occulted local stellar spectrum $F_{\mathrm{local}}(\lambda)$ is equal to the disk-integrated stellar spectrum $F_{\mathrm{out}}(\lambda)$ (see Sect. 6), so that Eq. 3 becomes:

$$\left(\frac{R_{\mathrm{pl}}(\lambda,t)}{R_\star}\right)^2 = \frac{LD_{\mathrm{mean}}}{LD(t)} \left(1 - \frac{(1-\delta(t))F_{\mathrm{i}}(\lambda,t)}{F_{\mathrm{out}}(\lambda,t)}\right). \qquad (4)$$

All transmission spectra fully in-transit were finally averaged ($\mathrm{T_{mean}}$) to create one transmission spectrum for each observed transit (right panels of Fig. 4).

4.2.4. Fringing correction

Our GIANO-B spectra presented a sinusoidal fringing pattern caused by the sapphire substrate (∼0.38 mm thick) placed above the sensitive part of the detector, which behaves as a Fabry-Pérot in generating interference fringing. Such fringing patterns must be corrected for in studying the He I triplet. We followed and re-adapted the second and third approaches (Method#1b-Method#2) presented in Guilluy et al. (2019). We focused on correcting this effect at the level of the final transmission spectra in order to have better control over fringing in the final transmission spectrum itself and to avoid risks in "overfitting" the data. First, for each planet, we binned $\mathrm{T_{mean}}$ (bin size of 0.2 nm), we thus computed the Lomb-Scargle periodogram to find the characteristic frequency of the periodic fringing signal present in the data f_{best}. We then selected the most prominent frequency of the periodogram, and we fitted the fringing pattern using a sine function $yfit = C + A\sin(2\pi\lambda f + \phi)$, where A is the amplitude, ϕ the phase, f is the fringing frequency (where we assumed f_{best} as starting point for the fit), and C is the overall offset. We finally corrected our final transmission spectra by $yfit$.

5. Interpretation of the transmission spectra

Somewhat surprisingly no He I absorption signature was detected in our sample, as can be seen in Fig. 4. This either means that the targeted planets have no extended atmosphere, which would be surprising given the strong irradiation of their H/He atmosphere; or that their thermosphere's metastable helium population is not dense enough to be detectable within the precision of the GIANO-B observations. Under this assumption, we can still put upper limits on the escape rate by fitting the transmission spectra with models of the planets' thermospheric structure.

5.1. Stellar modelling

Given the scarcity of stellar high-energy measurements, we calculated the X-EUV spectral energy distribution of the eight target stars in a consistent manner using Table 5 in Linsky et al. 2014. This formula depends on the total X-EUV flux emitted by the star, which is calculated based on the stellar age and Equations 3 and 4 from Sanz-Forcada et al. 2011.

5.2. Thermosphere modelling

We used an approximate 1D model, the *p-winds* (Dos Santos et al. 2022) code, largely based on the formulations of Oklopčić & Hirata (2018) and Lampón et al. (2020), to calculate the thermospheric structure and resulting signature of the metastable helium triplet. The atmospheric density and velocity profiles were calculated according to the Parker wind approximation, assuming an isothermal planetary outflow (Parker 1958). We assumed for all targets an atmospheric composition of 90 % H and 10 % He (a good approximation of the Jupiter H/He ratio) and an input stellar X-EUV spectrum (calculated as explained in Section 5.1). The code calculates only the density profiles of hydrogen in its neutral and ionized states, as well as that of helium in its neutral, excited, and singly ionized states. The signature of interest is the metastable transition at 1083.3 nm of the helium excited level. A theoretical ideal spectrum is calculated at mid-transit without taking into account geometrical effects and inhomogeneities of the stellar surface. This absorption signature is compared to the observed mean transmission spectrum to estimate upper atmosphere characteristics such as temperature and the mass-loss rates.

Since there is no clear evidence of a helium signature, we quickly explored the input parameter space of the *p-winds* models by varying only the isothermal temperature profile, T, and the total atmospheric escape rate, $\dot{M}$, while

---

[4] The limb-darkening correction is applied on the spectra aligned in the planet rest frame

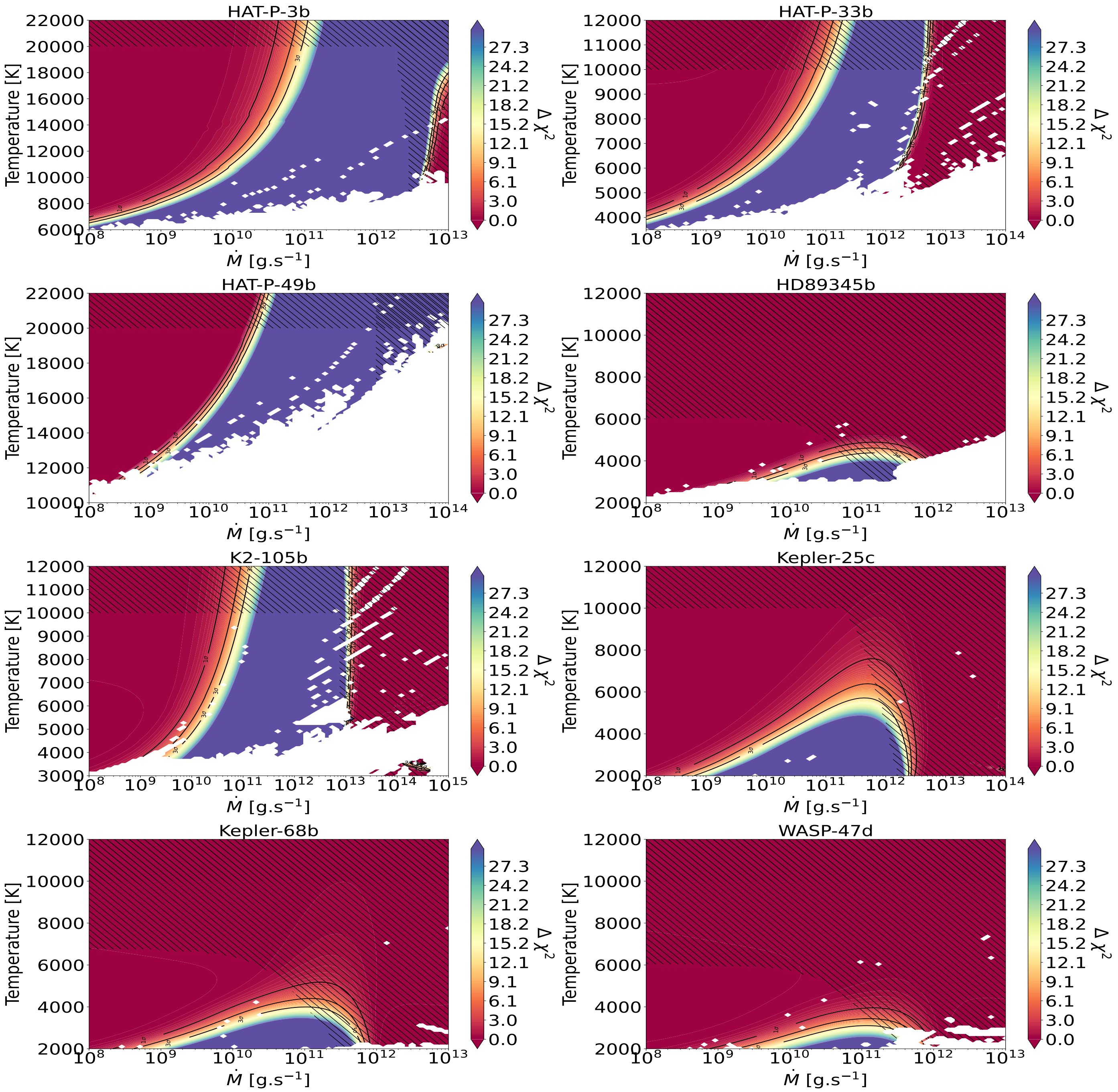

Fig. 5. $\Delta\chi^2$ maps of mass-loss rate and temperature for the planets of our survey. Regions of the parameter space in red are consistent with the non-detections in our data, while models in purple are strongly disfavored. The thermospheric model failed to converge in white regions. Hatched regions are physically excluded.

all other input parameters are fixed. For instance, H/He ratio was not a fitting parameter. We expect that this can slightly change the derived values, but the conclusion would still remain the same. In our models, the radius at the top of the simulated atmosphere was set to the Roche lobe (Eggleton 1983). We note that the value chosen for this upper radius has not been discussed in previous studies using the *p-winds* code or similar codes (e.g., Oklopčić & Hirata 2018; Lampón et al. 2020; Dos Santos et al. 2022; Kirk et al. 2022), even though it directly controls the amount of helium that contributes to the theoretical absorption signature. The preferred approach in the literature seems to be increasing the radius until the neutral triplet helium density no longer contributes significantly to the absorption signal. Yet this is hardly compatible with the change in nature of the atmosphere beyond the Roche lobe, from a collisional thermosphere shaped by planetary gravity, which may (at first order) still be described by a 1D vertical structure, to an asymmetrical exosphere shaped by the stellar gravity, radiation, and wind. Our choice to set the upper model radius at the Roche lobe is based on the reasonable assumption that once helium atoms escape into the exosphere, they cannot be excited into their metastable state by collisions anymore and are quickly photo-ionized so that these layers contribute little to the observed signature (as supported by the lack of clear detection of extended exospheric tails in the literature).

In our simulations, high escape rates lead to an increase in the total density of metastable helium in the thermosphere but the densest layers are shifted to higher altitudes above the Roche lobe, where they no longer contribute to the theoretical signature. This boundary effect is visible in Fig. 5, with the reappearance of fit regions compatible with the non-detection of an absorption signature in our data. Simulations at high escape rates are therefore model-biased and should be considered cautiously. Furthermore, we note that the code *p-winds* was unable to calculate the atmospheric structure in certain regions of the parameter space (shown in white in Fig. 5). It is still unclear whether this is a numerical issue or a truly non-physical regime for the thermosphere.

5.3. Parameter space exploration

We determined whether the models were compatible with the measured transmission spectra using χ^2 comparison. Since no absorption signature was detected for any of the planets we took the null hypothesis (a flat transmission spectrum) as the best-fit model and use $\Delta\chi^2 = \chi^2_{model} - \chi^2_{flat}$ as a criterion to determine 3-σ upper limits on the atmospheric mass-loss rate. We constrained the parameter space to realistic models in mass loss, using the maximum efficiency for a photoionization-driven isothermal Parker wind (Vissapragada et al. 2022), and in temperature, using the model of Salz et al. (2016) as a function of the gravitational potential of the planet. Below $\log(-\Phi_G) = \log GM_{pl}/R_{pl} = 13.0$ erg·g^{-1}, their model predicts temperatures lower than 10 000 K, while above this limit, it predicts temperatures lower than 20 000 K. χ^2 maps as a function of mass loss and temperature are shown in Fig. 5 for all planets in our sample. Table 2 gathers all the derived 3-σ upper limits.

6. Accurate stellar line profiles

Planet-occulted line distortions (POLD, Dethier & Bourrier 2023) can bias or even hide planetary absorption signatures in transmission spectra (Yan et al. 2017; Casasayas-Barris et al. 2020, 2021b). They appear in particular when one uses the disk-integrated stellar spectrum ($\mathrm{F_{out}}$) to normalize the spectrum that is absorbed by the planet and its atmosphere. Indeed, the line profiles of $\mathrm{F_{out}}$ are shaped by a combination of the local effects of stellar rotation and CLV from all over the stellar disk; thus, they are not necessarily representative of the line profiles occulted by the planet. To mitigate the POLDs one needs to define more accurate estimates of the local stellar spectrum occulted by the planetary disk at each exposure. However, this quantity is complex to estimate from observations, as stars cannot be resolved spatially.

To estimate the planet-occulted stellar spectrum, we fit a model to the measured disk-integrated spectrum, using a combination of analytical and simulated theoretical local spectra. The stellar disk is discretized by a 2D uniform square grid, each cell being associated with a specific local intensity spectrum.

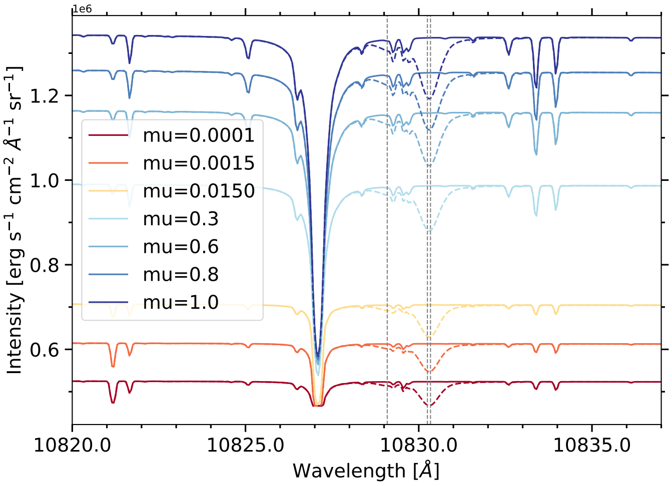

Fig. 6. Spectral intensities for different μ positions on the stellar disk of HAT-P-33 derived with `Turbospectrum`. The dotted spectra are obtained after the multiplication of the intensity spectra by the He I triplet spectral profile. $\mu = \sqrt{1-(x^2+y^2)}$ with (x, y) the coordinates of a point on the stellar disk of radius equal to one in the Cartesian referential centered on the stellar disk.

The simulated component of these intensity spectra is defined using the *Turbospectrum code for spectral synthesis*[5] (Plez 2012). This code uses MARCS photospheric models (Gustafsson et al. 2008)[6] and spectral line-lists from VALD3 database[7] (Ryabchikova et al. 2015) to generate synthetic spectra under the assumption of local thermodynamic equilibrium[8]. For each star, we used `Turbospectrum` to generate high-resolution intensity spectra for a series of positions along the stellar radius to sample broadband limb-darkening and CLV.
These synthetic spectra, however, do not contain the He I triplet lines at 10830Å as its formation in stellar atmospheres necessitates non-local thermodynamical equilibrium conditions that are usually met in chromospheric layers, whereas MARCS models focus on the photospheric layers. We thus calculate the He I triplet absorption lines analytically, assuming Gaussian cross-sections and a common temperature and density for the metastable helium gas. Figure 6 shows a series of intensity spectra across the stellar disk of HAT-P-33.

The series of synthetic+analytical intensity spectra is then interpolated over the whole stellar grid, and Doppler-shifted according to the local radial velocity set by the projected stellar rotational velocity (Bourrier et al. 2023). Subsequently, intensity spectra are scaled into local flux spectra using the surface of the stellar grid cells, and summed over the whole grid to derive a simulated disk-integrated spectrum of the target star. Finally, the disk-integrated spectra are convolved with GIANO-B instrumental response and resampled to match its spectral

---

[5] `https://github.com/bertrandplez/Turbospectrum2019`

[6] `https://marcs.astro.uu.se`

[7] `http://vald.astro.uu.se`

[8] We used the `interpol_marcs` module to derive a MARCS model for the exact values of temperature, metallicity and log g of our target stars. Available for downloads at `https://marcs.astro.uu.se/software.php`

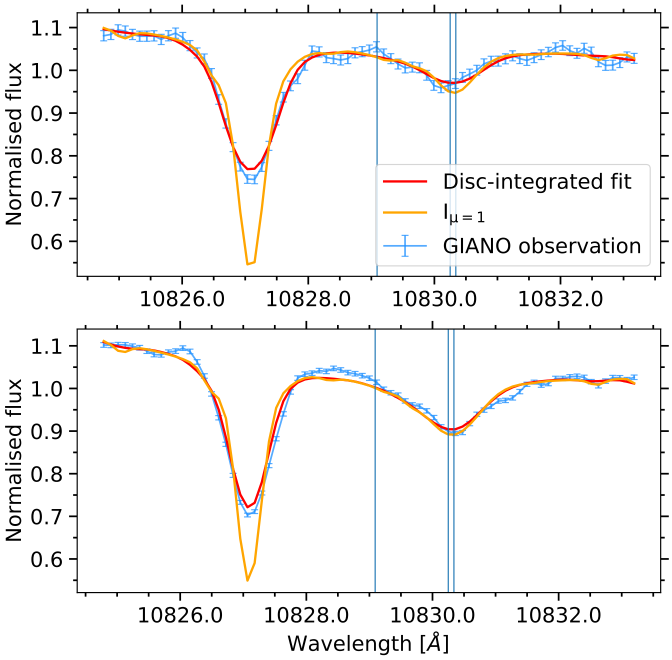

Fig. 7. Normalized spectra of HAT-P-33 (upper panel) and HAT-P-49 (lower panel). We show the best fit (red curve) to the observed (blue curve) disk-integrated spectrum, and the spectrum at the disk's center (orange curve). The blue vertical lines show the transition wavelength of the He I triplet.

resolution. The observed and simulated disk-integrated spectra are compared using a MCMC fit with free parameters set to the temperature and density of the metastable helium atoms.

Figure 7 shows the results of our fits for HAT-P-33 and HAT-P-49, which have the highest $v\sin i_\star$ of our sample, highlighting the local spectrum at disk's center that is later used in Eq. 3. We only applied this approach to the four targets with the highest $v\sin i_\star$, as POLDs are expected to be negligible for the other targets. For these slow rotators, the rotational broadening of the disk-integrated line profiles is small and they remain good proxies for the local planet-occulted lines, especially for the shallow He I triplet lines. We note that CLV is not accounted for in our analytical estimates of the He I lines.

We underline that even for the four fast-rotating targets for which we used a more accurate proxy for the planet-occulted stellar line the amplitude of the POLD was found to be comparable to the dispersion of the data. This is partly due to the shallowness of the He I triplet lines, and to the fact that POLDs partially smooth out when averaging transmission spectra in the planet rest frame over the transit window. Indeed, POLDs shift along the stellar surface RVs, while planetary signatures shift along the planet orbital RVs (see Fig. A.3). Therefore, our final interpretation is made based on the transmission spectra calculated with the disk-integrated spectrum.

7. Results

The presence of an extended and possibly escaping helium atmosphere would appear as an absorption feature in the transmission spectrum in the planet's rest frame at the position of the stellar helium triplet. Unfortunately, as shown in Fig. 4, we did not detect significant helium absorption features for any of our targets. We thus evaluated 3σ upper limits from the data itself as in Allart et al. (2023). Following an approach similar to that of Cubillos et al. (2017), we computed Allan plots (see Fig. A.4) to estimate the noise present in the data. We assumed the white noise σ_1 to be the standard deviation (hereafter, root mean square, rms) of the transmission spectrum, excluding the helium triplet region (1083.0-1083.6 nm). Then, we binned the transmission spectrum by bins of N elements each and calculated the rms of the binned transmission spectrum. We repeat the process for a wide range of N elements for bin (from 1 to 42). In the absence of correlated noise, σ_1 scales as $\sqrt{N}$. We then fitted the rms in a log-log space to derive the trend of the noise, the fitted rms at 0.075 nm is the 1 σ uncertainty. We set three times this value as the 3σ upper limit on the signature contrast, c.

An alternative approach to providing more rigorous estimations of the noise present in the data requires the use of Gaussian processes (See Appendix Sect. B). However, for the rest of the analysis, to maintain consistency with the results published in Allart et al. (2023), we used upper limits estimated from Allan plots.

We then derived an upper limit on the equivalent opaque radius $\delta_{\mathrm{R_P}}$, namely, the height of an opaque atmospheric layer that would produce the observed absorption signal, as:

$$\delta_{\mathrm{R_P}} = \sqrt{(R_\mathrm{P}^2 + R_\star^2 \times c)} - R_\mathrm{P}\,, \tag{5}$$

where R_p and $R_\star$ are the planetary and stellar radius, respectively.

We finally computed the quantity $\delta_{\mathrm{R_P}}/H_\mathrm{eq}$ (Nortmann et al. 2018), which expresses the number of scale heights (H_eq) probed by the atmosphere in the considered spectral range, with $H_\mathrm{eq} = \frac{k_\mathrm{B} T_\mathrm{eq}}{\mu g}$ and k_B the Boltzmann constant, T_eq the planetary equilibrium temperature (listed in Table A.2), g the planetary gravity computed from the planetary mass and radius (reported in Table 2), μ the mean molecular weight (for which we assumed a hydrogen-dominated atmosphere and hence a value of 1.3 times the mass of a hydrogen atom). Table 2 reports the derived $\delta_{\mathrm{R_P}}/H_\mathrm{eq}$ values for each investigated planet.

We explored how the derived constraints vary as a function of the stellar mass and XUV flux between 5 and 504 Å, which are the energies mainly responsible for the population of the metastable He I level (Sanz-Forcada et al. 2011)[9]. We focused on these two parameters because Allart et al. (2023) showed that they do yield visible trends with $\delta_{\mathrm{R_P}}/H_\mathrm{eq}$. Trends related to the excess of absorption and atmospheric extension are shown in the top and middle panels of Fig. 8. All our targets are outside the area of the parameter space, with masses between ∼0.6 and ∼0.85 M$_\odot$, as pointed out by Allart et al. (2023) to favor the He I detection. This range of stellar masses corresponds to K-stars, in agreement with the predictions

---

[9] For consistency, in Appendix in Fig. A.5 we reported also the same plots as a function of the insolation level of mid-UV flux, which accordingly to Oklopčić 2019 ionizes the Helium's metastable state

Table 2. He I measurements.

Target	Roche lobe [R_P]	g_P [m s^{-2}]	Excess of absorption [%]	H_{eq} [Km]	δ_{R_P}/H_{eq}	$F_{5-504\ \text{Å}}$ [10^3 erg s^{-1} cm^{-2}]	$\dot{M}$ 3σ [10^{10} g s^{-1}]
HAT-P-3b	3.647	17.5	< 1.9	424	92	7.968	7.772
HAT-P-33b	2.167	5.1	< 1.4	2231	33	6.195	8.205
HAT-P-49b	3.207	21.5	< 0.6	629	61	14.51	5.702
HD89345b	8.213	7.8	< 0.7	855	76	0.244	3.899
K2-105b	11.202	23.6	< 2.33	219	378	14.69	6.028
Kepler-25c	8.148	5.3	< 1.86	1192	82	1.019	65.26
Kepler-68b	8.722	15.2	< 0.72	533	112	1.176	8.134
WASP-47d	9.565	10.9	< 3.29	533	230	0.577	7.854

Notes. From left to right: Roche lobe (estimated following Eggleton 1983), planet's surface gravity, excess of absorption, atmospheric scale heights (computed by assuming μ=1.3, Sect 7), δ_{R_P}/H_{eq} (i.e. the 3σ upper limits), the stellar XUV flux at the planet position, and the mass-loss rates computed with the *p-winds* code at 3σ.

of Oklopčić (2019), thus our non-detections are not entirely unexpected. However, half of our non-detections do not agree with the XUV flux range found to favor the presence of He I in Allart et al. (2023), 1400-17800 erg s^{-1} cm^{-2}. However, the XUV flux values depend on the model and are associated with star ages, which are typically not well-constrained. So we have to be cautious with these values. Finally, as already highlighted in Allart et al. (2023), even if surprising, there are no clear correlations between $\dot{M}$ and the stellar mass or XUV flux (bottom panels of Fig. 8).

We chose to focus on the targets analyzed in this paper and in Allart et al. (2023), rather than other results from the literature because we derived the absorption, atmospheric extension, and mass-loss values homogeneously with the same methodology.

8. Summary and conclusions

In this paper, we describe our He I survey of 9 planets at the edge of the Neptunian desert, with the goal of understanding the role of photoevaporation in sculpturing this feature. We analyzed observations gathered with the high-resolution GIANO-B spectrograph mounted on the TNG, and we used the transmission spectroscopy technique to detect a possible extended or evaporating helium atmosphere in the investigated planets. We found no sign of planetary absorption at the position of the stellar He I triplet in any of the investigated targets, and we thus provided 3σ upper limits on the He I absorption. We underline that the GIANO-B transmission spectra are affected by various systematics that are not fully understood and difficult to properly remove. These systematics may be caused by low data quality (e.g., low S/N) or instrumental effects (e.g., auto-guide problems).

We interpreted our derived transmission spectra with the *p-wind* code (Dos Santos et al. 2022) and we attempted to interpret our findings by putting them in the wider context of the measurements presented in Allart et al. 2023 submitted. We searched for correlations with the stellar mass and XUV flux (e.g., Fossati et al. 2022), which are thought to be key drivers in the formation of the He I triplet. Constraints from our sample support the trend of δ_{R_P}/H_{eq}, with the stellar mass proposed by Allart et al. (2023), which remains a good indicator for the presence of metastable helium in exoplanet atmospheres. In addition, they are not incompatible with the trend highlighted in Allart et al. (2023) with the XUV flux as they are not constraining enough to reach a better precision. We stress the importance of carrying out helium surveys with the same instrument and analyzing them with the same data reduction technique, as heterogeneity can obscure any trends in the data (Vissapragada et al. 2022). Several instruments are now available to perform this kind of homogeneous survey such as NIRSPEC, SPIROU, CARMENES, and GIANO-B.

References

Akeson, R. L., Chen, X., Ciardi, D., et al. 2013, PASP, 125, 989
Allart, R., Bourrier, V., Lovis, C., et al. 2019, A&A, 623, A58
Allart, R., Bourrier, V., Lovis, C., et al. 2018, Science, 362, 1384
Allart, R., Lemée-Joliecoeur, P. B., Jaziri, A. Y., et al. 2023, arXiv e-prints, arXiv:2307.05580
Allart, R., Lovis, C., Pino, L., et al. 2017, A&A, 606, A144
Almenara, J. M., Díaz, R. F., Bonfils, X., & Udry, S. 2016, A&A, 595, L5
Alonso-Floriano, F. J., Snellen, I. A. G., Czesla, S., et al. 2019, A&A, 629, A110
Attia, O., Bourrier, V., Delisle, J. B., & Eggenberger, P. 2023, A&A, 674, A120
Attia, O., Bourrier, V., Eggenberger, P., et al. 2021, A&A, 647, A40
Baluev, R. V., Sokov, E. N., Jones, H. R. A., et al. 2019, MNRAS, 490, 1294
Battley, M. P., Kunimoto, M., Armstrong, D. J., & Pollacco, D. 2021, MNRAS, 503, 4092
Beaugé, C. & Nesvorný, D. 2013, ApJ, 763, 12
Bennett, K. A., Redfield, S., Oklopčić, A., et al. 2023, AJ, 165, 264
Benomar, O., Masuda, K., Shibahashi, H., & Suto, Y. 2014, PASJ, 66, 94
Bieryla, A., Hartman, J. D., Bakos, G. Á., et al. 2014, AJ, 147, 84
Bonomo, A. S., Desidera, S., Benatti, S., et al. 2017, A&A, 602, A107
Bourrier, V., Attia, O., Mallonn, M., et al. 2023, A&A, 669, A63
Bourrier, V., Lecavelier des Etangs, A., Ehrenreich, D., et al. 2018, A&A, 620, A147
Brogi, M., Giacobbe, P., Guilluy, G., et al. 2018, A&A, 615, A16
Bryant, E. M. & Bayliss, D. 2022, AJ, 163, 197
Cannon, A. J. & Pickering, E. C. 1993, VizieR Online Data Catalog, III/135A
Carleo, I., Youngblood, A., Redfield, S., et al. 2021, AJ, 161, 136
Casasayas-Barris, N., Orell-Miquel, J., Stangret, M., et al. 2021a, A&A, 654, A163
Casasayas-Barris, N., Palle, E., Stangret, M., et al. 2021b, A&A, 647, A26
Casasayas-Barris, N., Pallé, E., Yan, F., et al. 2020, A&A, 635, A206
Castro-González, A., Díez Alonso, E., Menéndez Blanco, J., et al. 2022, MNRAS, 509, 1075
Chan, T., Ingemyr, M., Winn, J. N., et al. 2011, AJ, 141, 179
Claudi, R., Benatti, S., Carleo, I., et al. 2017, European Physical Journal Plus, 132, 364
Crossfield, I. J. M. & Kreidberg, L. 2017, AJ, 154, 6

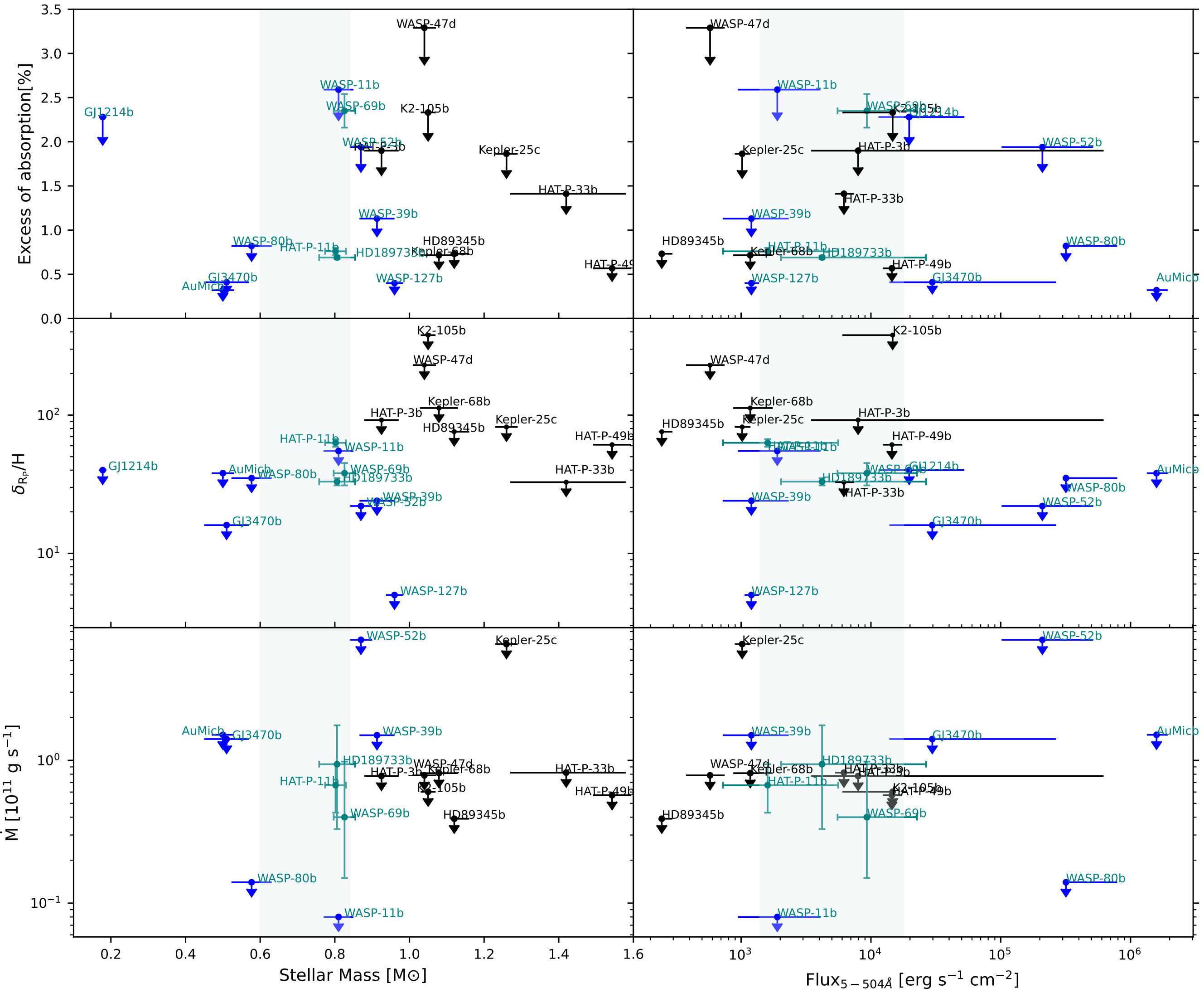

Fig. 8. Correlation plots. Excess of absorption (top panels), δ_{R_P}/H_{eq} (middle panels) and mass-loss rates (bottom panels) as a function of stellar mass and XUV irradiation at the planet position. Upper limits are given at 3σ. Blue stars are targets reported from Allart et al. (2023), the detections and the non-detections are plotted in dark- and light-blue, respectively. We note that K2-105 b observations suffered from GIANO-B's auto-guide problems and low S/N, so the limit we set on δ_{R_P}/H_{eq} is not constraining. We highlighted in gray the area of the parameter space that accordingly to Allart et al. (2023) seems to favor the detections. The errors on the XUV flux have been calculated with the error on the stellar ages.

Cubillos, P., Harrington, J., Loredo, T. J., et al. 2017, AJ, 153, 3
Cutri, R. M., Skrutskie, M. F., van Dyk, S., et al. 2003, VizieR Online Data Catalog, II/246
Czesla, S., Lampón, M., Sanz-Forcada, J., et al. 2022, A&A, 657, A6
Davis, T. A. & Wheatley, P. J. 2009, MNRAS, 396, 1012
Dethier, W. & Bourrier, V. 2023, A&A, 674, A86
dos Santos, L. A., Ehrenreich, D., Bourrier, V., et al. 2020a, A&A, 640, A29
dos Santos, L. A., Ehrenreich, D., Bourrier, V., et al. 2020b, A&A, 634, L4
Dos Santos, L. A., Vidotto, A. A., Vissapragada, S., et al. 2022, A&A, 659, A62
Eastman, J., Gaudi, B. S., & Agol, E. 2013, PASP, 125, 83
Eggleton, P. P. 1983, ApJ, 268, 368
Ehrenreich, D., Bourrier, V., Bonfils, X., et al. 2012, A&A, 547, A18
Ehrenreich, D., Bourrier, V., Wheatley, P. J., et al. 2015, Nature, 522, 459
Fossati, L., Guilluy, G., Shaikhislamov, I. F., et al. 2022, A&A, 658, A136
Gaidos, E., Hirano, T., Beichman, C., et al. 2022, MNRAS, 509, 2969
Gaidos, E., Hirano, T., Lee, R. A., et al. 2023, MNRAS, 518, 3777
Gaidos, E., Hirano, T., Mann, A. W., et al. 2020a, MNRAS, 495, 650
Gaidos, E., Hirano, T., Wilson, D. J., et al. 2020b, MNRAS, 498, L119
Gajdoš, P., Vaňko, M., & Parimucha, Š. 2019, Research in Astronomy and Astrophysics, 19, 041
Giacobbe, P., Brogi, M., Gandhi, S., et al. 2021, Nature, 592, 205
Gilliland, R. L., Marcy, G. W., Rowe, J. F., et al. 2013, ApJ, 766, 40
Grieves, N., Ge, J., Thomas, N., et al. 2018, MNRAS, 481, 3244
Guilluy, G., Andretta, V., Borsa, F., et al. 2020, A&A, 639, A49
Guilluy, G., Sozzetti, A., Brogi, M., et al. 2019, A&A, 625, A107
Gustafsson, B., Edvardsson, B., Eriksson, K., et al. 2008, A&A, 486, 951
Hartman, J. D., Bakos, G. Á., Torres, G., et al. 2011, ApJ, 742, 59
Hellier, C., Anderson, D. R., Collier Cameron, A., et al. 2012, MNRAS, 426, 739
Hirano, T., Krishnamurthy, V., Gaidos, E., et al. 2020, ApJ, 899, L13
Howe, A. R., Burrows, A., & Verne, W. 2014, ApJ, 787, 173
Kanodia, S., Cañas, C. I., Stefansson, G., et al. 2020, ApJ, 899, 29
Kanodia, S., Libby-Roberts, J., Cañas, C. I., et al. 2022, AJ, 164, 81
Kasper, D., Bean, J. L., Oklopčić, A., et al. 2020, AJ, 160, 258
Kausch, W., Noll, S., Smette, A., et al. 2015, A&A, 576, A78
Kawauchi, K., Murgas, F., Palle, E., et al. 2022, A&A, 666, A4
Kirk, J., Alam, M. K., López-Morales, M., & Zeng, L. 2020, AJ, 159, 115

Kirk, J., Dos Santos, L. A., López-Morales, M., et al. 2022, AJ, 164, 24
Kreidberg, L. 2015, PASP, 127, 1161
Kreidberg, L. & Oklopčić, A. 2018, Research Notes of the American Astronomical Society, 2, 44
Krishnamurthy, V., Hirano, T., Gaidos, E., et al. 2023, MNRAS, 521, 1210
Krishnamurthy, V., Hirano, T., Stefánsson, G., et al. 2021, AJ, 162, 82
Lammer, H., Selsis, F., Ribas, I., et al. 2003, ApJ, 598, L121
Lampón, M., López-Puertas, M., Lara, L. M., et al. 2020, A&A, 636, A13
Lavie, B., Ehrenreich, D., Bourrier, V., et al. 2017, A&A, 605, L7
Lecavelier Des Etangs, A. 2007, A&A, 461, 1185
Lecavelier des Etangs, A., Bourrier, V., Wheatley, P. J., et al. 2012, A&A, 543, L4
Lecavelier des Etangs, A., Vidal-Madjar, A., McConnell, J. C., & Hébrard, G. 2004, A&A, 418, L1
Linsky, J. L., Fontenla, J., & France, K. 2014, ApJ, 780, 61
Livingston, J. H., Crossfield, I. J. M., Petigura, E. A., et al. 2018, AJ, 156, 277
Lopez, E. D. & Fortney, J. J. 2014, ApJ, 792, 1
Luo, A. L., Zhao, Y. H., Zhao, G., & et al. 2018, VizieR Online Data Catalog, V/153
Mallonn, M., Poppenhaeger, K., Granzer, T., Weber, M., & Strassmeier, K. G. 2022, A&A, 657, A102
Mancini, L., Esposito, M., Covino, E., et al. 2018, A&A, 613, A41
Mansfield, M., Bean, J. L., Oklopčić, A., et al. 2018, ApJ, 868, L34
Marcy, G. W., Isaacson, H., Howard, A. W., et al. 2014, The Astrophysical Journal Supplement Series, 210, 20
Matsakos, T. & Königl, A. 2016, ApJ, 820, L8
Migaszewski, C. & Goździewski, K. 2018, MNRAS, 480, 1767
Mills, S. M., Howard, A. W., Weiss, L. M., et al. 2019, AJ, 157, 145
Mounzer, D., Lovis, C., Seidel, J. V., et al. 2022, A&A, 668, A1
Murray-Clay, R. A., Chiang, E. I., & Murray, N. 2009, ApJ, 693, 23
Narita, N., Hirano, T., Fukui, A., et al. 2017, PASJ, 69, 29
Ninan, J. P., Stefansson, G., Mahadevan, S., et al. 2020, ApJ, 894, 97
Nortmann, L., Pallé, E., Salz, M., et al. 2018, Science, 362, 1388
Oklopčić, A. 2019, ApJ, 881, 133
Oklopčić, A. & Hirata, C. M. 2018, ApJ, 855, L11
Orell-Miquel, J., Murgas, F., Pallé, E., et al. 2022, A&A, 659, A55
Owen, J. E. 2019, Annual Review of Earth and Planetary Sciences, 47, 67
Owen, J. E. & Lai, D. 2018, MNRAS, 479, 5012
Owen, J. E., Murray-Clay, R. A., Schreyer, E., et al. 2023, MNRAS, 518, 4357
Owen, J. E. & Wu, Y. 2017, ApJ, 847, 29
Palle, E., Nortmann, L., Casasayas-Barris, N., et al. 2020, A&A, 638, A61
Paragas, K., Vissapragada, S., Knutson, H. A., et al. 2021, ApJ, 909, L10
Parker, E. N. 1958, ApJ, 128, 664
Plez, B. 2012, Turbospectrum: Code for spectral synthesis
Rainer, M., Harutyunyan, A., Carleo, I., et al. 2018, in Society of Photo-Optical Instrumentation Engineers (SPIE) Conference Series, Vol. 10702, Ground-based and Airborne Instrumentation for Astronomy VII, 1070266
Ryabchikova, T., Piskunov, N., Kurucz, R. L., et al. 2015, Physica Scripta, 90, 054005
Salz, M., Czesla, S., Schneider, P. C., et al. 2018, A&A, 620, A97
Salz, M., Czesla, S., Schneider, P. C., & Schmitt, J. H. M. M. 2016, A&A, 586, A75
Sanchis-Ojeda, R., Winn, J. N., Marcy, G. W., et al. 2013, ApJ, 775, 54
Sanz-Forcada, J., Micela, G., Ribas, I., et al. 2011, A&A, 532, A6
Seager, S. & Sasselov, D. D. 2000, ApJ, 537, 916
Smette, A., Sana, H., Noll, S., et al. 2015, A&A, 576, A77
Spake, J. J., Sing, D. K., Evans, T. M., et al. 2018, Nature, 557, 68
Szabó, G. M. & Kiss, L. L. 2011, ApJ, 727, L44
Tripathi, A., Kratter, K. M., Murray-Clay, R. A., & Krumholz, M. R. 2015, ApJ, 808, 173
Turner, J. D., Leiter, R. M., Biddle, L. I., et al. 2017, MNRAS, 472, 3871
Van Eylen, V., Dai, F., Mathur, S., et al. 2018, MNRAS, 478, 4866
Vanderburg, A., Becker, J. C., Buchhave, L. A., et al. 2017, AJ, 154, 237
Vidal-Madjar, A., Lecavelier des Etangs, A., Désert, J. M., et al. 2003, Nature, 422, 143
Vissapragada, S., Knutson, H. A., Greklek-McKeon, M., et al. 2022, AJ, 164, 234
Vissapragada, S., Knutson, H. A., Jovanovic, N., et al. 2020, AJ, 159, 278
Vissapragada, S., Stefánsson, G., Greklek-McKeon, M., et al. 2021, AJ, 162, 222
Wang, Y.-H., Wang, S., Liu, H.-G., et al. 2017, AJ, 154, 49
Wyttenbach, A., Mollière, P., Ehrenreich, D., et al. 2020, A&A, 638, A87
Yan, F., Pallé, E., Fosbury, R. A. E., Petr-Gotzens, M. G., & Henning, T. 2017, A&A, 603, A73
Yu, L., Rodriguez, J. E., Eastman, J. D., et al. 2018, AJ, 156, 127
Zeng, L. & Sasselov, D. 2014, ApJ, 784, 96
Zhang, M., Knutson, H. A., Dai, F., et al. 2023, AJ, 165, 62
Zhang, M., Knutson, H. A., Wang, L., Dai, F., & Barragán, O. 2022a, AJ, 163, 67
Zhang, M., Knutson, H. A., Wang, L., et al. 2022b, AJ, 163, 68
Zhang, M., Knutson, H. A., Wang, L., et al. 2021, AJ, 161, 181

---

[1] INAF – Osservatorio Astrofisico di Torino, Via Osservatorio 20, 10025, Pino Torinese, Italy
[2] Observatoire Astronomique de l'Université de Genève, Chemin Pegasi 51b, 1290, Versoix, Switzerland
[3] Univ. Grenoble Alpes, CNRS, IPAG, 38000 Grenoble, France
[4] Département de Physique, Institut Trottier de Recherche sur les Exoplanètes, Université de Montréal, Montréal, Québec, H3T 1J4, Canada
[5] Space Telescope Science Institute, 3700 San Martin Drive, Baltimore, MD 21218, USA
[6] INAF – Osservatorio Astronomico di Brera, Via E. Bianchi, 46, 23807 Merate (LC), Italy

Acknowledgements. We thank the referee for the comments and suggestions. We thank V.l Andretta for his help. G.G. acknowledge financial contributions from PRIN INAF 2019, and from the agreement ASI-INAF number 2018-16-HH.0 (THE StellaR PAth project). R. A. is a Trottier Postdoctoral Fellow and acknowledges support from the Trottier Family Foundation. This work was supported in part by a grant from the Fonds de Recherche du Québec - Nature et Technologies (FRQNT). This work was funded by the Institut Trottier de Recherche sur les Exoplaneètes (iREx). This work has been carried out within the framework of the NCCR PlanetS supported by the Swiss National Sci- ence Foundation under grants 51NF40182901 and 51NF40205606. This project has received funding from the European Research Council (ERC) under the Eu- ropean Union's Horizon 2020 research and innovation programme (project Spice Dune, grant agreement No 947634). This material reflects only the authors views and the Commission is not liable for any use that may be made of the information contained therein. This work has made use of the VALD database, operated at Uppsala University, the Institute of Astronomy RAS in Moscow, and the University of Vienna. This work has made use of the *Turbospectrum code for spectral synthesis*

Appendix A: Additional figures and tables

Table A.1. Planets with He I study reported in the literature.

Planet	Status	Reference
WASP-11b	✗	Allart et al. 2023
WASP-12b	✗	Kreidberg & Oklopčić 2018
WASP-39b	✗	Allart et al. 2023
WASP-48b	✗	Bennett et al. 2023
WASP-52b	∼	Vissapragada et al. 2020; Kirk et al. 2022; Allart et al. 2023
WASP-69b	✓	Nortmann et al. 2018; Vissapragada et al. 2020; Allart et al. 2023
WASP-80b	✗	Fossati et al. 2022; Vissapragada et al. 2022; Allart et al. 2023
WASP-76b	✗	Casasayas-Barris et al. 2021a
WASP-107b	✓	Spake et al. 2018; Allart et al. 2019; Kirk et al. 2020
WASP-127b	✗	dos Santos et al. 2020a; Allart et al. 2023
WASP-177b	✗	Kirk et al. 2022; Vissapragada et al. 2022
HD189733b	✓	Salz et al. 2018; Guilluy et al. 2020; Zhang et al. 2022a; Allart et al. 2023
HD209458b	∼	Nortmann et al. 2018; Alonso-Floriano et al. 2019
HD97658b	✗	Kasper et al. 2020
HD63433b	✗	Zhang et al. 2022b
HD63433c	✗	Zhang et al. 2022b
HAT-P-11b	✓	Allart et al. 2018; Mansfield et al. 2018; Allart et al. 2023
HAT-P-18b	✓	Paragas et al. 2021; Vissapragada et al. 2022
HAT-P-26b	✓	Vissapragada et al. 2022
HAT-P-32b	✓	Czesla et al. 2022
NGTS-5b	∼	Vissapragada et al. 2022
55Cnce	✗	Zhang et al. 2021
Kelt-9b	✗	Nortmann et al. 2018
GJ3470b	∼	Ninan et al. 2020; Allart et al. 2023; Palle et al. 2020
GJ436b	✗	Nortmann et al. 2018
GJ1214b	∼	e.g.,Orell-Miquel et al. 2022; Kasper et al. 2020; Allart et al. 2023
GJ9827b	✗	Carleo et al. 2021; Krishnamurthy et al. 2023
GJ9827d	✗	Kasper et al. 2020; Carleo et al. 2021; Krishnamurthy et al. 2023
TOI-560b	✓	Zhang et al. 2022a, 2023
TOI-1728b	✗	Kanodia et al. 2020
TOI-1430b	✓	Zhang et al. 2023
TOI-1683b	✓	Zhang et al. 2023
TOI-1807b	✗	Gaidos et al. 2023
TOI-2076b	✗	Zhang et al. 2023; Gaidos et al. 2023
TOI-3757b	✗	Kanodia et al. 2022
TOI-1235b	✗	Krishnamurthy et al. 2023
TOI-2136b	✗	Kawauchi et al. 2022
Trappist-1b	✗	Krishnamurthy et al. 2021
Trappist-1e	✗	Krishnamurthy et al. 2021
Trappist-1f	✗	Krishnamurthy et al. 2021
V1298Taub	∼	e.g., Vissapragada et al. 2021; Gaidos et al. 2022
V1298Tauc	✗	e.g., Vissapragada et al. 2021
V1298Taud	✓	e.g., Vissapragada et al. 2021
AU Mic b	✗	Hirano et al. 2020
K2-25b	✗	Gaidos et al. 2020b
K2-100b	✗	Gaidos et al. 2020a

Notes. From left to right: the investigated planet, the status of the detection (with ✓, ✗, and ∼ indicating detections, non-detections, and not-clear results respectively), and references.

Table A.2. Adopted parameters

Parameter	Value	Reference
HAT-P-3		
• *Stellar parameters*		
Spectral type	K1	Grieves et al. (2018)
Stellar mass, $M_\star$ ($M_\odot$)	0.925 ± 0.046	Mancini et al. (2018)
Stellar radius, $R_\star$ ($M_\odot$)	0.850 ± 0.021	Mancini et al. (2018)
Stellar age, τ (Gyr)	$2.9^{+2.7}_{-4.9}$	Mancini et al. (2018)
Effective temperature, Teff (K)	5190 ± 80	Mancini et al. (2018)
Metallicity (dex)	0.24 ± 0.08 (Fe/H)	Mancini et al. (2018)
log g ($\log_{10}(\mathrm{cm\,s^{-2}})$)	4.545 ± 0.023	Mancini et al. (2018)
Systemic velocity, v_{sys} ($\mathrm{km\,s^{-1}}$)	-23.379680	DREAM I
Limb-darkening coefficients μ_1	0.216	EXOFAST[1]
μ_2	0.286	EXOFAST[1]
Stellar projected velocity, $v\sin i_\star$ ($\mathrm{km\,s^{-1}}$)	$0.46^{+0.22}_{-0.25}$	DREAM 1
Magnitude (J-band)	9.936±0.022	Cutri et al. (2003)
• *Planetary parameters*		
Orbital period, P (days)	2.89973797 ± 0.00000038	Baluev et al. (2019)
Transit epoch, T_0 ($\mathrm{BJD_{TDB}}$)	2454218.75960 ± 0.00016	DREAM I
Eccentricity, e	0.0 (fixed)	Mancini et al. (2018)
Argument of periastron, $\omega_\star$	90 (fixed)	Mancini et al. (2018)
Stellar reflex velocity, $K_\star$ ($\mathrm{m\,s^{-1}}$)	90.63 ± 0.58	Mancini et al. (2018)
Scaled separation, $a/R_\star$	9.8105 ± 0.2667	Mancini et al. (2018)
Orbital inclination, i	86.31 ± 0.19 deg	Mancini et al. (2018)
Planet-to-star radius ratio, $R_P/R_\star$	0.11091 ± 0.00048	Baluev et al. (2019)
Planetary mass, M_{pl} (M_{jup})	0.595 ±0.019	Mancini et al. (2018)
Planetary density, ρ_{pl} (g $\mathrm{cm^{-3}}$)	0.9750±0.1000	Mancini et al. (2018)
Projected spin-orbit angle, λ (deg)	$-25.3^{+29.4}_{-22.8}$	DREAM I
Planet radial-velocity semi-amplitude, K_{pl}($\mathrm{km\,s^{-1}}$)	145.2±2.4	This paper[2]
Equilibrium temperature, T_{eq}(K)	1170±17	Mancini et al. (2018)
HAT-P-33		
• *Stellar parameters*		
Spectral type	F4	Luo et al. (2018)
Stellar mass, $M_\star$ ($M_\odot$)	$1.42\ ^{+0.16}_{-0.15}$	Wang et al. (2017)
Stellar radius, $R_\star$ ($M_\odot$)	$1.91^{+0.26}_{-0.20}$	Wang et al. (2017)
Stellar age, τ (Gyr)	2.30 ± 0.30	Bonomo et al. (2017)
Effective temperature, teff (K)	$6460\ ^{+300}_{-290}$	Wang et al. (2017)
Metallicity (dex)	0.01 ± 0.31 [Fe/H]	Wang et al. (2017)
Surface gravity, log $g_\star$ (cgs)	$4.030^{+0.079}_{-0.090}$	Wang et al. (2017)
Systemic velocity, v_{sys} ($\mathrm{km\,s^{-1}}$)	23.080601	DREAM I
Limb-darkening coefficients μ_1	0.097	EXOFAST[1]
μ_2	0.301	EXOFAST[1]
Stellar projected velocity, $v\sin i_\star$ ($\mathrm{km\,s^{-1}}$)	15.57 ± 0.31	DREAM I
Magnitude (J-band)	10.263±0.021	Cutri et al. (2003)
• *Planetary parameters*		
Orbital period, P (days)	3.47447773 ± 0.00000066	DREAM I
Transit epoch, T_0 ($\mathrm{BJD_{TDB}}$)	2456684.86508 ± 0.00027	DREAM I
Eccentricity, e	$0.180\ ^{+0.110}_{-0.096}$	DREAM I
Argument of periastron, $\omega_\star$ (deg)	88^{+33}_{-34}	Wang et al. (2017)
Stellar reflex velocity, $K_\star$ $\mathrm{m\,s^{-1}}$	74.4±8.5	DREAM I
Scaled separation, $a/R_\star$	$5.69^{+0.58}_{-0.59}$	Wang et al. (2017)
Orbital inclination, i (deg)	$88.2\ ^{+1.2}_{-1.3}$	Wang et al. (2017)
Planet-to-star radius ratio, $R_P/R_\star$	$0.10097\ ^{+0.00056}_{-0.00052}$	Wang et al. (2017)
Planetary mass, M_{pl} (M_{jup})	$0.72\ ^{+0.13}_{-0.12}$	Wang et al. (2017)
Planetary density, ρ_{pl} (g $\mathrm{cm^{-3}}$)	$0.134^{+0.053}_{-0.042}$	Wang et al. (2017)
Projected spin-orbit angle, λ (deg)	5.9±4.1 deg	DREAM I
Planet radial velocity semi-amplitude, K_{pl}($\mathrm{km\,s^{-1}}$)	$160.6^{+6.9}_{-6.3}$	This paper[2]
Equilibrium temperature, T_{eq}(K)	1782±28	Hartman et al. (2011)

Table A.2. continued

Parameter	Value	Reference
HAT-P-49		
• *Stellar parameters*		
Spectral type	F3	DREAM I
Stellar mass, $M_\star$ ($M_\odot$)	1.543 ± 0.051	Bieryla et al. (2014)
Stellar radius, $R_\star$ ($R_\odot$)	$1.833{+}0.138_{-0.076}$	Bieryla et al. (2014)
Stellar age τ (Gyr)	1.50 ± 0.20	Bonomo et al. (2017)
Effective temperature, Teff (K)	6820 ± 52	Bieryla et al. (2014)
Metallicity (dex)	0.074 ± 0.080 [Fe/H]	Bieryla et al. (2014)
Surface gravity, log $g_\star$ (cgs)	4.10 ± 0.04	Bieryla et al. (2014)
Systemic velocity, v_{sys} ($\mathrm{km\,s^{-1}}$)	14.208478	DREAM I
Limb-darkening coeffcients μ_1	0.078	EXOFAST^1
μ_2	0.303	EXOFAST^1
Stellar projected velocity, $v\sin i_\star$ ($\mathrm{km\,s^{-1}}$)	$10.68^{+0.46}_{-0.47}$	DREAM I
Magnitude (J-band)	9.550 ± 0.020	Cutri et al. (2003)
• *Planetary parameters*		
Orbital period, P (days)	2.6915539 ± 0.0000012	DREAM I
Transit epoch, T_0 ($\mathrm{BJD_{TDB}}$) ($\mathrm{BJD_{TDB}}$)	$2456975.61736 \pm 0.00050$	DREAM I
Eccentricity, e	0.0 (fixed)	Bieryla et al. (2014)
Argument of periastron, $\omega_\star$ (deg)	90 (fixed)	Bieryla et al. (2014)
Stellar reflex velocity, $K_\star$ ($\mathrm{m\,s^{-1}}$)	177.6 ± 16.0	DREAM I
Scaled separation, $a/R_\star$	$5.13\ ^{+0.19}_{-0.30}$	Bieryla et al. (2014)
Orbital inclination, i (deg)	86.2 ± 1.7	Bieryla et al. (2014)
Planet-to-star radius ratio, $R_P/R_\star$	0.0792 ± 0.0019	Bieryla et al. (2014)
Planetary M_{pl} (M_{jup})	1.730 ± 0.205	Bieryla et al. (2014)
Planetary density, ρ_{pl} (g $\mathrm{cm^{-3}}$)	0.75 ± 0.17	Bieryla et al. (2014)
Projected spin-orbit angle, λ (deg)	-97.7 ± 1.8	DREAM I
Planet radial velocity semi-amplitude, K_{pl}($\mathrm{km\,s^{-1}}$)	176.5 ± 2.0	This paper^2
Equilibrium temperature, T_{eq}(K)	2131^{+69}_{-42}	Bieryla et al. (2014)
HD89345		
• *Stellar parameters*		
Spectral type	G5	Cannon & Pickering (1993)
Stellar mass, $M_\star$ ($M_\odot$)	$1.120^{+0.040}_{-0.010}$	Van Eylen et al. (2018)
Stellar radius, $R_\star$ ($R_\odot$)	$1.657^{+0.020}_{-0.004}$	Van Eylen et al. (2018)
Stellar age, τ (Gyr)	$9.40\ ^{+0.40}_{-1.30}$	Van Eylen et al. (2018)
Effective temperature, Teff (K)	5499 ± 73	Van Eylen et al. (2018)
Metallicity (dex)	0.45 ± 0.04 [Fe/H]	Van Eylen et al. (2018)
Surface gravity log $g_\star$ ($\log_{10}(\mathrm{cm\,s^{-2}})$)	$4.044^{+0.006}_{-0.004}$	Van Eylen et al. (2018)
Systemic velocity, v_{sys} ($\mathrm{km\,s^{-1}}$)	2.223394	DREAM I
Limb-darkening coeffcients μ_1	0.182	EXOFAST^{12}
μ_2	0.300	EXOFAST^1
Stellar projected velocity, $v\sin i_\star$ ($\mathrm{km\,s^{-1}}$)	0.58 ± 0.28	DREAM I
Magnitude (J-band)	8.091 ± 0.020	Cutri et al. (2003)
• *Planetary parameters*		
Orbital period, P (Days)	11.8144024 ± 0.0000066	DREAM I
Transit epoch T_0 ($\mathrm{BJD_{TDB}}$)	$2458740.81147 \pm 0.00044$	DREAM I
Eccentricity, e	0.208 ± 0.039	DREAM I
Argument of periastron ω (deg)	21.7 ± 19.1	DREAM I
Stellar reflex velocity, $K_\star$ ($\mathrm{m\,s^{-1}}$)	9.1 ± 0.5	DREAM I
Scaled separation, $a/R_\star$	13.625 ± 0.027	Van Eylen et al. (2018)
Orbital inclination, i (deg)	87.68 ± 0.10	DREAM I
Planet-to-star radius ratio, $R_P/R_\star$	0.03696 ± 0.00041	DREAM I
Planetary mass, M_{pl} (M_{jup})	0.112 ± 0.010	Van Eylen et al. (2018)
Planetary density, ρ_{pl} (g $\mathrm{cm^{-3}}$)	0.609 ± 0.067	Van Eylen et al. (2018)
Projected spin-orbit angle, λ (deg)	$74.2^{+33.6}_{-32.5}$	DREAM 1
Planet radial velocity semi-amplitude, K_{pl}($\mathrm{km\,s^{-1}}$)	$99.2^{+1.4}_{-0.9}$	This paper^2
Equilibrium temperature, T_{eq}(K)	1053 ± 14	Van Eylen et al. (2018)
K2-105		

Table A.2. continued

Parameter	Value	Reference
• *Stellar parameters*		
Spectral type	G5	This paper[5]
Stellar mass, $M_\star$ ($M_\odot$)	1.05 ± 0.02	Castro-González et al. (2022)
Stellar radius, $R_\star$ ($R_\odot$)	0.97 ± 0.01	Castro-González et al. (2022)
Stellar age, τ (Gyr)	>0.6	Narita et al. (2017)
Effective temperature, Teff (K)	5636^{+49}_{-52}	Castro-González et al. (2022)
Metallicity (dex)	$0.23^{+0.04}_{-0.03}$ [Fe/H]	Castro-González et al. (2022)
Surface gravity log $g_\star$ ($\log_{10}(\mathrm{cm\,s^{-2}})$)	4.49 ± 0.01	Castro-González et al. (2022)
Systemic velocity, v_{sys} ($\mathrm{km\,s^{-1}}$)	-32.390637	DREAM I
Limb-darkening coefficients μ_1	0.169	EXOFAST[1]
μ_2	0.299	EXOFAST[1]
Stellar projected velocity, $v\sin i_\star$ ($\mathrm{km\,s^{-1}}$)	$2.13^{+0.96}_{-0.92}$	DREAM I
Magnitude (J-band)	10.541±0.02	Cutri et al. (2003)
• *Planetary parameters*		
Orbital period, P (days)	8.2669897±0.0000057	DREAM I
Transit epoch, T_0 ($\mathrm{BJD_{TDB}}$)	$2458363.2387^{+0.00069}_{-0.000633}$	DREAM I
Eccentricity, e	0 (fixed)	DREAM I
Argument of periastron, ω (deg)	90 (fixed)	DREAM I
Stellar reflex velocity, $K_\star$ ($\mathrm{m\,s^{-1}}$)	9.4 ± 5.8	Narita et al. (2017)
Scaled separation, $a/R_\star$	17.39 ± 0.19	DREAM I
Orbital inclination, i (deg)	88.62 ± 0.10	DREAM I
Planet-to-star radius ratio, $R_P/R_\star$	0.03332 ± 0.00067	DREAM I
Planetary mass, M_{pl} (M_{jup})	0.094 ± 0.060	Narita et al. (2017)
Planetary density, ρ_{pl} (g cm^{-3})	$2.3^{+1.7}_{-1.6}$	This paper
Projected spin-orbit angle, (deg) λ	-81^{+50}_{-47}	DREAM I
Planet radial-velocity semi-amplitude, K_{pl}($\mathrm{km\,s^{-1}}$)	107.0±0.7	This paper[2]
Equilibrium temperature, T_{eq}(K)	814±12	Livingston et al. (2018)
Kepler-25		
• *Stellar Parameters*		
Spectral type	F8	DREAM I
Stellar mass, $M_\star$ ($M_\odot$)	1.26 ± 0.03	Benomar et al. (2014)
Stellar radius, $R_\star$ ($R_\odot$)	1.34±0.01	Benomar et al. (2014)
Stellar age, τ (Gyr)	2.75 ± 0.30	Benomar et al. (2014)
Effective temperature, Teff (K)	6354±27	Benomar et al. (2014)
Metallicity [Fe/H] (dex)	0.11±0.03	Benomar et al. (2014)
Surface gravity log g ($\log_{10}(\mathrm{cm\,s^{-2}})$)	4.285±0.003	Benomar et al. (2014)
Systemic velocity, v_{sys} ($\mathrm{km\,s^{-1}}$)	-8.633258	DREAM I
Limb-darkening coeffcients μ_1	0.106	EXOFAST[1]
μ_2	0.304	EXOFAST[1]
Stellar projected velocity, $v\sin i_\star$ ($\mathrm{km\,s^{-1}}$)	$8.89^{+0.59}_{-0.63}$	DREAM I
• *Planetary parameters*		
Magnitude (J-band)	9.764 ±0.020	Cutri et al. (2003)
⋆ Planet, *b*		
Orbital period, P (days)	6.2385347882	Battley et al. (2021)
Transit epoch, T_0 ($\mathrm{BJD_{TDB}}$)	$2458648.00807^{+0.00057}_{-0.00051}$	DREAM I
Eccentricity, e	$0.0029\ ^{0.0023}_{-0.0017}$	Mills et al. (2019)
$\sqrt{e}\cos\omega$	$0.042\ ^{0.017}_{-0.036}$	Mills et al. (2019)
$\sqrt{e}\sin\omega$	$0.007\ ^{0.038}_{-0.035}$	Mills et al. (2019)
Stellar reflex velocity $K_\star$ ($\mathrm{m\,s^{-1}}$)	2.6±0.7	This paper[3]
Orbital inclination i (deg)	$87.173^{0.084}_{-0.083}$	Mills et al. (2019)
Planet-to-star radius ratio $R_P/R_\star$	$0.019160\ ^{+5.1e-5}_{-4.8e-5}$	Mills et al. (2019)
Planetary M_{pl}	$0.0275\ ^{0.0079}_{-0.0073}$	Mills et al. (2019)
⋆ Planet *c*		
Orbital period P (days)	12.720370495 ± 0.000001703	Battley et al. (2021)
Transit epoch T_0 ($\mathrm{BJD_{TDB}}$)	$2458649.55482\ ^{+0.00057}_{-0.00051}$ $\mathrm{BJD_{TDB}}$	DREAM I
Eccentricity e	$0.0061\ ^{+0.0049}_{-0.0041}$	Mills et al. (2019)
$\sqrt{e}\cos\omega$	$-0.024\ ^{0.067}_{-0.053}$	Mills et al. (2019)
$\sqrt{e}\sin\omega$	$0.004\ ^{0.065}_{-0.062}$	Mills et al. (2019)

Table A.2. continued

Parameter	Value	Reference
Stellar reflex velocity, $K_\star$ ($\mathrm{m\,s^{-1}}$)	$3.6^{+0.3}_{-0.4}$	This paper[3]
Scaled separation, $a/R_\star$	18.336 ± 0.27	Mills et al. (2019)
Orbital inclination, i (deg)	$87.236\ ^{+0.042}_{-0.039}$	Mills et al. (2019)
Planet-to-star radius ratio, $R_P/R_\star$	0.03637 ± 0.00012	Mills et al. (2019)
Planetary mass, M_{pl} (M_{jup})	$0.0479\ ^{+0.0041}_{-0.0051}$	Mills et al. (2019)
Planetary density	$0.588^{+0.053}_{-0.061}$ g cm^{-3}	Mills et al. (2019)
Projected spin-orbit angle, λ	$-0.9^{+7.7}_{-6.4}$	DREAM I
Planet radial-velocity semi-amplitude, K_{pl}($\mathrm{km\,s^{-1}}$)	98.4 ± 0.8	This EXOFAST[2]
Equilibrium temperature, T_{eq}(K)	992 ± 8	This work[4]
$\star$ Planet, *d*		
Orbital period, P (days)	$122.40^{+0.80}_{-0.71}$ d	Mills et al. (2019)
Transit epoch, T_0 (BJD_{TDB})	$2455715.0^{+6.8}_{-7.2}$	DREAM I
Eccentricity, e	$0.13^{+0.13}_{-0.09}$	Mills et al. (2019)
$\sqrt{e}\ \cos\omega$	$0.07\ ^{0.027}_{-0.029}$	Mills et al. (2019)
$\sqrt{e}\ \sin\omega$	$0.16\ ^{0.23}_{-0.28}$	Mills et al. (2019)
Stellar reflex velocity, $K_\star$ ($\mathrm{m\,s^{-1}}$)	8.0 ± 0.2	This paper[3]
Minimum mass, $M_{pl}\ sini$ (M_{jup})	$0.226^{0.032}_{-0.031}$	Mills et al. (2019)
Kepler-68		
• *Stellar parameters*		
Spectral type	G1	Grieves et al. (2018)
Stellar mass, $M_\star$ ($M_\odot$)	1.079 ± 0.051	Gilliland et al. (2013)
Stellar radius, $R_\star$ ($R_\odot$)	1.243 ± 0.019	Gilliland et al. (2013)
Stellar age, τ (Gyr)	6.3 ± 1.7	Gilliland et al. (2013)
Effective temperature, Teff (K)	5793 ± 74	Gilliland et al. (2013)
Metallicity (dex)	0.12 ± 0.074 [Fe/H]	Gilliland et al. (2013)
Surface gravity, log g ($\log_{10}$($\mathrm{cm\,s^{-2}}$))	4.281 ± 0.008	Gilliland et al. (2013)
Systemic velocity, v_{sys} ($\mathrm{km\,s^{-1}}$)	-20.762823	DREAM I
Limb-darkening coefficients μ_1	0.148	EXOFAST[1]
μ_2	0.301	EXOFAST[1]
Stellar projected velocity, $v\sin i_\star$ ($\mathrm{km\,s^{-1}}$)	0.5 ± 0.5	DREAM I
Magnitude (J-band)	8.975 ± 0.046	Cutri et al. (2003)
• *Planetary parameters*		
$\star$ Planet *b*		
Orbital period, P (days)	$5.3987525913 \pm 0.0000005231$	Gajdoš et al. (2019)
Transit epoch, T_0 (BJD_{TDB})	$2455006.85878000 \pm 0.00007639$	Gajdoš et al. (2019)
Eccentricity, e	0.0 (fixed)	Mills et al. (2019)
Argument of periastron, ω (deg)	90 (fixed)	Mills et al. (2019)
Stellar reflex velocity, $K_\star$	$2.70^{+0.48}_{-0.49}$ m s^{-1}	Mills et al. (2019)
Scaled separation, $a/R_\star$	10.68 ± 0.14	Gilliland et al. (2013)
Orbital inclination, i (deg)	87.60 ± 0.90	Gilliland et al. (2013)
Planet-to-star radius, ratio $R_P/R_\star$	0.01700 ± 0.00046	Gilliland et al. (2013)
Planetary mass, M_{pl} (M_{jup})	$0.026\ ^{+0.007}_{-0.008}$	Gilliland et al. (2013)
Planetary density, ρ_{pl} (g cm^{-3})	$3.32\ ^{+0.86}_{-0.98}$	Gilliland et al. (2013)
Projected spin-orbit angle, λ (deg)	non-detection	DREAM I
Planet radial-velocity semi-amplitude, K_{pl}($\mathrm{km\,s^{-1}}$)	124.4 ± 2.0	This paper[2]
Equilibrium temperature, T_{eq}(K)	1280 ± 90	Gilliland et al. (2013)
$\star$ Planet *c*		
Orbital period, P (days)	$9.60502738150 \pm 0.0000132365$ d	Gajdoš et al. (2019)
Transit epoch, T_0 (BJD_{TDB})	$2454969.38207000 \pm 0.00110495$	Gajdoš et al. (2019)
Eccentricity, e	0.0 (fixed)	Mills et al. (2019)
Argument of periastron, ω (deg)	90 (fixed)	Mills et al. (2019)
Stellar reflex velocity, $K_\star$ ($\mathrm{m\,s^{-1}}$)	$0.59\ ^{+0.50}_{-0.52}$	Mills et al. (2019)
$\star$ Planet *d*		
Orbital period, P (days)	$634.6\ ^{+4.1}_{-3.7}$	Mills et al. (2019)
Transit epoch, T_0 (BJD_{TDB})	2455878 ± 11	Mills et al. (2019)
Eccentricity, e	$0.112\ ^{+0.035}_{-0.034}$	Mills et al. (2019)
Argument of periastron, ω (deg)	$-64.74^{+25.78}_{-20.63}$	Mills et al. (2019)
Stellar reflex velocity, $K_\star$ ($\mathrm{m\,s^{-1}}$)	$17.75^{+0.50}_{-0.49}$	Mills et al. (2019)

Table A.2. continued

Parameter	Value	Reference
WASP-47		
• *Stellar parameters*		
Spectral type	G9	Hellier et al. (2012)
Stellar mass, $M_\star$ ($M_\odot$)	1.040 ±0.031	Vanderburg et al. (2017)
Stellar radius, $R_\star$ ($R_\odot$)	1.137 ± 0.013	Vanderburg et al. (2017)
Stellar age, τ (Gyr)	$6.5\ ^{+2.6}_{-1.2}$	Almenara et al. (2016)
Effective temperature, Teff (K)	5552±75	Vanderburg et al. (2017)
Metallicity (dex)	0.38±0.05 [Fe/H]	Vanderburg et al. (2017)
Surface gravity, log g ($\log_{10}(\mathrm{cm\,s^{-2}})$)	4.3437±0.0063	Vanderburg et al. (2017)
Systemic velocity, $v_{\rm sys}$ ($\mathrm{km\,s^{-1}}$)	-25.847809453	Vanderburg et al. (2017)
Limb-darkening coefficients μ_1	0.179	EXOFAST[1]
μ_2	0.299	EXOFAST[1]
Stellar projected velocity, $v\sin i_\star$ ($\mathrm{km\,s^{-1}}$)	$1.80^{+0.24}_{-0.16}$	DREAM I
Magnitude (J-band)	10.613±0.022	Cutri et al. (2003)
• *Planetary parameters*		
⋆ Planet *b*		
Orbital period, P (days)	4.1591492 ±0.000006	Bryant & Bayliss (2022)
Transit epoch, T_0 ($\mathrm{BJD_{TDB}}$)	2457007.932103 ± 0.000019	Bryant & Bayliss (2022)
Eccentricity, e	0 (fixed)	Bryant & Bayliss (2022)
Argument of periastron, ω (deg)	90 (fixed)	Bryant & Bayliss (2022)
Stellar reflex velocity, $K_\star$ ($\mathrm{m\,s^{-1}}$)	140.84 ±0.40	Bryant & Bayliss (2022)
⋆ Planet *c*		
Orbital period, P (days)	588.8 ± 2.0	Bryant & Bayliss (2022)
Transit epoch, T_0 ($\mathrm{BJD_{TDB}}$)	2457763.1 ± 4.3	Bryant & Bayliss (2022)
Eccentricity, e	0.296 ± 0.016	Bryant & Bayliss (2022)
Argument of periastron, ω (deg)	112. ± 4.3	Bryant & Bayliss (2022)
Stellar reflex velocity, $K_\star$ ($\mathrm{m\,s^{-1}}$)	31.04 ± 0.40	Bryant & Bayliss (2022)
⋆ Planet *d*		
Orbital period, P (days)	9.03052118 ±0.00000753	DREAM I
Transit epoch, T_0 ($\mathrm{BJD_{TDB}}$)	2459426.5437 ±0.0028	DREAM I
Eccentricity, e	$0.010^{+0.011}_{-0.007}$	Bryant & Bayliss (2022)
Argument of periastron, ω (deg)	$16.5\ ^{+84.2}_{-98.6}$	Bryant & Bayliss (2022)
Stellar reflex velocity, $K_\star$ ($\mathrm{m\,s^{-1}}$)	4.26 ±0.37	Bryant & Bayliss (2022)
Scaled separation, $a/R_\star$	$16.34\ ^{+0.08}_{-0.11}$	Bryant & Bayliss (2022)
Orbital inclination, i (deg)	$89.55\ ^{+0.30}_{-0.27}$	Bryant & Bayliss (2022)
Planet-to-star radius ratio, $R_P/R_\star$	0.02876 ± 0.00017	Bryant & Bayliss (2022)
Planet mass, $M_{\rm pl}$ ($M_\oplus$)	14.2±1.3	Bryant & Bayliss (2022)
Planetary density, $\rho_{\rm pl}$ (g $\mathrm{cm^{-3}}$)	1.72±0.17	Bryant & Bayliss (2022)
Projected spin-orbit angle, λ (deg)	0±24	DREAM I
Planet radial-velocity semi-amplitude, $K_{\rm pl}$($\mathrm{km\,s^{-1}}$)	103.6±1.0	This paper[2]
Equilibrium temperature, $T_{\rm eq}$(K)	919±13	This paper[4]
⋆ Planet *e*		
Orbital period, P (days)	0.7895933 ± 0.0000044	Bryant & Bayliss (2022)
Transit epoch, T_0 ($\mathrm{BJD_{TDB}}$)	2457011.34862 ± 0.00030	Bryant & Bayliss (2022)
Eccentricity, e	0 (fixed)	Bryant & Bayliss (2022)
Argument of periastron, ω (deg)	90 (fixed)	Bryant & Bayliss (2022)
Stellar reflex velocity, $K_\star$ ($\mathrm{m\,s^{-1}}$)	4.55 ± 0.37	Bryant & Bayliss (2022)

Notes.

1. For a homogeneous analysis we used quadratic limb-darkening coefficients derived using the EXOFAST calculator `https://astroutils.astronomy.osu.edu/exofast/limbdark.shtml` (Eastman et al. 2013) in the J-band.
2. $K_{\rm pl} = \frac{2\pi a}{P}\frac{\sin i}{\sqrt{1-e^2}} = \left(\frac{2\pi G}{P}\right)^{\frac{1}{3}} \frac{(M_\star + M_{\rm pl})^{\frac{1}{3}} \sin i}{\sqrt{1-e^2}}$.
3. $K_\star = \left(\frac{2\pi G}{P}\right)^{\frac{1}{3}} \frac{M_{\rm pl} * \sin i}{M_\star^{2/3}\sqrt{1-e^2}}$.
4. $T_{\rm eq} = T_\star \left(\frac{R_\star}{2\,a}\right)^{1/2} (1 - A)^{1/4}$, where $R_\star$ is the stellar radius, a is the semi-major axis, A is the geometric albedo, we assumed an albedo of 0.2 (Crossfield & Kreidberg 2017).
5. Derived from `http://www.pas.rochester.edu/~emamajek/EEM_dwarf_UBVIJHK_colors_Teff.txt`

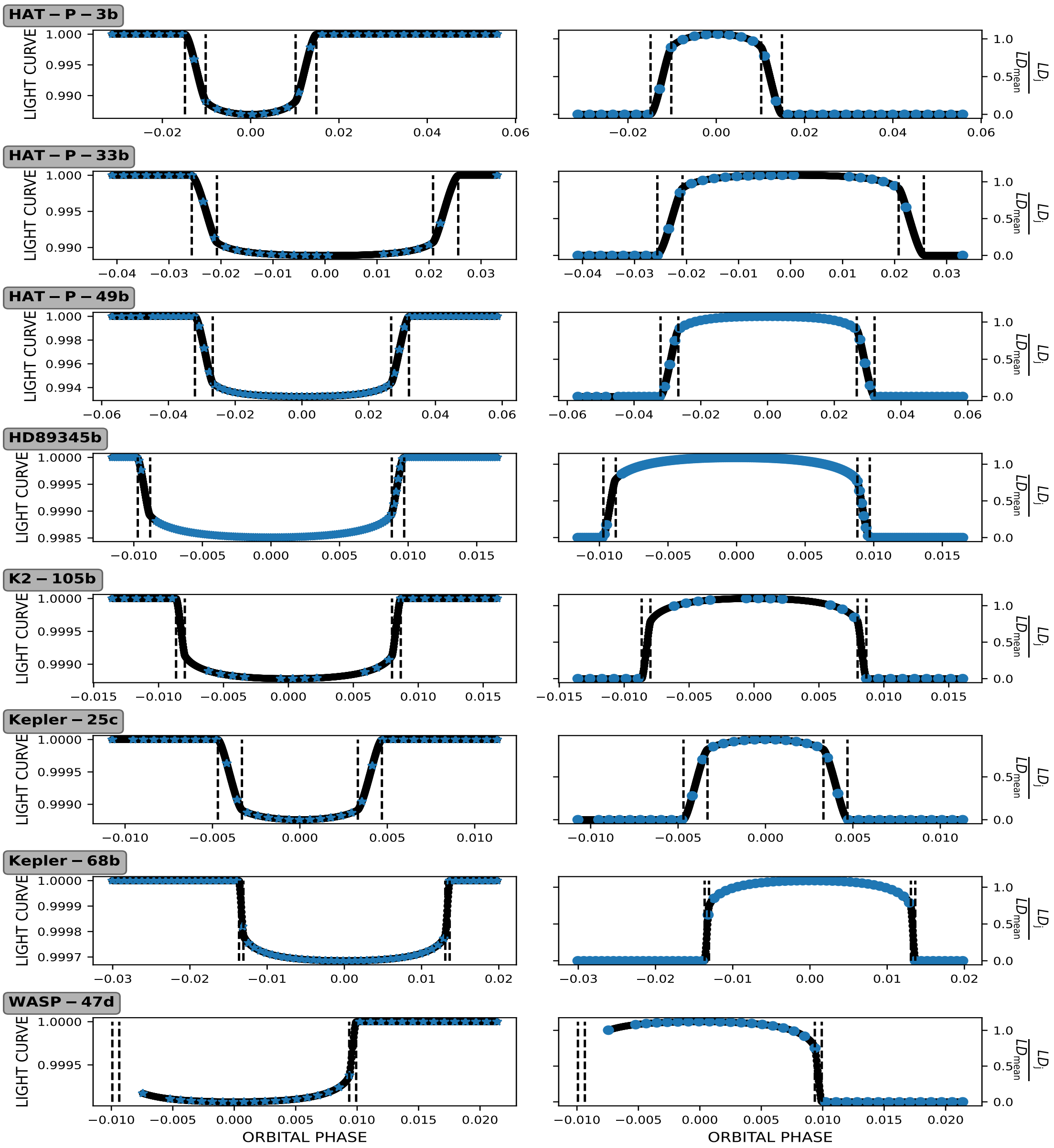

Fig. A.1. Light curves (left panels) and the limb-darkening ratio, namely, $\frac{LD_j}{LD_{mean}}$ with j the orbital phase (right panels) computed with the Python *batman* code (Kreidberg 2015) and the system parameters from Table A.2. The contact points t_1, t_2, t_3, and t_4 are marked with vertical black lines. Blue dots are the light curves and limb-darkening ratio at the observed phases.

Table A.3. Initial parameters adopted for Molecfit.

Parameter	Value	Significance
ftol	10^{-5}	χ^2 convergence criterion
xtol	10^{-5}	Parameter convergence criterion
molecules	H_2O	
ncont	4	Degree of coefficient for continuum fit
a_0	1	Constant term for continuum fit
$\omega_{gaussian}$	2.25	FWHM of Gaussian in pixels
kernel size	3	Size of Gaussian kernel in FWHM
slit width	0.5 arcsec	Slit width
MIPAS profile	equ	Equatorial profile
Atmospheric profile	True	Fixed grid
PWV	-1	Input for water vapor profile

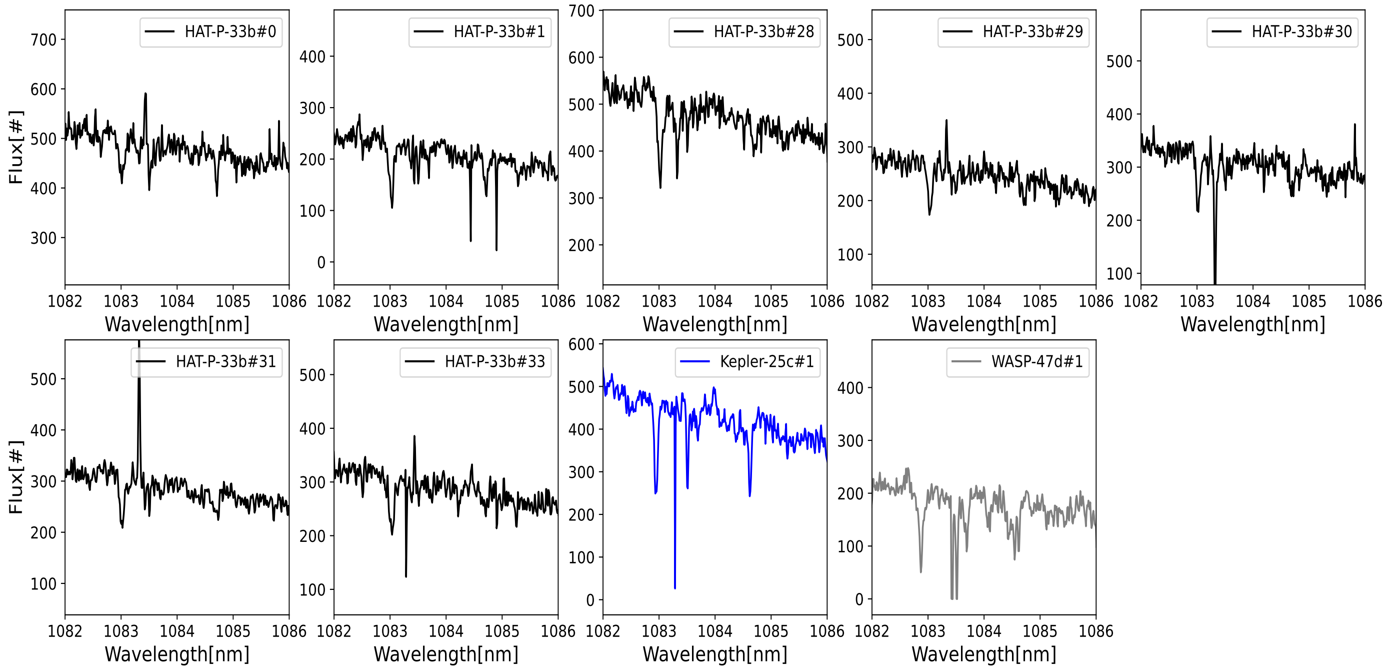

Fig. A.2. Exposures not considered in the analysis for the presence of outliers or low counts. Different colors correspond to different observing nights

.

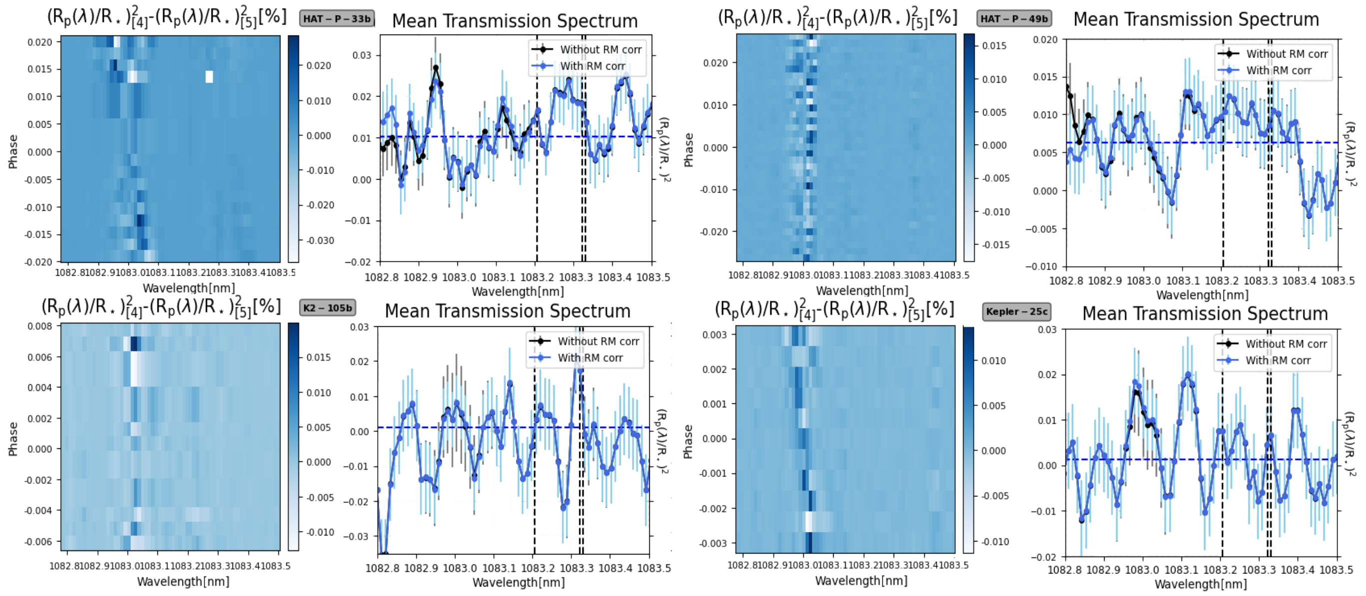

Fig. A.3. Difference between the full in-transit transmission spectra in stellar rest frame when both accounting and not accounting for the RM effects (left panel). Average full in-transit transmission spectrum in the planet rest frame when both accounting (blue line) and not accounting (black line) for the RM effect (right panel). Left panels also show the difference between the transmission spectra calculated with formula 3, with the RM correction, and 4, no RM correction applied, in the stellar rest frame. The RM signal creates a signature that is comparable to the dispersion in a given transmission spectrum and furthermore smoothes out when averaging over the transit because the RM signature shifts along the transit chord radial velocities.

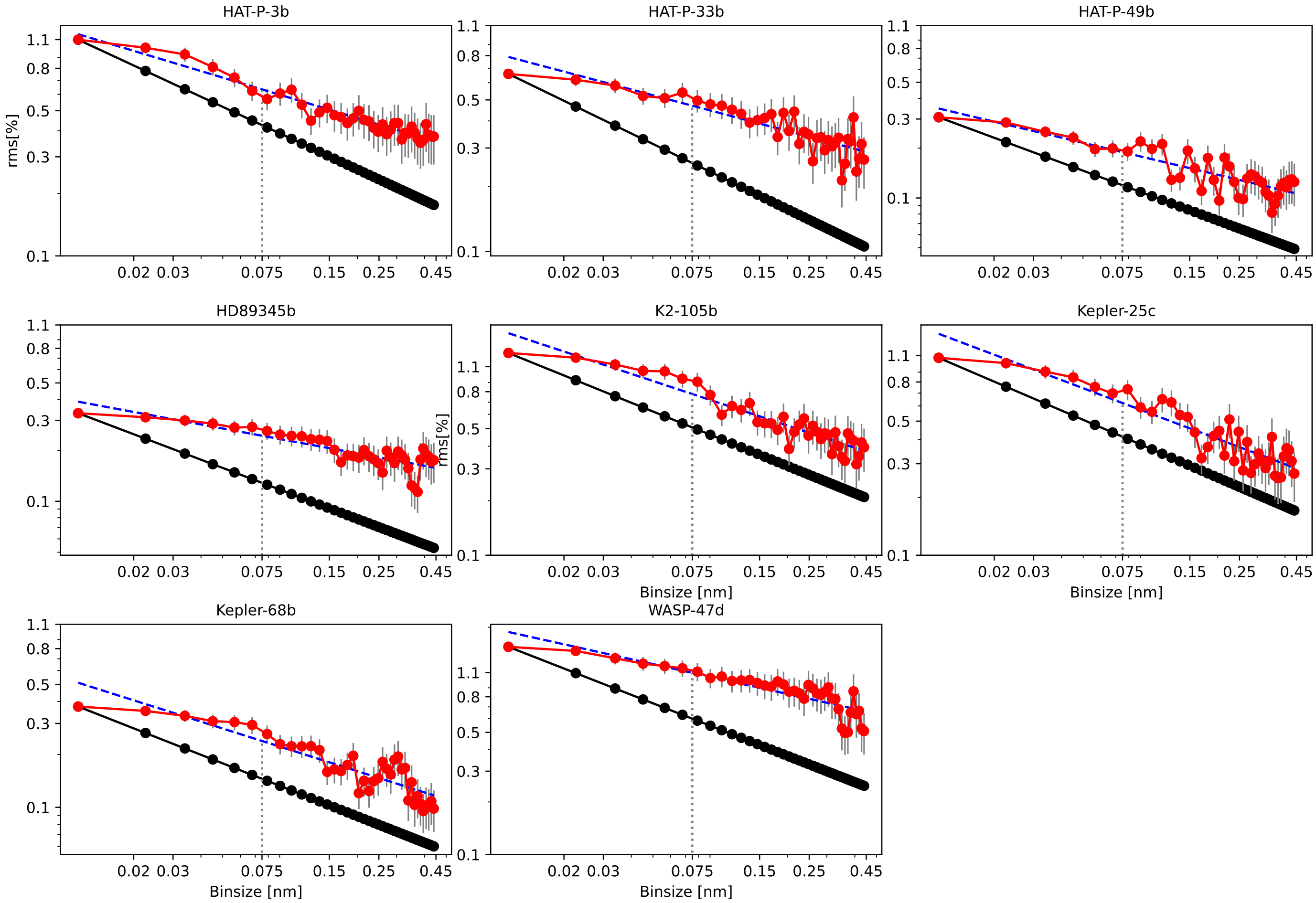

Fig. A.4. Allan plot computed on the average transmission spectra. The back lines are the expected rms for white noise (which scales with the number of points for bin). The red dotted curves are the standard deviation of the transmission spectrum after various binning of different bin size. The dashed blue lines are the best fit for the red curves (computed in log-log scale). The vertical gray lines are the derived 1σ uncertainty at 0.075 nm. The error bars denote this 1σuncertainty of the rms (Cubillos et al. 2017).

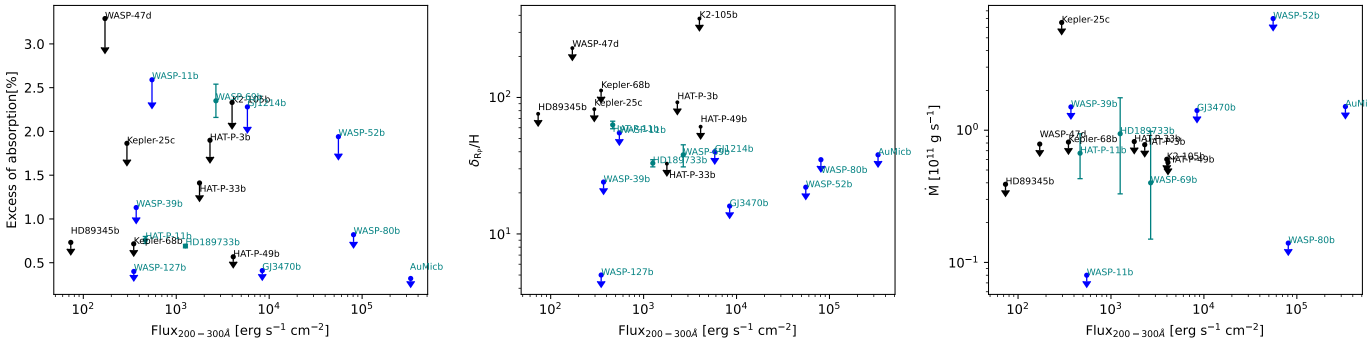

Fig. A.5. Correlation plots with the insolation level of mid-UV flux (200-300 Å). Same plot as in Fig. 8. As for the XUV flux between 5 and 504 Å, the He I absorption signal correlates with the received mid-UV flux; whereas when they are translated in terms of mass-loss rates, these trends seem to disappear.

Appendix B: Gaussian processes to derive upper limits on the helium absorption

To have a better description of the correlated noise present in the data, we performed a Differential Evolution Markov chain Monte Carlo (DEMCMC) fit of a Gaussian profile fixing the position at 1083.326 nm and the FWHM at 0.07 nm and varying the peak value, an offset for the continuum, an uncorrelated jitter, and a correlated noise modeled with a Gaussian process (GP) and a squared exponential kernel. From the posterior distribution, we were therefore able to derive the 3σ upper limits (the value to which 95% of the peak distribution is subject) at the position of the helium triplet marginalized over an uncorrelated jitter and the presence of correlated noise. The values are reported in Table B.1.

Table B.1. Upper limits on the excess of absorption.

Parameter	3σ[%]
HAT-P-3b	1.48
HAT-P-33b	1.17
HAT-P-49b	0.95
HD89345b	0.63
K2-105b	2.57
Kepler-25c	1.29
Kepler-68b	0.64
WASP-47d	3.11

Notes. 3σ upper limits calculated with the Gaussian processes.

D

Proposal CFHT - SPIRou: Coupling stellar activity with atmospheric escape variability in young planetary systems

Below is a copy of the proposal I submitted in March 2022 to the Canada-France-Hawaii Telescope and that is referenced to in Sec. 4.3.

Dethier 22BF013

Coupling stellar activity with atmospheric escape variability in young planetary systems

Semester : 2022B

Science Cat. : Solar system and exoplanets

Abstract

The 23 Myr old star V1298 Tau offers a rare opportunity to study the role of star-planet interactions in young planetary systems. Indeed, V1298 Tau hosts four transiting planets, one of which shows puzzling hints of atmospheric absorption in the helium triplet at 1083nm. A strong helium absorption was detected during the first half of planet b's transit, while the second half shows no evidence for absorption. This raises the tantalising possibility that V1298 Tau b has an escaping atmosphere dramatically shaped by star-planet interactions. We thus propose to observe transits of this planet at high temporal and spectral cadence with SPIRou to confirm this peculiar signature and monitor its short-term behaviour. The unique spectropolarimetric capabilities of SPIRou will further allow us to map the stellar magnetic field and wind structure at the epoch of our transit observations. These measurements will constrain 3D simulations of the atmosphere of V1298 Tau b and its host star. Subsequently, they will improve our knowledge of the role of star-planet interactions in the early evolution of close-in planetary systems.

Telescopes

Telescope	Observing mode	Instruments
CFHT	QSO Regular	SPIRou

Applicants

Name	Affiliation	Email	Country		Potential observer
William Dethier	Institut de planétologie et d'astrophysique de Grenoble	william.dethier@univ-grenoble-alpes.fr	France	Pi	
Dr Vincent Bourrier	University of Geneva (Department of Astronomy)	vincent.bourrier@unige.ch	Switzerland		
jerome bouvier	Institut de Planetologie et d'Astrophysique de Grenoble	jerome.bouvier@univ-grenoble-alpes.fr	France		
Benjamin FINOCIETY	IRAP	benjamin.finociety@irap.omp.eu	France		
Jean-François Donati	IRAP	jean-francois.donati@irap.omp.eu	France		
Gloria Guilluy	INAF - Osservatorio Astrofisico di Torino	gloria.guilluy@inaf.it	Italy		
Casper Farret Jentink	Observatoire de Genève	casper.farret@unige.ch	Switzerland		
Andrés Carmona	IPAG	andres.carmona@univ-grenoble-alpes.fr	France		
Alessandro Sozzetti	INAF - Osservatorio Astrofisico di Torino	alessandro.sozzetti@inaf.it	Italy		
Yassin Jaziri	University of Geneva (Department of Astronomy)	adam.jaziri@unige.ch	Switzerland		

Contact Author

Title		***Institute***	Institut de planétologie et d'astrophysique de Grenoble
Name	William Dethier	***Department***	
Email	william.dethier@univ-grenoble-alpes.fr	***Address***	414 Rue de la Piscine
Phone(first)	0033604758800	***Zipcode***	38400
Phone(second)		***City***	Saint-Martin-d'Hères
Fax		***State***	Isère
		Country	France

Requested Time (exposure + overheads) in hours (in nights for Classical)

25.0

Overall scheduling requirements

UT 2022/09/20 + UT 2023/01/19
Transit observations
5.5h from 9:30 to 15:00 UT on UT 2022/09/20
5.5h from 5:30 to 11:00 UT on UT 2023/01/19
Polarimetric observations: We request that each Stokes V 35-min spectropolarimetric observation is performed when the star is at Zenith ± 2h, for a total of 24 observations (total = 14h) spread out on the bright time periods of about 15 days containing the transits (as explained in the technical justification). We request that the observations are carried out when the star is visible with an airmass lower than ~1.5 and when the angular distance between the Moon and the star is larger than 5

Observing runs

Run	Instrument	Seeing	Config	Details
A	SPIRou	0.60 - 1.00" (SPIRou)	Observing mode: Spectroscopy Read-out mode : Default	comment Transit observations 5.5h from 9:30 to 15:00 UT on UT 2022/09/20 5.5h from 5:30 to 11:00 UT on UT 2023/01/19
B	SPIRou	0.60 - 1.00" (SPIRou)	Observing mode: Polarimetry Read-out mode : Default	Stokes V polarimetry Polarimetric observations: We request that each Stokes V 35-min spectropolarimetric observation is performed when the star is at Zenith ± 2h, for a total of 24 observations (total = 14h) spread out on the bright time periods of about 15 days containing the transits (as explained in the technical justification). We request that the observations are carried out when the star is visible with an airmass lower than ~1.5 and when the angular distance between the Moon and the star is larger than 5

Targets

Field	RA	Dec	Epoch		Runs	Moon	Seeing Lower	Seeing Upper	S/N	Magnitude	Diameter	Comments
V1298Tau	04:05:19.59	+20:09:25.5	J2000		B	any	0.6	1.5	130	8.191		The SNR value is in the H band. The rotation period of the star is ~2.9 days.
V1298Tau	04:05:19.59	+20:09:25.5	J2000		A	any	0.6	1.5	140	8.191		The SNR value is in the H band. The rotation period of the star is ~2.9 days.

Scientific justification:

Overall context.

With a growing number of atmosphere-harboring planets detected transiting their host star(s), the next step is naturally to characterize them more deeply by studying their atmospheric composition and structure. As numerical models are becoming better at simulating the behavior of planetary atmospheres (Oklopčić et al. 2018; dos Santos et al. 2021), high-resolution observations are valuable and precious to test and confirm these predictions. Besides, the temporal evolution of those planetary atmospheres is poorly constrained. It is still not well understood why some planets are able to keep their atmosphere over Myr to Gyr time scales, while others appear to have lost them rapidly.

A number of phenomena can influence this evolution, such as the stellar magnetic field, winds and radiation (Vidotto et al. 2020), although, their relative role in this matter still remains uncertain. **Studying atmospheres in young planetary systems is crucial to better constrain their behavior early in their life. It allows to study their initial conditions right after their formation and to evaluate the impact of star-planet interactions on their evolution.**

Glimpse onto a planet freshly out of the circumstellar disc:

As of today, 7 planets have been confirmed transiting around stars younger than 25 Myr old (David et al. 2016 – 2019; Plavchan et al. 2020). One of them is the planet V1298 Tau b which makes a suitable candidate for atmospheric studies. With a mass of 0.64 M_{Jup}, a radius of 0.868 R_{Jup} and an orbital period of 24.1396 days (David et al. 2019; Suárez Mascareño et al. 2021), it is part of a four planets system orbiting a 23 Myr, 1.101 M_{Sun}, 1.345 R_{Sun} K-type star (David et al. 2019). Until now, only a few attempts at detecting transit atmospheric absorption have been made on the planetary system of V1298 Tau: Feinstein et al. 2021 probed the Hα and CaII IRT lines of V1298 Tau c and found variations that are most probably due to stellar activity or star-planet interactions; Schlawin et al. 2021 also made observations of V1298 Tau c to search for Hα absorption signatures, but resulted in a non-detection; Vissapragada et al. 2021 observed planets d and b and obtained a tentative detection of HeI IR triplet absorption for V1298 Tau d. For planet b they had observations only during the second half of the transit and did not find evidence of excess HeI absorption. However, Gaidos et al. 2022 see an in-transit (planet b) decrease of the Equivalent Width of the HeI triplet that, surprisingly, starts before the white light transit and ends around the mid transit time. They have a hard time explaining this signal, solely, in terms of stellar origin. This suggests the atmosphere absorbs upstream of the planet, which is compatible with Vissapragada et al. 2021 observations. This peculiar feature hints at an interesting structure of the escaping atmosphere that could be the consequence of strong star-planet interactions. Whence, more **transit observations of V1298 Tau b are needed to assess the presence of this escaping helium atmosphere.**

As the XUV radiation field is on average 100 times greater for pre-main sequence stars than in main sequence stars (Johnstone et al 2015), it is expected to have a major impact on V1298 Tau b's atmosphere. Indeed, the upper atmosphere, the thermosphere, is driven to expand hydrodynamically due mainly to the absorption, and its subsequent heating, of this XUV radiation. This expanding upper atmosphere is likely to cover a broad area around the planetary opaque disc, yielding a higher probability to observe its transit. A suitable target element for transit observations is the neutral helium atom. As helium is the second lightest element, it is easily found at high altitudes in atmospheres and therefore should be part of the expanding thermosphere. Furthermore, conditions to excite atmospheric helium to its metastable state, corresponding to the triplet at 1083nm, are more favorable around young K-type stars (Oklopčić 2019). **SPIRou being a high-resolution spectropolarimeter operating in the near-infrared (0.95-2.50 µm) is therefore one of the most adapted instruments for such transit detections of an atmosphere**. This, instrument is in particular useful to (1) study the variations of the HeI triplet (1083 nm) lines, which in turn allows to characterize an expanding atmosphere as was demonstrated e.g. in Allart et al. 2019 with CARMENES, another high-resolution spectrograph and (2) characterize the stellar activity thanks to the use of Zeeman-Doppler Imaging (ZDI) (Semel et al. 1989; Brown et al. 199;, Donati & Brown 1997; Donati et al. 2006) as it has already been done for other young stars (Klein et al. 2021; Finociety et al. 2021, Figure 1 lower central panel). **Our goal is to use SPIRou to gather contemporaneous observations of V1298 Tau and of transits of V1298 Tau b. We will benefit from its spectropolarimetric capabilities to search for a connection between stellar activity and planetary atmospheric absorption in the HeI triplet.** At last, we will be able to interpret and put further constraints on the unusual feature detected by Gaidos et al. 2022.

The deepest atmospheric helium signature to be measured?

To provide estimates on the detectability of the variability of HeI absorption during a transit of V1298 Tau b, we based our simulations on a comparison with the planetary system WASP-107. WASP-107 is a 0.67 R_{Sun}, 0.683 M_{Sun}, 3.4 Gyr old K-type star (Piaulet et al 2021) hosting 2 planets. A detection with an almost 8 % excess absorption in the HeI IR triplet has been made by Allart et al. 2019 on WASP-107 b, which is a 0.924 R_{Jup}, 0.119 M_{Jup} planet with a period of 5.72149242 days (Močnik et al. 2017).

Using the system parameters previously mentioned for V1298 Tau from David et al. 2019 and for WASP-107 from Močnik et al. 2017, we found that for a same given stellar flux, V1298 Tau b receives ~ 2.25 times less irradiation than WASP-107 b due to its larger semi-major axis. However, with its younger age, V1298 Tau is expected to have on average an XUV flux ~100 times larger than that of main sequence stars (Johnstone et al 2015). Thus, V1298 Tau b would receive ~44.5 times the amount of XUV flux that WASP-107 b receives. We used the energy limited equation (Erkaev et al. 2007) along with Salz et al. 2016's correction laws to derive the mass loss rate of the two planets. We found that the total mass loss rate of V1298 Tau b would be ~1.32 times larger than that of WASP-107 b. **We thus expect the evaporation rate on V1298 Tau b to be at least of the same order as on WASP-107 b and to deliver a similar excess atmospheric absorption signature in the HeI triplet assuming a similar helium composition**.

Furthermore, using V1298 Tau's XUV flux value from Poppenhaeger et al. 2021 along with the energy limited formula, we derived the atmospheric mass loss rate of V1298 Tau b. We used this mass loss rate to constrain the properties of the thermospheric isothermal Parker wind (Oklopčić et al. 2018) in V1298 Tau b's atmosphere and derive its density and velocity profiles. With these atmospheric properties, we simulated a series of exposures of the transit of V1298 Tau b which we then used to compute the HeI triplet excess absorption during the transit. The resulting excess atmospheric absorption peaks at around ~ 9 to 10% in the HeI triplet during the transit, confirming the plausibility of the prediction made earlier. Computing the mean of the absorption over half the transit allows for a detection of the signal with a confidence level of ~ 30 sigma in the HeI triplet lines if we use a SNR of 88 (values of HeI triplet peaks for the half transit mean: 10.53 ±0.34 and 7.66 ±0.281, see Figure 1 upper central panel, black curve). **With our 3D forward modelling of the high-altitudes atmospheres on exoplanets, we are able to interpret these detected absorption signature's shape and magnitude in order to derive atmospheric properties such as density, velocity and temperature profiles (Figure 1 top left panel).** We will also confront the predicted mass loss rate to the observed one. This is important to evaluate whether a similar planet would retain its initial atmosphere on Gyr timescales. If not, this would suggest for another scenario, e.g., outgassing of water (Garcia et al. 2021) to explain the presence of atmospheres after the pre-main sequence phase.

To exploit this signal more deeply, we tested the detection of its temporal variability over one transit by reproducing an analogous event as was detected by Gaidos et al. 2022. We made the same simulation as before, but for which the excess atmospheric absorption during the second half of the transit was decreased by 1% with respect to the initial 9 to 10%. We then computed the mean of the excess absorption exposures separately over the two halves of the transit. The two means are shown in Figure 1 top central panel. Next, for each of the two curves, we computed the mean of the excess absorption, taken inside the wavelength interval covering the HeI triplet (the interval is represented by the black vertical lines in Figure 1 upper central panel). **We derived a value of 6.004 ± 0.065 % and of 5.404 ± 0.059 % for the mean absorption on the first half and second half of the transit respectively. Taking the difference between these two values shows we can detect a variation of 0.600 ± 0.088 %, that is ~ 6.818 times the uncertainty**. These simulations were performed given a timestep of 576s along with a SNR of 88 for each exposure, giving 14 exposures for each transit half. These values were derived with the SPIRou Exposure Time Calculator (exposure time 576s -35s of overhead = 541s which in turn gives a SNR of 140 in the H band and so a SNR of 88 for the 8th order of SPIRou).

This shows that SPIRou is largely capable of detecting the fading of an excess absorption signature during a transit.

Great opportunity to search for temporal variability

With such an intense absorption signature, our strategy is to observe two partial transits of V1298 Tau b at two different epochs. **This will allow us to study the direct effects of the stellar activity on the HeI atmospheric absorption at the time of a transit, but also to study how a change in stellar activity can impact this absorption signature (V1298 Tau's activity shows variations on a few months timescale; preliminary results).** That is possible thanks to the spectropolarimetry capabilities of SPIRou and ZDI techniques that allow to study the stellar surface magnetic field. In turn, with the knowledge of the stellar surface magnetic field, we can reconstruct the stellar winds (Figure 1 upper right panel) as well as the structure and properties of the stellar corona gas. Ultimately, with the knowledge of these derived information, we can reconstruct the Xray stellar emission which is a driver of escaping atmosphere (Jardine et al. 2010; Kavanagh et al. 2019). Spectropolarimetric observations also allow us to apply ZDI in order to reconstruct the distribution of the brightness features such as spots and plages, (Finociety et al. 2021) which can as well influence the detection and interpretation of atmospheric absorption variability (Feinstein et al. 2021).

In order to know the contemporaneous stellar activity to our transits and apply ZDI, we need Stokes I and V polarimetric observations (Semel 1989; Donati et al. 1997) on several nights before and after each transit to sample the rotation period of the star of ~2.9 days (David et al. 2019). Unfortunately, we cannot make use of the previous SPIRou observations of this star for this study. Indeed, we are not able to extrapolate the stellar activity on the long term as it is not yet well constrained (21BF021 happens one year before the requested observations of this proposal). The requested polarimetric observations will nevertheless also prove useful outside of the frame of this proposal. They will add to the observations collected during previous intensive monitoring of V1298 Tau with SPIRou. In the framework of the SLS it has been monitored between September 2020 and January 2021 and very recently in the framework of (21BF021) B. Finociety's PI proposal. **As such, it gives an opportunity to study the stellar activity and large-scale magnetic field (does a magnetic cycle exist?) on a longer term.** Finally, if the signal indeed proves to be that strong and should there be one unexploitable transit, **we will still be able to search for its short-term variability, though with less confidence, during a single half transit and derive the atmospheric properties of V1298 Tau b**. If no atmospheric helium is detected during the first half of the transit, it will further support the study of Vissapragada et al. 2021 and polarimetric observations will still be useful for stellar activity studies.

In conclusion, SPIRou observations of a planet so young will ultimately allow: (1) for insights on the atmospheric properties of planets under physical conditions close to the ones at the time of their birth; (2) to constrain the level of implication of specific stellar phenomena typical of pre-main sequence stars in a planet's atmospheric evolution; (3) to understand how the stellar activity interfere with atmospheric absorption detections.

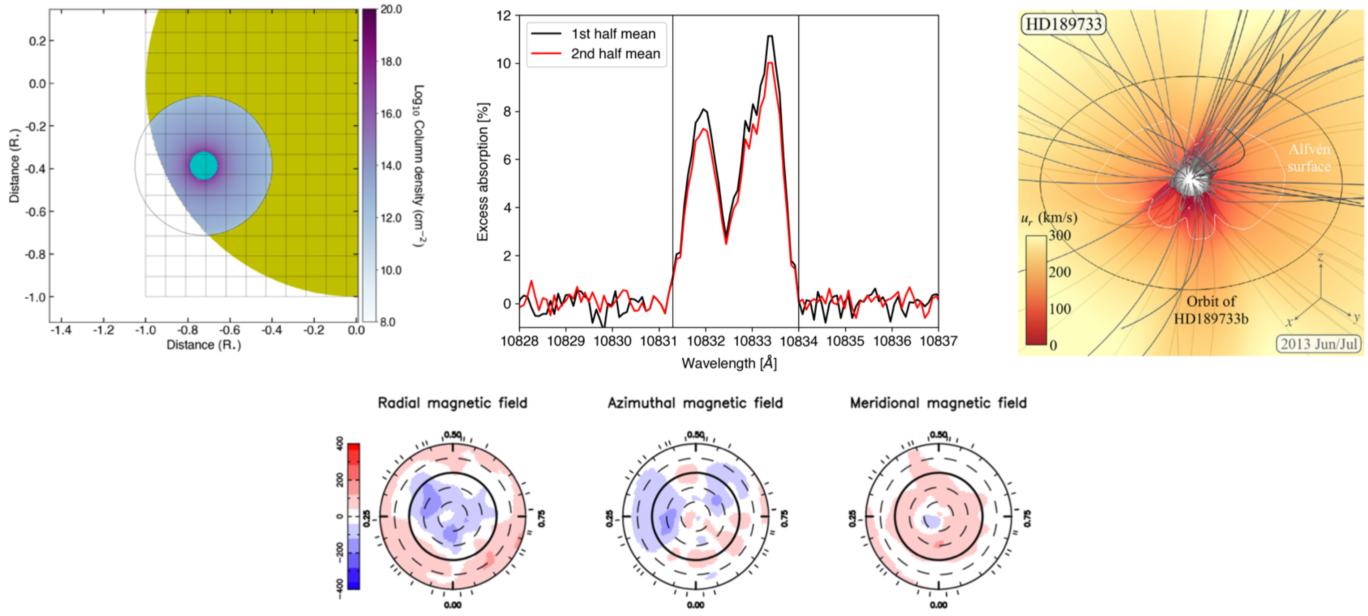

Figure 1: Upper left, simulated analytical column density for HeI IR triplet in V1298 Tau b' atmosphere. The cyan disc represents the planetary opaque disc. The color bar indicates the column density of HeI, the background yellow shape is the star's projected surface**. Upper central,** simulated mean of the helium excess absorption as a function of the wavelength over the first half of the transit (in black), over the second half (in red) for V1298 Tau b with a SNR of 88 and SPIRou's spectral resolution. The means peak at ~10% to 8% and ~9% to 7% for the black and red curves respectively. **Upper right,** stellar wind radial velocity profiles of HD189733 - reconstructed from surface magnetic field maps (R D Kavanagh et al. 2019) - in the orbital plane of HD189733 b, with overplotted stellar magnetic field lines (in grey), and the Alfvén surfaces (in white). **Lower central,** ZDI maps of the radial, azimuthal and meridional magnetic field components for V1298 Tau obtained from a simultaneous fit of Stokes *I* and Stokes *V* LSD profiles. For the magnetic field maps, red indicates positive radial, azimuthal and meridional fields that point outwards, counterclockwise and polewards, respectively. The star is shown in a flattened polar projection. The maps were made using SPIRou sectropolarimetric data from SLS 09/2020 – 12/2020 (preliminary work).

Technical justification

Observation strategy:

For this proposal we ask for observations that partly cover two transits of V1298 Tau b plus ~1 h before or after each transit using spectral mode.Based on ephemeris derived by Feinstein et al. 2022 from the latest observations of the system V1298 Tau by TESS between UT 2021 September 16 and UT 2021 October 12 and between UT 2021 October 12 and UT 2021 November 6 (TTV unknown for planet b), we computed the dates at which V1298 Tau b will transit during the 2022 second semester (see Figure 2). This leads us to request time on the nights of the UT 2022 September 20 and UT 2023 January 19. These two partial transits - one covering the three first quarters and the other covering the second half -, will allow us to search for the temporal variabilities of the atmospheric absorption signature described in the scientific justification, as they are happening on a 4 months interval. For the first night we request at least one hour of observation before the transit starts, at an airmass from 2.8 to 2. This is not ideal, but it is sufficient to construct the master out-of-transit flux which is a mean of the exposures taken during that period (therefore increasing the SNR). For the second transit, we request two and a half additional hours after the termination of the transit, up to airmass of 2.

In addition, we ask for 24 observations in Stokes V polarimetric mode to achieve a sampling of the rotation period of the star of ~2.9 days. To limit the variation of the stellar activity between the transit and the polarimetric observations, we need contemporaneous observations. We ask for 12 polarimetric sequences during the SPIRou run containing the first transit. These 12 sequences would need to be subdivided into 4 sets of 3 consecutive nights. One set needs to be made at the start of the run and another set at the end of the run. The 2 other sets can be placed at other times during the run. The same logic applies for the second transit.

We also estimated the dates at which V1298 Tau b will transit during the 2023 first and second semester and found no exploitable transits either because of moon contamination, lack of baseline before/after transit, too high airmasses values or major portions of the transits falling outside nighttime. The two proposed nights are not optimal, but remain almost unique options to observe V1298 Tau b in the coming year and a half.

Requested signal-to-noise ratio:

Using our estimates for the mass loss rate of V1298 Tau b, our simulations show that with a SNR of ~88, we are able to detect a 1% variation in the atmospheric absorption signature of helium of V1298 Tau b throughout the transit. A SNR of 88 in the 8th order of SPIRou's spectrograph (1,074.57-1,089.81 nm) corresponds to a SNR of 140 in the H band. We therefore ask for a SNR of 140 for the spectral mode exposures for the transits observations.

Concerning the polarimetric observations, we ask for the same SNR that was asked for polarimetric observations of the proposal 21BF021, that is SNR = 130 for each subexposure. This amounts to a SNR of ~ 270 in the H band for each polarimetric sequence.

Requested time:

We used the SPIRou Exposure Time Calculator to evaluate the needed exposure time to reach a SNR of 140 in the H band for each transit measurement in spectral mode. Using V1298 Tau's parameters: a magnitude in the band H of 8.191 and a Teff 4970 K, combined with a seeing of 0.8" and airmass of 1.5, we derived an exposure time of 541 s. Adding the overhead time gives a total time of 569 s for each exposure. **As we ask for a total of 11h of observations for the transits** this will amount to ~ 69 exposures distributed on (1) UT 2022 September 20 for 5.5 h from 9:30 to 15:00 UT and on (2) UT 2023 January 19 for 5.5 h from 5:30 to 11:00 UT.

For each Stokes V polarimetric sequence we ask for the same exposure time as for the observations collected in 2020 in the framework of SLS and in the proposal 21BF021, which is 2,100s of exposure time (~35 min with overhead time of 35s) that includes four polarimetric subexposures with an exposure time of 490s each. This allows to reach a SNR of 133 in the H band for each subexposure and of ~270 in the H band for each polarimetric sequence according to SPIRou Exposure Time Calculator. **The total time requested for the polarimetric sequences is 14 h.**

In total, we request 25 h of SPIRou observations.

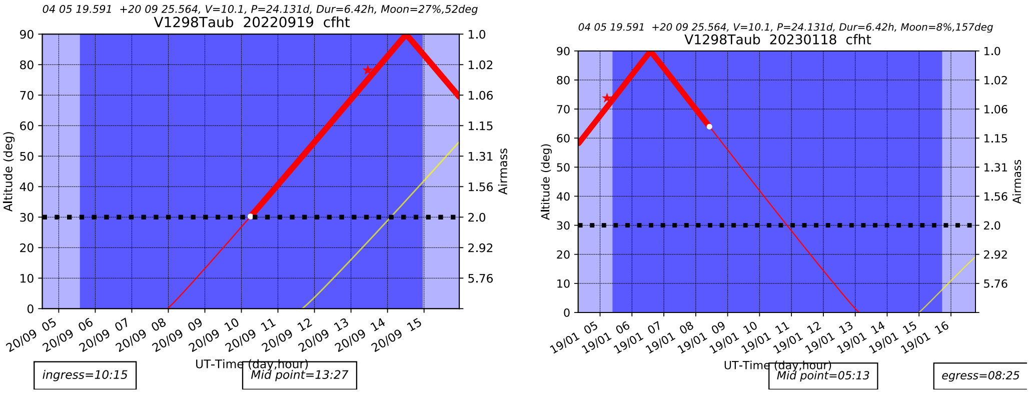

Figure 2: Predicted ephemeris of V1298 Tau b's transits during semester 2022B that we will exploit. The propagated uncertainty on the transit mid-point (T0) is ~1.25 h for first night and 1.5 h for the second.

References:

[1] : Karin I. Öberg et al 2011 ApJL 743 L1

[2] : Trevor J. David et al. 2019 ApJL 885 L12

[3] : Adina D. Feinstein et al 2021 AJ 162 213

[4] : Shreyas Vissapragada et al 2021 AJ 162 222

[5] : Everett Schlawin et al 2021 Res. Notes AAS 5 195

[6] : Adina D. Feinstein et al 2022 ApJL 925 L2

[7] : Suárez Mascareño, A et al. Rapid contraction of giant planets orbiting the 20-million-year-old star V1298 Tau. Nat Astron (2021)

[8] : Birkby, J., de Kok, R., Brogi, M., et al. 2013, The Messenger, 154, 57

[9] : Garcia, R., Barnes, R., Driscoll, P., & Meadows, V. (2021). Delayed Water Outgassing May Enable Planetary Habitability After an M Dwarf's Pre-Main Sequence Phase. Bulletin of the AAS, 53(1)

[10] : Donati J. F., et al., 2006, MNRAS, 370, 629

[11] : T. Močnik, C. Hellier, D. R. Anderson, B. J. M. Clark, J. Southworth, Starspots on WASP-107 and pulsations of WASP-118, *Monthly Notices of the Royal Astronomical Society*, Volume 469, Issue 2, August 2017, Pages 1622–1629

[12] : C. P. Johnstone et al 2015 ApJL 815 L12

[13] : High-resolution confirmation of an extended helium atmosphere around WASP-107b
R. Allart et al., A&A, 623 (2019) A58

[14] Energy-limited escape revised - The transition from strong planetary winds to stable thermospheres. M. Salz, et al. A&A, 585 (2016) L2.

[15] K Poppenhaeger et al. X-ray irradiation and evaporation of the four young planets around V1298 Tau, Monthly Notices of the Royal Astronomical Society, Volume 500, Issue 4, February 2021, Pages 4560–4572,

[16] David, T. *et al.* A Neptune-sized transiting planet closely orbiting a 5–10-million-year-old star. *Nature* **534,** 658–661 (2016).

[17] Plavchan, P *et al.* A planet within the debris disk around the pre-main-sequence star AU Microscopii. *Nature* **582,** 497–500 (2020).

[18] C Piaulet et al 2021 AJ 161 70

[19] Jardine, M., Donati, J., Arzoumanian, D., & De Vidotto, A. (2010). Modelling stellar coronal magnetic fields. Proceedings of the International Astronomical Union, 6(S273), 242-248.

[20] R D Kavanagh et al., MOVES – II. Tuning in to the radio environment of HD189733b, Monthly Notices of the Royal Astronomical Society, Volume 485, Issue 4, June 2019, Pages 4529–4538,

[21] Antonija Oklopčić and Christopher M. Hirata 2018 ApJL 855 L11

[22] p-winds: An open-source Python code to model planetary outflows and upper atmospheres. L. A. dos Santos, A. A. Vidotto, S. Vissapragada, M. K. Alam, R. Allart, V. Bourrier, J. Kirk, J. V. Seidel, D. Ehrenreich A&A, Forthcoming article

[23] A A Vidotto, A Cleary, Stellar wind effects on the atmospheres of close-in giants: a possible reduction in escape instead of increased erosion, Monthly Notices of the Royal Astronomical Society, Volume 494, Issue 2, May 2020, Pages 2417–2428

[24] Roche lobe effects on the atmospheric loss from "Hot Jupiters N. V. Erkaev, Yu. N. Kulikov, H. Lammer, F. Selsis, D. Langmayr, G. F. Jaritz and H. K. Biernat A&A, 472 1 (2007) 329-334

[25] Investigating the young AU Mic system with SPIRou: large-scale stellar magnetic field and close-in planet mass. Baptiste Klein et al. Monthly Notices of the Royal Astronomical Society, Volume 502, Issue 1, March 2021, Pages 188–205

[26] B Finociety et al. The T Tauri star V410 Tau in the eyes of SPIRou and TESS, Monthly Notices of the Royal Astronomical Society, Volume 508, Issue 3, December 2021, Pages 3427–3445

[27] Semel M., 1989, A&A, 225, 456

[28] Brown S. F., Donati J. F., Rees D. E., Semel M., 1991, A&A, 250, 463

[29] Donati J. F., Brown S. F., 1997, A&A, 326, 113

[30]: Antonija Oklopčić 2019 ApJ 881 133

[31] E Gaidos, T Hirano, C Beichman, J Livingston, H Harakawa, K W Hodapp, M Ishizuka, S Jacobson, M Konishi, T Kotani, T Kudo, T Kurokawa, M Kuzuhara, J Nishikawa, M Omiya, T Serizawa, M Tamura, A Ueda, S Vievard, Zodiacal exoplanets in time – XIII. Planet orbits and atmospheres in the V1298 Tau system, a keystone in studies of early planetary evolution, Monthly Notices of the Royal Astronomical Society, Volume 509, Issue 2, January 2022, Pages 2969–2978

Students involved

Student	Level	Applicant	Supervisor	Applicant	Expected completion date	Data required
William Dethier	Doctor	Yes	jerome bouvier	Yes	2023/12	Yes
Benjamin FINOCIETY	Doctor	Yes	Jean-François Donati	Yes	2022/09	No

Linked proposal submitted to this TAC: No

Linked proposal submitted to other TACs: No

Any other expenditure

Relevant previous Allocations: Yes

V1298 Tau was previously observed as part of the SPIRou Legacy Survey (SLS) and as part of B. Finociety's PI proposal 21BF021. The present PI proposal is aimed at a detailed characterisation of the atmosphere of planetary system of V1298Tau.

No additional remarks

Observing run info :

Run: A backup strategy: Computed
snr:140,etime:541,teff:4970,magh:8.191,seeing:0.8,h2o:1.6,airmass:1.5
Run: B backup strategy: Computed
snr:130,etime:474,teff:4970,magh:8.191,seeing:0.8,h2o:1.6,airmass:1.5

E

Introduction, résumé des chapitres et conclusion de la thèse en français

E.1 Introduction

La découverte de planètes en dehors de notre propre système solaire a ouvert un tout nouveau champ de recherche et a transformé notre compréhension de l'univers et de la place que l'homme y occupe. Une fois de plus, notre anthropocentrisme a été mis à mal, laissant entrevoir la possibilité que l'humanité ne soit pas unique et seule. Avec le nombre sans cesse croissant d'exoplanètes confirmées, plus de 5000[1] au moment de la rédaction de ce manuscrit, les chercheurs, poussés par la nature humaine de constamment chercher à comprendre ce qui nous entoure, ont dévoilé une vaste richesse de systèmes exoplanétaires divers. Certains de ces systèmes abritent de multiples planètes, des planètes géantes gazeuses de la taille de Jupiter et de Neptune, des planètes rocheuses de la taille de la Terre et de Mars et des planètes en orbite autour de plusieurs étoiles. Certaines de ces exoplanètes ont même été trouvées en orbite dans la zone tempérée de leur étoile hôte où elles pourraient, en théorie, abriter de l'eau liquide, essentielle à l'émergence de la vie telle que nous la connaissons sur Terre. Tous les nouveaux domaines d'étude qui ont émergé de ces découvertes permettent aux astronomes d'aujourd'hui de mieux comprendre notre propre monde, non pas comme une pièce unique, mais comme une partie d'un tout.

De manière légitime, aux yeux du grand public, l'étude des exoplanètes peut, à première vue, sembler inutile et sans intérêt pour la société. Cependant, de nombreuses raisons motivent les astronomes à se pencher sur ce sujet. Comme mentionné plus haut, les systèmes exoplanétaires découverts sont variés et, la plupart du temps, très différents de notre système solaire. Cette découverte soulève des questions sur l'évolution et le processus de formation des planètes en général, et l'étude des exoplanètes pourrait aider à comprendre comment la Terre et ses compagnons se sont formés et pourquoi ils se retrouvent dans une telle configuration. Par ailleurs, l'étude des exoplanètes autour d'étoiles similaires au Soleil passé, actuel et futur

---

[1] De exoplanet.eu, visité en août 2023.

pourrait nous aider à comprendre comment les planètes réagissent sous des conditions stellaires différentes, ce qui, en fin de compte, pourrait nous donner des indications sur le passé et l'avenir de la Terre.
En outre, l'observation des exoplanètes peut conduire les astronomes à identifier les caractéristiques de leurs atmosphères, telles que leur structure, les plages de températures et de pressions qu'elles peuvent avoir, les différentes compositions moléculaires et atomiques qu'elles sont capables de maintenir et même leur dynamique interne. La comparaison des résultats obtenus sur de nombreuses exoplanètes pourrait fournir des indices sur ce qui rend les conditions atmosphériques sur Terre si particulières qu'elles permettent d'accueillir la vie. Enfin, l'idée d'une vie ailleurs dans l'univers a inspire la science-fiction depuis de nombreuses décennies et a profondément alimenté la créativité des gens. Il se trouve en fait qu'une partie importante de la communauté vise à étudier l'habitabilité des planètes extrasolaires et même à détecter d'éventuels indicateurs d'une forme de vie dans leurs atmosphères. Ces études particulières ont définitivement rendu ces idées plus tangibles, ce qui pourrait éventuellement raviver l'intérêt et la confiance du grand public dans ces branches de la science.

Comme nous l'avons vu plus haut, les atmosphères sont indéniablement des portes ouvertes sur de nombreuses propriétés planétaires essentielles, et les astronomes n'ont pas attendu longtemps avant de se lancer dans leur chasse. Les premiers signes de la présence d'une atmosphère autour d'une exoplanète ont été détectés sur HD 209458 b, une demi-décennie après la découverte et la confirmation de la première exoplanète, 51 Pegasi b, en orbite autour d'une étoile de la séquence principale (Mayor & Queloz 1995; Charbonneau et al. 2002). Parmi les nombreux moyens que les astronomes ont trouvés pour étudier des objets si petits, si peu lumineux et si éloignés (voir, par exemple, Perryman 2018), la technique du transit s'est clairement révélée être une des plus rentables. Les figures E.1 et E.2 montrent la distribution des planètes détectées jusqu'à présent dans un diagramme de rayon et de masse en fonction de leurs périodes orbitales, respectivement. En outre, la spectroscopie de transit, qui étudie le changement du spectre d'une étoile en fonction de la longueur d'onde pendant le transit d'une planète - que ce soit à basse ou à haute résolution spectrale - est une technique puissante qui permet aux chercheurs d'étudier en profondeur les caractéristiques atmosphériques des exoplanètes. La comparaison des résultats de ces observations avec les prédictions et modèles théoriques a conduit à la détection de nombreuses espèces atomiques et moléculaires (voir tableau 1 de Guillot et al. 2022). De plus, l'analyse des signatures d'absorption que ces espèces induisent dans les données observationnelles lors du passage de l'atmosphère exoplanétaire permet de déduire les propriétés dynamiques ainsi que la composition et la structure thermique de ces atmosphères (Wyttenbach et al. 2017; Seidel et al. 2020; Yan et al. 2020).

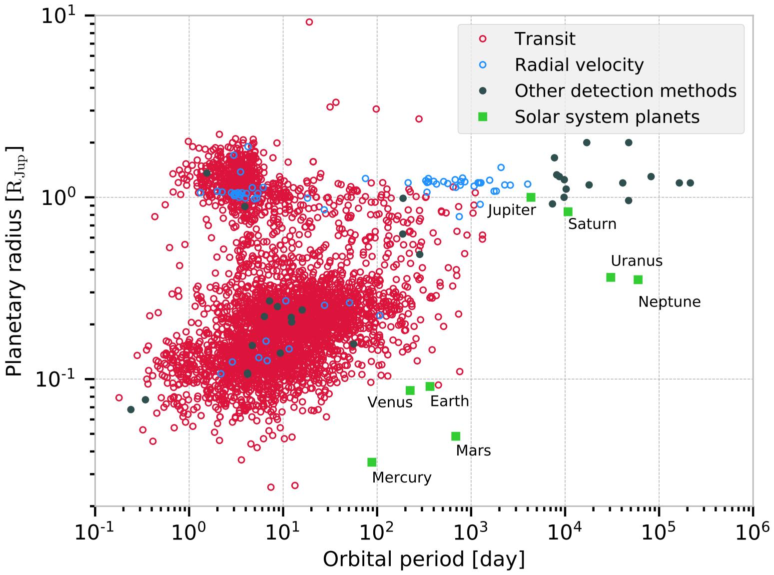

Fig. E.1.: Répartition du rayon planétaire en fonction de la période orbitale des exoplanètes confirmées. Les couleurs indiquent différentes techniques de détection. Les données proviennent du site web exoplanet.eu en utilisant le tutoriel API

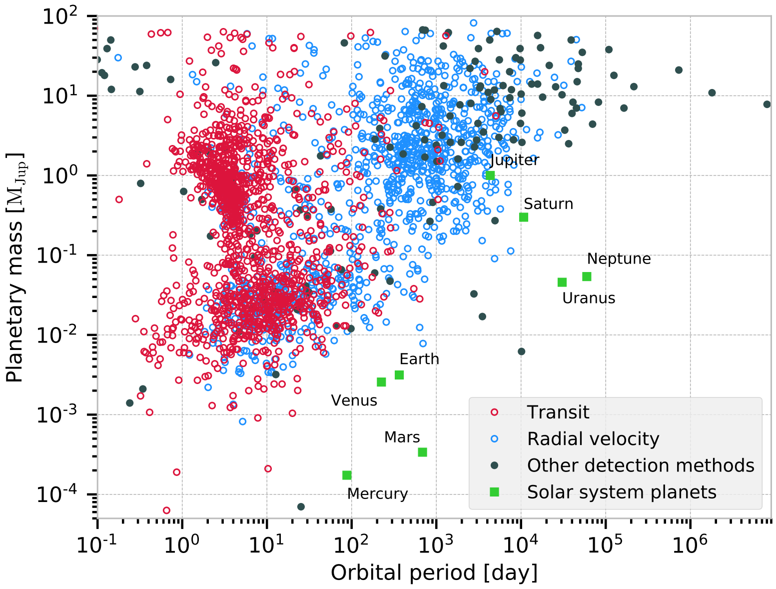

Fig. E.2.: Répartition de la masse planétaire en fonction de la période orbitale des exoplanètes confirmées. Les couleurs indiquent différentes techniques de détection. Les données proviennent du site web exoplanet.eu en utilisant le tutoriel API

E.1.1 Motivation

Les installations d'observation et les instruments dont elles sont équipées comptent parmi les outils les plus essentiels de l'astronomie. Ceux-ci évoluent et s'améliorent rapidement, permettant aux astronomes d'avoir plus d'opportunités d'étudier les exoplanètes dans de meilleures conditions grâce à des données observationnelles de meilleure qualité. À leur tour, les techniques et les modèles utilisés pour traiter les observations de transit doivent être à la hauteur de la qualité de ces données pour permettre les interprétations et les caractérisations les plus fidèles des exoplanètes et de leurs atmosphères. Cependant, au cours des dernières années, certains aspects physiques cruciaux ont été omis dans la plupart de ces modèles. Ces omissions ont même conduit, dans certains cas, à de potentielles fausses détections d'espèces atmosphériques. Une problématique qui a été correctement mise en lumière par les travaux de Casasayas-Barris et al. (2020, 2021).
A l'origine de ces erreurs d'interprétation se trouve l'oubli de phénomènes stellaires critiques. Ces phénomènes peuvent en effet induire des distorsions dans la signature d'absorption d'une planète en transit. Si ces contaminations ne sont pas prises en compte dans les modèles de transit planétaire, l'interprétation du signal atmosphérique risque d'être compromise. Il ne suffit donc pas de disposer d'un modèle robuste pour les atmosphères exoplanétaires. Sans un modèle approprié pour le spectre de l'étoile, les valeurs de température et de densité des éléments atmosphériques planétaires spécifiques qui sont extraites de ces observations pourraient être inexactes. Il est donc nécessaire de continuer à améliorer ces modèles et de tendre vers des simulations qui tiennent compte de l'image globale des transits planétaires, afin de ne pas se concentrer uniquement sur des parties spécifiques du phénomène et, en fin de compte, de permettre une meilleure caractérisation des atmosphères des exoplanètes.

Mon travail de thèse est consacré à répondre à ces problématiques. J'ai utilisé et amélioré un code numérique appelé EVaporating Exoplanet (EVE) (Bourrier & Lecavelier des Etangs 2013; Bourrier et al. 2015, 2016) pour simuler des transits réalistes d'exoplanètes et étudier la signature d'absorption que leur atmosphère peut induire dans les observations spectroscopiques à haute résolution.
L'un de mes principaux objectifs était d'améliorer ce code pour tenir compte d'une définition affinée du spectre stellaire qu'il utilise. Cette amélioration permet au code de décrire les variations locales du spectre stellaire sur la surface apparente de l'étoile avec une précision accrue. En retour, elle permet au code de générer des observations synthétiques de transit plus réalistes. Grâce à ce nouvel aspect, j'ai pu étudier en profondeur et mieux caractériser la contamination stellaire résiduelle présente dans les spectres d'absorption de transit.
Un autre de mes objectifs était d'adapter le code à l'environnement des objets

stellaires jeunes. Lorsque nous étudions l'atmosphère des planètes, nous nous intéressons aux planètes situées autour d'étoiles de la séquence principale, car elles nous donnent un aperçu des conditions actuelles sur les planètes dont l'âge est proche de celui de la Terre. Cependant, il est également intéressant d'étudier des planètes très jeunes afin d'avoir une idée des conditions initiales des planètes au moment de leur naissance. L'étude des planètes à tous les âges permet, une fois de plus, d'avoir une vision et une compréhension plus larges de l'évolution des conditions dans les atmosphères planétaires, ce qui est complémentaire à l'étude de l'habitabilité des planètes et de l'émergence de la vie.

L'étude des planètes autour des étoiles jeunes est encore un domaine émergent. Jusqu'à présent, peu de planètes ont été détectées en transit autour d'étoiles âgées de moins de $\sim$ 25 millions d'années. Les systèmes V1298 Tau (David et al. 2019), K2-33 (Mann et al. 2016), AUMic (Plavchan et al. 2020), HD 114082 b (Zakhozhay et al. 2022), HIP 67522 b (Rizzuto et al. 2020) et TOI-1097 (Wood et al. 2023) en sont des exemples notables. Seule une poignée de planètes ont été découvertes autour d'étoiles plus jeunes que $\sim$ 6 à 7 millions d'années, connues sous le nom d'étoiles T Tauri classiques, mais aucune n'a été détectée dans une configuration de transit. L'une des raisons les plus plausibles est que ces étoiles sont encore entourées d'un disque circumstellaire de gaz et de poussière, qui peut interférer avec les planètes en transit (Hartmann et al. 2016). Afin de faciliter la détection future de planètes en transit autour de jeunes objets stellaires, j'ai adapté le code EVE pour tenir compte de la présence d'un disque circumstellaire. De cette façon, je peux mieux comprendre et caractériser ses implications sur les observations de planètes en transit autour de ces étoiles.

E.1.2 Structure de la thèse

Ce manuscrit est divisé en quatre chapitres principaux, outre l'introduction et la conclusion. Dans le chapitre 2, j'introduis le contexte scientifique de cette thèse en décrivant de manière concise certains concepts théoriques clés pertinents pour les chapitres suivants. Dans le chapitre 3, j'explore en profondeur les effets de contamination que des phénomènes stellaires spécifiques induisent dans la signature d'absorption extraite des observations d'atmosphères exoplanétaires en transit. En outre, j'ai utilisé une approche encore peu commune, basée sur les améliorations que j'ai apportées au code EVE, pour réinterpréter les données de transit existantes de deux exoplanètes emblématiques et bien connues. Dans le chapitre 4, je présente un code que j'ai développé pour modéliser les raies stellaires locales du triplet infrarouge He I à partir d'observations du spectre stellaire. Dans le chapitre 5, je me concentre sur les objets stellaires jeunes et je décris comment j'ai inclus la présence d'un disque circumstellaire dans le code EVE. J'étudie également l'impact de ce disque sur la contamination stellaire dans les signatures d'absorption des planètes en transit.

Enfin, je conclus ce travail avec quelques perspectives et des moyens possibles pour continuer à améliorer les analyses des observations de transit planétaire.

E.2 Rappel scientifique

Dans ce chapitre, le contexte scientifique de ma thèse est présenté de manière concise, en mettant l'accent sur les aspects clés pertinents pour mon travail. J'introduis également quelques concepts théoriques fondamentaux utilisés dans les chapitres suivants pour permettre au lecteur d'avoir les connaissances nécessaires.

Je présente le concept des transits planétaires et comment il permet la détection et la caractérisation d'exoplanètes et de leurs atmosphères. Je détaille ce qu'est la spectroscopie de transit et comment elle nous permet de déterminer précisément les propriétés de l'atmosphère des exoplanètes à haute et basse résolution.
Ensuite, j'explique le fonctionnement de base d'un spectrographe, comment sont menées les observations de spectroscopie de transit, et comment le spectre d'absorption planétaire est couramment extrait de ces observations.
Je montre les différentes façons d'étudier les spectres d'absorption d'une planète en transit. Soit en regardant l'évolution temporelle de ce spectre pendant le transit pour accéder à la variation de la signature atmosphérique, soit en regardant la moyenne temporelle pour augmenter le rapport signal sur bruit. Je discute des avantages et inconvénients de chaque méthode.
Ensuite, je montre comment le spectre d'absorption d'une planète peut être affecté par des contaminations stellaires, notamment la rotation stellaire, les variations centre-bord dans les raies spectrales (CLV) et dans le continu (BLD).
J'explique également brièvement ce qu'est l'équilibre thermodynamique non local, car ce concept est utilisé ultérieurement dans la thèse.
Je présente également quelques-uns des paramètres orbitaux qui peuvent influencer la trajectoire de transit de la planète : l'obliquité, l'inclinaison planétaire et le paramètre d'impact.
Enfin, je présente les méthodes standard utilisées pour analyser les spectres d'absorption et comment elles tiennent compte des contaminations stellaires. Je présente ensuite brièvement le code EVE et ses avantages. J'explique également comment je calcule généralement le spectre stellaire synthétique que j'utilise en entrée du code EVE. Finalement, je présente comment le code EVE modélise les propriétés d'une atmosphère en expansion hydrodynamique, plus spécifiquement, son profil de température, de densité et vitesse. Une expansion hydrodynamique est l'un des états les plus courants dans lesquels se trouvent les exoplanètes en orbites proches.

E.3 Analyse combinée des raies d'absorption stellaires et planétaires via des simulations globales de transit

Dans ce chapitre, je présente et développe les résultats de ma publication intitulée *Combined analysis of stellar and planetary absorption lines via global forward-transit simulations* (Dethier & Bourrier 2023), qui a été publiée dans la revue *Astronomy & Astrophysics*. Cet article contient deux chapitres principaux, le premier vise à étudier en détail l'effet de la contamination stellaire causée par la rotation stellaire et la CLV sur le spectre d'absorption d'une exoplanète générique. Le second se concentre sur la réinterprétation de données de transit réelles de deux systèmes exoplanétaires spécifiques, en utilisant une approche globale qui combine la modélisation du spectre stellaire et la simulation des transits planétaires et atmosphériques.

Pour faire une étude qualitative représentative des effets de la contamination stellaire sur le spectre d'absorption mesuré d'une planète en transit, j'ai choisi de simuler la version idéalisée du transit du système planétaire HD 209458 b. Par idéalisé, je veux dire que j'ai pris en compte les paramètres stellaires et planétaires du système (voir Tableau 5.1), mais j'ai utilisé une excentricité de 0 et une inclinaison orbitale planétaire de 90° afin d'avoir une orbite planétaire circulaire qui passe par le centre du disque stellaire (paramètre d'impact de 0). HD 209458 b est un choix naturel car c'est l'une des premières exoplanètes à avoir été détectée par la méthode du transit et l'une des premières pour lesquelles une atmosphère a été détectée (Henry et al. 2000; Charbonneau et al. 2000, 2002). HD,209458 b figure également dans une série de nombreuses publications (voir, par exemple, exoplanetarchive.ipac.caltech.edu/HD20209458 et exoplanet.eu/hd209458b) et est donc une exoplanète bien connue.
Il est toutefois intéressant de noter que le signal du sodium atmosphérique qui a été initialement détecté pour ce système (Charbonneau et al. 2002) a été remis en question par Casasayas-Barris et al. (2020, 2021) qui ont montré que la signature observée autour des raies Na I D2 et D1 dans le spectre d'absorption provient très probablement d'une contamination stellaire causée par la rotation stellaire et la CLV. Cette contradiction suggère que les observations de transit de tels systèmes exoplanétaires pourraient être sujettes à une contamination qui peut être la source d'une mauvaise interprétation. L'étude et la caractérisation de ces types de contamination dans de tels systèmes exoplanétaires standards sont donc pertinentes pour construire une meilleure compréhension de leur comportement et tendre vers des propriétés planétaires déduites plus fiables. C'est cette constatation qui à motivé l'étude présenté dans ce chapitre.

Dans ce chapitre, je montre comment, en utilisant le code de modélisation de transit planétaire EVE et le code de synthèse spectrale *Turbospectrum*, j'ai simulé les spectres de transit planétaire d'un Jupiter chaud typique avec des atomes de sodium neutres dans son atmosphère dans différentes conditions stellaires et planétaires pour étudier en détails le comportement général des distorsions de raies occultées par la planète (POLDs) et leur impact sur son spectre d'absorption. Dans un premier temps, j'ai inclus individuellement dans mes simulations la rotation stellaire, les variations du centre-bord (CLV) et l'assombrissement centre-bord en bande large (BLD) afin d'étudier leurs contributions respectives aux POLDs et, par conséquent, leur influence sur la détectabilité d'une signature atmosphérique. En outre, pour chaque effet stellaire individuel, j'ai comparé les spectres d'absorption calculés avec différents spectres de substitut choisis comme approximations du spectre occulté par la planète. Grâce à l'approche de modélisation du code EVE, j'ai eu accès au spectre local exact absorbé par la planète à chaque instant du transit. Ce dernier m'a permis de calculer un spectre d'absorption non affecté que j'ai utilisé comme référence pour le comparer aux spectres d'absorption calculés avec ces autres spectres d'approximations.

J'énumère ci-dessous les principaux résultats de ce chapitre. L'une des principales conclusions de cette étude est que, dans l'ensemble, sans une évaluation précise des spectres stellaires occultés par la planète, il n'existe pas un substitut du spectre occulté par la planète universellement adéquat pour atténuer l'impact des POLD induits par la rotation stellaire, les CLV et les BLD.

- Dans le cas d'étoiles en rotation lente, les profils de raies disque-intégré reste un substitut décent aux profils de raies stellaires occultées par la planète, à moins que de fortes CLV ne soient présentes dans le spectre de l'étoile.

- Pour les étoiles en rotation modérée à rapide (dans cette étude, c'est-à-dire $\mathrm{v_{eq}} \sin(i_*) \gtrsim 3$ km s^{-1}), tous les substituts testés ont induit des POLDs dans les spectres d'absorption.

- Les POLDs induites par la rotation sont mieux minimisés avec des substituts décalés en longueur d'onde de par la vitesse radiale de la surface occultée par la planète à chaque exposition.

- Les POLDs induites par le CLV sont mieux minimisés avec le profil de raies local au centre du disque comme substitut des régions occultées par les planètes près du centre du disque stellaire apparent. Cependant, ils sont mieux minimisés avec le spectre stellaire disque-intégré comme substitut pour des régions occultées par les planètes près du limbe stellaire.

Les POLDs induites par la rotation peuvent atteindre des amplitudes comparables aux signatures typiques de l'absorption atmosphérique du Na I planétaire. Leur amplitude pic à pic augmente avec $\mathrm{v_{eq}}\sin(i_*)$. Dans le cas d'un paramètre d'impact nul, leur amplitude pic à pic diminue avec l'augmentation de l'obliquité planétaires. En général, les POLDs induits par les CLV sont de plus faible amplitude que ceux résultant d'une rotation stellaire modérée à rapide. Néanmoins, elles peuvent atteindre plusieurs dixièmes de pour cent, ce qui est de l'ordre de grandeur des signatures d'absorption Na I typiques. Les CLV deviennent donc une source principale d'interprétation erronée des signatures d'absorption atmosphérique pour les planètes en orbite autour d'étoiles à rotation lente.

L'impact du BLD sur les spectres d'absorption est plus faible que celui des CLV, mais il peut encore introduire un biais global. Ce biais global peut être éliminé mais nécessite l'utilisation d'un facteur multiplicatif estimé de manière adéquate à partir de lois analytiques d'assombrissement centre-bord, (voir par exemple Kopal 1950; Klinglesmith & Sobieski 1970; Diaz-Cordoves & Gimenez 1992).

Les signatures d'absorption atmosphérique sont davantage biaisées par les POLDs dans les expositions où la vitesse radiale de la planète est similaire à la vitesse radiale de la surface stellaire occultée. Lorsque la vitesse radiale de la planète suit la vitesse radiale de la surface stellaire occultée pendant toute la durée du transit, les signatures d'absorption atmosphérique peuvent être complètement cachées par les POLDs et devenir indétectables.

Finalement, dans la deuxième partie de ce chapitre, avec les connaissances que j'ai acquises en étudiant les distorsions stellaires dans les spectres d'absorption dans la première partie, j'ai réabordé de vraies observations de transit de deux exoplanètes intéressantes, à savoir HD 209458 b et MASCARA-1 b. J'ai reproduit d'abord le spectre d'absorption de HD 209458 b, présenté dans Casasayas-Barris et al. (2021), en utilisant des simulations du code EVE pour investiguer la présence potentielle d'une signature d'absorption Na I supplémentaire. J'ai confirmé les résultats de Casasayas-Barris et al. (2020, 2021) que les signatures observées autour des raies D2 et D1 du Na I dans le spectre d'absorption de HD 209459 b à haute résolution spectrale semblent être principalement composées de POLDs. Cependant, j'ai pu obtenir un meilleur ajustement entre les spectres d'absorption simulés et observés en incluant une atmosphère contenant des atomes de sodium autour de la planète en transit. Pour confirmer cette détection, il sera nécessaire d'effectuer une étude approfondie du signal en utilisant une combinaison de profils stellaires et planétaires précis, d'outils de modélisation tels qu'EVE et d'observations répétées du transit avec des spectrographes à haute résolution tels qu'ESPRESSO.

De même, j'ai simulé des transits de MASCARA-1 b afin d'étudier si des signatures d'absorption atmosphérique du sodium pouvaient être cachées dans les spectres ESPRESSO publiés dans.Casasayas-Barris et al. (2022). J'ai trouvé qu'en ajustant le $\mathrm{v_{eq}}\sin(i_*)$, l'abondance stellaire de sodium et la $\mathrm{i_{pl}}$, la caractéristique asymétrique dans le spectre d'absorption moyen autour des raies Na I D2 et D1 peut être entièrement expliquée par un POLD sans avoir besoin d'une atmosphère planétaire. Pour parvenir à cette conclusion, j'ai combiné un fit du spectre disque-intégré et du spectre d'absorption autour des raies du doublet du sodium.

Le travail présenté dans ce chapitre a été mené en se concentrant sur les raies Na I D2 et D1, et bien sûr, l'impact absolu des POLDs peut varier d'un système à l'autre et aussi d'une raie spectrale à l'autre. Cependant, il donne une idée du comportement qualitatif des POLDs dans les spectres d'absorption en fonction de divers paramètres stellaires et planétaires. Il montre également l'importance d'une meilleure compréhension de la façon dont les POLDs affectent le spectre d'absorption lors de la recherche de la présence d'une atmosphère planétaire. Enfin, il montre que l'utilisation d'une approche globale pour les simulations de transit - c'est-à-dire l'ajustement des profils de raies stellaires disque-intégrés et un modèle combiné des POLDs et des raies d'absorption atmosphériques planétaires - peut conduire à obtenir des contraintes atmosphériques planétaires plus fidèles depuis des spectres d'absorption, car elle permet de distinguer les signatures d'absorption planétaires de la contamination par les raies stellaires.

E.4 Spectre stellaire local des raies He I à 10830Å

Les observations qui se concentrent sur la détection de la signature d'absorption de l'hélium atmosphérique planétaire en transit se sont multipliées ces dernières années grâce aux spectrographes à haute résolution observant dans les longueurs d'onde infrarouges. Pour illustrer cet intérêt croissant, Guilluy et al. (2023) ont présenté une liste exhaustive des planètes qui ont fait l'objet d'études portant sur la détection de l'hélium dans les atmosphères planétaires (voir leur tableau A.1.). Ils ont listé un total de 46 cibles (ou 55, si l'on inclut les cibles de leur échantillon), qui ont été étudiées depuis 2018.
Les atmosphères riches en hydrogène et en hélium, soumises à un échauffement intense, sont susceptibles de subir un échappement hydrodynamique, car elles peuvent, en raison de leur nature légère, atteindre plus facilement les vitesses élevées nécessaires pour surmonter l'attraction gravitationnelle de la planète. Les espèces plus lourdes peuvent également être amenées dans les couches supérieures via des collisions avec les atomes d'hydrogène de l'atmosphère en expansion (Watson et al. 1981; Lammer et al. 2003; Vidal-Madjar et al. 2003). En considérant une composition solaire pour les atmosphères planétaires, on obtient un rapport hélium/hydrogène de $\sim 10/90$. L'hélium est donc une espèce à laquelle on s'attend dans les couches supérieures d'une atmosphère en expansion. Par conséquent, l'hélium atmosphérique planétaire a un fort potentiel pour produire de signatures d'absorption intenses

pendant le transit de la planète (par exemple jusqu'à $\sim 7\%$ d'excès d'absorption sur WASP-107 b dans Allart et al. (2019)) car il peut occuper une large région autour du corps planétaire opaque. L'hélium est donc un candidat clef dans l'étude des signatures d'absorption planétaires afin de déduire des propriétés sur la structure et la dynamique des hautes couches d'une atmosphère planétaire et, dans une certaine mesure, sur son état d'échappement (Seager & Sasselov 2000; Oklopčić & Hirata 2018; Lampón et al. 2020; Dos Santos 2022).

D'un point de vue observationnel, les longueurs d'onde infrarouges offrent la possibilité de sonder les couches atmosphériques pertinentes pour l'échappement, à savoir la thermosphère et l'exosphère, car elles englobent la région spectrale autour de 10830 Å, où les raies du triplet He I se forment (e.g. Allart et al. 2019). Le triplet He I métastable se trouve favorablement dans les thermosphères planétaires, car ces couches ont généralement des températures élevées et absorbent le flux XUV stellaire, qui sont nécessaires pour le mécanisme de formation de l'état métastable (voir plus de détails ci-dessous) (Oklopčić & Hirata 2018). De plus, la probabilité d'avoir des atomes d'hélium dans l'état métastable dans le milieu interstellaire est plutôt faible. Par conséquent, la contamination par des raies d'absorption supplémentaires provenant du milieu interstellaire dans les observations est négligeable (Indriolo et al. 2009; Allart et al. 2019). Cela confirme que les raies métastables du triplet He I sont un diagnostic crucial pour sonder les atmosphères planétaires et fait de l'hélium un élément fiable à prendre en compte pour les observations de transit.

Dans ce chapitre, je présente un modèle que j'ai développé pour reconstruire les profils des raies stellaires locales du triplet He I métastable à partir du spectre disque-intégré d'une étoile. Cette démarche a été motivée par le fait que les raies métastables du triplet He I ne peuvent pas être modélisées à partir des modèles photosphériques MARCS, car ces raies se forment généralement dans la chromosphère des étoiles. Comme je soutiens que les distorsions de raies occultées par les planètes devraient systématiquement être prises en compte dans les analyses des spectres d'absorption des transits planétaires, j'ai développé ce modèle pour obtenir une estimation des profils des raies locales du triplet He I. Cela me permet d'inclure ces profils de raies dans les grilles spectrales stellaires synthétiques utilisées en entrée dans le code EVE. Grâce à cet outil, les simulations du code EVE peuvent maintenant tenir compte des variations locales des profils des raies du triplet He I à travers le disque stellaire et donc des POLDs dans les spectres d'absorption de planètes en transit.
Je montre aussi dans ce chapitre comment j'ai utilisé une première version de ce modèle dans Guilluy et al. (2023) pour estimer le POLD dans une série de spectres d'absorption de diverses exoplanètes. J'y présente aussi l'intérêt d'avoir utilisé le modèle ainsi que les résultats que l'on en a tiré.

Ensuite, j'explique tout au long de ce chapitre comment j'ai amélioré et rendu plus réaliste le modèle pour prendre en compte davantage de physique. Notamment, je considère maintenant l'absorption et l'émission des atomes d'hélium. Mais aussi, l'introduction de deux couches de températures et densités distinctes, représentatives des deux zones de formations du triplet métastable He I dans les atmosphères stellaires (Vernazza et al. 1981; Andretta & Jones 1997). Et enfin, la prise en compte de la variation du parcours emprunté par le rayonnement dans les couches en fonction de la position sur le disque apparent de l'étoile.
J'ai l'intention de continuer à affiner ce modèle en termes de rapidité et de physique. Par exemple, une autre amélioration concevable qui pourrait être apportée au modèle à l'avenir est d'envisager une approche similaire à celle utilisée dans le code p-winds (Dos Santos et al. 2022) pour calculer les populations des niveaux d'hélium de manière plus cohérente dans les couches chromosphériques sur base du flux XUV de l'étoile.

Le modèle que j'ai présenté manque encore de nombreuses considérations physiques, et il existe des études qui utilisent des modèles plus sophistiqués intégrant tous les processus physiques pertinents pour calculer la formation des raies du triplet He I dans les atmosphères stellaires (voir par exemple, Asensio Ramos et al. (2008); Hintz et al. (2020) et HAZEL2). Cependant, ces modèles sophistiqués requièrent généralement d'importantes ressources de calcul qui ne sont pas toujours adaptées aux fits des observations. Mon objectif ultime est de rendre cet outil léger et disponible pour la communauté, afin que d'autres puissent l'utiliser pour prédire les POLDs auxquels ils devraient s'attendre dans leurs spectres d'absorption. Bien que j'aie fait certaines hypothèses importantes dans le développement de cet outil, il capture la physique essentielle et nécessaire pour donner des estimations de premier ordre des POLDs autour des raies du triplet He I. À l'avenir, cela aidera la communauté des exoplanètes à mieux interpréter les signatures d'absorption de l'hélium, ce qui est pertinent pour l'étude de l'échappement atmosphérique planétaire.

E.5 Les planètes en transit autour d'étoiles T Tauri

Dans ce chapitre, j'aborde la question de l'étude des planètes naissantes en transit autour des objets stellaires jeunes. Le nombre croissant d'exoplanètes confirmées suggère qu'une grande proportion d'étoiles hébergent un système planétaire (Borucki 2017). Il y a donc un intérêt au sein de la communauté pour tenter d'expliquer comment ces systèmes planétaires peuvent se former, d'apparence si facilement, dans le disque circumstellaire de gaz et de poussière entourant les jeunes étoiles

(Baruteau et al. 2016). De manière intéressante, en examinant les statistiques des systèmes planétaires, par exemple sur exoplanet.eu, il apparaît que la plupart des planètes détectées jusqu'à présent ont un demi-grand axe qui se situe autour ou en dessous de 0,1 UA, avec une partie significative d'entre elles ayant des masses similaires aux géantes gazeuses de notre système solaire. Ces statistiques contrastent quelque peu avec l'architecture du système solaire, car sa planète la plus proche, Mercure, a un demi-grand axe d'environ 0,38 UA et est environ 10 000 fois plus légère que Jupiter.

L'étude des planètes et de leur atmosphère juste après leur naissance permet d'obtenir un aperçu de leurs conditions initiales de formation et complète le grand nombre d'études sur les planètes des étoiles de la séquence principale (qui permettent des comparaisons avec le système solaire). Se plonger dans l'étude des planètes naissantes est une approche judicieuse pour contribuer à une compréhension exhaustive de l'évolution des systèmes planétaires.

Il est couramment admis qu'une étoile se forme après qu'un noyau pré-stellaire de gaz et de poussières subit une perturbation externe et se condense sous l'effet de sa propre force gravitationnelle (Shu 1977; Motte et al. 1998; Andre et al. 2000; Roggero 2021). Le centre de ce nuage en condensation va chauffer sous la pression croissante, et par conservation du moment angulaire, une structure de disque en rotation va se former autour du noyau central. Après environ un million d'années, la plupart de la matière initiale du nuage pré-stellaire a été accrétée, éjectée ou s'est transformée en étoile, et le reste se retrouve dans le disque. Cette structure de disque environnante de gaz et de poussières est communément appelée disque circumstellaire ou protoplanétaire. À ce moment, l'étoile est considérée comme étant née et devient visible : elle entre dans ce que l'on nomme la phase de T Tauri classique (cTTs). Après quelques millions d'années, l'étoile a accrété la majeure partie du disque circumstellaire de gaz et de poussières restant du noyau pré-stellaire initial. L'étoile continue de se contracter et finit par quitter la phase de pré-séquence principale de sa vie pour entrer dans la séquence principale.

Ces jeunes objets stellaires sont des systèmes très complexes comportant de nombreux phénomènes physiques se produisant dans leur environnement proche et qui ne sont pas présents sur les étoiles de la séquence principale. Ils ont généralement des champs magnétiques importants, typiquement autour de 1 à 3 kG (Donati & Landstreet 2009), contre jusqu'à 10 G pour le Soleil vu en tant qu'étoile (Vidotto 2016). Le champ magnétique des cTTs est suffisamment fort pour perturber le bord interne du disque circumstellaire. Cela crée des colonnes d'accrétion qui canalisent la matière le long des lignes de champ magnétique jusqu'à la surface stellaire où se forme un choc d'accrétion (Hartmann et al. 2016). Les bases de ces colonnes d'accrétion magnétosphériques déforment le bord interne du disque en ce qu'on appelle un warp (Bouvier et al. 1999). Ces distorsions sont principalement optiquement épaisses en raison de la poussière qu'elles contiennent. La présence de ces distorsions sur le bord interne du disque est la cause du phénomène observationnel appelé les "dippers". Les dippers se produisent généralement à une inclinaison stellaire élevée lorsque la ligne de visée de l'observateur est rasante à la surface du disque circumstellaire et lorsque le warp, en rotation avec le disque, croise son chemin, voir, par exemple, la Figure 6 et la Figure 7 de Bodman et al. (2017). Ce phénomène est la principale explication des dips visibles dans les courbes de lumière de certains objets stellaires jeunes (Bouvier et al. 1999; McGinnis et al. 2015; Bodman et al. 2017; Roggero et al. 2021; Roggero 2021).

Le phénomène des "dippers" se produit dans une configuration spécifique et semble donc peu probable. Cependant, des études statistiques ont été menées sur des échantillons de objets stellaires jeunes, et ont montré que entre 20 et 40 % de ces objets sont dans une configuration de "dipper" (Alencar et al. 2010; McGinnis et al. 2015; Cody & Hillenbrand 2018; Wang et al. 2023). De plus, cette configuration semble être la plus prometteuse pour espérer détecter un transit planétaire dans une cTTs. En effet, lorsque les planètes se forment dans le disque circumstellaire, les chances qu'elles sortent du plan du disque et entrent en orbite polaire sont plutôt faibles tant que le disque ne se dissipe pas. La recherche de planètes en transit à faible inclinaison stellaire dans de telles étoiles serait probablement infructueuse. Les chercher à une inclinaison stellaire élevée n'offrirait pas plus de possibilités, car l'étoile est complètement obscurcie par le disque dans une vue en côté, et par conséquent, aucun transit n'est observable. Ainsi, les "dippers" semblent offrir les meilleures opportunités pour espérer détecter une planète ou/et son atmosphère en transit, près du bord du disque interne. Il convient de mentionner que d'autres phénomènes, tels que les vents du disque et les vents stellaires, l'activité stellaire et les chocs d'accrétion, se produisent également à proximité de ces objets, ce qui les rend très complexes à étudier. Pour une revue des phénomènes physiques se produisant dans l'environnement des étoiles T Tauri classiques, voir Hartmann et al. (2016). Prendre en compte de manière auto-cohérente toutes les interactions entre l'étoile et le disque n'est pas une tâche facile et dépasse le cadre de ce travail. Dans cette étude, je me concentre uniquement sur l'effet de la déformation du disque interne sur le transit planétaire.

Dans ce chapitre je présente comment j'ai adapté le code EVE pour modéliser les étoiles "dipper" et étudier l'impact du warp interne sur les transits planétaires. En particulier, la rotation du warp pendant le transit planétaire est prise en compte. J'ai montré que le warp du disque interne peut avoir un impact sur les spectres d'absorption des planètes en transit, principalement parce que les profils des raies du spectre hors transit - utilisés dans le calcul des spectres d'absorption en transit - sont déformés par le warp occultant. Par conséquent, les distorsions des raies provoquées par l'occultation de la planète, qui peuvent affecter les spectres d'absorption, augmentent en raison de cette déformation. Cela peut entraver la caractérisation potentielle d'une signature d'absorption atmosphérique dans de telles observations.

Dans ce chapitre, je discute également du fait que le warp, qui se trouve fréquemment au rayon de co-rotation de l'étoile, tourne significativement pendant le transit des planètes. Cela rend l'analyse des observations de transit planétaire plus compliquée car les profils des raies du spectre disque-intégré varient considérablement sur un cycle de rotation du warp. Le calcul d'un spectre de référence hors transit devient alors non pertinent dans de tels cas, et la stratégie d'observation doit être adaptée.

Les statistiques que j'ai présentées indiquent qu'environ 50% des transits planétaires sont détectables en présence d'un warp. Cependant, ces statistiques sont vouées à changer en raison de l'interaction délicate entre la rotation stellaire, la géométrie du warp et l'architecture orbitale des planètes. En effet, comme l'ont montré McGinnis et al. (2015), non seulement la position du sommet du warp change au cours du temps, mais aussi sa hauteur et son extension azimutale peuvent varier (jusqu'à 10-20%) sur une échelle de temps de quelques jours. La surface de l'étoile occultée par le warp peut donc changer significativement d'un transit à l'autre, ajoutant de la complexité à ce type d'études. Une exploration plus approfondie de ces deux paramètres, devrait fournir de nouvelles valeurs pour nos statistiques. L'étude exploratoire qui est présentée dans ce chapitre pourrait grandement bénéficier d'observations de monitoring des objets stellaires en configuration de "dipper" avec une cadence temporelle élevée, comme celles présentées par McGinnis et al. (2015).

Utiliser une méthode similaire à celle présentée dans McGinnis et al. (2015) pour fitter la position et la forme du warp en fonction du temps sur des observations de courbes de lumière semble être une approche adaptée. Une fois que la position et la forme du warp sont contraintes par la photométrie à haute cadence temporelle, celles-ci peuvent être injectées dans le code EVE afin étudier les observations spectroscopiques contemporaines à haute résolution et haute cadence temporelle du système. En raison du mouvement du warp, nous devons adapter la manière dont nous analysons ces observations en spectroscopie de transit à haute résolution. Un spectre hors-transit moyen et unique n'est plus pertinent. L'utilisation du code EVE avec un modèle de warp contraint par la photométrie et un modèle de spectre stellaire robuste permettrait un fit exposition par exposition qui nous donnerait la possibilité de reconstruire les spectres disque-intégrés pendant le transit Ceux-ci seront alors utilisable dans le calcul des spectres d'absorption de la planète en transit.

En fin de compte, il est encore tôt pour conclure s'il est raisonnable de tenter de détecter des exoplanètes en transit autour des cTTs. La stratégie d'observation suggérée ci-dessus doit encore être testée, mais elle met en évidence la nécessité d’approches observationnelles et computationnelles détaillées adaptées de manière ponctuelle à chaque système étudié.

E.6 Conclusion

Les recherches que j’ai menées dans le cadre de cette thèse s’inscrivent dans un contexte plus large qui se concentre sur la caractérisation des exoplanètes et la compréhension de leur évolution à long terme. Cette communauté est animée par le désir de comprendre et de trouver des réponses aux raisons pour lesquelles les systèmes exoplanétaires sont si divers et parfois si différents de notre propre système solaire. L’étude des exoplanètes pourrait également nous aider à répondre à l’une des questions les plus énigmatiques : Qu’est-ce qui rend la Terre si propice à l’accueil de la vie telle que nous la comprenons?

La compréhension des exoplanètes - de leur formation, de leur évolution et de leurs propriétés - passe inévitablement par l’étude de leurs atmosphères, qui sont des fenêtres sur l’état passé, présent et futur de ces planètes. Une caractérisation non ambigüe de ces atmosphères est donc un aspect critique de l’étude des systèmes exoplanétaires. Mon travail de thèse a été motivé par la mise en évidence récente de la présence potentielle d’une contamination stellaire résiduelle dans les spectres d’absorption des planètes en transit et de leurs atmosphères, l’un de nos principaux diagnostics spectroscopiques. Plus précisément, il a été motivé par la nécessité d’identifier correctement l’origine de ces contaminations et de tenir compte de leurs distorsions associées afin d’éviter d’introduire un biais dans les propriétés atmosphériques déduites. Pour résoudre ce problème intriguant, j’ai utilisé le code de transits planétaires appelé EVaporating Exoplanets (EVE) et je l’ai mis à jour pour prendre en compte avec précision les contaminations stellaires. En fin de compte, les améliorations que j’ai apportées à ce code permettent des interprétations plus précises des signatures d’absorption qu’une atmosphère planétaire peut induire dans les observations de spectroscopie de transit.

Vers une meilleure caractérisation des atmosphères d’exoplanètes

La méthode de la spectroscopie de transit est l’une des techniques les plus avancées pour analyser les atmosphères exoplanétaires. Elle repose sur l’observation de l’étoile pendant le transit d’une planète afin d’identifier tout changement dans le spectre observé, qui indiquerait la signature d’absorption d’une atmosphère planétaire. Traditionnellement, pour extraire ces signatures, les spectres collectés pendant le transit sont directement divisés par le spectre de l’étoile collecté en dehors du transit. Cependant, il a récemment été démontré qu’une telle méthodologie est sujette à une contamination résiduelle du spectre stellaire. En effet, cette manière de calculer les spectres d'absorption induit des contributions parasites que nous appelons distorsions de raies occultées par les planètes ou POLDs. Ces contaminations proviennent de la non-uniformité du spectre stellaire sur la surface stellaire apparente, qui fait que la planète absorbe des spectres stellaires localement variables tout au long de son transit. Ces POLDs prennent parfois la forme de signatures d'absorption et d'émission et ont le potentiel d'affecter de manière significative la signature d'absorption atmosphérique de la planète, conduisant finalement à des interprétations erronées. Si ces effets stellaires ne sont pas traités correctement dans les simulations de transit planétaire, on risque de déduire des propriétés atmosphériques biaisées.

Dans le cadre de ma thèse, j'ai utilisé et étendu les capacités du code EVE, qui permet de générer des spectres stellaires synthétiques réalistes pendant les transits d'exoplanètes, en tenant compte de la géométrie 3D de l'architecture du système et de la structure atmosphérique. Le code EVE a l'avantage de pouvoir calculer l'absorption des spectres stellaires locaux pendant le transit, à la fois par la planète et par l'atmosphère simultanément. Il produit ainsi des observations synthétiques du transit planétaire qui sont directement comparables aux observations réelles. Cependant, un traitement raffiné des variations locales des spectres à travers le disque stellaire était nécessaire pour que le code prenne naturellement en compte les POLDs. Pour résoudre ce problème, j'ai couplé le code EVE avec un code de synthèse spectrale qui génère des spectres stellaires synthétiques locaux précis. Cette adaptation garantit que la planète simulée absorbe le bon spectre stellaire local à chaque étape du transit.
Grâce à cette amélioration, j'ai pu étudier en détail les contaminations stellaires induites dans les spectres d'absorption par les variations locales du spectre stellaire, à savoir la rotation stellaire et la variation centre-bord. L'étude que j'ai présentée dans le chapitre 3 a permis de mieux comprendre le comportement des POLD et leur impact individuel sur les signatures d'absorption atmosphérique. J'ai démontré l'utilité d'une approche globale lors de la simulation du transit planétaire, notamment en réexaminant les données d'observation de deux exoplanètes bien connues et particulières.

En utilisant tout le potentiel de l'approche de modélisation globale du code EVE, j'ai tiré de nouvelles conclusions sur ces deux systèmes. Pour le premier, HD 20948 b, j'ai montré la possible présence d'atomes de sodium dans l'atmosphère de la planète. Pour le second système, MASCARA-1 b, j'ai montré que les POLDs pouvaient entièrement expliquer le spectre d'absorption observé et qu'il n'y avait pas de signature détectable de sodium atmosphérique dans les observations. Ce type d'études bénéficierait grandement d'observations de bonne qualité et d'une modélisation avancée du spectre stellaire. L'exploration future des effets tridimensionnels de l'atmosphère stellaire pourrait être testée pour voir si différentes interprétations de la signature observée se dégagent. En outre, l'extension des modèles stellaires pour tenir compte des contributions chromosphériques dans des raies stellaires spécifiques qui sont connues pour se former partiellement dans des conditions chromosphériques, telles que le cœur des raies du doublet Na I, pourrait aider à affiner davantage les résultats. Notre approche devrait explorer et inclure d'autres phénomènes stellaires pour compléter ce que j'ai présenté. Par exemple, la rotation stellaire différentielle, le blueshift convectif et les inhomogénéités de la surface stellaire telles que les taches. Ces phénomènes sont des contributeurs potentiels aux POLD car ils affectent les spectres stellaires locaux d'une manière similaire à la CLV et à la rotation stellaire.

Les travaux présentés dans ce chapitre serviront de base pour comprendre comment et pourquoi les distorsions de raies occultées par la planète se forment dans les spectres d'absorption, mais aussi pour comprendre leur comportement et leur impact sur les signatures d'absorption atmosphérique. Avec la nouvelle génération de spectrographes à haute résolution tels que ESPRESSO/VLT, NIRPS à La Silla et ANDES/ELT, les POLDs deviendront une source dominante de contamination dans les spectres d'absorption des transits planétaires. Une approche similaire à celle que j'ai utilisée dans ce chapitre pour analyser les signatures d'absorption atmosphérique devrait être utilisée plus systématiquement afin de ne pas introduire des biais supplémentaires.

L'un des objectifs scientifiques du tout nouvel observatoire spatial, le télescope spatial James Webb, est d'observer les exoplanètes en transit et d'étudier leurs atmosphères. Le JWST est équipé de spectrographes qui observent les planètes avec une résolution spectrale basse à moyenne. Une question pertinente à se poser est la suivante : les spectres d'absorption à plus faible résolution sont-ils également affectés de manière significative par les distorsions des raies occultées par la planète ? L'expertise que j'ai développée au cours de ma thèse est idéale pour répondre à cette question. Une extension naturelle de mon travail de thèse est alors d'étudier les effets de la rotation stellaire et de la CLV dans de telles observations d'une manière similaire à celle présentée dans le Chapitre 3. Ces deux études seront complémentaires et pertinentes car la spectroscopie à moyenne et basse résolution permet d'accéder aux parties plus denses d'une atmosphère planétaire.

Enfin, j'ai participé à différentes collaborations grâce à l'expertise que j'ai développée sur les simulations de transit planétaire. Par exemple, j'ai participé à la publication *HEARTS VIII. Nondetection of sodium in the atmosphere of the aligned planet KELT-10b* par M. Steiner (Steiner et al. 2023). Les auteurs m'ont demandé de simuler le spectre d'absorption moyen pour un transit typique de la planète KELT - 10 b dans la région spectrale du doublet de sodium. Nous voulions comparer le spectre d'absorption qu'ils ont reconstruit à partir des observations HARPS au spectre d'absorption synthétique du corps opaque de KELT-10 b afin de mieux discriminer entre les POLDs et les signatures planétaires réelles. Le spectre d'absorption synthétique que j'ai calculé est présenté dans la figure 7 de l'article.

J'ai également travaillé avec l'étudiant en doctorat Adrien Masson et son superviseur le Dr. Sandrine Vinatier du LESIA, observatoire de Paris, pour effectuer des simulations avec le code EVE afin de les comparer à leurs spectres d'absorption qu'ils ont reconstruits à partir des observations SPIRou pour HD 189733 b dans la région spectrale du triplet infrarouge He I à 10830 Å.

Je collabore avec le doctorant Dany Mounzer de l'observatoire de Genève pour simuler le spectre d'absorption synthétique de HD 189733 b dans la région spectrale du doublet de sodium afin de le comparer au spectre d'absorption qu'il a reconstruit à partir des observations d'ESPRESSO. Ces deux dernières collaborations sont toujours en cours.

Je collabore actuellement avec un étudiant en Master de l'observatoire de Genève sur une étude qui se concentre sur l'analyse des spectres d'absorption des transits planétaires dans la région spectrale du doublet de sodium sur les mêmes observations que l'étude DREAM I (Bourrier et al. 2023). Dans cette étude, nous utiliserons une approche similaire à celle utilisée dans Dethier & Bourrier (2023) pour analyser les observations de HD 209458 b et MASCARA-1 b. C'est-à-dire, ajuster le spectre hors transit observé dans la région spectrale du doublet Na I. Ensuite, utiliser le code EVE pour simuler les transits des planètes pour chaque cible et rechercher d'éventuelles signatures atmosphériques du sodium. Dans le cadre de cette collaboration, j'ai co-supervisé un étudiant en licence dont la tâche consistait à utiliser une routine que j'ai développée pour ajuster le spectre stellaire hors transit observé dans les raies du doublet Na I de l'échantillon de cibles.

Une modélisation simplifiée mais efficace des raies de l'hélium

Les raies du triplet de l'hélium dans l'infrarouge autour de 10830 Åse sont révélées être d'excellents traceurs des hautes couches atmosphériques des planètes. En raison de cela, une proportion significative de la communauté des exoplanètes s'est concentrée sur l'étude de la signature de l'hélium dans les planètes en transit. Comme je l'ai présenté dans le Chapitre 3, les signatures d'absorption atmosphérique des planètes en transit sont soumises à des contaminations stellaires résiduelles, et l'hélium n'y fait pas exception. Pour simuler des observations de transit synthétiques réalistes et tenir compte de ces contaminations, il est nécessaire de disposer d'une connaissance précise du spectre stellaire local.

Malheureusement, les modèles actuellement disponibles publiquement pour les atmosphères stellaires, comme celui que j'ai utilisé tout au long de ce travail, ne tiennent pas compte des raies du triplet de l'He I. En effet, l'état métastable des atomes d'hélium permettant la formation de ces raies nécessite des conditions physiques généralement rencontrées dans les régions chromosphériques des atmosphères stellaires, tandis que ces modèles d'atmosphères stellaires se concentrent sur la photosphère. Pour résoudre ce problème, j'ai présenté, dans le chapitre 4, un modèle qui permet de reconstruire les raies stellaires locales de l'He I métastable à partir d'un ajustement au spectre disque-intégré observé d'une étoile. Les spectres stellaires locaux extraits peuvent être utilisés directement dans le code EVE pour remplir sa grille stellaire, permettant au code de faire des prédictions plus précises des POLDs dans la région spectrale des raies en triplet de l'He I. J'ai utilisé une version de ce modèle dans une publication visant à caractériser l'évaporation atmosphérique sur diverses exoplanètes (Guilluy et al. 2023). Plus précisément, grâce à l'utilisation du modèle, nous avons évalué les POLDs pour estimer leur impact sur les spectres d'absorption des cibles de l'étude avant toute autre exploration des signatures d'absorption.

Parce que la modélisation précise des POLDs est essentielle dans les simulations de transit planétaire, ce modèle de formation des raies de l'hélium doit être encore amélioré. Cette amélioration est également motivée par le nombre croissant d'observations et d'études se concentrant sur ces raies dans le contexte de la caractérisation des atmosphères des exoplanètes. Idéalement, la formation des raies de l'hélium devrait être traitée en détail par des modèles stellaires qui incluent à la fois la photosphère et la chromosphère. Cependant, ces types de modèles ne sont pas aussi généralisés que les modèles purement photosphériques, ce qui les rend difficiles à utiliser en pratique (par exemple Hintz et al. 2020).

Une amélioration naturelle du modèle consisterait alors à traiter de manière plus cohérente les processus contribuant à la formation des raies du triplet de l'hélium. Par exemple, prendre en compte le flux XUV stellaire dans le calcul de la population des niveaux triplet d'hélium métastable de manière similaire à Oklopčić & Hirata (2018) et utilisé dans le code *p-winds* (Dos Santos et al. 2022). Il s'agit d'une perspective prometteuse de mon travail, car une interface entre EVE et *p-winds* existe.

Dans sa version actuelle, le modèle a déjà montré ses capacités. Comme je prévois de le rendre publiquement disponible, il servira d'outil léger pour donner une première estimation des POLDs dans les spectres d'absorption reconstruits à partir des observations de transit. L'objectif final étant d'obtenir des propriétés plus fiables à partir des signatures d'absorption de l'hélium observées.

Étude des planètes en transit autour des étoiles de type T Tauri classiques

Parce que l'état de l'atmosphère d'une planète évolue constamment tout au long de sa vie, il est important d'étudier les planètes à tous les âges. Alors que les planètes autour d'étoiles d'âge similaire à celui du Soleil ont été découvertes en masse, les planètes autour d'étoiles jeunes sont plus difficiles à détecter. Jusqu'à présent, la technique la plus fructueuse pour la détection de planètes est la technique du transit. Cependant, sa pertinence pour l'étude des planètes en orbite autour d'étoiles jeunes reste encore à prouver. En effet, parmi les nombreux phénomènes physiques inhérents aux étoiles jeunes et qui compliquent leur étude, l'un se distingue par sa capacité à entraver la détection des planètes en transit dans ces systèmes. Les étoiles jeunes sont entourées d'un disque circumstellaire de gaz et de poussière, qui sont le lieu de naissance des planètes. Selon la configuration géométrique du système, le disque peut se trouver dans le champ de vision de l'observateur, cachant ainsi d'éventuelles planètes en transit.

Dans le chapitre 5, j'ai abordé le cas des étoiles dippers, une configuration spécifique dans laquelle les planètes pourraient éventuellement être observées en transit. Dans ces objets, la ligne de visée de l'observateur a une incidence rasante par rapport au disque et est périodiquement obstruée par une déformation du disque interne, appelée un "warp", induite par l'accrétion magnétosphérique du disque interne sur la surface stellaire.

Dans ce chapitre, je présente d'abord le modèle de disque et de warp que j'ai utilisé pour adapter le code EVE à l'environnement des étoiles jeunes. Ensuite, j'étudie l'impact du warp occultant sur les POLDs dans les spectres d'absorption d'une hypothétique planète en transit. J'ai montré comment le warp déforme les profils de raies du spectre stellaire disque-intégré, ce qui modifie à son tour les POLDs, par rapport à un cas sans disque ni warp. Enfin, j'explore l'effet du mouvement périodique du warp sur la détectabilité d'une planète en transit dans de tels systèmes.

Dans les systèmes étudiés dans ce chapitre, le spectre disque-intégré stellaire change constamment en raison de l'occultation périodique par le warp. L'utilisation d'un unique spectre hors-transit pour calculer les spectres d'absorption d'une planète en transit devient ainsi non pertinente. Plutôt, il serait nécessaire de pouvoir reconstruire le spectre disque-intégré en dehors, mais aussi pendant, le transit de la planète. Cela peut être réalisé en fittant les observations à chaque pas de temps du transit afin que la position du warp et le spectre disque-intégré (en l'absence d'occultation par la planète) puissent être prédits pendant le transit de la planète. Pour faciliter cette approche, une stratégie clé consisterait à combiner des observations spectroscopiques à haute résolution avec un monitoring photométrique à haute cadence temporelle de l'étoile. Le premier permet une connaissance précise de la variabilité du spectre stellaire et la détection de tout changement dans les raies spectrales stellaires qui pourrait indiquer l'absorption par une planète en transit et son atmosphère. Le second donne la possibilité de contraindre la forme et la position de la déformation du disque interne en fonction du temps (voir McGinnis et al. 2015). La forme de la déformation peut changer significativement entre les cycles de rotation, par exemple McGinnis et al. (2015) et la Figure 3 de Alencar et al. (2018), soulignant la nécessité de la photométrie et de la spectroscopie simultanées. Dans sa version actuelle, le code EVE est techniquement adapté pour effectuer l'analyse de telles observations.

Jusqu'à présent, le disque et le warp ont été considérés comme opaques. Cependant, le mélange de poussière et de gaz présent dans le disque a ses propres propriétés optiques. Par conséquent, les bords du warp pourraient ne pas être entièrement opaques aux longueurs d'onde examinées. À son tour, le warp en transit pourrait induire une signature dans le spectre d'absorption de la planète et potentiellement modifier les POLDs d'une manière difficilement prévisible. Heureusement, la nature polyvalente du code EVE lui permet d'introduire une meilleure description du disque, y compris des effets d'opacité.

Un autre aspect à considérer concernant les étoiles jeunes est leur niveau généralement élevé de flux XUV par rapport aux étoiles de séquence principale (Johnstone et al. 2015). Dans de telles conditions, on pourrait s'attendre à ce que les atmosphères planétaires dans ces systèmes soient étendues. Une atmosphère planétaire étendue pourrait augmenter la détectabilité de la planète. Si l'atmosphère est fortement étendue en raison du niveau élevé de flux XUV, elle pourrait transiter sans que le corps opaque de la planète ait besoin de transiter lui-même (Ehrenreich et al. 2012). Cela pourrait créer des signatures détectables et élargir l'intervalle de demi-grands axes dans lequel un transit est détectable, augmentant ainsi l'intervalle des inclinaisons stellaires exploitables. Le code EVE est déjà adapté à une telle exploration, grâce à son couplage avec le code *p-winds*. Un élément manquant pour une telle exploration est le flux XUV, une quantité complexe à collecter pour les étoiles lointaines. Cependant, un point de départ est le flux XUV récemment publié de l'étoile jeune V1298 Tau par Maggio et al. (2023), qui ont accepté de collaborer avec nous.

En raison des possibles interactions avec la magnétosphère stellaire et les vents stellaires, qui sont des sous-produits des interactions étoile-disque, la signature d'absorption de l'atmosphère en transit pourrait être différente de ce qui est attendu (par exemple Matsakos et al. 2015; Strugarek et al. 2019; Vidotto & Cleary

2020). Dans le projet SPIDI[2], auquel je participe, des modèles numériques de l'environnement proche des étoiles jeunes et des signatures radiatives qui y sont associées sont développés (Pantolmos et al. 2020; Tessore et al. 2023). Il est donc raisonnable de penser que les signatures d'une atmosphère en évaporation pourraient être détectables dans cet environnement complexe, à mesure que les signatures des interactions entre l'étoile et le disque sont de mieux en mieux contraintes.

L'approche que j'ai utilisée dans ce chapitre peut sembler heuristique, mais avec des instruments de plus en plus efficaces, des télescopes et des outils de modélisation avancés, les observations et l'étude des objets stellaires jeunes seront facilitées. Le code EVE sera adapté et prêt à relever le défi de confirmer la présence de planètes en transit autour d'étoiles jeunes.

La communauté travaillant sur les observations de transits d'exoplanètes, en particulier en spectroscopie à haute résolution, commence de plus en plus à tenir compte des contaminations stellaires dans leurs analyses des spectres d'absorption (voir par exemple Yan et al. 2017; Yan & Henning 2018; Casasayas-Barris et al. 2020, 2021, 2022; Zhang et al. 2022, et d'autres). L'expertise que j'ai développée dans la simulation des spectres d'absorption de transits exoplanétaires pendant ma thèse m'a permis de nouer de nouvelles collaborations avec d'autres groupes. Ces collaborations soulignent l'utilité de l'approche globale que j'ai contribué à construire avec les adaptations que j'ai apportées au code EVE. L'intérêt de la communauté pour des outils permettant d'estimer la contamination stellaire dans les spectres d'absorption de transits planétaires est tangible. En définitive, la prise en compte des POLDs dans l'analyse des spectres d'absorption planétaire devrait devenir systématique. Le travail que j'ai présenté vise à poser les bases pour un tel objectif avec pour but ultime une meilleure caractérisation des atmosphères des mondes lointains qui nous entourent.

---

[2] `https://spidi-eu.org`

Bibliography

Albrecht, S., Snellen, I., de Mooij, E., & Le Poole, R. 2009, in Transiting Planets, ed. F. Pont, D. Sasselov, & M. J. Holman, Vol. 253, 520–523

Alencar, S. H. P., Bouvier, J., Donati, J.-F., et al. 2018, A&A, 620, A195

Alencar, S. H. P., Teixeira, P. S., Guimarães, M. M., et al. 2010, A&A, 519, A88

Alexeeva, S., Ryabchikova, T., Mashonkina, L., & Hu, S. 2018, The Astrophysical Journal, 866, 153

Allart, R., Bourrier, V., Lovis, C., et al. 2018, Science, 362, 1384

Allart, R., Bourrier, V., Lovis, C., et al. 2019, A&A, 623, A58

Allende Prieto, C., Asplund, M., & Fabiani Bendicho, P. 2004, A&A, 423, 1109

Alvarez, R. & Plez, B. 1998, A&A, 330, 1109

Andre, P., Ward-Thompson, D., & Barsony, M. 2000, in Protostars and Planets IV, ed. V. Mannings, A. P. Boss, & S. S. Russell, 59

Andretta, V. & Jones, H. P. 1997, The Astrophysical Journal, 489, 375

Asensio Ramos, A., Trujillo Bueno, J., & Landi Degl'Innocenti, E. 2008, ApJ, 683, 542

Baruteau, C., Bai, X., Mordasini, C., & Mollière, P. 2016, Space Sci. Rev., 205, 77

Bello-Arufe, A., Knutson, H. A., Mendonça, J. M., et al. 2023, AJ, 166, 69

Benisty, M., Dominik, C., Follette, K., et al. 2022, arXiv e-prints, arXiv:2203.09991

Bergemann, M., Gallagher, Andrew J., Eitner, Philipp, et al. 2019, A&A, 631, A80

Bertout, C. 2000, A&A, 363, 984

Bodman, E. H. L., Quillen, A. C., Ansdell, M., et al. 2017, MNRAS, 470, 202

Bohn, A. J., Benisty, M., Perraut, K., et al. 2022, A&A, 658, A183

Boisse, I., Moutou, C., Vidal-Madjar, A., et al. 2009, A&A, 495, 959

Bonomo, A. S., Desidera, S., Benatti, S., et al. 2017, A&A, 602, A107

Borsa, F., Allart, R., Casasayas-Barris, N., et al. 2021, A&A, 645, A24

Borsa, F. & Zannoni, A. 2018, A&A, 617, A134

Borucki, W. J. 2017, Proceedings of the American Philosophical Society, 161, 38

Bourrier, V., Attia, O., Mallonn, M., et al. 2023, A&A, 669, A63

Bourrier, V., Ehrenreich, D., & Lecavelier des Etangs, A. 2015, A&A, 582, A65

Bourrier, V. & Lecavelier des Etangs, A. 2013, A&A, 557, A124

Bourrier, V., Lecavelier des Etangs, A., Ehrenreich, D., Tanaka, Y. A., & Vidotto, A. A. 2016, A&A, 591, A121

Bourrier, V., Lecavelier des Etangs, A., & Vidal-Madjar, A. 2014, A&A, 565, A105

Bouvier, J., Chelli, A., Allain, S., et al. 1999, A&A, 349, 619

Bouvier, J., Matt, S. P., Mohanty, S., et al. 2014, in Protostars and Planets VI, ed. H. Beuther, R. S. Klessen, C. P. Dullemond, & T. Henning, 433–450

Bruls, J. H. M. J. & Rutten, R. J. 1992, A&A, 265, 257

Casasayas-Barris, N., Borsa, F., Palle, E., et al. 2022, A&A, 664, A121

Casasayas-Barris, N., Palle, E., Stangret, M., et al. 2021, A&A, 647, A26

Casasayas-Barris, N., Pallé, E., Yan, F., et al. 2018, A&A, 616, A151

Casasayas-Barris, N., Pallé, E., Yan, F., et al. 2020, A&A, 635, A206

Catling, D. C. & Kasting, J. F. 2017, Atmospheric Evolution on Inhabited and Lifeless Worlds (Cambridge University Press)

Cauley, P. W., Wang, J., Shkolnik, E. L., et al. 2021, The Astronomical Journal, 161, 152

Cegla, H. M., Lovis, C., Bourrier, V., et al. 2016, A&A, 588, A127

Centeno, R., Trujillo Bueno, J., Uitenbroek, H., & Collados, M. 2008, ApJ, 677, 742

Chamberlain, J. W. 1963, Planet. Space Sci., 11, 901

Charbonneau, D., Brown, T. M., Latham, D. W., & Mayor, M. 2000, The Astrophysical Journal, 529, L45

Charbonneau, D., Brown, T. M., Noyes, R. W., & Gilliland, R. L. 2002, The Astrophysical Journal, 568, 377

Cody, A. M. & Hillenbrand, L. A. 2018, The Astronomical Journal, 156, 71

Czesla, S., Klocová, T., Khalafinejad, S., Wolter, U., & Schmitt, J. H. M. M. 2015, A&A, 582, A51

Czesla, S., Lampón, M., Sanz-Forcada, J., et al. 2022, A&A, 657, A6

D’Angelo, C. R. & Spruit, H. C. 2012, Monthly Notices of the Royal Astronomical Society, 420, 416

David, T. J., Cody, A. M., Hedges, C. L., et al. 2019, The Astronomical Journal, 158, 79

David, T. J., Petigura, E. A., Luger, R., et al. 2019, ApJ, 885, L12

Dethier, W. & Bourrier, V. 2023, A&A, 674, A86

Diaz-Cordoves, J. & Gimenez, A. 1992, Astronomy and Astrophysics, 259, 227

Donati, J. F. & Landstreet, J. D. 2009, ARA&A, 47, 333

Dos Santos, L. A. 2022, arXiv e-prints, arXiv:2211.16243

Dos Santos, L. A., Vidotto, A. A., Vissapragada, S., et al. 2022, A&A, 659, A62

Dravins, D. 1982, ARA&A, 20, 61

Edwards, S., Fischer, W., Hillenbrand, L., & Kwan, J. 2006, The Astrophysical Journal, 646, 319

Ehrenreich, D., Bourrier, V., Bonfils, X., et al. 2012, A&A, 547, A18

Ehrenreich, D., Lovis, C., Allart, R., et al. 2020, Nature, 580, 597

Gaidos, E., Hirano, T., Beichman, C., et al. 2022, MNRAS, 509, 2969

Gallagher, A. J., Bergemann, M., Collet, R., et al. 2020, A&A, 634, A55

Gray, D. F. 2005, The Observation and Analysis of Stellar Photospheres, 3rd edn. (Cambridge University Press)

Gressier, A., Lecavelier des Etangs, A., Sing, D. K., et al. 2023, A&A, 672, A34

Guillot, T., Fletcher, L. N., Helled, R., et al. 2022, arXiv e-prints, arXiv:2205.04100

Guilluy, G., Bourrier, V., Jaziri, Y., et al. 2023, arXiv e-prints, arXiv:2307.00967

Gully-Santiago, M., Morley, C. V., Luna, J., et al. 2023, arXiv e-prints, arXiv:2307.08959

Gunell, H., Maggiolo, R., Nilsson, H., et al. 2018, A&A, 614, L3

Gustafsson, B., Edvardsson, B., Eriksson, K., et al. 2008, A&A, 486, 951

Hartmann, L., Herczeg, G., & Calvet, N. 2016, ARA&A, 54, 135

Hartmann, L., Hewett, R., & Calvet, N. 1994, ApJ, 426, 669

Henry, G. W., Marcy, G. W., Butler, R. P., & Vogt, S. S. 2000, The Astrophysical Journal, 529, L41

Hintz, D., Fuhrmeister, B., Czesla, S., et al. 2020, A&A, 638, A115

Hooton, M. J., Hoyer, S., Kitzmann, D., et al. 2022, A&A, 658, A75

Huang, C., Koskinen, T., Lavvas, P., & Fossati, L. 2023, ApJ, 951, 123

Hubeny, I. & Mihalas, D. 2014, Theory of Stellar Atmospheres: An Introduction to Astrophysical Non-equilibrium Quantitative Spectroscopic Analysis, Princeton Series in Astrophysics (Princeton University Press)

Indriolo, N., Hobbs, L., Hinkle, K., & McCall, B. 2009, The Astrophysical Journal, 703

Johnstone, C. P., Güdel, M., Stökl, A., et al. 2015, The Astrophysical Journal Letters, 815, L12

Kirk, J., Dos Santos, L. A., López-Morales, M., et al. 2022, AJ, 164, 24

Klinglesmith, D. A. & Sobieski, S. 1970, AJ, 75, 175

Kopal, Z. 1950, Harvard College Observatory Circular, 454, 1

Krasnopolsky, V. A. 2019, Spectroscopy and Photochemistry of Planetary Atmospheres and Ionospheres. Mars, Venus, Titan, Triton and Pluto (Cambridge University Press)

Kurosawa, R., Romanova, M. M., & Harries, T. J. 2011, MNRAS, 416, 2623

Lamers, H. J. G. L. M. & Cassinelli, J. P. 1999, Introduction to Stellar Winds (Cambridge University Press)

Lammer, H., Selsis, F., Ribas, I., et al. 2003, ApJ, 598, L121

Lampón, M., López-Puertas, M., Lara, L. M., et al. 2020, A&A, 636, A13

Lecavelier Des Etangs, A. 2007, A&A, 461, 1185

Lecavelier des Etangs, A., Vidal-Madjar, A., McConnell, J. C., & Hébrard, G. 2004, A&A, 418, L1

Leenaarts, J., Golding, T., Carlsson, M., Libbrecht, T., & Joshi, J. 2016, A&A, 594, A104

Louden, T. & Wheatley, P. J. 2015, ApJ, 814, L24

Maggio, A., Pillitteri, I., Argiroffi, C., et al. 2023, ApJ, 951, 18

Mann, A. W., Newton, E. R., Rizzuto, A. C., et al. 2016, AJ, 152, 61

Mansfield, M., Bean, J. L., Oklopčić, A., et al. 2018, ApJ, 868, L34

Matsakos, T., Uribe, A., & Königl, A. 2015, A&A, 578, A6

Mayor, M. & Queloz, D. 1995, Nature, 378, 355

McGinnis, P. T., Alencar, S. H. P., Guimarães, M. M., et al. 2015, A&A, 577, A11

Motte, F., Andre, P., & Neri, R. 1998, A&A, 336, 150

Mounzer, D., Lovis, C., Seidel, J. V., et al. 2022, arXiv e-prints, arXiv:2209.00597

Moutou, C., Dalal, S., Donati, J. F., et al. 2020, A&A, 642, A72

Murray-Clay, R. A., Chiang, E. I., & Murray, N. 2009, ApJ, 693, 23

Nagel, E. & Bouvier, J. 2020, A&A, 643, A157

Nikolov, N., Sing, D. K., Fortney, J. J., et al. 2018, Nature, 557, 526

Nortmann, L., Pallé, E., Salz, M., et al. 2018, Science, 362, 1388

Oklopčić, A. & Hirata, C. M. 2018, ApJ, 855, L11

Orell-Miquel, J., Lampón, M., López-Puertas, M., et al. 2023, arXiv e-prints, arXiv:2307.05191

Owen, J. E. & Schlichting, H. E. 2023, arXiv e-prints, arXiv:2308.00020

Pantolmos, G., Zanni, C., & Bouvier, J. 2020, A&A, 643, A129

Parker, E. N. 1958, ApJ, 128, 664

Parker, E. N. 1964, ApJ, 139, 72

Perryman, M. 2018, The Exoplanet Handbook, 2nd edn. (Cambridge University Press)

Pietrow, A. G. M., Kiselman, D., Andriienko, O., et al. 2022, arXiv e-prints, arXiv:2212.03991

Pinilla, P., Benisty, M., de Boer, J., et al. 2018, ApJ, 868, 85

Plavchan, P., Barclay, T., Gagné, J., et al. 2020, Nature, 582, 497

Plez, B. 2012, Turbospectrum: Code for spectral synthesis

Pluriel, W. 2023, Remote Sensing, 15, 635

Pluriel, W., Leconte, J., Parmentier, V., et al. 2022, A&A, 658, A42

Queloz, D., Henry, G. W., Sivan, J. P., et al. 2001, A&A, 379, 279

Rebull, L. M., Stauffer, J. R., Cody, A. M., et al. 2020, AJ, 159, 273

Rizzuto, A. C., Newton, E. R., Mann, A. W., et al. 2020, The Astronomical Journal, 160, 33

Roggero, N. 2021, Theses, Université Grenoble Alpes

Roggero, N., Bouvier, J., Rebull, L. M., & Cody, A. M. 2021, A&A, 651, A44

Rutten, R. J. 1993, in National Solar Observatory / Sacramento Peak Summer Course

Rutten, R. J. 2003, Radiative Transfer in Stellar Atmospheres, 8th edn. (Utrecht University lecture notes)

Ryabchikova, T., Piskunov, N., Kurucz, R. L., et al. 2015, Physica Scripta, 90, 054005

Sanz-Forcada, J. & Dupree, A. K. 2008, A&A, 488, 715

Schunk, R. & Nagy, A. 2000, Ionospheres: Physics, Plasma Physics, and Chemistry, Atmos. Space Sci. Ser.

Seager, S. & Dotson, R. 2010, Exoplanets, The university of Arizona space science series (The university of Arizona press)

Seager, S. & Mallén-Ornelas, G. 2003, The Astrophysical Journal, 585, 1038

Seager, S. & Sasselov, D. D. 2000, ApJ, 537, 916

Seidel, J. V., Borsa, F., Pino, L., et al. 2023, A&A, 673, A125

Seidel, J. V., Ehrenreich, D., Pino, L., et al. 2020, A&A, 633, A86

Seidel, J. V., Ehrenreich, D., Wyttenbach, A., et al. 2019, A&A, 623, A166

Shu, F. H. 1977, ApJ, 214, 488

Sicilia-Aguilar, A., Manara, C. F., de Boer, J., et al. 2020, A&A, 633, A37

Snellen, I. A. G., Albrecht, S., de Mooij, E. J. W., & Le Poole, R. S. 2008, A&A, 487, 357

Stapelfeldt, K. R., Krist, J. E., Ménard, F., et al. 1998, The Astrophysical Journal, 502, L65

Stauffer, J., Cody, A. M., McGinnis, P., et al. 2015, The Astronomical Journal, 149, 130

Steiner, M., Attia, O., Ehrenreich, D., et al. 2023, A&A, 672, A134

Strugarek, A., Brun, A. S., Donati, J. F., Moutou, C., & Réville, V. 2019, ApJ, 881, 136

Talens, G. J. J., Albrecht, S., Spronck, J. F. P., et al. 2017, A&A, 606, A73

Tessore, B. 2017, Theses, Université Montpellier

Tessore, B., Soulain, A., Pantolmos, G., et al. 2023, A&A, 671, A129

Vernazza, J. E., Avrett, E. H., & Loeser, R. 1981, ApJS, 45, 635

Vidal-Madjar, A., Lecavelier des Etangs, A., Désert, J. M., et al. 2003, Nature, 422, 143

Vidal-Madjar, A., Sing, D. K., Lecavelier Des Etangs, A., et al. 2011, A&A, 527, A110

Vidotto, A. A. 2016, MNRAS, 459, 1533

Vidotto, A. A. & Cleary, A. 2020, MNRAS, 494, 2417

Villenave, M., Ménard, F., Dent, W. R. F., et al. 2020, A&A, 642, A164

Vissapragada, S., Stefánsson, G., Greklek-McKeon, M., et al. 2021, The Astronomical Journal, 162, 222

Volkov, A. N., Johnson, R. E., Tucker, O. J., & Erwin, J. T. 2011, ApJ, 729, L24

Wang, X.-L., Fang, M., Herczeg, G. J., et al. 2023, Research in Astronomy and Astrophysics, 23, 075015

Wardenier, J. P., Parmentier, V., Lee, E. K. H., Line, M. R., & Gharib-Nezhad, E. 2021, MNRAS, 506, 1258

Watson, A. J., Donahue, T. M., & Walker, J. C. G. 1981, Icarus, 48, 150

Wood, M. L., Mann, A. W., Barber, M. G., et al. 2023, AJ, 165, 85

Wyttenbach, A., Ehrenreich, D., Lovis, C., Udry, S., & Pepe, F. 2015, A&A, 577, A62

Wyttenbach, A., Lovis, C., Ehrenreich, D., et al. 2017, A&A, 602, A36

Yan, F., Casasayas-Barris, N., Molaverdikhani, K., et al. 2019, A&A, 632, A69

Yan, F. & Henning, T. 2018, Nature Astronomy, 2, 714

Yan, F., Pallé, E., Fosbury, R. A. E., Petr-Gotzens, M. G., & Henning, T. 2017, A&A, 603, A73

Yan, F., Pallé, E., Reiners, A., et al. 2020, A&A, 640, L5

Zakhozhay, O. V., Launhardt, R., Trifonov, T., et al. 2022, A&A, 667, L14

Zhang, M., Knutson, H. A., Dai, F., et al. 2023, AJ, 165, 62

Zhang, Y., Snellen, I. A. G., Wyttenbach, A., et al. 2022, A&A, 666, A47

List of Figures

List of Tables